

# UC Berkeley

## UC Berkeley Electronic Theses and Dissertations

### Title

Spatially resolved, quantitative measurement tools for complex, three-dimensional nanoporous systems

### Permalink

<https://escholarship.org/uc/item/5kt0h61t>

### Author

Su, Alison Nai-chen Carter

### Publication Date

2021

Peer reviewed|Thesis/dissertation

Spatially resolved, quantitative measurement tools for complex, three-dimensional  
nanoporous systems

by

Alison Su

A dissertation submitted in partial satisfaction of the  
requirements for the degree of

Joint Doctor of Philosophy with the University of California, San Francisco

in

Bioengineering

in the

Graduate Division

of the

University of California, Berkeley

Committee in charge:

Professor Amy E. Herr, Chair  
Professor Bo Huang  
Assistant Professor Markita P. Landry

Summer 2021

Spatially resolved, quantitative measurement tools for complex, three-dimensional  
nanoporous systems

Copyright 2021  
by  
Alison Su

## Abstract

Spatially resolved, quantitative measurement tools for complex, three-dimensional nanoporous systems

by

Alison Su

Joint Doctor of Philosophy with the University of California, San Francisco in  
Bioengineering

University of California, Berkeley

Professor Amy E. Herr, Chair

Spatial measurements can provide invaluable insight into complex, multidimensional systems by highlighting heterogeneities and/or features otherwise masked by bulk measurements. However, workflows designed to quantify spatial information require a multidisciplinary approach that includes meticulous consideration of the optics governing the system and spatial readout method to generate data that accurately represent the system of interest. Consequently, there is a need for robust workflows that quantify not only spatially resolved measurements, but also the accuracy of those measurements. To address this need, we sought to design spatially resolved quantification workflows to characterize salient properties of two distinct nanoporous systems: (1) equilibrium distribution of solutes between hydrogel and free solution, which can guide hydrogel design for specific functionalities, and (2) ultraviolet-C (UV-C) dose distribution across N95 filtering facepiece respirators, a metric that underpins the implementation of safe and effective decontamination protocols during crisis-capacity N95 shortages such as that observed during the COVID-19 pandemic.

We will first explore how three-dimensional quantification of equilibrium solute distributions between a nanoporous hydrogel and free solution (thermodynamic partitioning) can highlight important functional hydrogel properties. We will discuss the advantages and disadvantages of optical sectioning microscopy techniques to quantify thermodynamic partitioning, emphasizing the impact of measurement artefacts caused by refractive index mismatches in the optical path. To address these measurement artefacts, we will introduce and validate “aberration-compensated laser scanning confocal microscopy” (AC-LSCM), a dual technique and analytical pipeline that robustly quantifies spatially resolved thermodynamic partitioning *in situ*. Using AC-LSCM, we will examine how various structural changes introduced to the hydrogel influence not only the spatial partitioning behavior of solutes as compared to unmodified hydrogels, but also hydrogel-induced artefacts that can confound quantification.



Next, we will transition from studying three-dimensional nanoporous materials filled with water (hydrogels) to those filled with air (N95 filtering facepiece respirators). We will explore the importance of spatial resolution for UV-C dose measurements, especially on complex three-dimensional targets such as multilayered N95 respirators. To elucidate the underlying causes and effects of common UV-C dose measurement errors, we will review important optics principles governing UV-C spatial distribution and detection that reveal existing incompatibilities between the design of UV-C decontamination systems and UV-C sensors. To inform and validate safe and effective UV-C decontamination protocols of N95s, we apply principles from optics, physics, and colorimetry to convert UV-C photochromic indicators (PCIs) into robust quantitative UV-C dosimeters for on-N95 dose characterization. Using PCIs, we will characterize the impact of N95 shape on UV-C dose distribution and discuss important considerations associated with UV-C dose quantification using PCIs related to accuracy, UV-C specificity, dynamic range, and color readout.

We will then discuss how we can apply PCI quantification to perform simultaneous spatially resolved measurements of UV-C dose and viral inactivation across N95 respirator surfaces. By harnessing high resolution and modular optical simulations, we will examine how *in situ* PCI measurements synergize with *in silico* optical simulation results to rapidly inform design of dual UV-C dose/viral inactivation experiments. The results of these experiments highlight how N95 respirator shape substantially narrows the range between effective and N95-damaging UV-C treatments.

Finally, we explore the use of planar optical attenuators to extend PCI dynamic range and investigate how additional material in the optical path impacts measurement accuracy. Through an analytical model, we discuss the difference between diffuse and specular materials and material properties that influence both attenuation and measurement accuracy. For two example materials, we observe an inherent tradeoff between extending the dynamic range and maintaining measurement accuracy through angle-independent transmission.

In total, we introduce quantitative workflows to scrutinize, with spatial resolution, two complex, three-dimensional nanoporous systems: hydrogels (where nanopores are filled with water), and N95 filtering facepiece respirators (where nanopores are filled with air). Using a multidisciplinary framework, we discuss the origin of common measurement artefacts that can be captured during data acquisition and how we sought to address such artefacts. While careful consideration of the limitations of any measurement tool are paramount, we anticipate these measurement tools will continue to support and advance understanding of three-dimensional nanoporous systems by incorporating spatial information as part of the measurement readout.

To my family

# Contents

<b>Contents</b>	<b>ii</b>
<b>List of Figures</b>	<b>iv</b>
<b>List of Tables</b>	<b>vii</b>
<b>1 Introduction</b>	<b>1</b>
1.1 Thermodynamic partitioning in hydrogels . . . . .	1
1.2 UV-C decontamination of N95 respirators to address pandemic-induced world-wide shortages . . . . .	4
<b>Bibliography</b>	<b>10</b>
<b>2 <i>In Situ</i> Measurement of Thermodynamic Partitioning in Open Hydrogels</b>	<b>13</b>
2.1 Introduction . . . . .	13
2.2 Materials and Methods . . . . .	16
2.3 Results and Discussion . . . . .	21
2.4 Conclusions . . . . .	40
<b>Bibliography</b>	<b>42</b>
<b>3 Current Understanding of Ultraviolet-C Decontamination of N95 Filtering Facepiece Respirators</b>	<b>48</b>
3.1 Background . . . . .	48
3.2 Literature Review . . . . .	51
3.3 Efficacy of UV-C on inactivation of other pathogens . . . . .	56
3.4 Sunlight is not likely to be an effective decontamination approach for N95 FFRs	58
3.5 Integrity of N95 FFRs after UV-C treatment . . . . .	59
3.6 US federal guidelines: CDC, FDA, OSHA . . . . .	62
3.7 Other applications of UV-C for pathogen reduction . . . . .	62
3.8 Implementation strategies . . . . .	62
3.9 Summary and Outstanding Questions . . . . .	65
3.10 Conclusions . . . . .	66

<b>Bibliography</b>	<b>67</b>
<b>4 Best practices for germicidal ultraviolet-C dose measurement for N95 respirator decontamination</b>	<b>74</b>
4.1 Introduction . . . . .	74
4.2 Conclusions . . . . .	85
<b>Bibliography</b>	<b>86</b>
<b>5 Quantitative UV-C dose validation with photochromic indicators for informed N95 emergency decontamination</b>	<b>91</b>
5.1 Introduction . . . . .	91
5.2 Materials and Methods . . . . .	96
5.3 Results and Discussion . . . . .	105
5.4 Conclusions . . . . .	131
<b>Bibliography</b>	<b>133</b>
<b>6 Mapping of UV-C dose and SARS-CoV-2 viral inactivation across N95 respirators during decontamination</b>	<b>138</b>
6.1 Introduction . . . . .	138
6.2 Materials and Methods . . . . .	140
6.3 Results and Discussion . . . . .	152
6.4 Conclusions . . . . .	165
<b>Bibliography</b>	<b>167</b>
<b>7 Optical attenuators extend dynamic range but alter angular response of planar ultraviolet-C dosimeters</b>	<b>171</b>
7.1 Introduction . . . . .	171
7.2 Materials and Methods . . . . .	173
7.3 Results and Discussion . . . . .	177
7.4 Conclusions . . . . .	189
<b>Bibliography</b>	<b>190</b>
<b>8 Conclusions and future directions</b>	<b>195</b>
<b>Bibliography</b>	<b>197</b>
<b>A Chambered coverslip silanization</b>	<b>198</b>
<b>B Recommended reporting summary for studies using UV-C</b>	<b>200</b>

# List of Figures

1.1	Schematic of thermodynamic partitioning . . . . .	2
1.2	Example interactions that impact thermodynamic partitioning. . . . .	2
1.3	Relative spectral output of various sources used for UV-C germicidal irradiation	6
1.4	Specular and angular resposivities of commercial sensors marketed for water disinfection monitoring from six different manufacturers . . . . .	7
2.1	AC-LSCM setup . . . . .	15
2.2	Mask design for photopatterning partition coefficient SU-8 molds . . . . .	18
2.3	AC-LSCM analysis workflow . . . . .	20
2.4	Axial optical artefacts caused by refractive index mismatch in the light path . .	22
2.5	Image math performed to calculate $K$ . . . . .	23
2.6	Concentration vs. mean intensity of Alexa Fluor 647 . . . . .	23
2.7	Reflection z-series micrographs inform correction collar positioning . . . . .	25
2.8	Validation of AC-LSCM measurement system . . . . .	28
2.9	$K$ measured in macroscale gels using conventional mass balance and AC-LSCM.	29
2.10	Relationship between gel height and solution intensity ratio (SIR) over varying microscale PA gel densities . . . . .	29
2.11	Characterization of axial artefacts in 18%T microscale PA gels as a function of correction collar position. . . . .	30
2.12	CV vs. measured aberration ( $\delta_{SIR}$ ) for open microscale PA gels of varying densities	30
2.13	Preliminary microcassette partitioning experiments using photoactivated gels. .	32
2.14	Comparison of partitioning behavior of Ab* and Fab* in photoactivated BPMAC-containing and vehicle control gels. . . . .	33
2.15	Retention of Ab* and Fab* after unloading from gel. . . . .	34
2.16	Impact of median filter on quantification . . . . .	35
2.17	Partition coefficient, $K$ , is sensitive to PA gel formulation . . . . .	36
2.18	Two-layer gel setup and representative micrograph . . . . .	37
2.19	Two-layer gel structures exhibit more complex partitioning behavior than single-layer control gels of same nominal pore size. . . . .	38
2.20	Schematics and representative fluorescence intensity profiles of two-layer gel systems with different gel layer configurations in equilibrium with TI* . . . . .	40
2.21	Method for quantifying and correcting aberration-induced depth-dependence of in-gel fluorescence . . . . .	41

4.1	Factors affecting UV-C dose distribution and measurement for N95 decontamination. . . . .	77
5.1	Mechanism and challenges of UV-C for N95 decontamination . . . . .	93
5.2	Robust color measurement facilitates UV-C dose quantification from two PCI models . . . . .	107
5.3	Comparison dose-response curves of two different batches of PCI1 . . . . .	108
5.4	Comparison of alternative color difference metrics . . . . .	108
5.5	Comparison of calibration fit functions for PCI2 . . . . .	109
5.6	Calibration curve fit and relative uncertainty on measurements using red, green, and blue colorimetric absorbance . . . . .	111
5.7	Relative quantification uncertainty depends on both measured UV-C dose and measured $\Delta E$ uncertainty . . . . .	112
5.8	Relative uncertainty on measurements using alternate color difference metrics . . . . .	114
5.9	Assessing PCI specificity to germicidal UV-C wavelengths . . . . .	115
5.10	Radiometer correction factor . . . . .	117
5.11	Angular response affects quantification of spatial nonuniformity . . . . .	118
5.12	Correction factor validation using mask/aperture setup. . . . .	119
5.13	Correction factor validation using PCIs . . . . .	120
5.14	Spatial nonuniformity across the treatment plane measuring using simulation, radiometer, and both PCI models . . . . .	121
5.15	Image comparing physical sensors . . . . .	122
5.16	Quantifying PCIs elucidates UV-C treatment questions not measurable with radiometers . . . . .	123
5.17	PCIs for spatially resolved measurements . . . . .	125
5.18	Potential broader applications for UV-C quantification from PCIs using widely available color measurement tools . . . . .	126
5.19	Imaging quantification uncertainty using widely available tools . . . . .	127
5.20	Irradiance variability over time and between UV-C systems . . . . .	128
5.21	Optical attenuation as a method to extend PCI dynamic range beyond $1.0 \text{ J/cm}^2$ . . . . .	130
6.1	Two UV-C chambers have similar irradiance profiles over time and space . . . . .	141
6.2	Equivalent performance of two ILT1254 radiometers . . . . .	141
6.3	UV-C dose quantification from PCI color change. . . . .	142
6.4	PCI calibration curve is batch-dependent. . . . .	143
6.5	PCI angular response measurement . . . . .	144
6.6	Preprocessing of scanned N95 for optical model . . . . .	145
6.7	Map for <i>in-situ</i> measurements on chamber floor . . . . .	146
6.8	Optical model identifies paired measurement sites for <i>in-situ</i> PCI measurements . . . . .	147
6.9	Chamber floor map for on-N95 measurements. . . . .	148
6.10	Simulation correlates with <i>in-situ</i> measurements of UV-C distribution across chamber floor . . . . .	150

6.11	<i>In-situ</i> irradiance mapping determines coupon placement . . . . .	150
6.12	Chamber floor map for coupon study. . . . .	151
6.13	SARS-CoV-2 inactivation does not depend on expiration status of 3M 1860 N95 coupons used in this study . . . . .	152
6.14	Integrated optical modeling and <i>in-situ</i> PCI measurement pipeline for simultaneous & near-coincident on-N95 UV-C dose and viral inactivation measurements	153
6.15	Correspondence between simulated and <i>in-situ</i> measured on-N95 UV-C dose distribution using PCIs. . . . .	154
6.16	N95-to-N95 variation in morphology. . . . .	155
6.17	Measurement of UV-C dose required for SARS-CoV-2 inactivation on N95 coupons is informed by optical modeling and <i>in-situ</i> PCI dose measurements . . . . .	156
6.18	Correspondence between radiometer and PCI-measured UV-C doses during coupon experiments . . . . .	157
6.19	SARS-CoV-2 is inactivated by >3-log on N95 coupons when exposed to 0.5-1.5 J/cm <sup>2</sup> UV-C . . . . .	158
6.20	Chamber heating does not significantly impact SARS-CoV-2 inactivation . . . .	159
6.21	Hydrophobicity of 3M 1860 N95 coupons . . . . .	159
6.22	Paired on-N95 measurements of UV-C dose and log SARS-CoV-2 inactivation show correlated, several-fold variation in dose and inactivation across one decontamination chamber . . . . .	162
6.23	Normalized on-N95 SARS-CoV-2 dose-response curve for 2 N95 facepieces . . .	163
7.1	Schematics of measurement setups to characterize borosilicate transmittance and PCI-attenuator stack angular response . . . . .	174
7.2	UV-C chamber floor map for calibration curve measurements . . . . .	175
7.3	UV-C chamber floor map for on-N95 measurements . . . . .	176
7.4	Attenuator material properties govern dynamic range and angular response of PCI-attenuator stacks. . . . .	178
7.5	Attenuators extend PCI dynamic range. . . . .	181
7.6	Borosilicate transmittance measurement involves a maximum angle of incidence of 10.1° from apertured UV-C source. . . . .	182
7.7	Concordance of analytical and empirical angular response of PCIs stacked with specular and diffuse attenuator materials . . . . .	183
7.8	Analytical and empirical angular responses of PCI-attenuator pairs are concordant	184
7.9	On-N95 UV-C dose measurement error depends on attenuator and on-N95 location.	186
7.10	Use of incorrect calibration curve can yield dose-dependent measurement error .	188

# List of Tables

2.1	Composition of PEG-porogen polyacrylamide gels . . . . .	17
2.2	Parameters to estimate diffusion time ( $3\tau$ ) . . . . .	27
2.3	Partition coefficients of Ab* and Fab* in vehicle control and photoactivated 6%T w/v microscale PA gels . . . . .	32
2.4	$K$ of composite, two-layer gel structures measured by AC-LSCM . . . . .	37
3.1	Efficacy of UV-C for inactivation of microorganisms . . . . .	51
3.2	Impact of UV-C on N95 filtering facepiece respirator integrity . . . . .	60
3.3	Published implementation strategies for UV-C N95 respirator treatment . . . . .	63
4.1	Common pitfalls in UV-C dose measurement for N95 decontamination . . . . .	81
4.2	Importance of considering over- and under-reporting of UV-C dose . . . . .	82
5.1	Fit functions, inverse fit functions, and partial derivatives used in uncertainty calculations for calibrated measurements. . . . .	99
5.2	RM200QC measurement uncertainties for various metrics of color quantification and two PCI models . . . . .	100
5.3	Specifications for robust UV-C measurements . . . . .	105
5.4	Quantified on-N95 relative doses (normalized to the apex location 1 of the exterior of the central respirator) measured with PCI1 . . . . .	124
6.1	Additional optical model specifications . . . . .	145
7.1	Significance of linear correlation between true and measured dose for each attenuator and on-N95 location tested. . . . .	187



## Acknowledgments

“If I have seen further, it is by standing on the shoulders of giants.” - Isaac Newton

My path to graduate school was shaped by mentors who fostered my love for science. I learned so much under the guidance of Prof. Lisa Larkin and Prof. Jessica Schwartz, who patiently taught me the basics of scientific inquiry as an eager high school student in their labs. I am grateful to Prof. Barjor Gimi and Prof. Ormond MacDougald (and Prof. William Cawthorn), who took me on for research fellowships as an undergraduate. Prof. Karl Griswold and Prof. Tillman Gerngross both ignited my passion for biomolecular engineering, which ultimately led to my position at Adimab, where I had the honor to learn from Dr. Bianka Prinz and Dr. Hemanta Baruah.

I feel incredibly fortunate to have conducted my PhD research under the guidance of Prof. Amy Herr. Amy has an unbridled enthusiasm for science that is inspiring and contagious. Her dedication to mentorship propels her students to become better stewards of science. She expects nothing short of excellence (pressure makes diamonds, after all), but while you're putting in 110%, she's putting in 1000%. Amy encourages (and sometimes nudges) her students to step out of their comfort zone, and as a result, I know that I have become a more inquisitive, thoughtful, and outspoken scientist. Thank you, Amy, for everything.

Though lab ethos originates at the top, lab culture, and ultimately much of the graduate school experience, is shaped by the people you interact with day-to-day. Members of the Herr lab are some of the most brilliant, hardworking, and kind people I've had the honor to work with and learn from during graduate school. I am so appreciative of the lab culture they cultivate, which values curiosity and perseverance alongside collaboration and camaraderie. I am particularly grateful for the mentorship and research guidance provided by Herr lab alumni Eli, Elaine, John, Hector, Shaheen, Kevin, and Julea, as well as thoughtful discussions with Anjali, Alden, Louise, Gabi, and Ana. I was incredibly lucky to join the Herr lab alongside Alisha, Kristine, and Andoni, who have provided endless support as we've sprinted this marathon together. A special thanks to Alisha, for braving multiple undergraduate classes with me - you are so kind and thoughtful, and your ability to juggle 4 billion things at once baffles me. And Doni - thank you for your endless support both inside and outside lab. We did not let them break us down to dust, we know that there's a place for us, for we are glorious. I thank my lucky stars for Samantha, whose scientific prowess, kindness, and generosity greatly influenced my graduate school experience.

I was also fortunate to receive guidance from several faculty members across UC Berkeley and UCSF. Thank you to my qualifying exam committee, including Prof. Aaron Streets, Prof. Dan Fletcher, Prof. Jim Wells, & Prof. Evan Miller for helpful feedback and suggestions on the partitioning work, and to my outside dissertation committee members Prof. Bo Huang and Prof. Markita Landry, who both asked thoughtful questions and exhibited extraordinary patience when Zoom sabotaged our meetings. Though I did not interact with

her directly, I want to thank Prof. Jennifer Doudna for always smiling and waving to me when we'd cross paths.

The research presented in this dissertation was not conducted alone, but through collaborations with some truly incredible scientists outside of the Herr lab. I am grateful to have worked with Dr. Ben Smith, whose passion for microscopy is contagious. I was both humbled and honored to be a part of the N95DECON team, who inspired me and frequently lifted my spirits as we lived through a global pandemic together. From that team, I would specifically like to thank close collaborators Dr. Josh Molho and Dr. Halleh Balch. The SARS-CoV-2 work would not have been possible without Dr. Allison Roberts and Dr. Guillaume Golovkine, as well as Prof. Sarah Stanley. It was such a privilege to learn from and collaborate with Dr. C. Cameron Miller, Dr. Toni Litorja, Thomas Larason, and Clarence Zarobila from the National Institute of Standards and Technology. I am also thankful for Dr. Csilla Timár-Fülep, who provided technical support as I learned the ins and outs of Zemax OpticStudio.

Much of this work required access to specialized instruments on campus. A big thank you to Holly Aaron & Feather Ives (Molecular Imaging Core), Paul Lum & Dr. Naima Azgui (Biomolecular Nanotechnology Center), and Dr. Mary West (Stem Cell Facility) for providing training and for maintaining and troubleshooting such complex devices. We also received generous donations from numerous sources during the COVID-19 pandemic that made the N95 UV-C decontamination studies possible. Thanks to: Dr. S. Subbiah and David Lineberger for loaning us an OpticStudio Pro license; Leigh Veasey and Claes Lindahl for UV-C 254 dots; Daniel Tristan, Gustavo Garcia, Betty Cheng, and Prof. Dorian Liepmann for customized UV-C equipment; Ron Moody for loaning us an extra radiometer; and Dr. Aenor Sawyer, Dr. Nichole Starr, Kristen Bole, and OTM Oakland, CA for N95 respirators.

Of course, none of this work would have been possible without financial support from the National Science Foundation Graduate Research Fellowship and the Tom & Stacey Siebel Foundation Siebel Scholarship. I am additionally grateful to funding from the National Institutes of Health, and the UC Berkeley College of Engineering Dean's COVID-19 Emergency Fund.

It takes a village to navigate graduate school. I am indebted to Catherine Dea and Rocío Sanchez, who patiently solved all of my administrative questions. A huge thank you to the Stanley Hall Receiving Team for delivering countless packages, and the Stanley Hall Facilities team for their efforts to keep Stanley Hall both beautiful and operational. I am also incredibly grateful for Dr. Sharon Smart, who profoundly improved my graduate school experience.

Finally, I'd like to thank my family. To my mom and dad, who raised me to believe that I could achieve anything I put my mind to, and subsequently supported me unconditionally as I sought those achievements. To Elizabeth and Andrew, for so many dinners full of laughs, love, encouragement, and ice cream, who inspire and remind me to live in the present moment. To Nanny and Boppy, who were with me every step of the way. To Wally, the best dog anyone could ever dream of. And to my partner Ellen, whose compassion and

steadfast resolve never cease to amaze me. Thank you for always believing in me, anchoring me, bolstering me through the lows, and celebrating with me during the highs.

# Chapter 1

## Introduction

Spatial composition and context are frequently valuable to scientific measurements and advancements. Oncology research, for example, benefits from multiple levels of spatial information: the microenvironment surrounding a tumor plays an important role in cancer development, prognosis, and therapeutic response [1, 2], the heterogeneity and spatial distribution of cells within that tumor can underpin therapeutic resistance [3], and even within individual cells, subcellular protein localization is linked to function and/or dysfunction [4]. With increasing evidence that spatial context can provide valuable insight, spatially resolved measurements are an area of growing interest. Just last year, “spatially resolved transcriptomics” was named Method of the Year by *Nature Methods* [5], and within the last 10 years, the Nobel Prize in Chemistry has been awarded twice in recognition of microscopy advancements: once for super-resolution microscopy (2014), and a second time for cryogenic electron microscopy (2017). The added value of spatial context to measurements motivated the work presented in this dissertation, which focuses on the development of spatially resolved quantification workflows to characterize properties of two different nanoporous systems: (1) thermodynamic partitioning of solutes into nanoporous hydrogels, and (2) UV-C dose distribution across nanoporous N95 filtering facepiece respirators.

### 1.1 Thermodynamic partitioning in hydrogels

#### Motivation

Hydrogels are a class of versatile materials harnessed across myriad fields, from wastewater treatment to cosmetic and hygiene product development to biomedical engineering [6]. Within the field of biomedical engineering, hydrogels have served as scaffolds for applications such as drug delivery [7], cell and tissue engineering [8], and analytical sensing [9]. Hydrogels find such broad utility in part due to their highly tunable physicochemical properties; tuning these properties enables the same hydrogel material to serve as a drug release vehicle as well as an analyte-binding sensor.

One important adjustable property of interest when designing hydrogels is permeability, which encompasses both solute transport (diffusion) and equilibrium distribution (thermodynamic partitioning) [10]. Thermodynamic partitioning occurs when two immiscible phases (e.g., hydrogel and solute-containing solution) are brought into contact; the solute will distribute between the two phases until equilibrium is achieved (Figure 1.1) [11]. Ther-

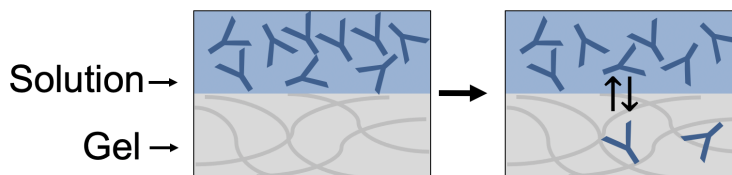


Figure 1.1: Thermodynamic partitioning between gel and solution distributes solute between both phases until equilibrium is achieved. This process is depicted schematically with antibody as an example solute.

ermodynamic partitioning is influenced by all of the interactions that can occur between the gel and solute, such as electrostatic, hydrophobic, and size-based interactions [11]; thus, the partitioning behavior of a given solute can be engineered by altering the gel-solution system (Figure 1.2).

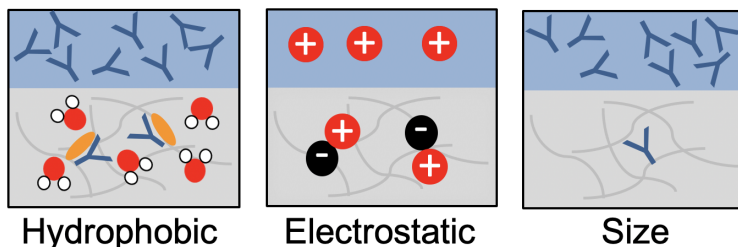


Figure 1.2: Schematic depicting example interactions that impact thermodynamic partitioning.

Thermodynamic partitioning is quantified through a partition coefficient,  $K$ , defined as the ratio at equilibrium of solute concentration in the gel and surrounding free solution [11]:

$$K = \frac{[solute]_{gel}}{[solute]_{solution}} \quad (1.1)$$

Note that empirical  $K$  measurements represent a combination of all gel-solute interactions, some of which may not be reversible when the gel is introduced to solute-free solution for desorption. As a result, in cases where solute release or additional information about which interactions are present is important, solute unloading must also be assessed.

## Partition coefficient measurement landscape

Here, we briefly summarize three techniques for quantifying thermodynamic partitioning of solutes into hydrogels and discuss advantages and disadvantages of each.

- **Mass balance:** The most common  $K$  measurement approach, mass balance (also termed “back extraction”, or “solution depletion” in literature) applies a material balance to indirectly quantify  $K$  based on the volume ( $V$ ) of the gel and solution and the initial and final solute concentration ( $[C]_{0,soln}$  and  $[C]_{f,soln}$ , respectively) in surrounding solution after equilibrium is established [12]:

$$K = \frac{V_{sol}}{V_{gel}} \left( \frac{[C]_{0,soln}}{[C]_{f,soln}} - 1 \right) \quad (1.2)$$

$[C]_{0,soln}$  and  $[C]_{f,soln}$  can be measured using spectroscopy to quantify the magnitude of solute absorbance in free solution at a distinguishing wavelength before and after gel-solution equilibration [12]. Thus, the mass balance approach can measure solute in its final application format without additional labels (e.g., fluorescent tags) required for readout. Modifications to solutes, including the addition of fluorescent tags, will alter partitioning behavior and potentially confound results if the solute will not be modified in the same way for end-use. As a bulk measurement approach, however, mass balance measurements cannot provide information on the spatial distribution of solute throughout the hydrogel. Spatial information can highlight heterogeneities and other local phenomena that govern functionality [13].

- **Size-exclusion chromatography:** Also an indirect measurement method like the mass balance approach, size-exclusion chromatography (SEC) uses a column packed with gel beads to measure  $K$  [14, 15]. The governing principle of SEC is that larger, non-interacting solutes are excluded from the gel bead volume, and thus will elute faster compared to smaller solutes which partition into the gel beads and subsequently take longer to flow through the column.  $K$  can be calculated based on the elution volume ( $V_e$ ), void volume ( $V_0$ , volume not occupied by gel beads), and total column volume ( $V_t$ ) using the following equation [15]:

$$K = \frac{V_e - V_0}{V_t - V_0} \quad (1.3)$$

Similar to the mass balance approach, SEC does not require labeling of the solute for visualization, but as a result also does not provide information on the spatial distribution of solutes within the gel beads. Additionally, SEC is limited in sensitivity as there is high uncertainty for measurements of small  $K$  values where the numerator of Eq. 1.3 approaches 0 [15].

- **Fluorescence microscopy:** Fluorescence microscopy harnesses fluorescently labeled solutes to measure  $K$  directly, where fluorescence intensity ( $I$ , background subtracted) serves as a proxy for solute concentration:

$$K = \frac{[\text{solute}]_{\text{gel}}}{[\text{solute}]_{\text{solution}}} = \frac{I_{\text{gel}}}{I_{\text{solution}}} \quad (1.4)$$

Eq. 1.4 is only valid within the solute concentration range where intensity is linear with fluorophore concentration. Unlike mass balance and SEC, fluorescence microscopy is a direct measurement approach that can illuminate the spatial distribution of the solute within the hydrogel with 3-D resolution through the use of optical sectioning techniques such as confocal microscopy. However, readout requires fluorescent labeling fluorescence labels can affect solute partitioning in multiple ways by adding volume to the relative solute size and/or altering the effective isoelectric point [16]. Specialized microscopy techniques exist that can capture spatial distribution of non-fluorescent solutes, such as confocal Raman microscopy which measures sample-specific molecular vibrational patterns [17].

Unfortunately, there is rarely a “one size fits all” approach for scientific measurements. As a result, researchers must first identify and prioritize parameters of interest in order to select or design a measurement method that best suits the research question. Here, we were acutely interested in investigating how partitioning influences nanoporous polyacrylamide hydrogel performance as an immunoassay scaffold, where the solute of interest (immunoprobe) is frequently fluorescently labeled for endpoint readout. Thus, this application synergizes with the fluorescence microscopy approach for partitioning measurements, as the influence of the dye on  $K$  mimics the end assay format. However, microscopy is subject to optical aberrations, which confound quantification [18]. As a result, measurement tools that characterize the impact of system design on quantification are paramount to accurate  $K$  quantification using fluorescence microscopy, as will be discussed in Chapter 2.

## 1.2 UV-C decontamination of N95 respirators to address pandemic-induced worldwide shortages

### Motivation

On March 17<sup>th</sup>, 2020, Alameda County issued a “shelter-in-place” order in response to the emerging COVID-19 pandemic, which would claim  $\sim 2.8$  million lives globally over the next year, and  $>4$  million lives at the time of this writing [19]. The unprecedented demand for personal protective equipment like multilayered, nanoporous, made-for-single-use N95 filtering facepiece respirators, caused a worldwide shortage; a survey for 20,000 nurses in the United States conducted between July and August of 2020 by the American Nurses

Association [20] revealed that 68% were required by their facilities to reuse designed-for-single-use N95 respirators. On March 23<sup>rd</sup>, 2020, I joined <https://www.n95decon.org/>, a scientific consortium spanning the public and private sectors focused on understanding, compiling, and disseminating literature on N95 respirator decontamination for crisis capacity reuse. Amy’s subteam focused specifically on ultraviolet-C (UV-C) irradiation as an N95 decontamination method; the rest of the work presented in this dissertation is centered around these efforts.

### UV-C basics and terminology:

The ultraviolet spectrum can be subclassified into 3 different regions: UV-A (315-400 nm), UV-B (280-315 nm) and UV-C (100-280 nm) [21]. Germicidal UV-C irradiation harnesses a subset of the UV-C spectrum (200-280 nm) that overlaps significantly with the absorption spectra of nucleic acids and proteins. This overlap imparts wavelength-dependent germicidal efficacy, as the UV-C photons are absorbed by nucleic acids and proteins associated with pathogens and catalyze photochemical reactions that hinder replication [22].

The term “irradiance” refers to the number of photons incident on a surface over time per unit area. Following Lambert’s cosine law [23], the irradiance at non-normal incidence  $\theta$  is reduced from normal incidence by a factor of  $\cos(\theta)$ . The cumulative spectral irradiance over time is defined as the fluence:

$$\text{Fluence} = \int_{t_1}^{t_2} I(\lambda) dt \quad (1.5)$$

Differences in genetic/proteinic composition cause pathogens to vary in UV-C susceptibility (i.e., differing action spectra); as a result, the germicidal dose for a given pathogen is defined as the fluence weighted by the pathogen action spectrum,  $S(\lambda)$  [21]:

$$\text{Effective dose} = \int_{t_1}^{t_2} I(\lambda) \cdot S(\lambda) dt \quad (1.6)$$

Note that the term “fluence” accounts for photons incident from all directions, while the term “radiant exposure” refers specifically to photons incident on a surface over time [21]. In the literature, the term “dose” is frequently applied to describe the photons incident on a sensor surface (radiant exposure), which is subsequently referenced as the “dose” required for pathogen inactivation. “Dose” is used similarly in this dissertation to remain consistent with most UV-C decontamination literature. The UV-C dose required for inactivation is typically reported in terms of  $\log_{10}$  reduction, where 3- $\log_{10}$  reduction corresponds to 99.9% inactivation.

### UV-C measurement landscape:

The UV-C dose required to inactivation a specific pathogen is typically determined in a highly controlled research setting where both dose and pathogen inactivation can be characterized.



Pathogen inactivation measurements are laborious and, in the case of N95s, involve extensive modification of the respirator to assess pathogen recovery; thus, UV-C dose measurements are the cornerstone for safe and effective implementation of UV-C decontamination protocols. However, UV-C dose measurements are deceptively simple and are often reported without sufficient detail for reproduction.

Recalling that decontamination efficacy is wavelength-dependent, accurate measurements of UV-C dose associated with pathogen reduction requires the source and sensor to be spectrally matched. However, commonly used UV-C sources vary in their relative spectral outputs (and consequently, relative germicidal effectiveness, see Eq. 1.6) (Figure 1.3). Low

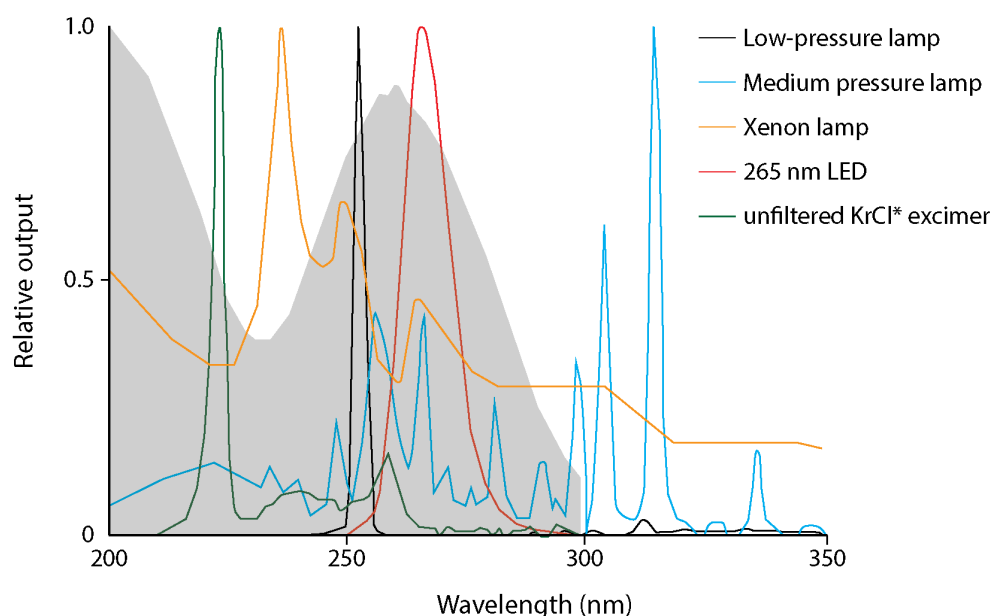


Figure 1.3: Relative spectral output of various sources used for UV-C germicidal irradiation. All spectra are normalized to the maximum output within the 200-350 nm range. Gray shaded region indicates relative DNA absorbance.

pressure mercury/amalgam lamps are the gold standard and emit near-monochromatically at 254 nm, near the peak absorption of nucleic acids (an amalgam is frequently used to replace pure mercury to impart enhanced temperature stability [22]). In contrast, excimer lamps emit predominantly at  $\sim 222$  nm [24] while medium pressure mercury lamps and xenon arc lamps emit over a broader spectrum that extends beyond the UV-C range (200-400 nm and 100-1000 nm, respectively) [25]. UV-C LEDs are compact, mercury-free alternatives with tunable wavelength output across the germicidal UV-C range [26] but tend to be less efficient than other UV-C sources. Adding further complexity, the spectral sensitivity of UV-C sensors marketed for germicidal applications is not standardized, and as a result, can vary significantly between different sensors marketed for germicidal dose monitoring (Figure 1.4A).

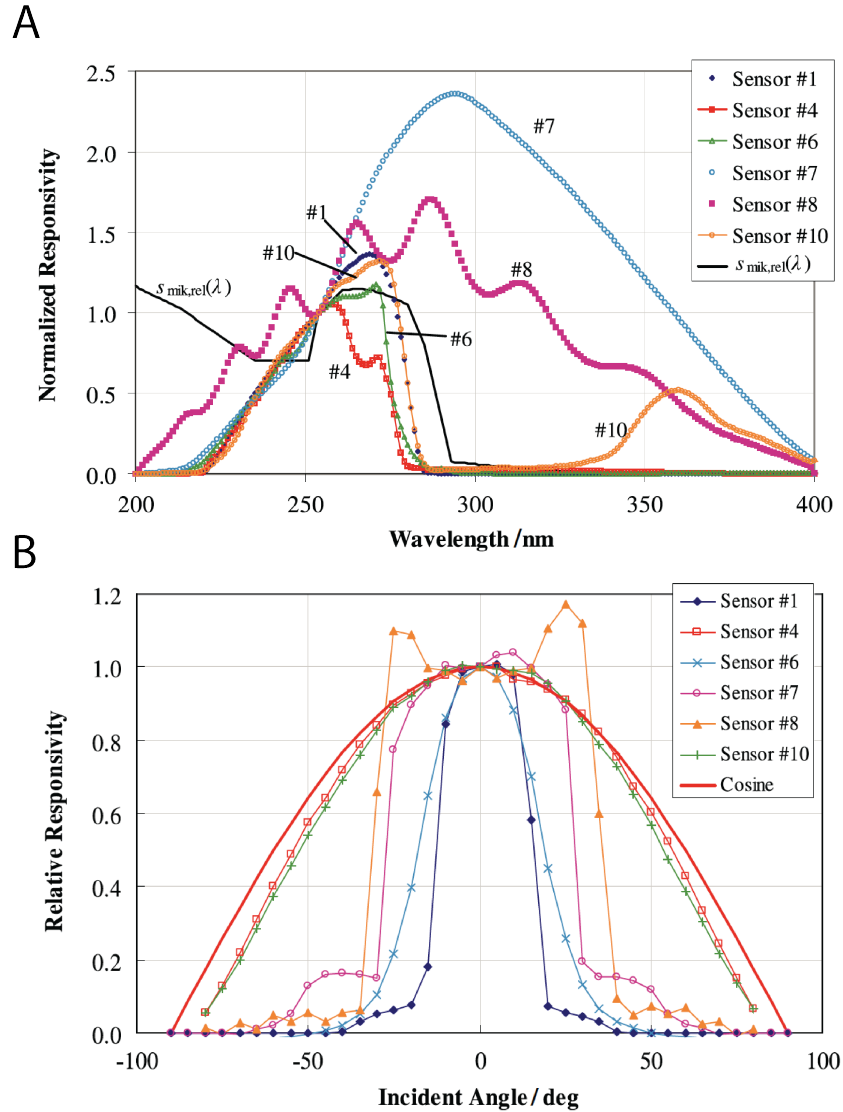


Figure 1.4: Spectral and angular responsivities of commercial sensors marketed for water disinfection monitoring from six different manufacturers vary substantially. (A) Relative (normalized to 254 nm) spectral responsivities of sensors.  $s_{mik,rel}(\lambda)$  indicates normalized microbicidal action spectrum. (B) Relative angular responses of sensors compared to ideal cosine response. ©BIPM and IOP Publishing Ltd. Figures reproduced from [27] by permission from IOP Publishing. All rights reserved.

In practice, the combined variation in spectral output and spectral sensitivities between UV-C sources and sensors, respectively, stymies reproducibility. Currently, different sensors can report different “germicidal” doses for the same nominal UV-C source output due to varying sensor spectral sensitivities. In a worst-case scenario observed during the COVID-19 pandemic, manuscripts were posted on preprint servers that reported UV-C measurements

collected with a spectrally mismatched sensor. One such manuscript was highlighted in a New York Times article [28] a day after posting; over the eight days that elapsed between the release of the New York Times article and a revised preprint posting, the article may have been viewed up to 66,000 times, according to MedRxiv reported metrics.

UV-C dose measurements are further hindered by complex governing optics. Dose is a function not only of wavelength, but also of distance and angle of incidence (Lambert’s cosine law) [22]. Sensors are typically designed and calibrated for use with collimated UV-C, and have been shown to vary in angular responses (and consequently measurement inaccuracies) to non-collimated UV-C common among commercial decontamination systems (Figure 1.4B). The effects of these measurement errors on implementation are further amplified by the wide diversity of UV-C system configurations and currently make replication and interpretation of UV-C decontamination studies near impossible.

## Dissertation overview

Chapter 1 introduces the background and motivation, as well as an overview of the work presented in this dissertation.

Chapter 2 presents the design, validation, and application of a laser scanning confocal-based microscopy and post-imaging analysis workflow, termed “**A**bserration-**c**ompensated **l**aser **s**canning **c**onfocal **m**icroscopy” (AC-LSCM), for measuring spatially resolved *in situ* thermodynamic partitioning of fluorescently labeled solutes in open, nanoporous microscale hydrogels. We discuss how refractive errors are introduced during imaging and we design AC-LSCM to harness the free solution surrounding the gel as an intrinsic control to quantify system- and gel-introduced aberrations that confound  $K$  quantification. After validation, we apply AC-LSCM to quantify  $K$  of fluorescently labeled solutes in single- and multilayer polyacrylamide hydrogels. Additionally, we scrutinize solute interactions with a UV photoactive polyacrylamide gel that incorporates a benzophenone methacrylamide backbone, and we investigate how the introduction of a progen that aggregates polyacrylamide chains during polymerization alters  $K$ .

Chapter 3 launches into the work performed during the COVID-19 pandemic by presenting a review of the landscape of N95 UV-C decontamination literature compiled by the UV-C subteam of N95DECON.org. The goal of this work was to understand, synthesize, and succinctly disseminate on an open access platform existing research on N95 decontamination. To highlight the rapid timeline of this work, we began writing version 1 on March 30<sup>th</sup> of 2020, and the document was released publicly two days later on N95DECON.org on April 1<sup>st</sup>. The review continued to undergo multiple revision cycles and was ultimately published in the journal *Applied Biosafety*.

Chapter 4 dives into the intricacies associated specifically with accurate UV-C dose measurements, with particular focus on decontamination protocols that target N95s. We discuss common measurement pitfalls in this field, as well as the consequences within both the research and clinical settings. In an effort to reduce mis- and under-reporting of key UV-C study criteria, we propose a reporting checklist targeted for authors to fill out prior to

submitting their work to a preprint server to assess whether they have included sufficient detail.

Chapter 5 describes a method to quantify commercially available UV-C photochromic (color-changing) indicators (PCIs) as robust UV-C dosimeters to assess UV-C dose distribution across N95 respirators. We present novel workflows rooted in colorimetry fundamentals to translate PCI color change into quantitative UV-C dose measurements. We discuss why high throughput, low cost, and surface-like PCIs are advantageous for N95 UV-C system configuration design and validation. Through analysis of two different UV-C PCI models, we highlight important technical specifications and application considerations and limitations end-users should evaluate prior to implementation of the PCI quantification workflow.

Chapter 6 introduces a novel measurement capability that extends the PCI quantification workflow developed in Chapter 5: simultaneous UV-C dose and SARS-CoV-2 inactivation measurements on intact N95 respirators within a commercial UV-C system. Using a CAD rendering of an N95 respirator and optical ray trace modeling software, we develop and validate a computational pipeline that illuminates N95 surfaces likely to receive the lowest and highest UV-C doses for informed and targeted *in situ* UV-C dose measurements. Finally, leveraging optical simulations and UV-C photochromic indicator measurements in parallel, we demonstrate how these two workflows can synergize to inform design of novel viral inactivation experiments that directly probe the relationship between SARS-CoV-2 inactivation and UV-C dose variation across N95 surfaces by quantifying both metrics simultaneously.

In Chapter 7, we investigate the use of planar optical attenuators stacked in front of PCIs to extend PCI dynamic range, and how the attenuators influence PCI measurement accuracy. Through an analytical model, we highlight the inherent tradeoffs between attenuation and angle-independent transmittance by assessing both model specular and model diffuse planar attenuators. The angular response and dynamic range of bare PCIs, as well as PCIs stacked behind two different attenuator materials, are quantified using an apertured UV-C source and compared to analytical model predictions. Finally, the two attenuator materials are stacked in front of PCIs affixed to N95 surfaces of varying slope, and the PCI quantification accuracy is evaluated within the context of a commercially available N95 UV-C decontamination system.

Finally, Chapter 8 presents a summary of the work included in this dissertation, as well as potential future directions. Appendices include additional details and protocols for reference.

# Bibliography

1. Tsujikawa, T. *et al.* Prognostic significance of spatial immune profiles in human solid cancers. *Cancer Science* **111**, 3426–3434. doi:10.1111/CAS.14591 (2020).
2. Junttila, M. R. & Sauvage, F. J. d. Influence of tumour micro-environment heterogeneity on therapeutic response. *Nature* *2013 501:7467* **501**, 346–354. ISSN: 1476-4687. doi:10.1038/nature12626 (2013).
3. Dagogo-Jack, I. & Shaw, A. T. Tumour heterogeneity and resistance to cancer therapies. *Nature Reviews Clinical Oncology* **15**, 81–94. doi:10.1038/NRCLINONC.2017.166 (2018).
4. Lundberg, E. & Borner, G. H. H. Spatial proteomics: a powerful discovery tool for cell biology. *Nature Reviews Molecular Cell Biology* *2018 20:5* **20**, 285–302. ISSN: 1471-0080. doi:10.1038/s41580-018-0094-y (2019).
5. Marx, V. Method of the Year: spatially resolved transcriptomics. *Nature Methods* *2021 18:1* **18**, 9–14. ISSN: 1548-7105. doi:10.1038/s41592-020-01033-y (2021).
6. Bahram, M., Mohseni, N. & Moghtader, M. *An Introduction to Hydrogels and Some Recent Applications in Emerging Concepts in Analysis and Applications of Hydrogels* (InTech, 2016). doi:10.5772/64301.
7. Li, J. & Mooney, D. J. Designing hydrogels for controlled drug delivery. *Nature Reviews Materials* **1**, 1–17. ISSN: 20588437. doi:10.1038/natrevmats.2016.71 (2016).
8. Slaughter, B. V. *et al.* Hydrogels in Regenerative Medicine. *Advanced Materials* **21**, 3307–3329. doi:10.1002/adma.200802106 (2009).
9. Le Goff, G. C. *et al.* Hydrogel microparticles for biosensing. *European Polymer Journal* **72**, 386–412. doi:10.1016/j.eurpolymj.2015.02.022 (2015).
10. Kanduč, M. *et al.* How the Shape and Chemistry of Molecular Penetrants Control Responsive Hydrogel Permeability. *ACS Nano* **15**, 614–624. doi:10.1021/acsnano.0c06319 (2021).
11. Gehrke, S. H. *et al.* Factors Determining Hydrogel Permeability. *Annals of the New York Academy of Sciences* **831**, 179–184. ISSN: 00778923. doi:10.1111/j.1749-6632.1997.tb52194.x (2006).

12. Lazzara, M. J. & Deen, W. M. Effects of concentration on the partitioning of macromolecule mixtures in agarose gels. *Journal of Colloid and Interface Science* **272**, 288–297. doi:10.1016/j.jcis.2003.10.008 (2004).
13. Zielinska, K. *et al.* Partitioning of Humic Acids between Aqueous Solution and Hydrogel: Concentration Profiling of Humic Acids in Hydrogel Phases. *Langmuir* **30**, 2084–2092. doi:10.1021/la4050094 (2014).
14. Fawcett, J. & Morris, C. Molecular-Sieve Chromatography of Proteins on Granulated Polyacrylamide Gels. *Separation Science* **1**, 9–26 (1966).
15. Morris, C. J. O. R. & Morris, P. Molecular-Sieve Chromatography and Electrophoresis in Polyacrylamide Gels. *Biochem. J* **124**, 517–528. doi:10.1042/bj1240517 (1971).
16. Bingaman, S., Huxley, V. H. & Rumbaut, R. E. Fluorescent dyes modify properties of proteins used in microvascular research. *Microcirculation* **10**, 221–231. ISSN: 10739688. doi:10.1038/sj.mn.7800186 (2003).
17. Giridhar, G., Manepalli, R. R. & Apparao, G. *Confocal Raman Spectroscopy in Spectroscopic Methods for Nanomaterials Characterization* 141–161 (2017). ISBN: 9780323461467. doi:10.1016/B978-0-323-46140-5.00007-8.
18. Sanderson, J. *Optical Aberrations of the Microscope in Understanding Light Microscopy* 101–125 (John Wiley & Sons, Ltd, 2019). doi:10.1002/9781118696736.ch6.
19. World Health Organization. *WHO Coronavirus (COVID-19) Dashboard* <https://covid19.who.int> (2021).
20. American Nurses Foundation & American Nurses Association. *COVID-19 survey series: PPE survey #2* <https://www.nursingworld.org/practice-policy/work-environment/health-safety/disaster-preparedness/coronavirus/what-you-need-to-know/pulse-on-the-nations-nurses-covid-19-survey-series-ppe-2/> (2021).
21. Sliney, D. H. Radiometric Quantities and Units Used in Photobiology and Photochemistry: Recommendations of the Commission Internationale de l’Eclairage (International Commission on Illumination). *Photochemistry and Photobiology* **83**, 425–432. ISSN: 00318655. doi:10.1562/2006-11-14-RA-1081 (2007).
22. Kowalski, W. *Ultraviolet Germicidal Irradiation Handbook: UVGI for Air and Surface Disinfection* ISBN: 978-3-642-01999-9 (Springer Science & Business Media, Berlin, Heidelberg, 2010).
23. Reifsnnyder, W. E. Radiation geometry in the measurement and interpretation of radiation balance. *Agricultural Meteorology* **4**, 255–265. ISSN: 00021571. doi:10.1016/0002-1571(67)90026-X (1967).
24. Bergman, R. S. Germicidal UV Sources and Systems. *Photochemistry and Photobiology* **97**. eprint: <https://onlinelibrary.wiley.com/doi/pdf/10.1111/php.13387>, 466–470. ISSN: 1751-1097. doi:<https://doi.org/10.1111/php.13387> (2021).

25. Condón, S., Álvarez, I. & Gayán, E. *Non-thermal Processing — Pulsed UV Light* in *Encyclopedia of Food Microbiology (Second Edition)* (eds Batt, C. A. & Tortorello, M. L.) 974–981 (Academic Press, Oxford, 2014). ISBN: 978-0-12-384733-1. doi:10.1016/B978-0-12-384730-0.00398-0.
26. Lawal, O. & Cosman, J. UV-C LED Devices and Systems: Current and Future State. *IUVA News* **20**, 7 (2018).
27. Larason, T. & Ohno, Y. Calibration and characterization of UV sensors for water disinfection. *Metrologia* **43**, S151–S156. ISSN: 0026-1394, 1681-7575. doi:10.1088/0026-1394/43/2/S30 (2006).
28. Gorman, J. Disposable N95 Masks Can Be Decontaminated, Researchers Confirm. *The New York Times*. ISSN: 0362-4331 (2020).

## Chapter 2

# *In Situ* Measurement of Thermodynamic Partitioning in Open Hydrogels

Reprinted with permission from A. Su, B. E. Smith, & A. E. Herr, “*In Situ* Measurement of Thermodynamic Partitioning in Open Hydrogels”, *Analytical Chemistry*, 2020. Copyright 2020 American Chemical Society.

Reprinted in part with permission from: S. Jeeawoody, K. A. Yamauchi, A. Su, & A. E. Herr, “Laterally Aggregated Polyacrylamide Gels for Immunoprobed Isoelectric Focusing”, *Analytical Chemistry*, 2020. Copyright 2020 American Chemical Society.

### 2.1 Introduction

Hydrogels find broad biomedical utility as drug delivery vehicles, cell encapsulation platforms, and scaffolds for diagnostics among other applications [1–4]. Microscale hydrogels are tens of microns thick with modifiable properties to optimize function for a specific application. Changing hydrophilicity, pore size, and/or electrostatic characteristics of a microscale hydrogel will modulate the thermodynamic properties of the gel-solute system. One thermodynamic property critical to gel design is partitioning, which governs solute load and release from a hydrogel. Partitioning is characterized by an equilibrium partition coefficient,  $K$ , defined as the ratio of the solute concentration inside the gel to the solute concentration in the surrounding free solution when the system is at equilibrium:

$$K = \frac{[solute]_{gel}}{[solute]_{solution}} \quad (2.1)$$



where  $[\text{solute}]_{\text{gel}}$  and  $[\text{solute}]_{\text{solution}}$  are the concentrations of solute in-gel and in solution, respectively [5].  $K$  depends on all interactions that occur between gel and solute: [5]

$$\ln K = \ln K_{\text{size}} + \ln K_{\text{hphob}} + \ln K_{\text{elec}} + \ln K_{\text{conf}} + \ln K_{\text{other}} \quad (2.2)$$

In Eq. 2.2,  $K_{\text{size}}$ ,  $K_{\text{hphob}}$ ,  $K_{\text{biosp}}$ ,  $K_{\text{elec}}$ , and  $K_{\text{conf}}$  refer to contributing partition coefficients due specifically to the size of the solute and gel pores, hydrophobic interactions, biospecific affinity (e.g., between a ligand and its target), electrostatic interactions, and conformational changes (e.g., folded vs. unfolded proteins), respectively. Other interactions (e.g. hydrogen bonding and Van der Waals forces), are grouped into the  $K_{\text{other}}$  term [5, 6]. All of these interactions can govern gel performance [7]. For example, environmentally responsive hydrogels for drug delivery have been designed to swell in specific physiological conditions to increase the effective pore size of the hydrogel, stimulating release of the cargo drug [8]. The pore size of hydrogels for cell transplantation can be optimized to protect encapsulated cells from the host immune system while allowing permeation of key nutrients and release of therapeutics [9, 10]. The gel network and any added functional groups influence the performance of hydrogels as immunoassay scaffolds, as the sensitivity of the assay is directly related to partitioning of immunoreagents into the hydrogel network to complex with the target [4, 11–13]. Therefore, understanding thermodynamic partitioning – including dependencies on interactions between gel and solute – informs design of microscale hydrogels.

The most prevalent technique to measure  $K$  values of solutes in hydrogels uses indirect mass balance/back-extraction methods [14–19]. However, this method is unable to provide information on the spatial distribution of the solute within the hydrogel, which can yield critical insight into local material properties of the hydrogel. Properties of interest include pore-density distribution in unilaminar and multilaminar structures, balances between surface adsorption vs. absorption, charge distribution, and uniformity of functionalization [20, 21]. Fluorescence microscopy can also be used to determine  $K$ , with the caveats that a solute must be amenable to fluorescence labeling and that the fluorescence intensity of the label is linearly proportional to solute concentration. In general, fluorescence intensity is linearly proportional to concentration when the absorbance of the solution is <5% [22, 23]. Absorbance is dependent on the solute concentration, the imaging depth, and the extinction coefficient of the fluorophore [24]. Given these caveats, we can write:

$$K = \frac{[\text{solute}]_{\text{gel}}}{[\text{solute}]_{\text{solution}}} = \frac{I_g}{I_{s,c}} \quad (2.3)$$

where  $I_g$  is the in-gel fluorescence intensity and  $I_{s,c}$  is the in-solution fluorescence intensity above the coverslip (Figure 2.1).

For direct calculation of  $K$ , wide-field fluorescence microscopy ideally measures the lateral (within the x-y plane) solute distribution within hydrogels [25, 26]. However, wide-field microscopy inherently detects fluorescence throughout the axial (along z-depth) field of view. Consequently, *in situ* measurements of  $K$  on hydrogels submerged in a liquid bath (open hydrogel systems) will be skewed by both the image plane depth and surrounding fluorescence

(i.e., fluid layer on top of hydrogel structure) [26]. The measurements will be a convolution of fluorescence at the image plane and any background fluorescence. Also importantly, when a sample has differences in  $K$  axially [20, 21, 27] and/or radially [28–30], such differences are not directly measurable using wide-field fluorescence microscopy. In cases where only the lateral solute distribution is of interest and there is no fluorescent solution layer above or below the gel, wide-field fluorescence microscopy is suitable for measuring  $K$ . Nevertheless, for open microscale hydrogel systems where the volumetric solute distribution is of interest, wide-field microscopy is not effective.

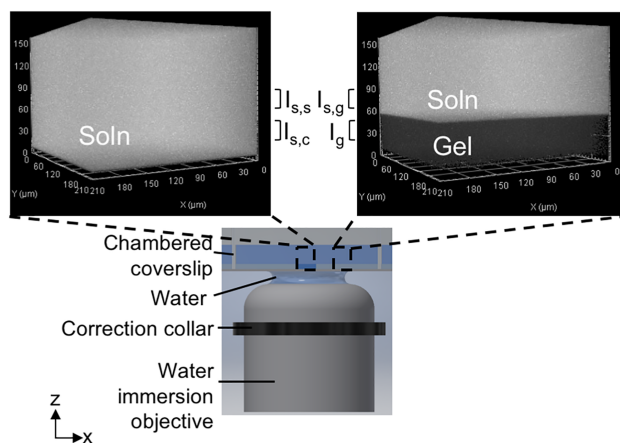


Figure 2.1: AC-LSCM uses chambered coverslips interfacing with a correction collar-fitted water immersion objective to compensate for aberrations induced by the coverslip. Each chamber holds a microscale PA gel polymerized with a well in the center. Fluorescence micrographs of both the gel and the fluid-filled well are acquired. Surrounding free solution serves as a reference for measuring both gel-independent optical artefacts and gel-dependent artefacts.

to the PA hydrogel backbone and 2) physical modification of the PA hydrogel microarchitecture impacts solute partitioning and the implications for immunoassays performed in-gel. Finally, we use AC-LSCM to characterize spatially resolved *in situ*  $K$  in thicker ( $>100\ \mu\text{m}$ , two-layered PA gels. In summary, we present an accessible analytical technique that can be used to directly quantify and validate the spatially resolved *in situ* partitioning of solutes in hydrogels, directing the custom engineering of hydrogels for a wide range of applications. Furthermore, with a multi-immersion objective, AC-LSCM is more broadly applicable to determining  $K$  and the corresponding accuracy of the  $K$  measurement of any sample with

Optical sectioning techniques (e.g., laser-scanning confocal, multi-photon microscopy) meet the specifications for our system and have been used to measure  $K$  [31–34]. However, optical aberrations still introduce both lateral and axial measurement artefacts; therefore, any optical artefacts need to be minimized and remaining artefacts quantified and controlled for to permit accurate quantitation [35, 36]. We therefore developed an aberration-compensated laser scanning confocal microscopy (AC-LSCM) technique that interfaces with gels fabricated on chambered coverslips to measure spatially resolved *in situ*  $K$  in open hydrogel systems. With this technique, we address two key criteria: the (i) minimization and (ii) quantification of optical artefacts that could confound quantitation in any fluorescence microscopy-based  $K$  measurement. We then measure *in situ*  $K$  of a model protein in microscale polyacrylamide (PA) gels spanning a range of pore sizes and validate the  $K$  values both with theory and experimentally determined values reported by others. We further study how a 1) chemical modification

reference solution refractive index between the limits of the objective (commonly 1.33-1.52).

## 2.2 Materials and Methods

### Chemicals/reagents

40%T, 3.3%C acrylamide/bis-acrylamide (29:1) (A7802), N,N,N',N'-tetramethylethylenediamine (T9281), ammonium persulfate (A3678), bovine serum albumin (BSA, A7030), 10 kDa poly(ethylene glycol) (PEG, 92897), and soybean trypsin inhibitor (TI, T6522) were purchased from Sigma Aldrich. 1.5 M Tris-HCl, pH 8.8 was purchased from Teknova (T1588). Tris-buffered saline with Tween (TBST) (10X) was procured from Cell Signaling Technology (9997S). Alexa Fluor 647-labeled donkey anti-rabbit IgG antibody (Ab\*, A31573) was obtained from Life Technologies. Alexa Fluor 647-conjugated donkey anti-goat IgG Fab fragment (Fab\*, 705-607-003) was purchased from Jackson ImmunoResearch. Deionized water (18.2 M $\Omega$ ) was acquired using an Ultrapure water system from Millipore. N-[3-[(3-benzoylphenyl)formamido]propyl] methacrylamide (BPMAC) was custom synthesized by PharmAgra Laboratories and resuspended in dimethyl sulfoxide (DMSO).

### Micrograph acquisition

All micrographs were acquired on a Carl Zeiss LSM 710 AxioObserver inverted laser scanning confocal microscope using a C-Apochromat 40 $\times$ /1.1 NA water-immersion objective with correction collar. The 633 nm line of a helium-neon laser was used to excite Alexa Fluor 647 and to perform reflected light confocal microscopy of the coverslip-sample interface to find the optimal correction collar setting. Fluorescence was imaged using a 488/561/633 nm dichroic filter and a pinhole set to 1.0 Airy units. Three-dimensional image stacks of fluorescence were captured over a 212.55  $\mu\text{m}$   $\times$  212.55  $\mu\text{m}$  field of view with 0.71  $\mu\text{m}$   $\times$  0.71  $\mu\text{m}$   $\times$  0.70  $\mu\text{m}$  cubic voxels. The samples were imaged from the coverslip-sample interface to at least 120  $\mu\text{m}$  into the sample. Reflected light confocal microscopy was used to identify the starting z-position of the coverslip surface to image baseline autofluorescence of gels in solute-free buffer. Reflected light confocal images were acquired using a T80/R20 partial mirror over a 212.55  $\mu\text{m}$   $\times$  212.55  $\mu\text{m}$  field of view with 0.71  $\mu\text{m}$   $\times$  0.71  $\mu\text{m}$   $\times$  0.10  $\mu\text{m}$  cubic voxels.

### Correction collar positioning

The optimal position of the correction collar was found by measuring the average intensity of the field of view at the z-position yielding the highest average intensity (i.e. the glass-sample interface). Peak intensity values were recorded at each collar position. The collar was adjusted until a maximum peak intensity was observed. 3D image stacks were then acquired

at different correction collar positions to illustrate changing reflection intensity z-profiles at the coverslip-sample interface.

## PA gel fabrication

PA hydrogels of varying density (%T w/v acrylamide) and 3.3% bis-acrylamide crosslinker were fabricated inside silanized [37] (appendix A) chambered coverslips (ibidi, 80427). Samples used for the same experiment were fabricated on chambered coverslips from the same lot to minimize coverslip thickness variation. The gel precursor solution was prepared as described previously [37]. For unmodified PA gels, 3 mM BPMAc in the precursor was replaced with water. For vehicle control gels, 3 mM BPMAc was replaced with DMSO. To modify the PA microarchitecture, we used 10 kDa PEG as the preformed hydrophilic polymer and leveraged porogen gel fabrication conditions developed by Righetti and colleagues [38]. The PA gel matrix is formed from incorporation of acrylamide monomers and bisacrylamide cross-linkers into a randomly organized hydrogel network, inducing heterogeneity in pore size [5, 39, 40]. We distinguish the six PA gel conditions within the PA-PEG experiments by defining 6%T 3.3%C APS/TEMED gels as “benchmark gels,” 6%T 8%C APS/TEMED + 0% PEG gels as “negative control gels,” 6%T 8%C + 0.5% PEG gels as “0.5% PEG highly porous PA gels,” 6%T 8%C + 1% PEG gels as “1% PEG highly porous PA gels,” 6%T 8%C + 1.5% PEG gels as “1.5% PEG highly porous PA gels,” and 6%T 8%C APS/TEMED + 2% PEG gels as “2% PEG highly porous PA gels” (Table 2.1). All gels for the PA-PEG experiments contained 5 mM BPMAc.

Table 2.1: Composition of polyacrylamide gels. Primary components of all gel conditions used in this work, following standard gel fabrication techniques in [41]. Concentrations reported as % are %w/v.

Gel nomenclature	Benchmark gel	Negative control gel	0.5% PEG Highly porous gel	1% PEG Highly porous gel	1.5% PEG Highly porous gel	2% PEG Highly porous gel
Acrylamide content	6 %T	6 %T	6 %T	6 %T	6 %T	6 %T
Bisacrylamide : acrylamide ratio	3.3 %C	8 %C	8 %C	8 %C	8 %C	8 %C
10 kDa PEG	0.0 %	0.0 %	0.5 %	1.0 %	1.5 %	2.0 %

After deposition of precursor into the chamber, a  $\sim 9 \text{ mm} \times 19 \text{ mm}$  photopatterned glass-weighted silicon mold with a 30-40  $\mu\text{m}$  tall square feature was placed upside down on top of the precursor. The silicon molds were diced from a photopatterned wafer fabricated using soft lithography and a photomask (Figure 2.2A). While not used for experiments presented here, a revised, higher throughput and user-friendly mask was designed (Figure 2.2B) that increases the number of molds/wafer from 8 to 23 and generates guides to simplify the wafer dicing step.

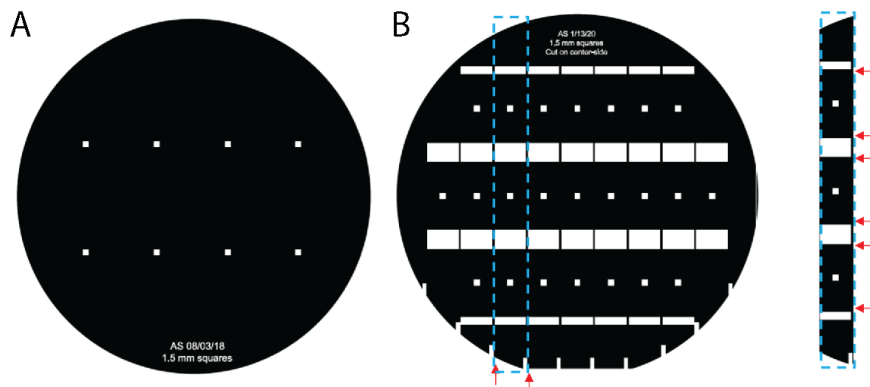


Figure 2.2: Masks for photopatterning silicon wafers to fabricate molds for partition coefficient measurements on chambered coverslips. (A) Original partition coefficient mask that generates 8 molds/wafer. (B) Revised mask that generates 23 molds/wafer and includes guides for dicing. Red arrows indicate locations where the wafer should be scribed/diced. The vertical guides should be used first, followed by the horizontal guides to cut each piece to size.

Polymerization proceeded for 20 min before the mold was released, leaving in each chamber a microscale PA hydrogel with a well in the center (Figure 2.1). Gels were then rinsed with deionized water and stored in  $1\times$  TBST overnight at  $4^{\circ}\text{C}$ . PA-PEG gels were incubated for 16-24 h in  $1\times$  TBST to allow for diffusion of soluble PEG porogen out of the PA gel network, thus forming pores, then rinsed in deionized water for 30 min before use. BPMAC-containing gels were exposed to UV light using a collimated mercury lamp ( $20\text{ mW}/\text{cm}^2$  at 365 nm, Optical Associates, Inc.) in  $1\times$  TBST for 5 min and washed for 1 h prior to introduction of fluorescently labeled solute in solution. Multilayer PA gels were fabricated using featureless wafer pieces and Kapton tape applied directly to the chamber bottom to form the well in the gel due to difficulty in aligning wafer features for layer-by-layer fabrication. The bottom layer gel was first polymerized around a  $40\text{ }\mu\text{m}$  tall Kapton tape (Caplinq, PIT0.5S/6.4) feature. The bottom layer gel was then dried to facilitate addition of a layer of  $70\text{ }\mu\text{m}$  Kapton tape (Ted Pella, 16090-6) on top of the  $40\text{ }\mu\text{m}$  tape layer. The bottom gel was then rehydrated before deposition of the second gel precursor and subsequent polymerization. Both layers of Kapton tape were removed after gel fabrication.

## Partition coefficient measurements using AC-LSCM

Soybean trypsin inhibitor was covalently labeled with Alexa Fluor 647 (TI\*) using a protein labeling kit (Invitrogen, A20173) (degree of labeling between 0.7-0.8). For separation of labeled protein from free dye, P-6 fine resin (Bio-Rad, 150-4134) was used. Single-layer PA gels were incubated in  $1.5\text{ }\mu\text{M}$  TI\* or  $0.67\text{ }\mu\text{M}$  of Alexa Fluor 647-labeled immunoprobe in 2% BSA in  $1\times$  TBST solution for  $>60$  min in the dark at room temperature before imaging. Multilayer gels were incubated in  $1.5\text{ }\mu\text{M}$  TI\* for  $>240$  min before imaging. Micrographs of

gels and solution surrounding gels incubated in solute-free buffer were used for background subtraction. The autofluorescence of unmodified PA microscale gels incubated in solute-free buffer was found to be independent of PA gel density, so only one gel density was ultimately used for background subtraction for the unmodified PA gels during image analysis.

## Measurements of fluorescence retention after unloading

The test solution was removed from the gel chamber and replaced with  $1 \times$  TBST solution for  $\geq 2$  h, with a buffer exchange after 30 min to allow for complete unloading of the solute from gel. Gels were then reimaged to measure retained solute after unloading.

## Micrograph analysis and quantitation

To standardize the post-imaging processing, a custom macro in ImageJ 1.52i (NIH) was written that uses well-known algorithms to identify regions for analysis (Figure 2.3, analysis code available at: [https://github.com/Llamero/Gel\\_partition\\_analysis\\_macro](https://github.com/Llamero/Gel_partition_analysis_macro)). In line with image processing best practices, the code maintains equal information content (number of optical sections) between micrographs used for the same calculation. A  $1 \times 1 \times 1$  3D median filter is applied to the raw micrographs before quantitation to reduce pixel noise while preserving image resolution. To reduce high-frequency noise when identifying the key transition regions, a  $1 \times 1 \times 1$  3D Gaussian (low-pass) filter is applied to copies of the micrographs.

## Partition coefficient measurements using mass balance

We devised a corollary experiment to compare the AC-LSCM methodology to a conventional mass-balance technique. The solution-depletion mass-balance technique relies on indirect determination of the in-gel solute concentration through measurement of the change in solute concentration in the equilibrating solution [14, 19, 42]. To ascertain  $K$  from the solution-depletion technique, a material balance analysis establishes:

$$K = \frac{V_{sol}}{V_{gel}} \left( \frac{[solute]_{0,soln}}{[solute]_{f,soln}} - 1 \right) \quad (2.4)$$

Here,  $V_{sol}$  and  $V_{gel}$  are the volumes of solution and hydrated gel, respectively.  $[solute]_{0,soln}$  and  $[solute]_{f,soln}$  are the starting and final concentration of solute in solution, respectively.

Note that practicalities of the mass-balance measurement (i.e., detectable solute fluorescence decrease in bath, mechanical robustness of gels during handling, need to dry surfaces of gels) require gel structures that are notably thicker than those used for AC-LSCM (e.g., 0.04 mm). Non-attached 6%T PA gels were fabricated using 2 mm thick spacers, then diced into  $9 \text{ mm} \times 19 \text{ mm} \times 2 \text{ mm}$  replicates. The surface area of the gels after dicing was estimated using bright-field microscopy. The height of the gels was determined after completion of the experiment. Gels equilibrated with fluorescent solute were sliced in the axial direction

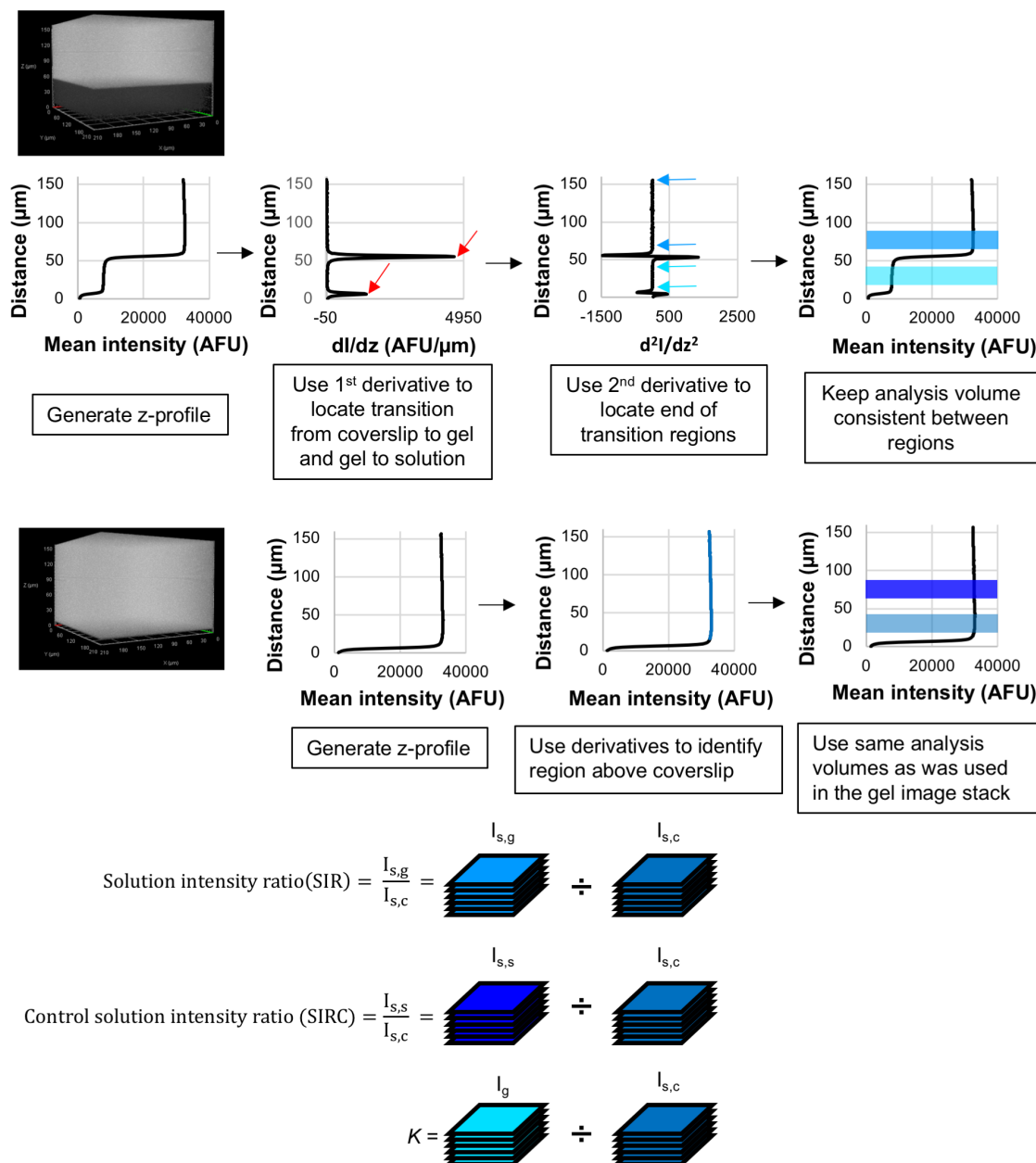


Figure 2.3: Analysis workflow for automated spatially resolved  $K$  calculations and depth-dependent axial aberration quantitation.

to generate thin sections that were gently blotted and placed on their side for imaging the gel height (now in the x-y plane) using widefield fluorescence microscopy. Swollen gels were measured to be  $\sim 2.2$  mm thick and verified using calipers. Prior to incubation in solute, gels were gently blotted with weigh paper to remove excess fluid from the gel surfaces. Gels were incubated in 400  $\mu$ l of 1.5  $\mu$ M TI\* for  $> 24$  h at room temperature in chambered coverslips

sealed with Parafilm on a rotator. The ratio of  $[solute]_{0,soln}$  and  $[solute]_{f,soln}$  was measured as the ratio of the solution fluorescence in chambers without gel structures (to control for adsorption of solute to the chamber surface) to the solution fluorescence in gel-containing chambers. Fluorescence was measured using a Tecan Infinite M200 Pro with excitation at 640 nm and emission collected at 670 nm. The measured solute-containing solution was re-applied to the gels and the gels were imaged using the AC-LSCM technique adapted for these thicker gels. Note that because these macroscale gels were not attached to the chambered coverslips, a small fluid layer was present between the coverslip and gel during imaging.

## 2.3 Results and Discussion

### Measuring the spatially resolved *in situ* $K$ of open hydrogels

We first sought to design an LSCM measurement technique suitable for reporting spatially resolved *in situ*  $K$  values from open hydrogel systems. To report solute distribution throughout the entire volume of a gel, AC-LSCM uses the surrounding free solution as an intrinsic reference. This free solution reference allows AC-LSCM to measure both gel-independent optical artefacts and gel-dependent artefacts. Both types of artefacts confound  $K$  quantitation. In particular, gel-independent artefacts are addressable in the design of the experimental setup, including by lowering solute concentration to reduce absorption and adjusting the objective correction collar to minimize refractive errors. To further enhance design of the experimental setup for reproducibility, we report a companion computational algorithm to precisely define regions of interest and perform quantification.

When measuring  $K$ , we consider both axial (along  $z$  depth) and lateral (within the  $x$ - $y$  plane) artefacts. Monochromatic depth-dependent axial optical artefacts, such as spherical aberrations, arise predominantly as signal attenuation with increasing depth into the sample (Figure 2.4) [35]. One main cause of these signal attenuating artefacts are refractive index ( $n$ ) mismatches in the light path relative to the immersion medium of the objective (e.g., air, water, oil), which can arise from: i) the interface between the immersion medium (water) and the coverslip, ii) the interface between the coverslip and the gel, and iii) differences in  $n$  between the immersion medium and the sample [35, 36]. In this study, the sample is the wetted microscale hydrogel. Lateral artefacts arise from optical aberrations (e.g., coma, astigmatism) and non-uniform illumination and/or resolution across the field of view (vignetting). Considering artefacts, the calculation of  $K$  using fluorescence microscopy is more accurately described as a convolution of the true intensity ( $I(x,y,z)$ ), artefacts in the axial direction ( $f(z)$ ), and artefacts in the lateral direction ( $f(x,y)$ ). Lateral artefacts, such as vignetting, are introduced by the finite apertures within the optical path and thus are independent of imaging depth. These lateral artefacts can be normalized during analysis by dividing a 3D image stack by a known uniform reference image stack (Figure 2.5). The calculation of  $K$  inherently incorporates division by a known reference stack, as the bulk solution should be perfectly uniform in intensity, and thus any observed differences are



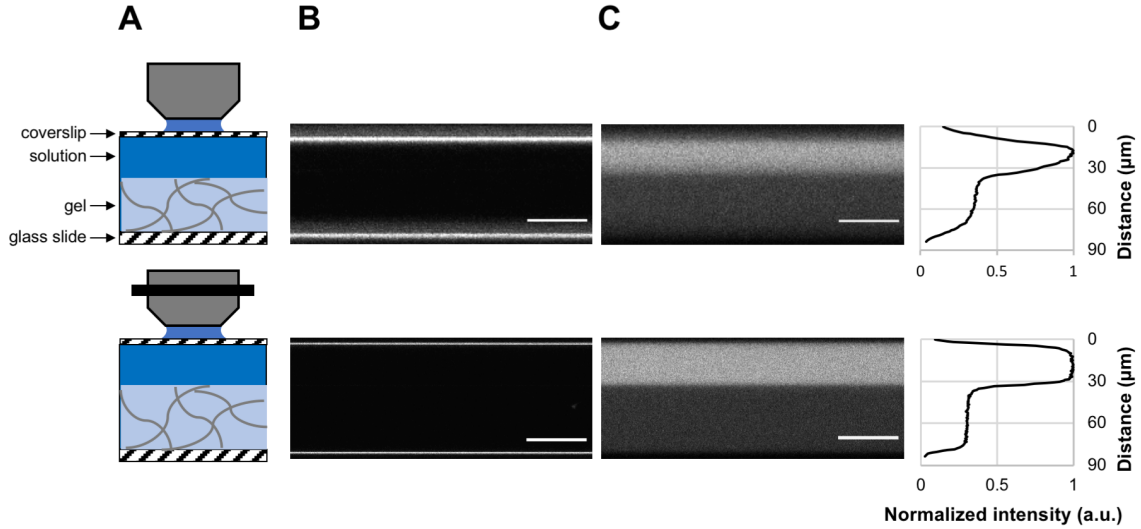


Figure 2.4: Comparison of micrographs acquired using a water immersion objective (top) and a water immersion objective with a correction collar (bottom). A) Schematic of microscope/sample setup. B) Reflection x-z series from coverslip-solution interface to gel-glass slide interface. C) x-z fluorescence micrographs and normalized intensity profiles of Ab\* from the same 8%T w/v PA microscale gel. These data were acquired on a Zeiss LSM 880 NLO AxioExaminer upright microscope with a 40 $\times$ /1.2 NA water immersion objective with a correction collar and a 20 $\times$ /1.0 NA water immersion objective. Scale bars represent 10  $\mu\text{m}$  in the horizontal direction. 2D x-z line profiles were captured as 425.10  $\mu\text{m}$  wide by a z step size of 0.21  $\mu\text{m}$  (20 $\times$  objective) or as 425.10  $\mu\text{m}$  wide by a z step size of 0.10  $\mu\text{m}$  (40 $\times$  objective). Images cropped to the same field of view. a.u. = arbitrary units.

known to be artefacts:

$$K = \frac{I_g}{I_{s,c}} = \frac{I_{gel}(x, y, z) \times f_{gel}(z) \times f(x, y)}{I_{soln}(x, y, z) \times f_{soln}(z) \times f(x, y)} = \frac{I_{gel}(x, y, z) \times f(x, y)}{I_{soln}(x, y, z) \times f(x, y)} \quad (2.5)$$

The result of Eq. 2.5 is an image stack containing information on the lateral and axial distribution of solute after normalizing for lateral artefacts, still confounded by any axial aberrations (discussed in the following paragraphs). The lateral normalization can be validated by measuring the lateral intensity profile of an optical section in the  $K$  stack (Figure 2.5).

$K$  is calculated from micrographs collected using an inverted LSCM system to image open PA hydrogels fabricated on chambered coverslips. Each hydrogel houses a fluid-filled well designed for collection of matched (i) in-gel fluorescence,  $I_g$ , and (ii) in-solution fluorescence,  $I_{s,c}$  (Figure 2.1). Fluorescence intensity is linear with solute concentration over the ranges considered (Figure 2.6). The microscale hydrogel is fabricated by casting gel precursor on top of a chambered coverslip underneath a photopatterned silicon mold (see Experimental Methods, Figure 2.1) [37]. The chambered coverslip-gel system here supports *in situ*  $K$

$$K = \frac{I_g}{I_{s,c}} = \frac{I_{\text{gel}}(x, y, z) \times f_{\text{gel}}(z) \times f(x, y)}{I_{\text{soln}}(x, y, z) \times f_{\text{soln}}(z) \times f(x, y)} = \frac{I_{\text{gel}} \times f_{\text{gel}}(z)}{I_{\text{soln}} \times f_{\text{soln}}(z)}$$

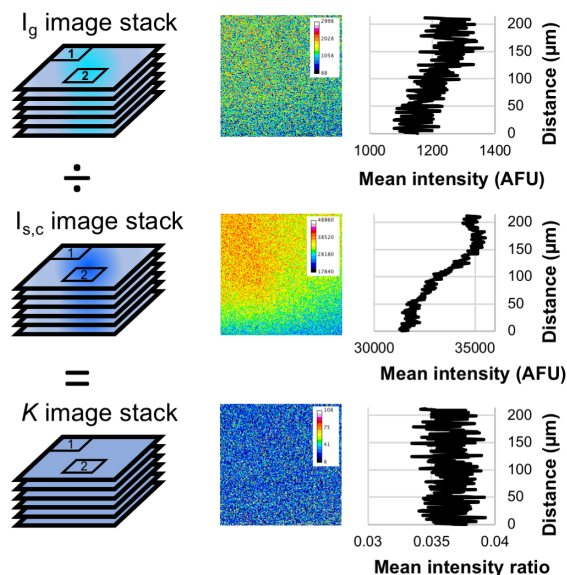


Figure 2.5: Schematic of the image math performed to calculate  $K$  (left), with representative micrographs from within the image stacks shown as false-colored heatmaps to illustrate lateral artefacts (center) and accompanying intensity profiles (right).

measurements, in contrast to a commonly reported direct  $K$  measurement technique which involves removal of the gel from bulk solution for imaging [43, 44]. To investigate solute-gel interactions, chambered coverslips facilitate sample handling for measuring  $I_g$  both after solute loading and after solute unloading.

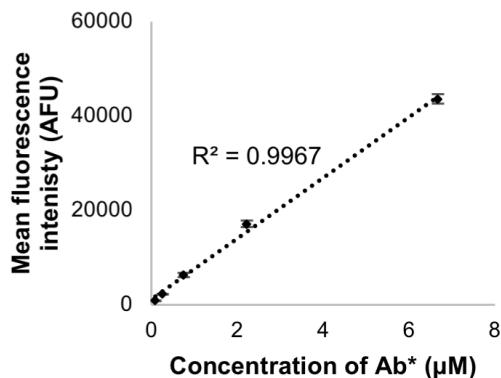


Figure 2.6: Mean fluorescence intensity is linear with concentration for Ab\* with a degree of labeling of  $\sim 4.3$ . Analysis was performed on solution at a depth of  $\sim 100 \mu\text{m}$  using a custom macro in ImageJ. Error bars represent standard deviation of triplicate measurements.

To closely match the  $n$  of PA hydrogels [45], AC-LSCM employs a water-immersion objective fitted with a correction collar. The correction collar counteracts axial artefacts induced by mismatch between  $n$  of the coverslip and  $n$  of water [46, 47], and is set accurately using reflected light confocal microscopy. Reflected light confocal microscopy uses reflected excitation light to inform adjustment of the correction collar for each specific sample; the reflection is created by an interface with a refractive index mismatch. The reflected light serves as a proxy for the axial resolution of the microscope and can therefore be used to determine the accurate position of the collar. When the correction collar is accurately positioned, the peak intensity of the reflected light will be maximized. Concomitantly, the full-width half maximum of the axial profile will be minimized. On the other hand, when the correction collar is not positioned accurately, axial aberrations will be present. These axial aberrations will cause a decrease in the measured peak intensity of the reflected light due to the distortion of the excitation light [36] and the axial intensity profile will spread longitudinally. Given that myriad factors alter the effective thickness of a #1.5 coverslip, setting the correction collar at 170  $\mu\text{m}$  for a #1.5 coverslip should not be expected to consistently correct aberrations. Observed deviations from ideal include: a wide tolerance of #1.5 coverslip thicknesses (160 - 190  $\mu\text{m}$ ), wear-and-tear of the correction collar over time, the wavelength dependence of refraction, and fluctuation in the movable internal lens position in an objective with temperature. Instead, we adopt a reflection microscopy calibration technique [47, 48] designed to optimize the correction collar setting for each imaging session.

Using our LSCM system, we imaged the coverslip-sample interface across a range of correction collar positions (140, 150, 170, and 190  $\mu\text{m}$ ). The accurate correction collar setting was determined to be 150  $\mu\text{m}$  for #1.5H chambered coverslips (170  $\pm$  5  $\mu\text{m}$ ) (Figure 2.7A), a position that differs from the anticipated position by 20  $\mu\text{m}$ .

Having identified the optimal correction collar position for the open microscale hydrogel system, we next sought to understand what impact the position of the correction collar has on fluorescence and  $K$  quantitation. Testing three different correction collar positions representing under-, accurate, and over-adjustment (140, 150, and 170  $\mu\text{m}$ , respectively), we observed that the position of the correction collar changes the measured intensity profile over a given imaging depth (Figure 2.7B). The measured peak fluorescence intensity in-gel and in-solution is lower when the collar is not accurately adjusted, regardless of whether the collar is under- or over-adjusted. Furthermore, we observe different slopes of the solution intensity profile with depth (Figure 2.7C). Interestingly, when the correction collar is over-adjusted (in the anticipated collar position of 170  $\mu\text{m}$  for #1.5H coverslips), we observe a positive slope of fluorescence with increasing imaging depth. These results for our microscale hydrogel system corroborate previous findings that the position of the correction collar impacts quantitation of measured fluorescence intensity profiles [35, 36]. Due to the depth-dependence of fluorescence intensities in both the over- and under-adjusted collar conditions, we anticipated observing a depth-dependent  $K$ , where  $\frac{I_g}{I_{(s,c)}} \neq \frac{I_g}{I_{(s,g)}}$ . Interestingly, we did not observe a large difference in the  $K$  measurements at different correction collar positions for 6%T w/v microscale PA hydrogels (Figure 2.7D). We hypothesize that the effect of

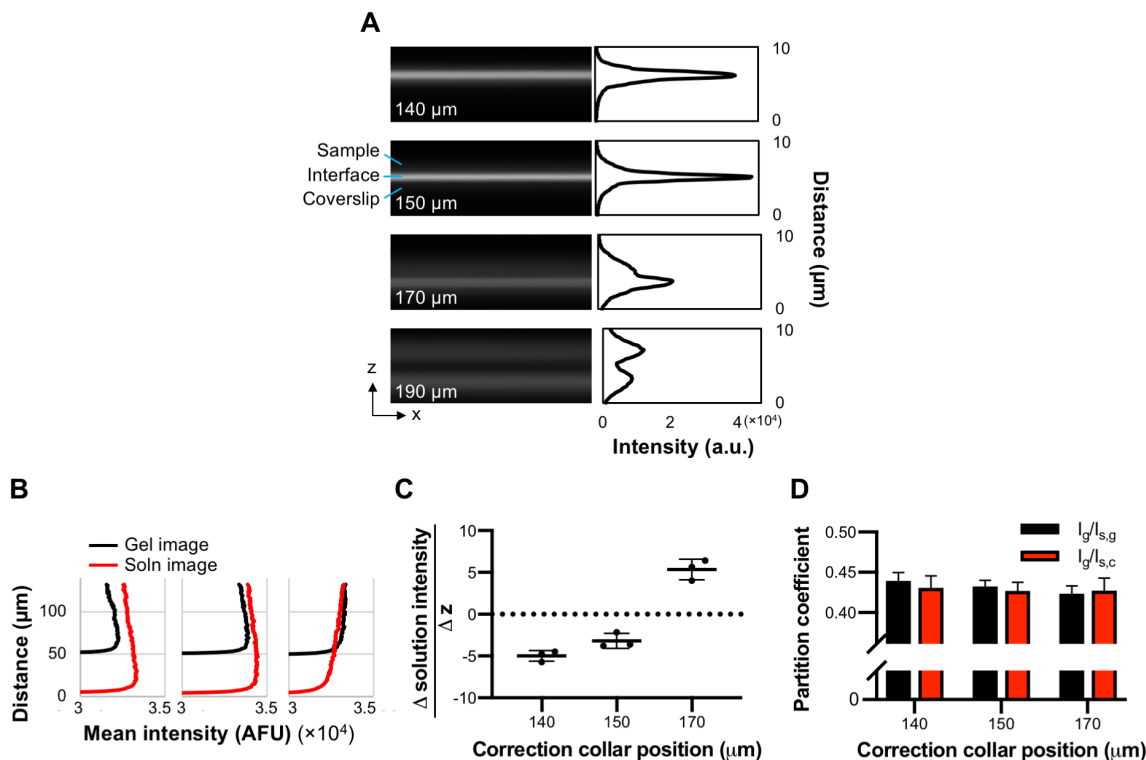


Figure 2.7: A) Reflection z-series and corresponding intensity profiles of the coverslip-sample interface for accurate correction collar positioning prior to  $K$  measurements. a.u. = arbitrary units. Numbers in bottom left of each micrograph indicate correction collar position. B) Intensity profiles of gel and solution images demonstrate the impact of an under-adjusted (140  $\mu\text{m}$ ), correctly adjusted (150  $\mu\text{m}$ ), and an over-adjusted collar (170  $\mu\text{m}$ ), respectively. C) Average slopes of the solution image intensity profiles with increasing depth for different correction collar positions. D) Impact of correction collar positioning on  $K$  measurements.

the correction collar on  $K$  is mitigated by a combination of a ratiometric measurement and the technical variation introduced by adjusting the correction collar position between every image.

While actively minimizing mismatches in  $n$  between the coverslip and solution, we also quantify the effects of any remaining refractive errors introduced by the gel. As shown in Figure 2.1, the open nature of the system provides a solution layer above the gel (with corresponding fluorescence,  $I_{s,g}$  that is fluidically connected and in equilibrium with the solution in the well directly above the coverslip (with corresponding fluorescence  $I_{s,c}$ ). Therefore, in the absence of refractive errors, we can write the ratio of solution fluorescence intensities as:

$$\text{Solution intensity ratio (SIR)} = \frac{I_{s,g}}{I_{s,c}} = 1 \quad (2.6)$$

Gel-induced artefacts can therefore be quantified by measuring the deviation of SIR from

1.0 ( $\delta_{SIR}$ ) for every  $K$  measurement. The  $\delta_{SIR}$  value reports accuracy of the AC-LSCM measurement (e.g.,  $\delta_{SIR} = 0.10$  indicates that the  $K$  value could be inaccurate by as much as 10%). Conventional LSCM imaging and data analysis fails to capture the impact of gel-induced artefacts on  $K$  quantitation, a primary contribution of the AC-LSCM technique reported here.

We can also control for inaccurate correction collar positioning by measuring fluorescence signal with depth in the solution filling the well. To do this, we compare the solution fluorescence intensity at the same depth as that used from the gel micrograph ( $I_{s,s}$ ) to the solution intensity in the well proximal to the coverslip ( $I_{s,c}$ ) (Figure 2.1). The estimated absorbance of solution is minimal for the concentrations and imaging depths used [49]. Therefore, with an accurately positioned correction collar, the intensity of solution should be depth-invariant:

$$\text{Control solution intensity (ratio) (SIR}_c) = \frac{I_{s,s}}{I_{s,c}} = 1 \quad (2.7)$$

$SIR_C$  provides real-time data validating the optimal correction collar position for every  $K$  measurement, replacing the need to collect reflection micrographs throughout the experiment. The advent of multi-immersion objectives makes AC-LSCM compatible with any fluorescence microscopy-based  $K$  measurement where the solution has  $n$  between 1.33-1.52. The objective should be matched to  $n$  of the solution and can be verified by measuring  $SIR_C$ .

## Assessing $K$ in solute and hydrogel system governed by size-exclusion

We then utilized AC-LSCM to study gel-solute interactions in open microscale unmodified PA gel systems. Ogston's ideal size-exclusion model, which assumes that  $K = K_{size}$  (from Eq. 2.3), posits that  $K$  for a given solute will decrease in a log-linear manner as gel density increases [50]:

$$K = K_{size} = \exp\left[-\phi\left(1 + \frac{R_h}{a_f}\right)^2\right] \quad (2.8)$$

where  $\phi$  represents polymer volume fraction (related to pore size for a uniform suspension of fibers),  $R_h$  is the hydrodynamic radius of the partitioning solute, and  $a_f$  corresponds to the polymer fiber radius. Thus, as gel density increases,  $\phi$  increases, and the average pore size of the gel decreases. Decreasing pore size results in increased exclusion of a given solute from the gel matrix. Various solutes have been shown to follow Ogston's ideal size-exclusion model in PA gels larger than the microscale dimension studied here [26, 51, 52]. Using the AC-LSCM system, we assessed  $K$  in 6%T, 9%T, 12%T, 15%T, and 18%T w/v microscale PA gels (all with bis-acrylamide density equal to 3.3%C). Note that the lateral resolution of the microscope (100s of nm) does not resolve the estimated pore size [53] of any PA gels in this study (radii of 10s of nm); therefore, we do not anticipate observed lateral differences in  $K$ . Microscale gels were 40-60  $\mu\text{m}$  thick ( $z$ ). As solute, we studied the 20.1 kDa protein TI labeled with Alexa Fluor 647 (TI\*). TI\*-containing solution and hydrogel were incubated until

equilibrium was reached ( $>60$  min). The diffusion time to equilibrium ( $3\tau$ , Table 2.2) was estimated using the equation for 2D diffusion combined with a hindered in-gel diffusion model :  $\tau = \frac{z^2}{2D_{gel}}$ , where  $z$  is the height of the gel and  $D_{gel}$  is the in-gel diffusion coefficient estimated from the empirically derived relationship [54]:  $D_{gel} = D_{H_2O} \times \exp(-3.03 \times R_h^{0.59} \times \%T^{0.94})$ .  $D_{H_2O}$  is estimated using the Stokes-Einstein equation:  $D_{H_2O} = \frac{k_B T}{6\pi\eta_{H_2O}R_h}$ , where  $\eta$  and  $k_B$  are viscosity and Boltzmann's constant, respectively.

 Table 2.2: Parameters to estimate diffusion time ( $3\tau$ )

Solute	$R_h$ (Å)	$D_{H_2O}$ ( $\mu m^2/s$ )	$z$ ( $\mu m$ )	%T	$3\tau$ (min)
TI*	24.5	100	40	18	49
TI*	24.5	100	110	15	90
Ab*	61	40	40	6	12

In considering Ogston's theory, we converted gel density (%T w/v) to  $\phi$ , adjusting for a lower percent bis-acrylamide used in this study ( $\phi = 0.0093 \times \%T - 0.03151$ ) [55]. We used  $R_h \sim 24.5$  Å for TI\* [56, 57]. Because the  $K$  measurements were performed in 2% ( $\sim 300$   $\mu M$ ) BSA solution, we adjust the model to account for interactions between BSA and TI\* based on the following equation [14]:

$$K_{TI^*} = \exp[-\phi\alpha_{TI^*,PA}(s, f) + \alpha_{TI^*,TI^*}(s, s)(1 - K_{TI^*})\chi_{TI^*} + \alpha_{TI^*,BSA}(s, s)(1 - K_{BSA})\chi_{BSA}] \quad (2.9)$$

where  $\phi$  is the polymer volume fraction,  $\alpha$  is a dimensionless interaction term,  $\chi$  is the solute volume fraction in bulk solution, and "s" and "f" denote "sphere" and "fiber", respectively.

For the system considered here, Eq. 2.9 can be simplified based on the following information:

1. The interaction between TI\* and PA are described by Ogston's ideal size exclusion model:  $-\phi \times \alpha_{TI^*,PA}(s, f) = -\phi(1 + \frac{R_{h,TI^*}}{a_f})^2$ .
2. The interaction between dilute TI\* molecules is approximately 0:  $\alpha_{TI^*,TI^*}(s, s) = 0$ .
3. The interaction between BSA molecules can be expressed in terms of known relationships [14, 26]:

- From Lazzara and Deen [14]:  $\alpha_{TI^*,BSA}(s, s) = (1 + \frac{R_{h,TI^*}}{R_{h,BSA}})^3$  where  $R_{h,TI^*} = 36$  Å.
- $\chi_{BSA}$  is related to the mass concentration of BSA ( $\rho_{BSA}$ ) and the specific volume of BSA [58, 59] ( $\nu_{BSA}$ ) by following relationship:  $\chi_{BSA} = \rho_{BSA} \times \nu_{BSA} = 20 \frac{g}{L} \times 7.33 \times 10^{-4} \frac{L}{g} = 0.01466$ .
- The best fit of  $K_{BSA}$  to Ogston's size exclusion model reported by Tong and Anderson [26] is:  $K_{BSA} = \exp\left[-\phi\left(1 + \frac{R_{h,BSA}}{a_f}\right)^2\right] = \exp\left[-\phi\left(1 + \frac{36\text{Å}}{5.9\text{Å}}\right)^2\right]$ .

Eq. 2.9 therefore simplifies to:

$$K_{TI^*} = \exp \left[ -\phi \left( 1 + \frac{R_{h,TI^*}}{a_f} \right)^2 + \left( 1 + \frac{R_{h,TI^*}}{R_{h,BSA}} \right)^3 \left( 1 - \left[ \exp \left[ -\phi \left( 1 + \frac{36\text{\AA}}{5.9\text{\AA}} \right)^2 \right] \right) \right] \times 0.01466 \right] \quad (2.10)$$

$K$  values were equated following Eq. 2.10, and uniform lateral distribution of solute throughout the gels was observed after normalization of lateral artefacts (Figure 2.5). The experimentally determined  $K$  values follow the anticipated size-exclusion model trend of a log-linear decrease in  $K$  with increasing gel density (Figure 2.8A). Our results fit the adjusted Ogston model with  $R^2 > 0.98$  and yielded  $a_f = 5.9 \text{ \AA}$ , which agrees with previous findings for PA gels of similar composition [26].

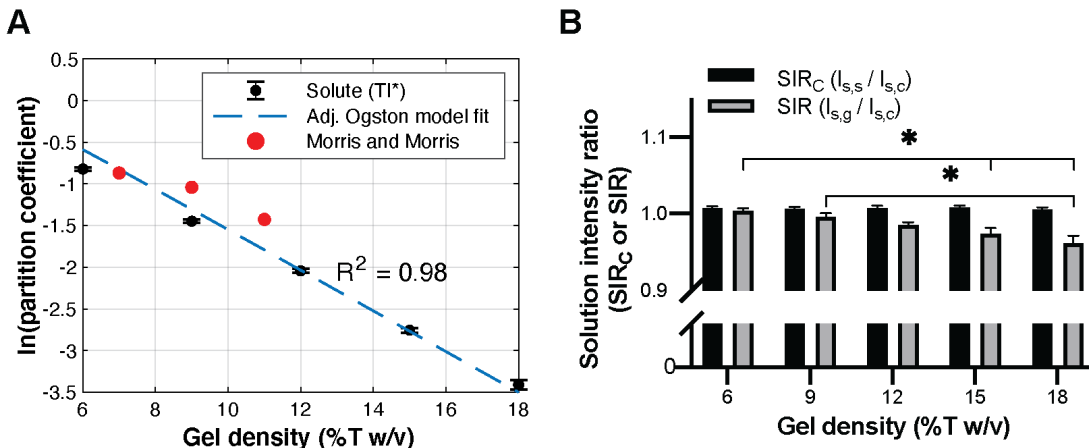


Figure 2.8: Validation of AC-LSCM measurement system. A) AC-LSCM is used to measure  $K$  of TI\* in varying density microscale hydrogels (black datapoints) compared to the adjusted Ogston model (dashed blue line) and published values (red datapoints). B) Characterization of axial artefacts over varying gel densities. Error bars indicate standard deviation of  $N = 4$  replicates. \* $p < 0.05$ , Kruskal-Wallis test with Dunn’s multiple comparison test.

We further compared our experimentally determined  $K$  values to previously reported  $K$  values for TI measured using size-exclusion chromatography in PA gels with similar acrylamide and bis-acrylamide concentrations to this study (Figure 2.8A) [60]. Morris and Morris [60] report  $K$  values of 0.419, 0.353, and 0.240 for TI in 7%T, 9%T, and 11%T w/v PA hydrogels (all with 3%C). Including the fluorophore labeling of TI (increasing the effective  $R_h$  by  $\sim 7 \text{ \AA}$ ), the estimates of Morris and Morris corroborate the  $K$  values measured here [57]. Furthermore, no significant difference is observed in the  $K$  value of TI\* when comparing a mass-balance technique to AC-LSCM adapted for macroscale gels (Figure 2.9,  $N = 3$  replicates;  $p > 0.9999$ , Mann-Whitney U-test).

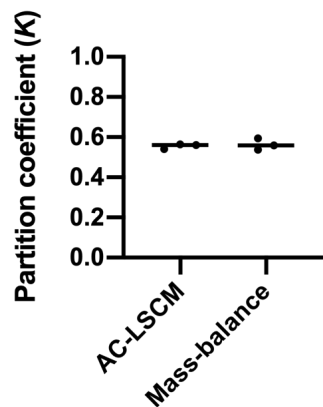


Figure 2.9:  $K$  measured using AC-LSCM does not differ significantly from mass-balance in macroscale gels ( $N = 3$  replicates,  $p > 0.05$ , Mann-Whitney U-test). AC-LSCM measurements were taken  $< 40 \mu\text{m}$  deep into the gel. The analysis code was modified to account for a thin fluid layer present between the coverslip and unattached macroscale gel during imaging.

From the 3D micrograph stacks used to calculate  $K$  (Figure 2.1), we also characterized axial aberrations by quantifying SIR and  $\text{SIR}_C$  defined in Eqs. 2.6 and 2.7, respectively. We anticipated  $\text{SIR}_C$  would remain close to 1.0 across all conditions, as the correction collar was set at the beginning of the experiment using reflected light confocal microscopy and all coverslips originated from the same lot. We observed no significant deviation of  $\text{SIR}_C$  over the conditions tested, verifying accurate positioning of the correction collar and minimal solution absorption (Figure 2.8B,  $N = 4$  replicates,  $p = 0.6312$ , Kruskal-Wallis test with Dunn's multiple comparison test). In contrast, SIR decreases from 1.0 with increasing gel density, with significant differences between gel densities (Figure 2.8B,  $N = 4$  replicates,  $p = 0.0015$ , Kruskal-Wallis test with post-test Dunn's multiple comparisons). The decreasing SIR does not appear to be due to increasing gel height (Figure 2.10). Rather, we hypothesize that SIR decreases with

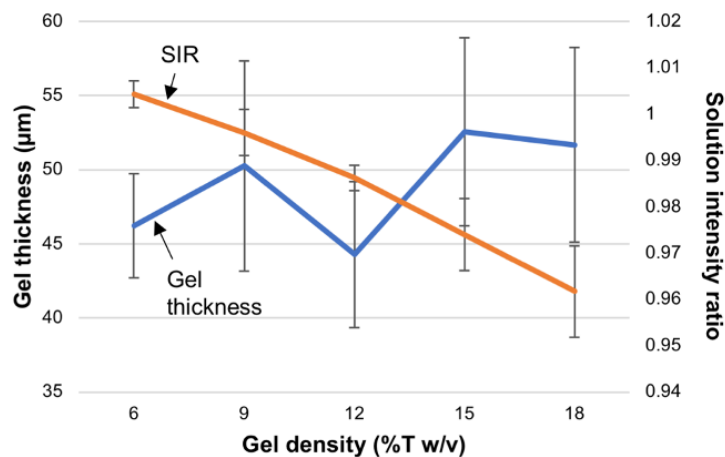


Figure 2.10: The decrease in solution intensity ratio (SIR) observed with increasing gel density is not due to increasing gel thickness. Error bars indicate standard deviation for  $N = 4$  replicates.

increasing gel density due to a measured decline in  $I_{s,g}$  caused by increasing  $n$  of the gel. As  $n$  of the gel increases, the difference between  $n$  of the gel and  $n$  of the immersion medium



(water) increases [45]. This difference has been shown to cause a decline in measured intensity with imaging depth [35, 36]. Conversely, if the correction collar position is set to the coverslip specification of 170  $\mu\text{m}$  (i.e., without using reflected light confocal microscopy position-determination), the collar position will be over-adjusted and artificially compensate for aberrations induced by denser gels, resulting in  $\text{SIR} > 1.0$  (Figure 2.11). An over-adjusted collar reports erroneous impact of aberrations on  $K$ , which could ultimately propagate to inaccurate quantitation of  $K$ .

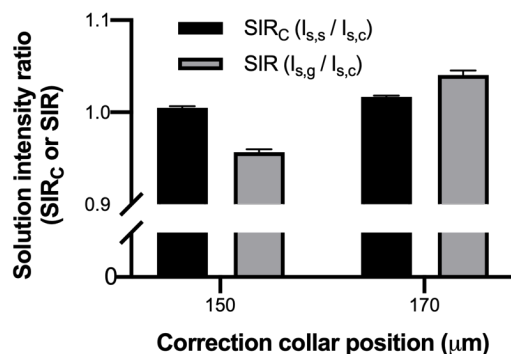


Figure 2.11: Characterization of axial artefacts in 18%T microscale PA gels when the correction collar is set using reflected light confocal microscopy (150  $\mu\text{m}$ ) vs. when the correction collar is set using coverslip thickness specifications (170  $\mu\text{m} \pm 5 \mu\text{m}$ ).  $N = 3$  replicates.

To assess the impact of axial artefacts on quantitation, we compared  $\delta_{\text{SIR}}$  to the coefficient of variation (CV) measured for each gel density (Figure 2.12). We observe a CV equal to or greater than  $\delta_{\text{SIR}}$  for each gel density, which suggests that axial aberrations are negligible for the conditions studied here. We hypothesize that, in addition to the  $n$  of these hydrogels being closely matched to the  $n$  of water, axial artefacts are further mitigated by the relatively short axial length of these gels, which reduces the required imaging depth and, concomitantly, depth-dependent artefacts.

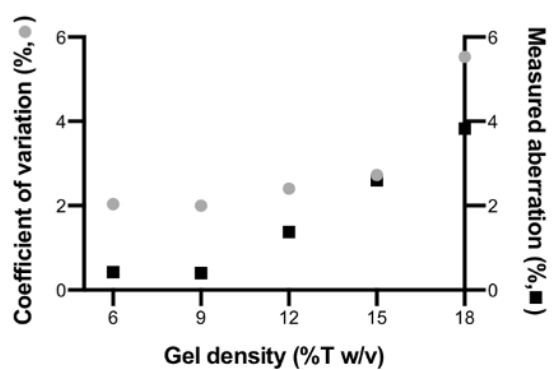


Figure 2.12: Comparison of the coefficient of variation between technical replicates and measured aberration ( $\delta_{\text{SIR}}$ , the deviation of the SIR from 1.0).

## Characterization of partitioning behavior of differently sized solutes in modified PA gels

Modifying PA structure imparts tailored functionality, including the introduction of new interactions, such as hydrophobic [42, 61], or biospecific [62] interactions (Eq. 2.3), between the altered PA gel matrix and the solute. Modification by conjugation of a photoactive molecule to the PA gel backbone introduces light-triggered solute-gel interactions. Benzophenone is a light-activated molecule that forms covalent bonds with compatible solutes through hydrogen abstraction and can be incorporated into the PA gel backbone during polymerization in the form of BPMAC [4, 63]. The impact of incorporation and photoactivation of BPMAC in PA microscale hydrogels on partitioning behavior of solutes (both after loading and after unloading) has not yet been studied. We apply the AC-LSCM measurement system to investigate this modification with 3D resolution.

We hypothesize that photoactivation of BPMAC-containing PA gels prior to introduction of solute could influence the partitioning behavior of solutes in the following ways: 1) BPMAC reaction with neighboring acrylamide strands would decrease the effective gel pore size and therefore decrease  $K$ , 2) attractive interactions between BPMAC and solute (e.g., hydrophobic or biospecific) would raise  $K$ , 3) a combination of 1 and 2, or 4) BPMAC modification of the PA gel yields no influence on partitioning behavior. Given that the ideal size-exclusion model requires that all solute molecules unload from the gel in solute-free solution, size-based and attractive interactions are independently measurable. The AC-LSCM technique differentiates the two phenomena by measuring both  $K$  and retention of solute after unloading of solute from the microscale PA gels [43].

We first sought to understand how solute loading ( $K$ ) and unloading (retention) scales with solute size in BPMAC-containing gels. We compared a commonly used immunoprobe, an antibody (Ab,  $R_h = 5.41$  nm), to a smaller antigen-binding antibody fragment (Fab,  $R_h = 2.91$  nm) [64]. Both were labeled with Alexa Fluor 647 for fluorescence visualization (Ab\* and Fab\*). We observed that photoactivated BPMAC-containing gels retain considerably more Fab\* and Ab\* after loading and subsequent unloading compared to vehicle control gels in the presence or absence of UV exposure or gels containing BPMAC without UV exposure (Figure 2.13). Therefore,  $K$  values and retained in-gel immunoprobe fluorescence after unloading were measured for the two most relevant conditions: vehicle control gels and photoactivated BPMAC-containing gels. Importantly, the 3D resolution provided by the AC-LSCM system provides critical insight into the spatial distribution of retention, not obtainable with indirect methods or wide-field fluorescence microscopy.

Anticipated  $K$  values were estimated using Eq. 2.8, Eq. 2.10 (adjusted to account for BSA interactions), and the parameters determined previously for PA gels used in this study (Table 2.3). Interestingly, the observed  $K$  value for Ab\* in vehicle control gels exceeds that predicted by theory by 89% (Eq. 2.8) and 52% (Eq. 2.10) (Table 2.3). One possible explanation for the discrepancy between the measured and theoretical  $K$  values could stem from our assumption that Alexa Fluor 647 adds  $\sim 7$  Å to  $R_h$ ; depending on the label site, we hypothesize that the dye may not contribute significantly to  $R_h$  for larger molecules.

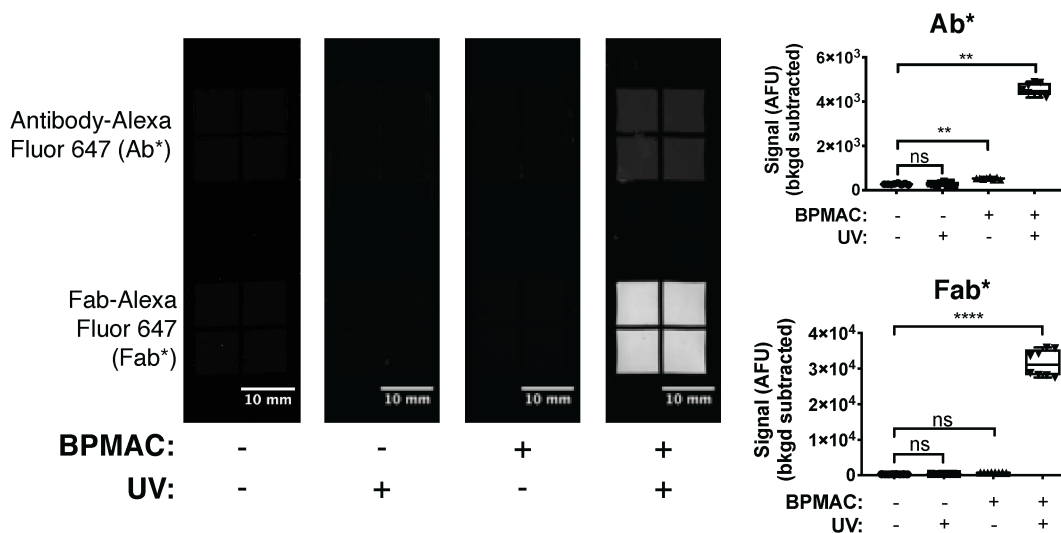


Figure 2.13: Representative micrographs demonstrating higher intensity of fluorescently labeled probes in BPMAC-functionalized gels after exposure to UV (top) and fluorescence intensity quantitation (bottom). \*\* $p < 0.05$ , \*\*\*\* $p < 0.0001$ , ns = non-significant,  $N = 8$  replicates, one-way ANOVA with Dunnett’s multiple comparison test.

Table 2.3: Partition coefficients of Ab\* and Fab\* in vehicle control and photoactivated 6%T w/v microscale PA gels

	$K_{Ab^*}$	$K_{Fab^*}$
Theory (Eq. 2.8)	0.045	0.30
Theory (Eq. 2.10)	0.056	0.32
Vehicle control gels	$0.085 \pm 0.004$	$0.368 \pm 0.005$
Photoactivated gels	$0.097 \pm 0.007$	$0.407 \pm 0.011$

If  $R_h$  of Ab\* is assumed to equal  $R_h$  of Ab (54 Å), the anticipated  $K$  value is 0.089 (Eq. 2.8) or 0.101 (Eq. 2.10), closer to the measured value. Also notable is the observation that the measured  $K$  value for Ab\* in 6%T w/v gels is only 50% of the reported  $K$  value for Ab\* in 8%T w/v microscale PA gels measured previously using widefield fluorescence [4]. Though the experimental conditions were not identical, our results using AC-LSCM suggest the importance of optical sectioning techniques for accurate  $K$  measurements in these open microscale hydrogel systems.

To determine what impact the incorporation and photoactivation of BPMAC has on  $K$  values of Ab\* and Fab\*, we compared  $K$  values in UV-exposed BPMAC-modified PA gels to vehicle control gels (Table 2.3). We observe a statistically significant ( $\sim 10\%$ ) increase in  $K$  values for both Ab\* and Fab\* in photoactivated BPMAC-modified PA gels compared to controls ( $N = 4$  replicates, Mann-Whitney U-test,  $p = 0.0286$ , Figure 2.14A). These higher  $K$  values in BPMAC-photoactivated PA gels indicate that the inclusion and photoactivation of

BPMAC causes a shift in the thermodynamic equilibrium state of the immunoprobes towards the gel phase, likely due to attractive interactions between the solutes and immobilized BPMAC.

As described earlier, important to quantitation is the measurement of SIR and  $SIR_C$  for all experimental conditions. All ratios were close to 1.0 (Figure 2.14B), confirming that the correction collar was accurately positioned and that activated BPMAC does not introduce additional axial artefacts.

We also investigated whether Ab\* and Fab\* are retained in photoactivated BPMAC-modified PA gels after unloading in solute-free buffer, how retention is distributed throughout the gel in all three dimensions, and if the amount retained depends on solute size. These questions are critical not only for a fundamental understanding of how photoactivated BPMAC influences PA gel-solute interactions, but also because these photoactivatable gels are currently essential for targeted proteomic electrophoretic cytometry assays in their ability to serve as both a separation matrix (for electrophoresis) and an immunoblotting scaffold (for a subsequent immunoassay) [4, 65]. Given that the background and noise generated by immunoprobe in in-gel immunoassays is directly related to retention of immunoprobe in the gel after unloading, understanding how this photoactivated BPMAC-modified gel matrix impacts immunoprobe partitioning behavior is critical [11]. After the micrographs to calculate  $K$  were acquired, all gels were subjected to solute unloading in  $1 \times$  TBST for  $>2$  h and imaged to quantify remaining in-gel solute fluorescence. The mean fluorescence intensities after washout of Ab\* and Fab\* in both gel conditions are presented in Figure 2.14C.

The results show that significant amounts of both Ab\* and Fab\* remain in the gel after unloading compared to vehicle control gels ( $N = 4$  replicates, Mann-Whitney U-test,  $p = 0.0286$ ). Furthermore, axial intensity profiles establish that retention of both immunoprobes throughout the gels is uniform in all three dimensions (Figure 2.15), establishing that reten-

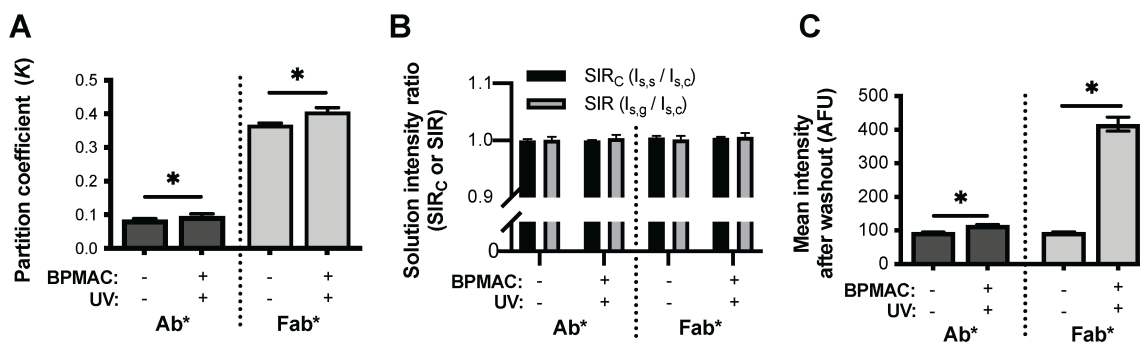


Figure 2.14: Comparison of partitioning behavior of Ab\* and Fab\* in photoactivated BPMAC-containing and vehicle control gels. A)  $K$  of immunoprobes in photoactivated BPMAC-modified gels and vehicle control gels. B) Characterization of solution intensity ratios reveal minimal axial aberrations. C) Comparison of retention of both immunoprobes after unloading in photoactivated BPMAC-containing gels compared to control gels. Error bars indicate standard deviation of  $N = 4$  replicates. \* $p < 0.05$ , Mann Whitney U-test.

tion is not caused by adsorption of solute to the outer surface of the gel. We hypothesize that probe retention is caused by one of three potential mechanisms of interaction with BPMAC after UV exposure: 1) formation of benzopinacol [63], which forms hydrophobic interactions with the probes, 2) continued reactivity of BPMAC, resulting in covalent bonds forming between immunoprobe and gel backbone, or 3) formation of an “IgG-like” epitope that is reactive with both immunoprobes.

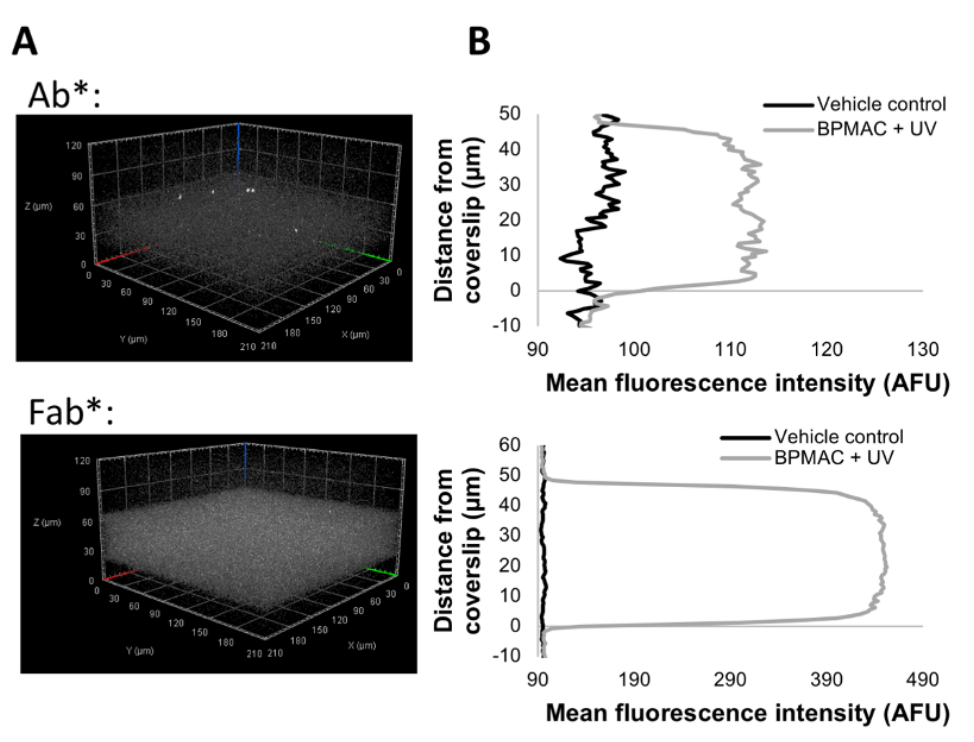


Figure 2.15: Retention of Ab\* and Fab\* after unloading from gel. A) Representative micrographs of photoactivated BPMAC-containing gels (BPMAC + UV) after unloading of immunoprobe. B) Representative intensity profiles of vehicle control and BPMAC + UV PA gels comparing the retained fluorescence after unloading of immunoprobe. Note that a  $1 \times 1 \times 1$  median 3D filter was applied prior to generation of the intensity profiles to reduce pixel noise.

To understand the impact of immunoprobe size on partitioning behavior in photoactivated gels, we compared the ratios of  $I_g$  after to  $I_g$  before washout for both Ab\* and Fab\*, which normalizes for different degrees of labeling between the two probes. We find that Fab\* is significantly ( $5.4\times$ ) more retained than Ab\* in photoactivated BPMAC-containing gels ( $N = 4$  replicates, Mann-Whitney U-test,  $p = 0.0286$ ). Note that the median filter applied for image analysis lowers the average mean intensity in-gel after unloading much more than after loading: the average mean intensity in-gel after unloading is lowered by  $\sim 55\%$  and  $\sim 35\%$  compared to  $3.2\%$  and  $1.7\%$  after loading for Ab\* and Fab\*, respectively (Figure 2.16). Therefore, the fraction of retained fluorescence in-gel is an underestimate. We

attribute the increased retention of smaller immunoprobe to the higher in-gel Fab\* concentration compared to Ab\* ( $\sim 270$  nM vs.  $\sim 65$  nM), resulting in more availability to interact with BPMAC which is present in excess (3 mM in the precursor solution). The higher retention of Fab\* has degrading implications for the analytical sensitivity of in-gel immunoassays using smaller immunoprobes: even though Fab\* has a higher  $K$  value than Ab\*, higher retention after washout leads to higher background signal.

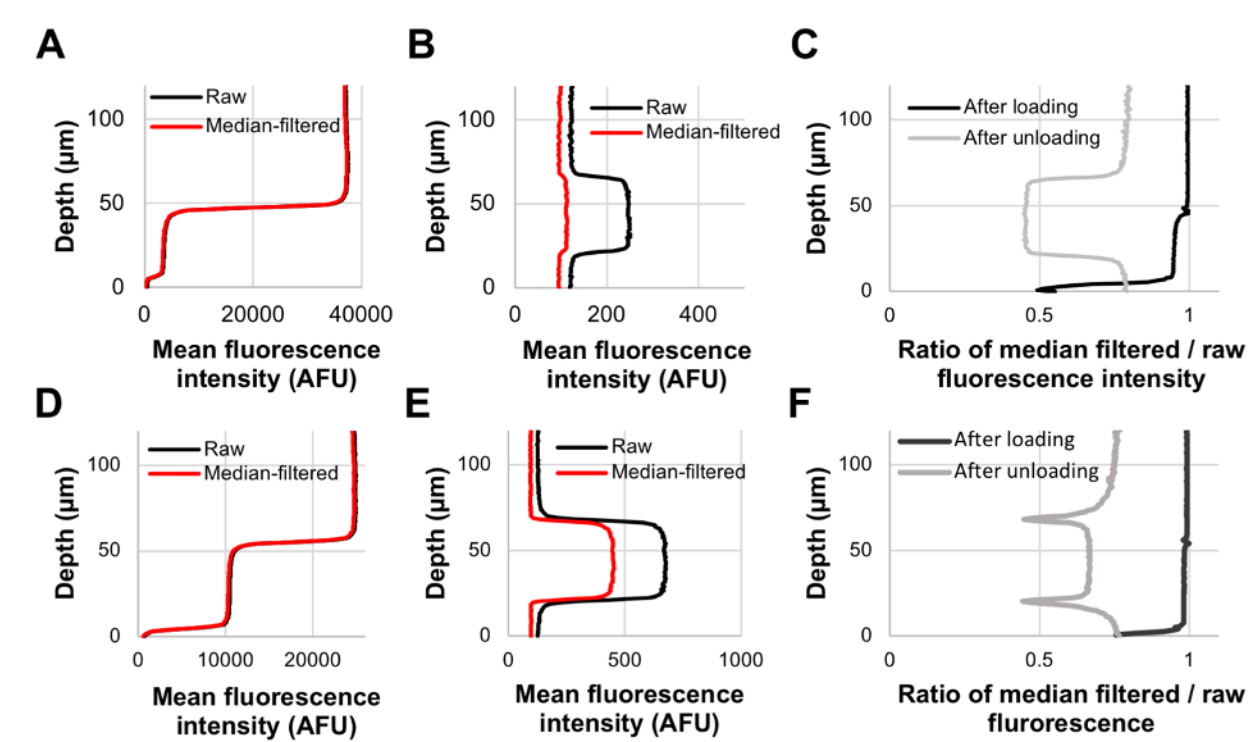


Figure 2.16: Differential impact of  $1 \times 1 \times 1$  median 3D filter on in-gel fluorescence intensity profiles. (A) Comparison of raw and median-filtered average fluorescence intensities with depth for gel image after loading of Ab\*. (B) Comparison of raw and median-filtered average fluorescence intensities for gel image after unloading of Ab\*. (C) Measured ratios of median-filtered to raw average fluorescence intensities before and after unloading of Ab\*. (D-F) Same as A-C, except with Fab\* as solute.

### Assessing $K$ in PA gels with physically modified microarchitecture

In addition to the introduction of new interactions, we sought to investigate how physical modifications to the hydrogel microarchitecture impact  $K$ . We studied Ab\* partitioning into PA gels designed to offer a larger mean pore radius by inducing lateral aggregation by including a preformed hydrophilic polymer (i.e., PEG) during PA gel polymerization [66]. Incorporation of PEG creates a bimodal pore size distribution in the resultant hydrogel,

with open fluidic spaces formerly occupied by the porogen and small pores created between bundles of polyacrylamide [38, 67, 68]. For these “highly porous” PA gel formulations, the mean pore radius can be  $\sim 250$  nm (quantified for a 5%T, 4%C PA gel incorporating 2% PEG with a PA bundle radius at 150 nm), a 100-fold increase [38]. After polymerization, the unfunctionalized PEG freely diffuses out of the PA gel network; however, a small fraction of the PEG is thought to remain within the PA gel as a semi-interpenetrating network, which may inhibit in-gel diffusion of soluble species [66]. Thus, we hypothesize that  $K$  will increase with the PEG concentration in the gel precursor due to increasing mean pore size. We measured  $K$  in PA microscale hydrogels containing 0-2.0% (in 0.5% increments) PEG in the gel precursor (Figure 2.17). As controls, we also studied two PA gel formulations similar to published formats (i.e., 6%T 3.3%C PA gel; mean pore radius  $\sim 5-92$  nm; and fiber radius  $\sim 0.5$  nm [38, 53]).

As anticipated, we observed a  $K$  for the 2% PEG highly porous PA gels that was significantly larger than both the benchmark gels and negative control gels (benchmark gels,  $K = 0.11 \pm 0.01$ ; negative control gels,  $K = 0.20 \pm 0.01$ ; 2% PEG highly porous PA gels,  $K = 0.35 \pm 0.02$ ; mean  $\pm$  standard deviation;  $N = 3-6$  gels). These observed  $K$  values are corroborated by confocal microscopy of PA gel formulations similar to our benchmark gel formulations [69]. Characterization of PA gels created under lateral chain aggregation conditions by scanning electron microscopy (SEM) reports similar porosity [38].

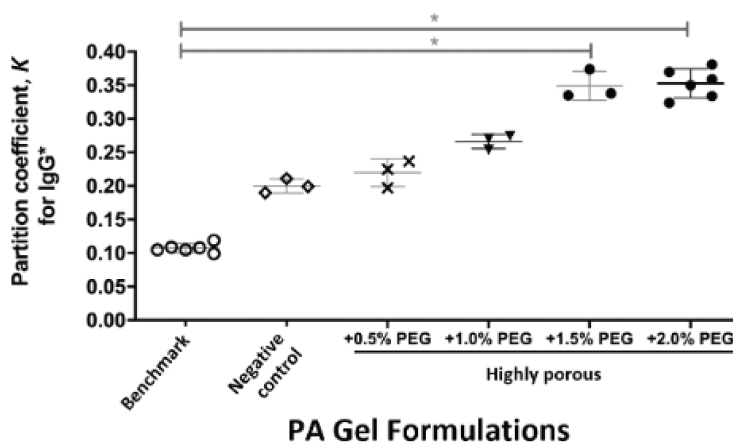


Figure 2.17:  $K$  is sensitive to PA gel formulation. Partitioning of Ab\* into the hydrogel network indicates a statistically significant increase in  $K$  due to the gel formulation and incorporation of PEG. Mean and standard deviation marked for  $N = 3-6$  gels per condition, one-way ANOVA with Kruskal-Wallis test and post-hoc Dunn’s multiple comparison test with  $p < 0.05$  (\*).

The 2-fold increase in  $K$  between the benchmark gels and negative control gel is hypothesized to arise from bisacrylamide aggregating into bundles in the higher %C formulation, as has been previously observed (20%C and 60%C PA gels) [70], and corroborated by freeze-etched transmission electron microscopy (TEM) of similar PA gel formulations [71] and an observed decrease in elastic modulus [72] (10%C PA gels versus lower %C PA gels).



## Assessing $K$ in multi-layered PA gels

We next considered a two-layer PA gel structure and applied AC-LSCM to measure  $K$  along the z-axis of the composite system (Figure 2.18). The two-layer gel comprises a large-pore-size gel layered atop a smaller-pore-size gel. The two-layer gel is fabricated layer-by-layer on a chambered coverslip. The bottom gel is cast from a 15%T w/v precursor solution ( $15\%T_{nom}$ , “nom” = nominal). A 6%T w/v precursor solution is polymerized *in situ* on the hydrated bottom gel to form the top gel ( $6\%T_{nom}$ ). After fabrication, the composite structure is immersed in a solution of TI\*. Using AC-LSCM, we measured  $K$  in each layer of the two-layer gel structure (which required small adjustments to the analysis script to identify multiple gel layers) and in each of two control gel configurations, which comprised single-layer gels having the same nominal gel composition as each layer from the two-layer gel (Table 2.4).

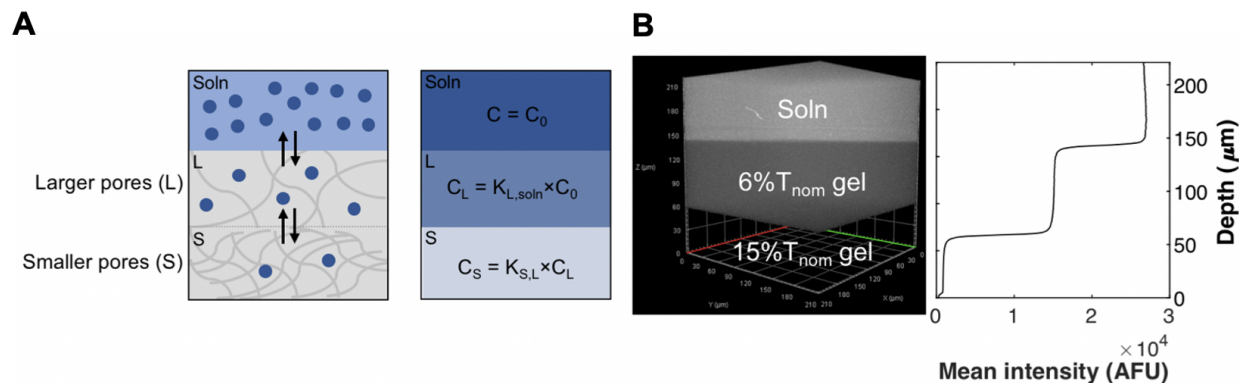


Figure 2.18: A) Schematic exhibiting how solute partitioning can vary axially in multi-layered gels, highlighting the importance of 3D spatial resolution. The subscripts of  $K$  indicate the source of the concentrations with which  $K$  is calculated for the equation. B) Representative fluorescence micrograph and corresponding intensity profile of two-layer gel system which is comprised of two gel layers seated on a chambered coverslip. A solution of TI\* is applied to the top of the sandwich structure for the  $K$  measurements.

Table 2.4:  $K$  of composite, two-layer gel structures measured by AC-LSCM

$K$	Two-layer ( $N = 4$ )	Single-layer ( $N = 4$ )
6%T formulation	$0.52 \pm 0.01$	$0.44 \pm 0.02$
15%T formulation	$0.021 \pm 0.001$	$0.067 \pm 0.003$

In comparison to control gels, the  $K$  value for the top gel layer was 18% larger than that of the single-layer 6%T control gel ( $N = 4$  replicates;  $p = 0.0286$ , Mann-Whitney U-test). For the bottom layer of the two-layer gel system, we observed a  $K$  value that is 69% smaller than the single-layer 15%T control gel ( $N = 4$  replicates;  $p = 0.0286$ , Mann-Whitney U-test)



(Figure 2.19A). We next sought to understand why the effective  $K$  values measured for each layer of the two-layer gel structure differ from the  $K$  values of each gel when fabricated as a single gel layer.

First, when considering the top layer of the two-layer structure, we note that the top layer sits atop the hydrated 15%T<sub>nom</sub> bottom gel layer, whereas the single-layer control gel sits atop a chambered coverslip. Consequently, in the two-layer configuration, we expect excess water from the hydrated 15%T<sub>nom</sub> gel to dilute the concentration of acrylamide monomer in the 6%T precursor solution, prior to polymerization of the 6%T layer. A single-layer gel will not experience this dilution effect. In the two-layer system, the dilution process will create a lower effective pore size in the top layer than that expected from the nominal 6%T of the precursor solution.

Second, when considering the bottom layer, we expect that the layer-by-layer fabrication approach will see diffusion of free monomer from the top layer precursor solution into the polymerized bottom layer. The diffusion of monomer into the 15%T network will create a denser network than expected from the nominal 15%T of the precursor solution. The generation of smaller pore sizes caused by an acrylamide concentration gradient has been reported in photopolymerized PA gels [73]. In that study, a gradient of pore sizes along the main axis of diffusion was observed. We observe not a gradient, but an apparent uniform distribution of TI\* throughout the 15%T<sub>nom</sub> gel layer, indicative of a uniform pore size distribution (Figure 2.18).

To consider whether the uniformity of partitioning (used as a proxy for pore size) observed in the two-layer system contradicts the hypothesis that acrylamide diffusion causes the smaller pore sizes observed in both systems, we recall that the spatial uniformity of pore size in the bottom gel depends on whether the system is transport- or reaction-limited. This

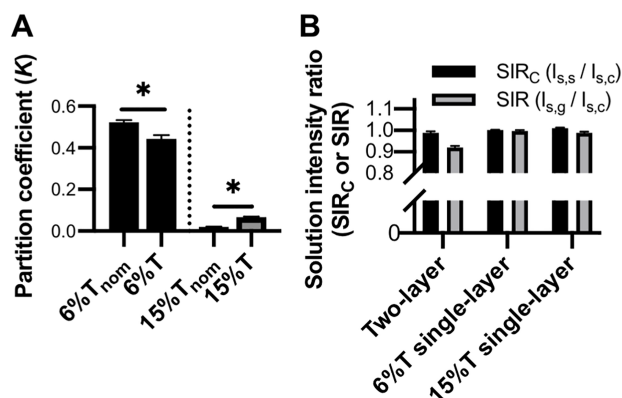


Figure 2.19: Two-layer gel structures exhibit more complex partitioning behavior than single-layer control gels of same nominal pore size. A)  $K$  of TI\* in each layer of the two-layer gel (“nom”) compared to control single-layer gel. B) Characterization of solution intensity ratios to assess axial aberrations. Error bars indicate standard deviation of  $N = 4$  replicates. \* $p < 0.05$ , Mann-Whitney U-test.

can be determined by evaluating the Damköhler number (Da) of the system, which compares the transport equilibrium time ( $\tau_{transport}$ ) to the reaction equilibrium time ( $\tau_{reaction}$ ):  $Da = \frac{\tau_{transport}}{\tau_{reaction}}$ . Chemical polymerization of acrylamide using low %C has been shown to near completion after 12-15 min [40], which suggests  $\tau_{reaction}$  on the order of min, while the small size and fast diffusivity of acrylamide lead to an estimated  $\tau_{transport} \sim 2$  sec in solution ( $\sim 9$  sec in a 40  $\mu\text{m}$  15%T gel) [74]. These timescales produce  $Da \ll 1$ , indicating a reaction-limited system. Thus, analysis of the Damköhler number demonstrates that the uniform distribution observed in this study using chemically polymerized gels is consistent with theory.

Third, we must account for the differing solute concentration boundary conditions of the 15%T gel in the two configurations. In the two-layer gel, the top 6%T<sub>nom</sub> layer creates a boundary condition where the solute concentration interfacing with the 15%T<sub>nom</sub> gel layer is not the bulk solution concentration  $C_0$ , but rather the concentration in the 6%T<sub>nom</sub> gel,  $C_{6\%T_{nom}} = K_{6\%T_{nom}} \times C_0$  (Figure 2.18). In a multi-layered system dominated by size-exclusion partitioning where one layer is screened from the bulk solution phase, past studies have shown that the screened layer will not reach equilibrium with the bulk solution phase, resulting in a lower  $K$  value when  $K$  is measured with respect to the bulk solution concentration [75]. This applies to the system considered here when images are acquired far from the gel edges and equilibrium is established along the shorter axial  $z$  dimension but not the lateral dimension [75]. Interestingly, when the configuration of the two-layer gel system is reversed, only a single gel layer is distinguishable using AC-LSCM (Figure 2.20). The observed uniformity in gel pore size is consistent with the analysis presented and is likely due to a combination of a denser network formed during polymerization of the dense top gel layer, and the low concentration of solute available to partition into the bottom gel due to the solute concentration boundary condition.

Finally, we consider depth-dependent aberrations and their influence on measured  $K$  values. We observe  $\delta_{SIR} = 8\%$  in the two-layer gels, greater than those of the control 6%T ( $\delta_{SIR} = 0.3\% \pm 0.5\%$ ) and 15%T ( $\delta_{SIR} = 1.1\% \pm 0.6\%$ ) single-layer gels and greater than  $\delta_{SIRC}$  ( $\delta_{SIRC} = 1.7\% \pm 0.9\%$ ) ( $N = 4$  replicates, Figure 2.19B). The deviation from 1.0 is expected and stems from the larger thickness of the two-layer gels ( $>100 \mu\text{m}$ ) compared to the single-layer control gels (20-60  $\mu\text{m}$ ). The thicker gels increase the imaging depth required to reach  $I_{s,s}$  and therefore enhance depth-dependent aberrations. In this case, the 8% decrease in solution intensity after imaging through the gel is larger than the CV of the  $K$  values measured in both the 6%T<sub>nom</sub> gel ( $CV_K = 2.0\%$ ) and 15%T<sub>nom</sub> gel ( $CV_K = 4.6\%$ ) layers. The depth-dependent aberrations introduced by the gel act to reduce the measured solute fluorescence intensity  $I_g$  in the gel. Therefore, the reduced fluorescence intensity measured in the gel would also be observed using standard LSCM. However, the AC-LSCM technique additionally reports the accuracy of the  $I_g$  measurement. Through the  $\delta_{SIR}$  value, AC-LSCM estimates the degree of optical aberration-induced, depth-dependent variation in  $I_g$ , thus allowing a user to determine the accuracy of  $K$ . For example, in the system studied here, the  $I_g$  value in both the 6%T<sub>nom</sub> and the 15%T<sub>nom</sub> gel layers has a  $\delta_{SIR} = 0.08$  (Figure 2.19B). A  $\delta_{SIR}$  of 0.08 means that  $K$  is within 8% of the measured value. To

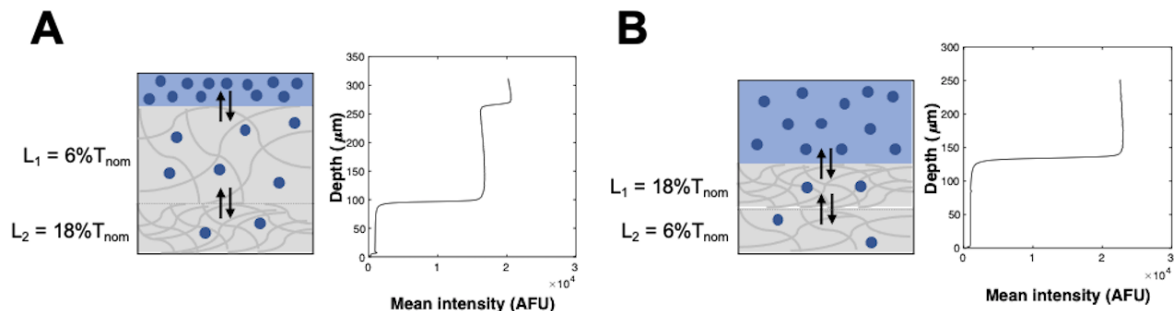


Figure 2.20: Schematics and representative fluorescence intensity profiles of two-layer gel systems ( $6\%T_{\text{nom}}$  and  $18\%T_{\text{nom}}$ ) with different gel layer configurations in equilibrium with  $\text{TI}^*$ . A) Two-layer gel configuration with larger pore size  $6\%T_{\text{nom}}$  gel fabricated on top of a smaller pore size  $18\%T_{\text{nom}}$  gel. Note the distinct two different gel layers detectable using AC-LSCM. B) Two-layer gel configuration with smaller pore size  $18\%T_{\text{nom}}$  gel fabricated on top of a larger pore size  $6\%T_{\text{nom}}$  gel. Note the single homogeneous gel layer detectable using AC-LSCM. In this case, the lengths  $L_1$  and  $L_2$  are estimates.

further reduce uncertainty in the  $K$  measurement, an empirical relationship describing the aberration-induced depth-dependence of the in-gel fluorescence signal could be established by fabricating a gel ‘wedge’ having a top surface with a constant incline from the coverslip to the maximum gel thickness. The gel wedge would be incubated with the fluorescent solute, and the variable thickness of the gel would quantify the impact of depth-dependent aberrations on measured fluorescence ( $\delta_{SIR}$ ), for all  $z$ -positions in the gel. The concentration distribution of the solute – throughout the thickness of the gel – then would be determined by correcting the measured fluorescence signal by the known amount of aberration at each height. To ensure that the entire light path is contained within the gel (to avoid additional refractive errors during imaging), the angle of the gel ( $\theta_{\text{gel}}$ ) must be greater than the angle of the numerical aperture (NA) of the light path (Figure 2.21). Given that  $\text{NA} = n \times \sin(\theta_{\text{NA}})$  where  $\theta_{\text{NA}}$  is the half-angle of light emerging from the objective, for the 1.1 NA objective used in this study, the angle of the gel must be greater than  $\arcsin(\text{NA}/n) = \arcsin(1.1/1.33) = 56^\circ$ .

## 2.4 Conclusions

We report on AC-LSCM, a measurement tool for quantifying spatially resolved partitioning behavior of solutes in open microscale hydrogel systems. The measurement system minimizes and quantifies optical artefacts that could further confound analysis while providing 3D spatial information on the distribution of solute within different hydrogel systems. We quantify the effect of pore size, chemical modifications to the gel backbone, and physical modifications to the gel microarchitecture on partitioning of proteins into microscale PA gels. We find that while unmodified microscale PA gels follow size-exclusion partitioning, modification of the PA backbone with an activated BPMAC photocapture moiety results in spatially uniform,

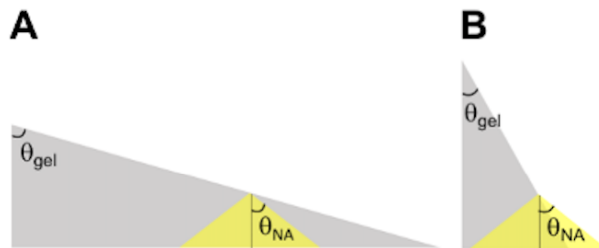


Figure 2.21: Schematic illustrating how the angle of the gel ( $\theta_{gel}$ ) must be greater than the angle of the numerical aperture of the objective ( $\theta_{NA}$ ) to avoid refractive errors when imaging gels with constantly increasing thickness. A)  $\theta_{gel} > \theta_{NA}$ . B)  $\theta_{gel} < \theta_{NA}$ .

size-dependent retention of immunoprobes. This is intriguing, as benzophenone has been reported to be stable under ambient light and only remains in the activated state on the order of  $\mu\text{s}$  [63]. Additionally, we observe that  $K$  values increase with PEG concentration incorporated in the gel precursor, supporting the hypothesis that larger mean pore sizes are formed. We further characterize the partitioning characteristics of composite multilaminate gels using AC-LSCM. We measure the differential partitioning of solute in the distinct gel layers. Partitioning analysis revealed deviations in  $K$  of a model solute in the layers of these composite gels compared to single-layer control gels, consistent with theory. Overall, AC-LSCM and the accompanying analysis process presented in this study provide a data-rich framework for characterizing 3D partitioning of solutes in complex hydrogel structures with high precision and accuracy that can be readily extended beyond hydrogel systems to measure  $K$  in other systems, such as solid-phase microextraction systems that have applications ranging from environmental to biomedical and pharmaceutical to physicochemical [76].

# Bibliography

1. Álvarez-Paino, M., Muñoz-Bonilla, A. & Fernández-García, M. Antimicrobial Polymers in the Nano-World. *Nanomaterials* **7**, 1–44. doi:10.3390/nano7020048 (2017).
2. Appleyard, D. C. *et al.* Bar-coded hydrogel microparticles for protein detection: synthesis, assay and scanning. *Nature Protocols* **6**, 1761–1774. doi:10.1038/nprot.2011.400 (2011).
3. Kamperman, T. *et al.* Single-Cell Microgels: Technology, Challenges, and Applications. *Trends in Biotechnology* **36**, 850–865. doi:10.1016/j.tibtech.2018.03.001 (2018).
4. Hughes, A. J. *et al.* Single-cell western blotting. *Nat Methods* **11**, 749–755. doi:10.1038/nmeth.2992 (2014).
5. Gehrke, S. H. *et al.* Factors Determining Hydrogel Permeability. *Annals of the New York Academy of Sciences* **831**, 179–184. ISSN: 00778923. doi:10.1111/j.1749-6632.1997.tb52194.x (2006).
6. Albertsson, P. Partition of cell particles and macromolecules in polymer two-phase systems. *Advances in Protein Chemistry* **24**, 309–341. ISSN: 00653233. doi:10.1016/S0065-3233(08)60244-2 (1970).
7. Peppas, N. A. *et al.* Hydrogels in Biology and Medicine: From Molecular Principles to Bionanotechnology. *Advanced Materials* **18**, 1345–1360. ISSN: 0935-9648. doi:10.1002/adma.200501612 (2006).
8. Lowman, A. *et al.* Oral delivery of insulin using pH-responsive complexation gels. *Journal of Pharmaceutical Sciences* **88**, 933–937. ISSN: 0022-3549. doi:10.1021/JS980337N (1999).
9. Lin, F. & Sun, A. Microencapsulated islets as bioartificial endocrine pancreas. *Science* **210**, 908–910 (1980).
10. Nafea, E. H. *et al.* Immunoisolating semi-permeable membranes for cell encapsulation: Focus on hydrogels. *Journal of Controlled Release* **154**, 110–122. doi:10.1016/j.jconrel.2011.04.022 (2011).
11. Vlassakis, J. & Herr, A. E. Effect of Polymer Hydration State on In-Gel Immunoassays. *Analytical Chemistry* **87**, 11030–11038. doi:10.1021/acs.analchem.5b03032 (2015).

12. Choi, N. W. *et al.* Multiplexed Detection of mRNA Using Porosity-Tuned Hydrogel Microparticles. *Analytical Chemistry* **84**, 9370–9378. doi:10.1021/ac302128u (2012).
13. Appleyard, D. C., Chapin, S. C. & Doyle, P. S. Multiplexed Protein Quantification with Barcoded Hydrogel Microparticles. *Analytical Chemistry* **83**, 193–199. doi:10.1021/ac1022343 (2011).
14. Lazzara, M. J. & Deen, W. M. Effects of concentration on the partitioning of macromolecule mixtures in agarose gels. *Journal of Colloid and Interface Science* **272**, 288–297. doi:10.1016/j.jcis.2003.10.008 (2004).
15. Kosto, K. B., Panuganti, S. & Deen, W. M. Equilibrium partitioning of Ficoll in composite hydrogels. *Journal of Colloid and Interface Science* **277**, 404–409. doi:10.1016/j.jcis.2004.04.063 (2004).
16. Yoon, S. C. & Jhon, M. S. The transport phenomena of some model solutes through postcrosslinked poly(2-hydroxyethyl methacrylate) membranes with different tactic precursors. *Journal of Applied Polymer Science* **27**, 3133–3149. ISSN: 10974628. doi:10.1002/app.1982.070270834 (1982).
17. Peng, C.-C. & Chauhan, A. Extended cyclosporine delivery by silicone-hydrogel contact lenses. *Journal of Controlled Release* **154**, 267–274. doi:10.1016/j.jconrel.2011.06.028 (2011).
18. Lei, J. *et al.* Synthesis and Characterization of Poly(ethylene glycol) Methacrylate Based Hydrogel Networks for Anti-Biofouling Applications. *Macromolecular Materials and Engineering* **298**, 967–980. ISSN: 14387492. doi:10.1002/mame.201200297 (2013).
19. Buehler, K. L. & Anderson, J. L. Solvent Effects on the Permeability of Membrane-Supported Gels. *Ind. Eng. Chem. Res.* **41**, 464–472. doi:10.1021/ie010321z (2002).
20. Dursch, T. *et al.* Fluorescent solute-partitioning characterization of layered soft contact lenses. *Acta Biomaterialia* **15**, 48–54. ISSN: 1742-7061. doi:10.1016/J.ACTBIO.2014.11.046 (2015).
21. Watkins, A. W., Southard, S. L. & Anseth, K. S. Characterizing multilaminated hydrogels with spatially varying network structure and solute loading using confocal laser scanning microscopy. *Acta Biomaterialia* **3**, 439–448. doi:10.1016/j.actbio.2006.11.006 (2007).
22. Parker, C. A. & Rees, W. T. Fluorescence spectrometry. A review. *The Analyst* **87**, 83. ISSN: 0003-2654. doi:10.1039/an9628700083 (1962).
23. Kubista, M. *et al.* Experimental correction for the inner-filter effect in fluorescence spectra. *The Analyst* **119**, 417–419. ISSN: 0003-2654. doi:10.1039/AN9941900417 (1994).
24. F. Swinehart, D. The Beer-Lambert Law. *Journal of Chemical Education* **39**, 333–335. doi:10.1021/ed039p333 (1962).

25. Russell, S. M. & Carta, G. Mesh Size of Charged Polyacrylamide Hydrogels from Partitioning Measurements. *Industrial and Engineering Chemistry Research* **44**, 8213–8217. doi:10.1021/ie050079m (2005).
26. Tong, J. & Anderson, J. L. Partitioning and Diffusion of Proteins and Linear Polymers in Polyacrylamide Gels. *Biophysical Journal* **701**, 1505–1513 (1996).
27. Herrmann, A. *et al.* Spatial Separation of Microbeads into Detection Levels by a Bioorthogonal Porous Hydrogel for Size-Selective Analysis and Increased Multiplexity. *Analytical Chemistry* **91**, 8484–8491. doi:10.1021/acs.analchem.9b01586 (2019).
28. Linden, T. *et al.* Visualizing patterns of protein uptake to porous media using confocal scanning laser microscopy. *Separation Science and Technology* **37**, 1–32. ISSN: 1520-5754. doi:10.1081/SS-120000319 (2002).
29. Ljunglöf, A. & Thömmes, J. Visualising intraparticle protein transport in porous adsorbents by confocal microscopy. *Journal of Chromatography A* **813**, 387–395. ISSN: 00219673. doi:10.1016/S0021-9673(98)00378-1 (1998).
30. Blasi, L. *et al.* Uptake and distribution of labeled antibodies into pH-sensitive microgels. *Acta Biomaterialia* **6**, 2148–2156. doi:10.1016/j.actbio.2009.12.031 (2010).
31. Thomas, F. A. *et al.* Introducing a fluorescence-based standard to quantify protein partitioning into membranes. *BBA - Biomembranes* **1848**, 2932–2941. doi:10.1016/j.bbamem.2015.09.001 (2015).
32. Zielinska, K. *et al.* Partitioning of Humic Acids between Aqueous Solution and Hydrogel: Concentration Profiling of Humic Acids in Hydrogel Phases. *Langmuir* **30**, 2084–2092. doi:10.1021/1a4050094 (2014).
33. Vagias, A. *et al.* Diffusion and Permeation of Labeled IgG in Grafted Hydrogels. *Macromolecules* **50**, 4770–4779. doi:10.1021/acs.macromol.7b00514 (2017).
34. Kotsmar, C. *et al.* Aqueous Solute Partitioning and Mesh Size in HEMA/MAA Hydrogels. *Macromolecules* **45**, 9177–9187. doi:10.1021/ma3018487 (2012).
35. Hell, S. *et al.* Aberrations in confocal fluorescence microscopy induced by mismatches in refractive index. *Journal of Microscopy* **169**, 391–405. ISSN: 00222720. doi:10.1111/j.1365-2818.1993.tb03315.x (1993).
36. Michielsen, S. Aberrations in confocal spectroscopy of polymeric materials: Erroneous thicknesses and intensities, and loss of resolution. *Journal of Applied Polymer Science* **81**, 1662–1669. ISSN: 0021-8995. doi:10.1002/app.1597 (2001).
37. Kang, C.-C. C. *et al.* Single cell-resolution western blotting. *Nat Protoc* **11**, 1508–1530. ISSN: 1750-2799. doi:10.1038/nprot.2016.089 (2016).
38. Righetti, P. G. *et al.* ‘Laterally aggregated’ polyacrylamide gels for electrophoresis. *Electrophoresis* **13**, 587–595. ISSN: 15222683. doi:10.1002/elps.11501301119 (1992).
39. Menter, P. *Acrylamide Polymerization - A Practical Approach*. *BioRad technical note 1156*.

40. Gelfi, C. & Righetti, P. G. Polymerization kinetics of polyacrylamide gels I. Effect of different cross-linkers. *Electrophoresis* **2**, 213–219. doi:10.1002/elps.1150020404 (1981).
41. Righetti, P. G. *Isoelectric Focusing: Theory, Methodology and Application* (eds Work, T. S. & Work, E.) (Elsevier Biomedical, 1983).
42. Varshosaz, J. & Falamarzian, M. Drug diffusion mechanism through pH-sensitive hydrophobic/polyelectrolyte hydrogel membranes. *European Journal of Pharmaceutics and Biopharmaceutics* **51**, 235–240. doi:10.1016/S0939-6411(01)00126-6 (2001).
43. Dursch, T. J. *et al.* Water-soluble drug partitioning and adsorption in HEMA/MAA hydrogels. *Biomaterials* **35**, 620–629. doi:10.1016/j.biomaterials.2013.09.109 (2014).
44. Hagel, V., Haraszti, T. & Boehm, H. Diffusion and interaction in PEG-DA hydrogels. *Biointerphases* **8**. doi:10.1186/1559-4106-8-36 (2013).
45. Stejskal, J. & Horská, J. Refractive index increments of polyacrylamide and comments on the light scattering from its solutions. *Die Makromolekulare Chemie* **183**, 2527–2535. ISSN: 0025-116X. doi:10.1002/macp.1982.021831022 (1982).
46. Keller, H. E. *Objective Lenses for Confocal Microscopy in Handbook of Biological Confocal Microscopy* (ed Pawley, J. B.) Third, 145–161 (Springer, 2006).
47. Schwertner, M., Booth, J. & Wilson, T. Simple optimization procedure for objective lens correction collar setting. *Journal of Microscopy* **217**, 184–187. ISSN: 0022-2720. doi:10.1111/j.1365-2818.2005.01431.x (2005).
48. Wan, D.-S., Rajadhyaksha, M. & Webb, R. H. Analysis of spherical aberration of a water immersion objective: Application to specimens with refractive indices 1.33–1.40. *Journal of Microscopy* **197**, 274–284. ISSN: 00222720. doi:10.1046/j.1365-2818.2000.00635.x (2000).
49. Kao, S., Asanov, A. N. & Oldham, P. B. A Comparison of Fluorescence Inner-Filter Effects for Different Cell Configurations. *Instrumentation Science & Technology* **26**, 375–387. ISSN: 1525-6030. doi:10.1080/10739149808001906 (1998).
50. Ogston, A. G. The spaces in a uniform random suspension of fibres. *Transactions of the Faraday Society* **54**, 1754. ISSN: 0014-7672. doi:10.1039/TF9585401754 (1958).
51. Sellen, D. B. Laser light scattering study of polyacrylamide gels. *Journal of Polymer Science Part B: Polymer Physics* **25**, 699–716. ISSN: 08876266. doi:10.1002/polb.1987.090250401 (1987).
52. Williams, J. C., Mark, L. A. & Eichholtz, S. Partition and Permeation of Dextran in Polyacrylamide Gel. *Biophysical Journal* **75**, 493–502. doi:10.1016/S0006-3495(98)77538-1 (1998).



53. Holmes, D. L. & Stellwagen, N. C. Estimation of polyacrylamide gel pore size from Ferguson plots of linear DNA fragments. II. Comparison of gels with different crosslinker concentrations, added agarose and added linear polyacrylamide. *Electrophoresis* **12**, 612–619. ISSN: 0173-0835. doi:10.1002/elps.1150120903 (1991).
54. Park, I. H., Johnson, C. S. & Gabriel, D. A. Probe diffusion in polyacrylamide gels as observed by means of holographic relaxation methods: search for a universal equation. *Macromolecules* **23**, 1548–1553. ISSN: 0024-9297. doi:10.1021/ma00207a052 (1990).
55. Baselga, J. *et al.* Effect of Crosslinker on Swelling and Thermodynamic Properties of Polyacrylamide Gels. *Polymer Journal* **21**, 467–474. doi:10.1295/polymj.21.467 (1989).
56. Sweet, R. M. *et al.* Crystal Structure of the Complex of Porcine Trypsin with Soybean Trypsin Inhibitor (Kunitz) at 2.6-Å Resolution. *Biochemistry* **13**, 4212–4228. doi:10.1021/bi00717a024 (1974).
57. Moparthi, S. B. *et al.* Conformational modulation and hydrodynamic radii of CP12 protein and its complexes probed by fluorescence correlation spectroscopy. *FEBS Journal* **281**, 3206–3217. doi:10.1111/febs.12854 (2014).
58. Peters, T. *Serum Albumin* in *The Plasma Proteins* 133–181 (Elsevier, 1975). doi:10.1016/B978-0-12-568401-9.50010-4.
59. Ratner, B. D. *et al.* *Biomaterials Science: An Introduction to Materials in Medicine* Second Ed., 815. ISBN: 0-12-582463-7 (Elsevier Academic Press, 2004).
60. Morris, C. J. O. R. & Morris, P. Molecular-Sieve Chromatography and Electrophoresis in Polyacrylamide Gels. *Biochem. J* **124**, 517–528. doi:10.1042/bj1240517 (1971).
61. Lee, S. C. *et al.* Hydrotropic Polymers: Synthesis and Characterization of Polymers Containing Picolynicotinamide Moieties. *Macromolecules* **36**, 2248–2255. doi:10.1021/ma021629k (2003).
62. Gil, E. S. & Hudson, S. M. Stimuli-responsive polymers and their bioconjugates. *Progress in Polymer Science* **29**, 1173–1222. doi:10.1016/j.progpolymsci.2004.08.003 (2004).
63. Dormán, G. *et al.* The Life of Pi Star: Exploring the Exciting and Forbidden Worlds of the Benzophenone Photophore. *Chemical Reviews* **116**, 15284–15398. doi:10.1021/acs.chemrev.6b00342 (2016).
64. Armstrong, J. *et al.* The hydrodynamic radii of macromolecules and their effect on red blood cell aggregation. *Biophysical Journal* **87**, 4259–4270. doi:10.1529/biophysj.104.047746 (2004).
65. Tentori, A. M., Yamauchi, K. A. & Herr, A. E. Detection of Isoforms Differing by a Single Charge Unit in Individual Cells. *Angewandte Chemie International Edition* **55**, 12431–12435. ISSN: 14337851. doi:10.1002/anie.201606039 (2016).

66. Lee, A. G. *et al.* Development of Macroporous Poly(ethylene glycol) Hydrogel Arrays within Microfluidic Channels. *Biomacromolecules* **11**, 3316–3324. doi:10.1021/bm100792y (2010).
67. Asnaghi, D. *et al.* Large-scale microsegregation in polyacrylamide gels (spinodal gels). *The Journal of Chemical Physics* **102**, 9736–9742. ISSN: 0021-9606. doi:10.1063/1.468792 (1995).
68. Wensch, E., de Besi, P. & Righetti, P. G. Conventional isoelectric focusing and immobilized pH gradients in ‘macroporous’ polyacrylamide gels. *Electrophoresis* **14**, 583–590. ISSN: 0173-0835. doi:10.1002/elps.1150140192 (1993).
69. Su, A., Smith, B. E. & Herr, A. E. In Situ Measurement of Thermodynamic Partitioning in Open Hydrogels. *Analytical Chemistry* **92**, 875–883. doi:10.1021/acs.analchem.9b03582 (2020).
70. Righetti, P. G., Brost, B. C. W. & Snyder, R. S. On the limiting pore size of hydrophilic gels for electrophoresis and isoelectric focussing. *Journal of Biochemical and Biophysical Methods* **4**, 347–363. doi:10.1016/0165-022X(81)90075-0 (1981).
71. Röchel, R., Steere, R. L. & Erbe, E. F. *Transmission-electron microscopic observations of freeze-etched polyacrylamide gels* tech. rep. (1978), 563–575.
72. Denisin, A. K. & Pruitt, B. L. Tuning the Range of Polyacrylamide Gel Stiffness for Mechanobiology Applications. *ACS Applied Materials & Interfaces* **8**, 21893–21902. ISSN: 1944-8244. doi:10.1021/acsami.5b09344 (2016).
73. Hou, C. & Herr, A. E. Ultrashort Separation Length Homogeneous Electrophoretic Immunoassays Using On-Chip Discontinuous Polyacrylamide Gels. *Analytical Chemistry* **82**, 3343–3351. ISSN: 0003-2700. doi:10.1021/ac100182j (2010).
74. Fuxman, A. M., Mcauley, K. B. & Schreiner, L. J. Modelling of polyacrylamide gel dosimeters with spatially non-uniform radiation dose distributions. *Chemical Engineering Science* **60**, 1277–1293. doi:10.1016/j.ces.2004.09.079 (2005).
75. Liu, L., Li, P. & Asher, S. A. Entropic trapping of macromolecules by mesoscopic periodic voids in a polymer hydrogel. *Nature* **397**, 1145–1163. doi:10.1038/19066 (1999).
76. Smith, R. M. *Applications of Solid Phase Microextraction* (ed Pawliszyn, J.) ISBN: 978-0-85404-525-9. doi:10.1039/9781847550149 (Royal Society of Chemistry, Cambridge, 1999).

## Chapter 3

# Current Understanding of Ultraviolet-C Decontamination of N95 Filtering Facepiece Respirators

Reproduced with permission from: S. M. Grist, A. Geldert, A. Gopal, A. Su, H. B. Balch, & A. E. Herr, "Current Understanding of Ultraviolet-C Decontamination of N95 Filtering Facepiece Respirators", *Applied Biosafety*, 2021.

### 3.1 Background

The COVID-19 pandemic has led to severe shortages of single-use N95 filtering facepiece respirators (FFRs) worn by health care workers and first responders, and ultraviolet-C (UV-C) irradiation has been identified by the Centers for Disease Control and Prevention (CDC) as one of the most promising methods for N95 FFR decontamination under crisis-capacity conditions [1]. UV-C is already implemented for airborne pathogen inactivation and other applications in hospitals [2]; however, UV-C decontamination of N95 FFRs involves additional considerations. Access to consolidated information on N95 FFR decontamination approaches is essential to maintaining a robust response to COVID-19. In this review, we examine the current understanding in the peer-reviewed literature regarding the use of UV-C irradiation for N95 FFR treatment.

In 2006, the US National Academies outlined that effective decontamination of personal protective equipment (PPE) like the N95 FFR requires (1) inactivation of pathogens (e.g., the SARS-CoV-2 virus), (2) maintenance of both the fit and filtration efficiency of the N95 FFR, and (3) harmlessness to the user (e.g., no toxic residues, minimal risk of cross-contamination) [3]. Here, we review and summarize the ability of UV-C decontamination to meet these critical criteria, to help inform risk management decisions under crisis-capacity conditions.

## UV-C fundamentals and mode of action

UV-C inactivates pathogens primarily by introducing crosslinks between adjacent nucleic acid residues, thus damaging DNA and RNA and hindering reproduction [4–7]. UV-C decontamination is critically dependent on two factors: the wavelength applied and the dose (fluence).

First, energy must be applied at the appropriate ultraviolet (UV) wavelength (i.e., the germicidal UV-C region of the electromagnetic spectrum, with high efficacy near 260 nm [8]). UV sources emitting at wavelengths much beyond 260 nm, such as sunlight at the earth’s surface (after UV-C has been absorbed by the earth’s ozone layer [9]), tanning bed lamps, or other consumer products, have minimal or no germicidal efficacy [7]. UV radiation at 254 nm has  $> 10\times$  higher germicidal efficacy compared with UV radiation at 300 nm or longer wavelengths [10].

Second, sufficient UV-C dose (fluence) must be delivered to the pathogens [7]. Fluence ( $\text{J}/\text{cm}^2$ ) is defined as the integrated radiant (UV-C) power incident upon an infinitesimally small surface during the exposure period [11]. The term “UV-C dose” ( $\text{J}/\text{cm}^2$ ) is widely used in the decontamination literature to denote UV-C fluence [11]. “Fluence” is the technically accurate term to describe the UV-C energy incident on the N95 surface, whereas “dose” refers to the fraction of incident energy absorbed at that surface. Nevertheless, to remain consistent with the cited literature and field, we use the term “dose” in this review when describing measured UV-C energy incident at the N95 surface.

The minimum dose required for pathogen inactivation depends on both the irradiation wavelength and the specific pathogen, with some pathogens requiring much higher UV-C doses for inactivation than others (e.g., certain bacterial spores compared to enveloped, single-stranded RNA viruses) [12]. A pathogen’s “action spectrum” describes relative inactivation efficacy as a function of wavelength, and action spectra typically have a peak near 260 nm (the maximum absorption of nucleic acids) [8]. The minimum dose required for inactivation also depends upon the material on or in which pathogens are present (e.g., air, surfaces, or aqueous media) [7].

Because biological validation of inactivation is often impractical or impossible to integrate into each and every treatment cycle, the UV-C dose measurement serves as the critical physical link between viral inactivation evidence and efficacy of each exposure. Dose ( $\text{J}/\text{cm}^2$ ) is the product of irradiance ( $\text{W}/\text{cm}^2$ ) and exposure time (s), assuming constant irradiance [11]. Because UV-C irradiance is dependent on the distance and angle from the UV-C source [13], UV-C irradiance, and therefore dose, needs to be empirically measured at the precise location of the objects to be decontaminated, in the specific configuration used for UV-C treatment. These measurements must be performed using calibrated sensors (e.g., radiometers, dosimeters, or sensor strips) with specificity to the germicidal wavelength range output by the UV-C source, and appropriate sensitivity and dynamic range (range of measurable irradiances and doses).

## Threshold for SARS-CoV-2 inactivation

The efficacy of N95 decontamination methods is typically evaluated by assessing the  $\log_{10}$  reduction in active pathogens on N95 FFRs after decontamination treatment. For example, a  $3\text{-log}_{10}$  reduction (subsequently referred to as “3-log reduction”) corresponds to 99.9% inactivation of the pathogen under consideration compared to a positive control. As per US Food and Drug Administration (FDA) guidelines for N95 FFR decontamination Emergency Use Authorizations (EUAs),  $\geq 3\text{-log}$  reduction in nonenveloped viral activity is required to achieve the minimally acceptable “Tier 3” level of bioburden reduction [14]. Therefore, in this review, we emphasize  $\geq 3\text{-log}$  reduction of SARS-CoV-2 or its analogues, based on the minimally acceptable log reduction listed in the FDA EUA guidance and in accordance with previous studies of UV-C N95 FFR decontamination [15, 16]. However, it is important to note that the UV-C dose required to  $\geq 3\text{-log}$  reduction is pathogen-dependent [7]. Thus, the UV-C dose required to achieve  $\geq 3\text{-log}$  reduction of SARS-CoV-2 (an enveloped virus) may not necessarily yield  $\geq 3\text{-log}$  reduction of nonenveloped virus, bacteria, or other pathogens required for various levels of FDA EUA approval.

## Safety considerations

UV-C is hazardous to human health, and as a result, sufficient skin and eye protection must be worn to protect processing personnel. According to the American Conference of Governmental Industrial Hygienists (ACGIH), the exposure dose limit per person per day is  $0.003\text{ J/cm}^2$  for UV radiation in the 200–315 nm region of the electromagnetic spectrum [17]; this same  $0.003\text{ J/cm}^2$  dose limit was identified by Directive 2006/25/EC of the European Parliament and of the Council for all UV radiation (180–400 nm) [18]. Similarly, the National Institute for Occupational Safety and Health (NIOSH) recommends a total permissible 8-h dose of  $\sim 0.0046\text{ J/cm}^2$  for 260 nm irradiation, for unprotected eyes or skin [19]. Given the high UV-C irradiances emitted by sources typically used for UV-C decontamination, an unprotected user risks exposure to this dose in seconds under accidental illumination [20, 21]. Thus, proper engineering controls for UV-C systems must ensure that all users are adequately protected before the UV-C source is turned on, and full PPE must be worn for eye and skin protection. Furthermore, in addition to UV-C concerns, processing personnel should treat all respirators (including ones that have undergone UV-C treatment) as contaminated, and wear appropriate PPE to reduce pathogen exposure risk from respirator handling [22].

## Literature Review Process

In writing this review, we aimed to summarize the current evidence regarding UV-C treatment of N95 FFRs with respect to the critical criteria outlined by the US National Academies: (1) inactivation of pathogens (e.g., the SARS-CoV-2 virus), (2) maintenance of both the fit and filtration efficiency of the N95 FFR, and (3) harmlessness to the user (e.g., no toxic residues) [3]. We searched PubMed, Google Scholar, Google, and library databases for key-

words such as “UV-C,” “N95,” “filtering facepiece respirator,” “decontamination,” “UVGI,” and “mask” to identify relevant primary research articles.

Studies that are not yet peer-reviewed should be interpreted with particular caution, so we elected not to include academic or commercial studies posted to preprint servers in this review. We do, however, cite relevant hospital implementations and other work (e.g., federal guidance and summaries from professional societies) that do not normally go through peer review before public availability.

## 3.2 Literature Review

### Potential for SARS-CoV-2 inactivation

Several studies have demonstrated UV-C viral reduction of influenza and non-SARS-CoV-2 coronaviruses on N95 FFRs [15, 16, 23]. These viruses are hypothesized to be suitable SARS-CoV-2 analogues because they are also enveloped, single-stranded RNA viruses. A non-peer-reviewed report to the FDA by the contracting research laboratory Applied Research Associates (ARA) [16] found that UV-C treatment of 1.0 J/cm<sup>2</sup> at the surface of N95 FFR coupons from one FFR model yielded no detectable virus ( $\geq 3.95$ -log reduction) for six influenza and coronavirus strains considered, including MERS-CoV and SARS-CoV [24]. Even when viral inoculations were covered with artificial skin oil or saliva as soiling agents, N95 coupons yielded no detectable virus after UV-C treatment. Similar UV-C doses were effective for H5N1 and H1N1 in separate, peer-reviewed studies (Table 3.1) [23, 25]. At a UV-C dose of 0.5 J/cm<sup>2</sup>, the viable virus remaining on N95 FFR coupons was 2–3 log lower than on positive control coupons, but detectable, indicating that a UV-C dose of 0.5 J/cm<sup>2</sup> may be insufficient for viral inactivation [16].

Table 3.1: Efficacy of UV-C for inactivation of microorganisms

<i>Refs.</i>	<i>Organism, soiling agent, &amp; method of application</i>	<i>Material</i>	<i>UV-C dose</i>	<i>Efficacy</i>	<i>UV-C source</i>
<b>Influenza and coronavirus strains: ssRNA enveloped virus</b>					
Ozog et al. [26]	SARS-CoV-2; 10 $\mu$ L drop pipetted on strap and multiple locations on N95 facepiece	5 N95 FFR models (3M 1860, 8210, 8511, 9211; Moldex 1511)	$\sim 1.5$ J/cm <sup>2</sup>	$\geq 3$ -log reduction for 1/5 FFR model facepieces and 2/5 FFR model straps	254-nm UV-C (Custom-manufactured by Daavlin; Byron, OH)

Fischer et al. [27]	SARS-CoV-2; 50 $\mu$ L deposited by pipette	N95 FFR (AOSafety N9504C)	$\sim 1.98 \text{ J/cm}^2$ ( <i>estimated from manufacturer-specified irradiance</i> )	$\sim 3$ -log reduction	LED high-power UV germicidal lamp (260-285 nm; LEDi2)
Smith et al. [28]	Pooled SARS-CoV-2 clinical samples; 100 $\mu$ L deposited by pipette	N95 FFR (medical grade: 3M 1860, 1870+; industrial grade: 3M 8511)	$0.63 \text{ J/cm}^2$	Substantial reduction in infectivity (via SARS-CoV-2 RNA measurement) for only the 3M 1870+ FFR model	254-nm UV-C (General Electric 30W Germicidal T8 bulb)
Lore et al. [23]	H5N1 droplets	N95 FFR (3M 1860, 3M 1870)	$1.8 \text{ J/cm}^2$	$>4$ -log reduction	254-nm UV-C (Ultraviolet Products, Upland CA, USA)
Mills et al. [15]	H1N1. 1 $\mu$ L drops of suspension deposited by pipette. AS or ASO was placed on top of dried virus solution to study the effects of soiling.	N95 FFR (15 models)	$1.0 \text{ J/cm}^2$	$\geq 3$ -log reduction for 12/15 FFR model facepieces and 7/15 FFR model straps for all soiling conditions	254-nm UV-C (Fresh-Aire UV; Jupiter FL).
Heimbuch & Harnish - Option Task B [16]	Influenza strains (H1N1, H5N1, H7N9), MERS-CoV, SARS-CoV, all pipetted as 1 $\mu$ L drops. AS or ASO was placed on top of dried virus solution to study the effects of soiling.	N95 FFR (3M 1870)	$1.0 \text{ J/cm}^2$	No detectable virus ( $\geq 3.95$ -log reduction) for all organisms for all soiling conditions	254-nm UV-C (Mineralight <sup>®</sup> XX-20S 20-W UV bench lamp)
Heimbuch & Harnish - Base Task 4 [16]	H1N1, pipetted as 1 $\mu$ L drops and dried. AS or ASO was placed on top of dried virus solution to study the effects of soiling.	N95 FFR (15 models)	$1.0 \text{ J/cm}^2$	$\geq 3$ -log reduction for 11/15 FFR models and 4/15 FFR straps for all soiling conditions	254-nm UV-C (Fresh-Aire UV)

Walker & Ko [24]	Murine hepatitis virus (coronavirus)	Air <sup>a</sup>	$1.83 \times 10^{-3}$ J/cm <sup>2</sup>	3-log reduction <sup>a</sup>	254-nm UV-C (Lumalier, Memphis, TN)
<b>MS2: ssRNA nonenveloped virus</b>					
Vo et al. [29]	MS2 droplets	N95 FFR (Willson N1105)	4.32 J/cm <sup>2</sup>	3-log reduction	254-nm UV-C (5.5 mg Hg; lamp type TUV 36TS 4P SE; lamp voltage 94 V; lamp wattage, 40 W.)
Fisher & Shaffer [30]	MS2 aerosol	N95 FFR (6 models)	0.32-40 J/cm <sup>2</sup> (equates to 0.1 J/cm <sup>2</sup> at the internal filtering medium due to model-dependent attenuation)	≥2.9-log reduction	254-nm UV-C (TUV 36T5 40 W, Philips, Somerset NJ)
Woo et al. [31]	MS2 droplets (9-10 μm) and aerosol (1-2 μm), in water, BE, or AS	N95 FFR (3M 1870)	3.6 J/cm <sup>2</sup>	Droplets: 4.8-, 2.7-, 2.5-log reduction in water, BE, AS Aerosols: 5.2-, 3.0-, 2.7-log reduction in water, BE, AS	254-nm UV-C (UVG-11, UV Products, Cambridge, UK)
Tseng & Li [32]	MS2	Surfaces	~0.006-0.010 J/cm <sup>2</sup>	>3-log reduction	254-nm UV-C (TUV 8W/G8 T5, Philips Electronic Instruments, Eindhoven, The Netherlands)
<b>Vegetative bacteria &amp; bacterial spores</b>					
Lin et al. [33]	<i>Bacillus subtilis</i> spores, aerosolized	N95 FFR (3M 8210)	2.27 J/cm <sup>2</sup> , 5.7 J/cm <sup>2</sup>	2.27 J/cm <sup>2</sup> → ~2.7-log reduction 5.7 J/cm <sup>2</sup> → No detectable spores	254-nm UV-C (UVGL-58, VUP LLC, Upland, CA)



Bentley et al. [34]	<i>E. coli</i> , <i>P. aeruginosa</i> , <i>S. aureus</i> (drug-sensitive and drug-resistant), <i>S. pseudointermedius</i> (drug-sensitive and drug-resistant). 1-2 mL suspension deposited by pipette.	Microfiber, polyester, and cotton fabric swatches	0.27 J/cm <sup>2</sup>	>2.5-log reduction for all bacteria on all fabrics. No detectable bacteria in 20/24 conditions.	254-nm UV-C (American Ultraviolet Inc., Lebanon, IN)
Wallace et al. [35]	<i>C. difficile</i> spores (with and without tri-part soiling agent) MRSA and MS2 (with and without 5% FBS)	Glass and plastic	0.17-0.63 J/cm <sup>2</sup>	<i>C. difficile</i> : ~2.1-log reduction with soiling agent across all UV-C doses; ~3.2-log reduction without soiling agent across upper 3 doses. MRSA: ~2.9-log reduction with FBS, ~3.4-log reduction without FBS MS2: ~3.7-log reduction with FBS, ~2.9-log reduction without FBS	254-nm UV-C (Lightbest Co., Ltd, Changzhou, China)
<b>Vegetative fungi</b>					
Fu et al. [36]	5 <i>Candida</i> strains	Bed sheets	0.075 J/cm <sup>2</sup>	>3-log reduction in all strains	254-nm UV-C (Thermo Fisher Scientific, Waltham, MA)

<sup>a</sup>Estimate-based measured viral susceptibility to UV-C in air.

AS, artificial saliva; ASO, artificial skin oil; BE, beef extract; FBS, fetal bovine serum; FFR, filtering facepiece respirators; MRSA, methicillin-resistant *Staphylococcus aureus*; UV-C, ultraviolet-C.

Heimbuch and Harnish also studied the efficacy of UV-C viral inactivation across 15 different models (intact FFRs rather than coupons) [16]. In 11 out of the 15 models tested, a UV-C dose of 1.0 J/cm<sup>2</sup> at the N95 surface was effective in inactivating H1N1 influenza by  $\geq 3$ -log. The same study found that UV-C treatment was effective for the elastic straps of only 4 of 15 models; thus, straps may require a secondary decontamination method. N95 FFR models with a hydrophilic facepiece were less effectively decontaminated with UV-C than hydrophobic models [16]. Similarly, related studies measured  $\geq 3$ -log reduction in H1N1

viability on the facepieces of 12 of 15 tested models and on the elastic straps of 7 of 15 tested models [15].

In addition to the N95 FFR model, other factors may influence UV-C inactivation efficacy. High humidity decreases UV-C efficacy on generic surfaces [32] and on the surfaces of N95 FFRs [31] suggesting that a drying step before N95 FFR treatment could be beneficial. Soiling agents (including from saliva and mucus) have been found to reduce UV-C inactivation efficacy of MS2 bacteriophage from N95 FFRs [31]. The effect of soiling agents on UV-C treatment efficacy likely depends on the exact concentration and composition of the soiling agent, and/or how the soiling agent is applied (e.g., mixed in with pathogens or applied on top of pathogen inoculation). In addition to fluids such as saliva and mucus [31], sunscreen or other types of cosmetics may further attenuate UV-C irradiation during treatment [37]. Attenuation is dependent on the thickness and absorption coefficients of the applied materials [38].

Pathogen inoculation mode may also impact UV-C treatment efficacy: N95 FFRs inoculated with larger MS2 droplets (9–10  $\mu\text{m}$ ) generally had lower UV-C bioburden reduction efficiencies in response to a 3.6  $\text{J}/\text{cm}^2$  dose compared with FFRs inoculated with smaller MS2 aerosols (1–2  $\mu\text{m}$ ) [31]. Given that studies use a variety of methods to apply pathogens on an N95 FFR (aerosols, droplets, and/or pipetted solution), the question of whether the pathogen application method impacts UV-C treatment efficacy merits further study. It is also important to note that the impact of soiling agents and pathogen application method may differ depending on pathogen type, just as the minimally acceptable UV-C dose depends on pathogen type (as described in the “Efficacy of UV-C on inactivation of other pathogens” section). For example, MS2 is commonly used as a surrogate virus in inactivation studies due to its high culturability [39], but as a nonenveloped virus, MS2 generally requires higher UV-C doses for inactivation compared with enveloped viruses like SARS-CoV-2 (Table 3.1).

Together, the studies reported in the ssRNA enveloped virus section of Table 3.1 suggest a minimally acceptable UV-C dose of  $\sim 1.0 \text{ J}/\text{cm}^2$  for 3-log inactivation of viruses similar to SARS-CoV-2 on N95 material. Research on UV-C inactivation of SARS-CoV-2 is ongoing. Smith et al. observed that 0.63  $\text{J}/\text{cm}^2$  of 254 nm UV-C led to a substantial reduction of SARS-CoV-2 RNA infectivity in cell culture for only one out of three N95 models tested [28]. It should be noted that this RNA-based assessment of viral infectivity differs from the plaque or 50% tissue culture infectious dose ( $\text{TCID}_{50}$ ) assays more commonly used for viral inactivity measurements. It remains unclear whether UV-C would more fully decontaminate SARS-CoV-2 from multiple N95 models if a dose above the minimally acceptable 1.0  $\text{J}/\text{cm}^2$  were applied, or if respirators were inoculated with a lower SARS-CoV-2 titer that more closely represents a realistic exposure expected for a health care worker.

Ozog et al. also characterized SARS-CoV-2 inactivation at multiple locations on intact N95 FFR facepieces and straps exposed to 254-nm UV-C [26]. The authors report that  $\sim 1.5 \text{ J}/\text{cm}^2$  of 254-nm UV-C applied to both sides of the N95 yielded  $\geq 3$ -log inactivation of SARS-CoV-2 in all studied locations on the facepieces of 1 out of 5 N95 models and on the straps of 2 out of 5 N95 models. However, measurement of  $\geq 3$ -log inactivation was not possible on many models in this study, because the difference between the limit of detection

of the TCID<sub>50</sub> assay used to assess viral activity and the viral activity on the unexposed control N95 was often <3 log. In addition, Kohli et al. demonstrate (with a similar UV-C system) that the UV-C dose varies across the surface of the N95 FFR [40]; thus, as with many studies on decontamination of intact N95 respirators, the actual dose at each location studied may differ substantially from the 1.5 J/cm<sup>2</sup> nominal dose.

Other recent studies have investigated the impact of LED and pulsed UV sources on SARS-CoV-2 inactivation on N95s. One recent article reports SARS-CoV-2 inactivation in one N95 FFR model after UV-C treatment using an LED source [27]. However, caution should be exercised in interpretation or adoption of the reported approach, as the reported UV-C dose was calculated based on a single manufacturer-specified irradiance value, when irradiance may actually change over source lifetime due to slight changes in configuration and decay in LED output. As a result, even though the results suggest that UV-C LED sources could be promising, the study is difficult—perhaps even impossible—to accurately reproduce.

Similarly, another recent article reporting SARS-CoV-2 inactivation after UV treatment with a pulsed xenon source also shows significant viral inactivation (>4.79-log); however, the dose associated with this level of inactivation is not reported [41]. These data underscore the importance of accurate measurement and reporting of wavelength and UV-C dose for reproducible viral inactivation protocols. The National Institutes of Standards and Technology and the International Ultraviolet Association are actively collaborating to develop standards to assess the efficacy of UV devices for decontamination [42]. An American Society for Testing and Materials (ASTM) standard for evaluating UV-C efficacy for inactivating the influenza virus on textile surfaces such as N95 FFRs has been developed [43]. In addition to describing appropriate experimental steps, the standard stresses the importance of accurate, rigorous UV-C dose measurements.

### 3.3 Efficacy of UV-C on inactivation of other pathogens

#### UV-C susceptibility of different pathogens in air, water, and on surfaces

The UV-C dose required to inactivate pathogens in air, water, and on surfaces is organism-dependent, due to organism-to-organism differences in nucleic acid structure and nucleotide content, as well as varying amounts of UV-absorbing proteins and other photoprotective components [12]. Higher UV-C doses are generally required to inactivate bacterial and fungal spores, compared to viruses and vegetative bacteria [7]. Among viruses, ~3× higher UV-C doses are required to inactivate viruses with double-stranded RNA or DNA on surfaces, compared to single-stranded viruses; higher dose requirements in double-stranded viruses are attributable to more robust repair mechanisms, as the second strand can serve as a template

for repair [32].

While enveloped viruses are generally more susceptible to inactivation by mechanical and chemical agents [44], it is unclear whether the UV-C susceptibility of enveloped and nonenveloped viruses differs. Blázquez et al. found that in water, enveloped viruses were inactivated with lower UV-C doses than nonenveloped viruses [45]. However, the mechanism for the observed difference between enveloped and nonenveloped virus susceptibility in water is not understood, nor is it clear whether the same pattern holds for viruses in air or on substrates.

### UV-C susceptibility of different pathogens on N95 FFRs and textiles

The minimum UV-C dose required to inactivate both enveloped and nonenveloped viruses on N95 FFRs is several hundred-fold higher than doses typically used for decontamination of similar pathogens on nonporous surfaces [12], in air, and in solution (Table 3.1), because UV-C is attenuated upon passing through the N95 FFR layers. UV-C irradiances that reach the internal N95 filtering media are  $\sim 3\text{--}400\times$  lower than the irradiance at the FFR surface, depending on the FFR model [30]. In addition, due to this limited and model-dependent UV-C transmission through N95 FFRs [46], both sides of the FFR should be illuminated with the minimally acceptable UV-C dose, and this dose may not effectively decontaminate all layers of varying FFR models.

Different pathogens are also expected to have different UV-C susceptibility on N95 FFRs, although the study of UV-C inactivation of different pathogens on N95 FFRs is limited. MS2, a nonenveloped virus, has generally been reported to require higher UV-C doses to achieve 3-log reduction from N95 FFRs [29, 30] compared with enveloped influenza and coronaviruses [15, 16]; however, it is unclear whether other differences in study design (e.g., FFR model and method of virus application to the FFR) also contribute to the difference in required UV-C dose.

While UV-C has been demonstrated to inactivate several species of vegetative bacteria and bacterial spores on N95 FFRs and other textiles [33, 34, 36, 47–49], 3-log reduction was not always demonstrated and it is unclear how many bacterial pathogens would be inactivated by the  $1.0\text{ J/cm}^2$  UV-C dose required for SARS-CoV-2 analogue inactivation on most N95 FFR models. For example, UV-C inactivation of *Clostridium difficile* on N95 FFRs has not been studied. However, much higher UV-C doses are required to inactivate *C. difficile* spores on non-porous surfaces ( $\sim 0.17\text{--}0.63\text{ J/cm}^2$ ) [35] compared with MS2 on surfaces ( $\sim 0.006\text{--}0.010\text{ J/cm}^2$ ) [32]. It has yet to be studied whether the same trend (higher UV-C doses required to inactivate *C. difficile* spores compared with MS2 on non-porous surfaces) would hold true in the case where these organisms are on N95 FFRs. In addition, *Enterococcus faecium* in polycotton swatches was inactivated to a lower degree ( $<1.97\text{-log}$  reduction) by UV-C [48] compared with laundering (3-4-log reduction) [50], although the applied UV-C dose was not specified [33], making it challenging to compare and reproduce

results. While UV-C treatment is expected to significantly reduce the risk of contamination, not every pathogen present on or within an FFR may be decontaminated by UV-C; and thus, health care personnel should continue to handle the respirator as if contaminated and reuse only their own FFR. Any UV-C treatment approach should be accompanied by an industrial hygiene workflow involving user training and sterile processing to minimize risk of cross-contamination [22].

### 3.4 Sunlight is not likely to be an effective decontamination approach for N95 FFRs

The CDC does not list sunlight as an appropriate method of N95 FFR decontamination [1]. UV-C radiation from sunlight is absorbed by the top layer of the atmosphere and negligible UV-C radiation reaches the surface of the earth [51]. The UV component of sunlight at the earth's surface consists of UV-A (320–400 nm) and UV-B (280–320 nm) radiation. UV-A radiation is considered nongermicidal, while UV-B radiation has germicidal effects, which are much weaker than that of UV-C [7]. Theoretical calculations for the necessary sunlight exposure time needed to achieve UV-B germicidal effects in US cities (equivalent to a 1.0 J/cm<sup>2</sup> UV-C dose) suggest timescales of 57–5,000 days, depending on season and geographic location [10]. Furthermore, studies with simulated sunlight showed minimal to no effect in inactivating MS2 and human adenovirus on the surface of fresh produce [52].

UV-B radiation has some germicidal effects; studies of UV-B irradiation on MS2 bacteriophage and murine noroviruses in aqueous suspension demonstrated a 4-log reduction with UV-B doses of 0.909 and 0.367 J/cm<sup>2</sup>, respectively [53]. To reach these doses, 0.34–4.2 h of sunlight exposure would be required, assuming UV-B irradiance from sunlight of ~60–300  $\mu\text{W}/\text{cm}^2$  (although UV irradiance from sunlight varies significantly depending on geographic location, season, and time of day) [54]. For comparison, 4-log reduction of MS2 in phosphate-buffered saline solution [55] required ~0.07 J/cm<sup>2</sup> of UV-C—over an order of magnitude lower. UV-C dose required for viral inactivation in N95 FFRs is several hundred-fold higher than for viral inactivation in water, air, or on hard nonporous surfaces (Table 3.1) [7].

Sunlight reaching the earth's surface does not contain UV-C, but we would expect a similar trend for the longer wavelengths, with orders of magnitude higher UV-B doses being required for viral inactivation on N95s compared with water/air/nonporous surfaces. Thus, many days of sunlight exposure would be required to achieve a sufficient virucidal UV dose on N95 FFRs, in agreement with theoretical estimates [10, 56]. Currently, there is no evidence in the peer-reviewed literature of viral inactivation of SARS-CoV-2 on N95 FFRs by sunlight. Thus, extensive experimental verification and biological validation must be performed before considering sunlight as a decontamination method for N95 FFRs.

### 3.5 Integrity of N95 FFRs after UV-C treatment

Controlled laboratory studies have subjected 15 N95 FFR models to 10–20 donning/doffing cycles and UV-C treatment (1.0–1.2 J/cm<sup>2</sup> per cycle), then assessed: strap elasticity (with Imada force tester), particle penetration and breathing resistance (TSI 8130 automated filter tester to evaluate respirator function according to the CDC [57]), and fit factor (Static Advanced Headform StAH connected to TSI PortaCount 8038 automated breathing machine, subjected to a 240-s respiration test, testing for a fit factor >100) [16]. Although donning and doffing yielded a statistically significant difference in fit factor for some models, minimal detrimental effects due to UV-C exposure specifically were observed for respirator fit, air flow resistance, or particle penetration from this dose (10 cycles, 1.0–1.2 J/cm<sup>2</sup> per cycle) of UV-C [16].

Similarly, another study found that doses of 1–10 J/cm<sup>2</sup> of UV-C (either at 254 or 265 nm) did not significantly affect filtration efficiency, material properties, pressure drop, or tensile strength of two N95 FFR models [58]. Other evaluations corroborated acceptable FFR performance after low-dose ultraviolet germicidal irradiation (UVGI) treatment [59], although Ozog et al. did report (in a Letter to the Editor) that certain N95 FFR models failed qualitative fit testing either after one to two cycles (1.5 J/cm<sup>2</sup> per side, per cycle) or before any UV-C exposure at all, highlighting the importance of verifying N95 FFR fit regularly [60]. To approximate multiple decontamination cycles, application of 18.4 J/cm<sup>2</sup> (to the exterior convex surface) and 4.6 J/cm<sup>2</sup> (to the interior concave surface) 254 nm UV-C to three N95 respirator models was performed, and was found to significantly decrease the fit factor, but fit factors remained above the acceptable threshold of 100 [28].

At 100–1000× higher UV-C doses (120–950 J/cm<sup>2</sup>), a substantial effect (>90% in some cases, but highly variable across N95 FFR models) on respirator material breaking strength was observed [61]. As variation in response to UV-C is to be expected from different N95 FFR models, the respirator must pass the “user seal check” as recommended by the CDC after decontamination to ensure that respirator fit integrity is maintained [62].

As summarized in Table 3.2, the minimum 1.0 J/cm<sup>2</sup> UV-C dose necessary for SARS-CoV-2 analogue inactivation on most N95 FFR models has been found to minimally impact N95 fit and filtration performance over 10–20 treatment cycles. Aside from the effect of UV-C itself, it is possible that repeated donning and doffing may cause FFR fit to reach unacceptable levels within a lower number of cycles. One study found N95 FFR fit to decline with each donning and doffing without additional decontamination processes; for some N95 models, fit was found to fall below the US Occupational Health and Safety Administration (OSHA) standards after 5 donning/doffing cycles, while others maintained fit for >15 donning/doffing cycles [63].

Table 3.2: Impact of UV-C on N95 filtering facepiece respirator integrity

Refs.	FFR model	UV-C dose (J/cm <sup>2</sup> )	Particle penetration	Breathing resistance (mmH <sub>2</sub> O) (max = 25)	Respirator material damage	Strap damage	Source
Heimbuch & Harnish [16]	N95 FFRs (15 models)	1.0-1.2	0.18-3.29% (10 cycles) 0.12- 2.74% (20 cycles)	4.53-14.93	No observable effect from UV-C. Some fit degradation from donning/doffing.	No significant difference from UV-C alone. Some fit degradation from donning and doffing.	254-nm UV-C (Fresh-Aire UV)
Lindsley et al. [61]	3M 1860 3M 9210 GE 1730 KC 46727	120-950 120-950 120-950 120-950	1-2.5% 1-2.5% 3-5% 3-5%	10-13 10-13 10 15-20	General decrease of strength 120 J/cm <sup>2</sup> dose = 2 layers significantly impacted 950 J/cm <sup>2</sup> = 10 layers significantly impacted	Statistically significant decrease in breaking strength for dose ≥590 J/cm <sup>2</sup> (≥10% decrease of mean strength)	254-nm UV-C
Zhao et al. [58]	3M 1860, Moldex 1500	1.0-10	3% (no effect of UV-C)	No significant change after irradiation	No change in contact angle, no new peaks or decrease in peak height in FTIR spectra, no apparent change in material structure by electron or optical microscopy	No significant change after irradiation	254-nm and 265-nm UV-C
Smith et al. [28]	3M 1860, 1870+, and 8511	18.4 at exterior surface, 4.6 at interior surface	Significantly reduced “FIT score”, but average “FIT score” remains acceptable at ≥100 (2-log particle reduction threshold).	Not studied	Not studied	Not studied	254-nm UV-C (General Electric 30W Germicidal T8 bulb)

Ozog et al. [26]	3M 1860, 9210, 8210; Cardinal Health N95 R/S; Moldex 1512	1.5 to each side of FFR	Passed saccharin solution aerosol qualitative fit test [63] for 20/25 cycles (3M 1860), 2/2 cycles (3M 9210), 1/2 cycles (3M 8210 and Cardinal Health N95 R/S), 2/3 cycles (Moldex 1512)	Not studied	Not studied	Not studied	254-nm UV-C (Daavlin Desktop UVC Germicidal Lamp)
------------------	---	-------------------------	--	-------------	-------------	-------------	---

FTIR, Fourier Transform Infrared.



## 3.6 US federal guidelines: CDC, FDA, OSHA

Due to a limited supply of N95 FFRs in the unprecedented COVID-19 pandemic, the CDC has provided guidance that health care workers can practice extended use or limited reuse of N95 FFRs [64]. In addition, the CDC has provided guidance to hospitals on methods for decontaminating N95 FFRs during a crisis [1]. Consistent with all N95 FFR treatments for reuse, UV-C is viewed as risk mitigation for extraordinary circumstances rather than complete decontamination [64].

At present, OSHA states that cosmetics or other barriers should not be present during regular respirator use [37]. EUAs that the FDA has granted for other methods of N95 FFR decontamination during the COVID-19 pandemic also stipulate that cosmetics not be present on respirators sent for decontamination [65]. After decontamination, the CDC recommends that a “user seal check” is performed when the respirator is donned to ensure an adequate seal [1]. A user seal check after every decontamination cycle is especially important because there is evidence that the fit factor of N95 respirators decreases with numerous donning/doffing cycles [63].

## 3.7 Other applications of UV-C for pathogen reduction

UV-C decontamination is also in broader use: as per the recommendations of the CDC and the Healthcare Infection Control Practices Advisory Committee (HICPAC), UV-C (254 nm peak) is widely used in US healthcare facilities for pathogen reduction in air [2], and UV-C has found extensive use in water treatment [8]. In some settings, UV-C is also used for surface decontamination [66]. NIOSH offers guidelines for applying upper-room UVGI to kill or inactivate airborne tuberculosis bacteria in hospitals [67].

Any new method for UV-C treatment should be verified through an institution’s internal review processes before implementation, which may include applying for an FDA EUA [14] and referencing frequently updated CDC guidelines.

## 3.8 Implementation strategies

The University of Nebraska Medical Center (UNMC) published one of the first protocols [20] demonstrating implementation of UV-C treatment of N95s (including N95 FFR handling logistics and treatment), which has been the basis of additional research and discussion for UV-C treatment of N95 FFRs during the 2020 COVID-19 pandemic [21, 22]. The UNMC protocol exposes each side of N95 FFRs to 0.9–1.2 J/cm<sup>2</sup>, depending on FFR position within the treatment field [20]. This UNMC Process Flow is a 51-step process defined by role (health care worker, courier, UVGI associate) and covers the safe handling (intake, transport, processing, return), labeling (UV-C-decontaminated N95 FFRs should be returned to their

specific original user as the process is not expected to be sterilizing) [22], and ancillary PPE and hygiene required for the protocol. As with any decontamination strategy, an appropriate industrial hygiene workflow involving user training [68], sterile processing, and other critical considerations must be implemented to avoid cross-contamination or damage to the N95. The Association for Professionals in Infection Control and Epidemiology (APIC) has recently disseminated guidance for infection prevention workflows for UV-C treatment of N95 FFRs during the COVID-19 crisis, in collaboration with N95DECON [22]. Additional implementation strategies are summarized in Table 3.3.

Table 3.3: Published implementation strategies for UV-C N95 respirator treatment

Authoring group	Implementation type	UV-C source type
University of Nebraska Medical Center [20]	Hospital protocol for room-scale N95 UV-C treatment with full processing workflow (with personnel roles)	254 nm UV-C (ClorDiSys Torch)
University of Chicago Medical Center [21]	Hospital protocol for room-scale N95 UV-C treatment with full processing workflow	254 nm UV-C (Surfacide Helios)
APIC [22]	Implementation guidance for infection prevention workflows for N95 UV-C treatment	N/A
Ontiveros et al. [69]	Peer-reviewed study on characterization of a room-scale hospital UV-C treatment system for N95 processing	254 nm UV-C (Diversey Moon-Beam3)
Purschke et al. [70]	Peer-reviewed study on design and characterization of cabinet-based N95 UV-C treatment system targeted at lower-resource settings	254 nm UV-C
Wilde et al. [71]	Peer-reviewed ray-trace modeling workflow for UV-C N95 treatment chamber design	254 nm UV-C
Bentancor & Vidal [72]	Peer-reviewed design of a room-scale UV-C treatment system (not designed for N95 UV-C treatment specifically)	254 nm UV-C

All but two surveyed studies demonstrating viral inactivation on N95 FFRs used low-pressure mercury UV-C sources with peak emission at 254 nm. Because both pathogen inactivation and transmittance (through materials such as N95 layers) are wavelength-dependent [7], sources with different emission spectra (e.g., LED sources, medium-pressure mercury sources, or pulsed xenon sources) could also be effective for viral inactivation but will have different minimum doses for viral inactivation. Implementation of these sources must specifically assess the minimally acceptable dose through viral inactivation studies with accurate dose measurements. Both research and validation dose measurements for any source must use appropriate, wavelength-matched detectors.

Validation of (1) UV-C viral inactivation and (2) subsequent N95 FFR reuse suitability

(e.g., filtration efficiency, fit factor) is widely considered in the peer-reviewed literature and should be considered for all new processes [15, 16, 23, 63]. Both of these critical features are dependent on UV-C dose, as summarized in Tables 3.1 and 3.2. From studies using SARS-CoV-2 viral analogues, UV-C treatment design must exceed a value of  $1.0 \text{ J/cm}^2$  for all surfaces of each N95 FFR and the delivered dose should ideally be verified with every UV-C cycle, but periodically at a minimum (e.g., daily, after a set number of cycles).

Dose measurements should be performed with an accurately calibrated (e.g., traceable to standards such as those from the National Institute of Standards and Technology) UV-C-specific sensor to measure the irradiance or dose at each FFR position. Variation in irradiance is anticipated across the exposure area; the total exposure time should be chosen such that all N95 FFR surfaces are exposed to at least the minimally acceptable dose of  $1.0 \text{ J/cm}^2$ .

As is true with any form of light, shadowing reduces the dose of UV-C that a target receives. Thus, shadows on the target N95 FFR(s) should be avoided by the following: (1) providing UV-C illumination to both sides of the FFR, and/or flipping the N95 FFRs midtreatment to ensure all surfaces are exposed to the minimally acceptable UV-C dose, (2) lining walls, ceiling, and other surfaces with UVC-reflective materials to increase delivered UV-C dose [73], and (3) ensuring there are no obstructions or materials between the N95 FFRs and the UV-C source that could block the line-of-sight or attenuate the UV-C before reaching the N95. It is important to note that standard soda-lime and borosilicate glass block almost all UV-C [74].

In addition to shadowing, it is important to note that irradiance depends on the distance from the source as well as the angle of incidence of UV-C on the N95 surface by Lambert's Cosine Law [13]; as such, the complex 3D morphology of the N95 surface impacts the dose delivered to various regions of the respirator and needs to be considered when designing UV-C treatments.

It is imperative to use caution and validate each source, as not all UV sources provide the required UV-C wavelength range, irradiance, or irradiance uniformity. Even more critically, there have been reports of UV sources falsely claiming to be germicidal, with emitted wavelength ranges not consistent with germicidal efficacy [75]. In addition, UV-C sources emitting wavelengths below 210 nm can produce ozone [7], which is hazardous to human health.

As a result, it is critical to measure the wavelength and irradiance of UV-C sources with sensors specific to UV-C to ensure sources emit radiation within the UV-C germicidal range (200–280 nm with peak efficacy at  $\sim 260 \text{ nm}$ ). Viral inactivation efficacy has been reported to be  $\sim 10\times$  lower at 300 nm (beyond UV-C range) compared with 254 nm [8, 56], highlighting the importance of using appropriate sources emitting in the UV-C range. The measured UV-C-specific irradiance values should then be used to calculate the time required to reach a minimum UV-C dose in excess of  $1.0 \text{ J/cm}^2$  across all N95 FFR surfaces.

### 3.9 Summary and Outstanding Questions

Important points and open questions regarding UV-C treatment of N95 FFRs are summarized here:

1. N95 decontamination processes are only to be considered during crisis-capacity surges, after exhausting contingency-capacity and other crisis-capacity strategies [1].
2. Direct exposure to UV-C is harmful to humans. Proper engineering controls must be established before using UV-C systems to ensure that all users are protected from the UV-C source before the source is turned on [17, 19].
3. UV-C only inactivates viruses subjected to at least the minimally acceptable UV-C dose. There remain open questions about UV-C penetration into the materials of the various N95 FFR models used in health care, as the amount of penetration varies widely across N95 FFR models [30, 70]. Although the ARA report [16] and related peer-reviewed literature [15] demonstrate  $>3$ -log viral reduction (measured from fluid extraction from the N95 FFR materials as described in the ASTM standard for viral inactivation testing [43]), live virus could persist inside the N95 FFR after UV-C treatment. As such, UV-C and other deactivation approaches should be viewed as risk mitigation for extraordinary circumstances rather than complete decontamination. In addition, shadowed or highly angled regions of the N95 may be exposed to lower- than-expected UV-C doses, and thus, pathogens in these locations may be less effectively inactivated.
4. UV wavelengths of 175–210 nm can generate ozone, which is hazardous to human health. Some low pressure UV lamps and most medium-pressure UV lamps emit some 185 nm UV and thus will generate ozone [7]; if there is the possibility of ozone generation, adequate ventilation should be confirmed within the working area to minimize ozone risk to operators. If possible, select UV-C sources with minimal or no ozone generation.
5. The configuration or orientation of UV-C sources may generate shadows (as is the case for any type of light, not just UV-C), and the configuration of N95 FFRs should be designed to avoid or mitigate shadow generation on the FFR surface. For instance, UV-reflective materials may be used and/or N95 FFRs may be rotated and/or flipped to ensure that the adequate dose is applied across the entire surface area of the FFR (and this dose should be validated with a UV-C-specific sensor).
6. Reports have demonstrated residual virus on N95 FFR straps after UV-C exposure (likely due to the ability of N95 FFR attachment straps to twist and be shadowed from the UV-C), suggesting a need for supplementary decontamination of the elastic straps [15, 16]. Mills et al. suggest wiping N95 FFR straps with a compatible disinfectant [15]. If this additional step is used, extra caution should be used to avoid touching the

N95 FFR facepiece as common disinfectant chemicals can degrade N95 FFR function [76].

7. Although  $\geq 1.0$  J/cm<sup>2</sup> dose of UV-C resulted in  $\geq 3$ -log reduction in viral activity of SARS-CoV-2 analogues on most N95 FFR models, such an observation does not imply sterility or full decontamination of the N95 FFR, as the N95 may still be contaminated with other pathogens that might not be similarly susceptible to UV-C irradiation (Table 3.1).

### 3.10 Conclusions

UV-C N95 treatment protocols should be implemented only if there is a dire shortage of N95 FFRs and appropriate federal and institutional approvals. While research on the UV-C dose necessary for SARS-CoV-2 inactivation on N95 materials is ongoing, estimates can be drawn from the extensive body of literature evidence for similar viruses. Accurate measurements of dose and wavelength in forthcoming SARS-CoV-2 inactivation studies would outline effective and reproducible protocols for this virus.

Currently, the existing research suggests that, if implemented properly with validation of the delivered UV-C dose to the FFR, it is likely that UV-C applied at a minimum dose of  $\geq 1.0$  J/cm<sup>2</sup> inactivates SARS-CoV-2 on the outer layers of nonshadowed regions of N95s based on results from similar viruses [15, 16, 23]. As all but one of the dose measurements for viral inactivation reported here used 254 nm sources, there is an opportunity for future research to rigorously assess minimum doses required for viral inactivation with the diverse landscape of UV-C sources and matched detectors.

UV-C has shown promise as an effective method for inactivation of viruses and bacterial spores on N95 respirator material; however, UV-C cannot inactivate pathogens that are not irradiated with the minimum dose. For that reason, UV-C may not effectively decontaminate inner layers of the FFR and an auxiliary method of decontamination is suggested for elastic straps.

We note that as of November 14, 2020, no EUA has been granted for UV-C decontamination of N95 FFRs. Because UV-C processes to inactivate SARS-CoV-2 on N95 FFRs are not expected to result in sterilization (killing of all microorganisms), N95 FFRs treated with UV-C should be returned to the same user to avoid user-to-user cross-contamination. N95 FFR model-dependent viral inactivation efficacy has been reported. We stress that (1) after each round of irradiation, a user seal check should be performed, (2) extended cycles of doffing and redonning may affect FFR fit, and (3) that the FFR should not be considered fully decontaminated after UV-C treatment, as there may be other pathogens contaminating the FFR whose activity may not be fully reduced by UV-C. Thus, UV-C treatment should be viewed as risk management rather than complete decontamination or sterilization. Health care personnel should continue to handle the respirator as if the PPE is contaminated and reuse only their own N95 FFR.

# Bibliography

1. Centers for Disease Control and Prevention. *Decontamination and Reuse of Filtering Facepiece Respirators* <https://www.cdc.gov/coronavirus/2019-ncov/hcp/ppp-strategy/decontamination-reuse-respirators.html> (2020).
2. Schulster, L. *et al.* *Guidelines for environmental infection control in health-care facilities. Recommendations from CDC and the Healthcare Infection Control Practices Advisory Committee (HICPAC)*. tech. rep. (American Society for Healthcare Engineering/American Hospital Association, Chicago, IL, 2019).
3. Institute of Medicine. *Reusability of Facemasks During an Influenza Pandemic: Facing the Flu* tech. rep. (The National Academies Press, Washington, DC, 2006). doi:10.17226/11637.
4. Anderson, J. *et al.* Inactivation of food-borne enteropathogenic bacteria and spoilage fungi using pulsed-light. *IEEE Transactions on Plasma Science* **28**, 83–88. ISSN: 00933813. doi:10.1109/27.842870 (2000).
5. Ito, A. & Ito, T. Absorption spectra of deoxyribose, ribosephosphate, ATP and DNA by direct transmission measurements in the vacuum-UV (150-190 nm) and far-UV (190-260 nm) regions using synchrotron radiation as a light source. *Photochemistry and Photobiology* **44**, 355–358. ISSN: 0031-8655, 1751-1097. doi:10.1111/j.1751-1097.1986.tb04675.x (1986).
6. Jay, J. M. *Modern Food Microbiology* (ed Heldman, D. R.) ISBN: 978-1-4615-7478-1. doi:10.1007/978-1-4615-7476-7 (Springer US, Boston, MA, 1995).
7. Kowalski, W. *Ultraviolet Germicidal Irradiation Handbook: UVGI for Air and Surface Disinfection* ISBN: 978-3-642-01999-9 (Springer Science & Business Media, Berlin, Heidelberg, 2010).
8. U.S. Environmental Protection Agency & C. *Ultraviolet Disinfection Guidance Manual for the Final Long Term 2 Enhanced Surface Water Treatment Rule* tech. rep. EPA 815-R-06-007 (U.S. Environmental Protection Agency Office of Water, Washington, DC, 2006), 436.
9. U.S. Environmental Protection Agency. *UV Radiation* tech. rep. EPA 430-F-10-025 (2010).

10. Sagripanti, J.-L. & Lytle, C. D. Inactivation of influenza virus by solar radiation. *Photochem. Photobiol.* **83**, 1278–1282. ISSN: 0031-8655. doi:10.1111/j.1751-1097.2007.00177.x (2007).
11. Bolton, J. R. & Linden, K. G. Standardization of Methods for Fluence (UV Dose) Determination in Bench-Scale UV Experiments. *Journal of Environmental Engineering* **129**, 209–215. ISSN: 0733-9372, 1943-7870. doi:10.1061/(ASCE)0733-9372(2003)129:3(209) (2003).
12. Malayeri, A. H. *et al.* Fluence (UV dose) required to achieve incremental log inactivation of bacteria, protozoa, viruses and algae. *IUVA News* **18**, 4–6 (2016).
13. Reifsnnyder, W. E. Radiation geometry in the measurement and interpretation of radiation balance. *Agricultural Meteorology* **4**, 255–265. ISSN: 00021571. doi:10.1016/0002-1571(67)90026-X (1967).
14. Center for Devices and Radiological Health. *Recommendations for Sponsors Requesting EUAs for Decontamination and Bioburden Reduction Systems for Face Masks and Respirators During the Coronavirus Disease 2019 (COVID-19) Public Health Emergency* tech. rep. FDA-2020-D-1138 (Center for Devices and Radiological Health, 2020).
15. Mills, D. *et al.* Ultraviolet germicidal irradiation of influenza-contaminated N95 filtering facepiece respirators. *American Journal of Infection Control* **46**, e49–e55. ISSN: 01966553. doi:10.1016/j.ajic.2018.02.018 (2018).
16. Heimbuch, B. & Harnish, D. *Research to Mitigate a Shortage of Respiratory Protection Devices During Public Health Emergencies* tech. rep. HHSF223201400158C (Applied Research Associates, Inc., 2019).
17. American Conference of Governmental Industrial Hygienists. *TLV's and BEI's based on the documentation of the threshold limit values for chemical substances and physical agents and biological exposure indices* ISBN: 978-1-60726-105-6 (Cincinnati, OH, 2019).
18. European Parliament, Council of the European Union. Directive 2004/39/Ec of the European Parliament and of the Council of 21 April 2004 on the minimum health and safety requirements regarding the exposure of workers to risks arising from physical agents (artificial optical radiation). *Official Journal of the European Union* **114**, 38–59. doi:10.1007/978-1-137-54507-7\_21 (2006).
19. National Institute for Occupational Safety and Health. *A recommended standard for occupational exposure to...ultraviolet radiation* tech. rep. 73-11009 (National Institute for Occupational Safety and Health, 1972).
20. Lowe, J. J. *et al.* *N95 Filtering Facepiece Respirator Ultraviolet Germicidal Irradiation (UVGI) Process for Decontamination and Reuse* tech. rep. (2020).
21. Brickman, J. *et al.* *Optimization, Validation, and Implementation of a UV Disinfection Method for N95 Face Masks* tech. rep. (2020).

22. APIC and N95DECOR suggested guidance for infection prevention and workflow for UV-C decontamination of N95 FFRs during COVID-19 tech. rep. (Association for Professionals in Infection Control and Epidemiology, 2020).
23. Lore, M. B. *et al.* Effectiveness of Three Decontamination Treatments against Influenza Virus Applied to Filtering Facepiece Respirators. *The Annals of Occupational Hygiene* **56**, 92–101. ISSN: 0003-4878. doi:10.1093/annhyg/mer054 (2011).
24. Walker, C. M. & Ko, G. Effect of ultraviolet germicidal irradiation on viral aerosols. *Environ. Sci. Technol.* **41**, 5460–5465. ISSN: 0013-936X. doi:10.1021/es070056u (2007).
25. Heimbuch, B. K. *et al.* A pandemic influenza preparedness study: Use of energetic methods to decontaminate filtering facepiece respirators contaminated with H1N1 aerosols and droplets. *American Journal of Infection Control* **39**, e1–e9. ISSN: 0196-6553. doi:10.1016/j.ajic.2010.07.004 (2011).
26. Ozog, D. M. *et al.* The Effect of Ultraviolet C Radiation Against Different N95 Respirators Inoculated with SARS-CoV-2. *International Journal of Infectious Diseases*, 224–229. ISSN: 12019712. doi:10.1016/j.ijid.2020.08.077 (2020).
27. Fischer, R. J. *et al.* Effectiveness of N95 Respirator Decontamination and Reuse against SARS-CoV-2 Virus. *Emerging Infectious Diseases* **26**. ISSN: 1080-6059. doi:10.3201/eid2609.201524 (2020).
28. Smith, J. S. *et al.* Effect of various decontamination procedures on disposable N95 mask integrity and SARS-CoV-2 infectivity. *Journal of Clinical and Translational Science* **5**. ISSN: 2059-8661. doi:10.1017/cts.2020.494 (2020).
29. Vo, E., Rengasamy, S. & Shaffer, R. Development of a test system to evaluate procedures for decontamination of respirators containing viral droplets. *Appl. Environ. Microbiol.* **75**, 7303–7309. ISSN: 0099-2240, 1098-5336. doi:10.1128/AEM.00799-09 (2009).
30. Fisher, E. & Shaffer, R. A method to determine the available UV-C dose for the decontamination of filtering facepiece respirators: UV-C decontamination of respirators. *Journal of Applied Microbiology* **110**, 287–295. ISSN: 13645072. doi:10.1111/j.1365-2672.2010.04881.x (2011).
31. Woo, M.-H. *et al.* Effects of Relative Humidity and Spraying Medium on UV Decontamination of Filters Loaded with Viral Aerosols. *Applied and Environmental Microbiology* **78**, 5781–5787. ISSN: 0099-2240, 1098-5336. doi:10.1128/AEM.00465-12 (2012).
32. Tseng, C.-C. & Li, C.-S. Inactivation of Viruses on Surfaces by Ultraviolet Germicidal Irradiation. *Journal of Occupational and Environmental Hygiene* **4**, 400–405. ISSN: 1545-9624, 1545-9632. doi:10.1080/15459620701329012 (2007).
33. Lin, T.-H. *et al.* Relative survival of *Bacillus subtilis* spores loaded on filtering facepiece respirators after five decontamination methods. *Indoor Air*. ISSN: 1600-0668. doi:10.1111/ina.12475 (2018).



34. Bentley, J. J. *et al.* Can ultraviolet light C decrease the environmental burden of antimicrobial-resistant and -sensitive bacteria on textiles? *Vet. Dermatol.* **27**, 457–e121. ISSN: 0959-4493, 1365-3164. doi:10.1111/vde.12377 (2016).
35. Wallace, R. L., Ouellette, M. & Jean, J. Effect of UV-C light or hydrogen peroxide wipes on the inactivation of methicillin-resistant *Staphylococcus aureus*, *Clostridium difficile* spores and norovirus surrogate. *J. Appl. Microbiol.* **127**, 586–597. ISSN: 1364-5072, 1365-2672. doi:10.1111/jam.14308 (2019).
36. Fu, L. *et al.* Different efficacies of common disinfection methods against *Candida auris* and other *Candida* species. *J. Infect. Public Health.* ISSN: 1876-0341, 1876-035X. doi:10.1016/j.jiph.2020.01.008 (2020).
37. OSHA. *OSHA Technical Manual, Section VIII - Use of Respirators* [https://www.osha.gov/dts/osta/otm/otm\\_viii/otm\\_viii\\_2.html#8](https://www.osha.gov/dts/osta/otm/otm_viii/otm_viii_2.html#8). Accessed: 2020-4-22.
38. Mayerhöfer, T. G. & Popp, J. Beer's law derived from electromagnetic theory. *Spectrochimica Acta Part A: Molecular and Biomolecular Spectroscopy* **215**, 345–347. ISSN: 1386-1425. doi:10.1016/j.saa.2019.02.103 (2019).
39. Tseng, C.-C. & Li, C.-S. Inactivation of Virus-Containing Aerosols by Ultraviolet Germicidal Irradiation. *Aerosol Science and Technology* **39**, 1136–1142. ISSN: 0278-6826, 1521-7388. doi:10.1080/02786820500428575 (2005).
40. Kohli, I. *et al.* UVC Germicidal Units: Determination of Dose Received and Parameters to be Considered for N95 Respirator Decontamination and Reuse. *Photochemistry and Photobiology* **96**, 1083–1087. ISSN: 1751-1097. doi:10.1111/php.13322 (2020).
41. Simmons, S. E. *et al.* Deactivation of SARS-CoV-2 with pulsed-xenon ultraviolet light: Implications for environmental COVID-19 control. *Infection Control and Hospital Epidemiology*, 1–4. ISSN: 0899-823X. doi:10.1017/ice.2020.399 (2020).
42. Poster, D. L. *et al.* Innovative Approaches to Combat Healthcare-Associated Infections Using Efficacy Standards Developed Through Industry and Federal Collaboration. *Proceedings of SPIE—the International Society for Optical Engineering* **10730**. ISSN: 0277-786X. doi:10.1117/12.2500431 (2018).
43. ASTM International. *Standard Test Method for Determining Antimicrobial Efficacy of Ultraviolet Germicidal Irradiation against Influenza Virus on Fabric Carriers with Simulated Soil* tech. rep. E3179-18 (2019).
44. *Guidelines on viral inactivation and removal procedures intended to assure the viral safety of human blood plasma products* tech. rep. 924 (World Health Organization, 2004).
45. Blázquez, E. *et al.* Evaluation of the effectiveness of the SurePure Turbulator ultraviolet-C irradiation equipment on inactivation of different enveloped and non-enveloped viruses inoculated in commercially collected liquid animal plasma. *PLoS One* **14**, e0212332. ISSN: 1932-6203. doi:10.1371/journal.pone.0212332 (2019).

46. Fisher, E. M., Williams, J. L. & Shaffer, R. E. Evaluation of Microwave Steam Bags for the Decontamination of Filtering Facepiece Respirators. *PLoS ONE* **6** (ed Jefferson, T.) e18585. ISSN: 1932-6203. doi:10.1371/journal.pone.0018585 (2011).
47. Kenar, L. *et al.* Comparative sporicidal effects of disinfectants after release of a biological agent. *Mil. Med.* **172**, 616–621. ISSN: 0026-4075. doi:10.7205/milmed.172.6.616 (2007).
48. Smolle, C. *et al.* Effectiveness of automated ultraviolet-C light for decontamination of textiles inoculated with *Enterococcus faecium*. *J. Hosp. Infect.* **98**, 102–104. ISSN: 0195-6701, 1532-2939. doi:10.1016/j.jhin.2017.07.034 (2018).
49. Tomas, M. E. *et al.* The Ebola disinfection booth: evaluation of an enclosed ultraviolet light booth for disinfection of contaminated personal protective equipment prior to removal. *Infect. Control Hosp. Epidemiol.* **36**, 1226–1228. ISSN: 0899-823X, 1559-6834. doi:10.1017/ice.2015.166 (2015).
50. Tano, E. & Melhus, A. Level of decontamination after washing textiles at 60°C or 70°C followed by tumble drying. *Infection Ecology & Epidemiology* **4**, 24314. ISSN: 2000-8686. doi:10.3402/iee.v4.24314 (2014).
51. CDC. *Guidelines for Environmental Infection Control in Health-Care Facilities: Recommendations of CDC and the Healthcare Infection Control Practices Advisory Committee (HICPAC)* tech. rep. (U.S. Department of Health, Human Services, Centers for Disease Control, and Prevention (CDC)., 2019).
52. Carratalà, A. *et al.* Effect of temperature and sunlight on the stability of human adenoviruses and MS2 as fecal contaminants on fresh produce surfaces. *Int. J. Food Microbiol.* **164**, 128–134. ISSN: 0168-1605, 1879-3460. doi:10.1016/j.ijfoodmicro.2013.04.007 (2013).
53. Lee, J. E. & Ko, G. Norovirus and MS2 inactivation kinetics of UV-A and UV-B with and without TiO<sub>2</sub>. *Water Res.* **47**, 5607–5613. ISSN: 0043-1354, 1879-2448. doi:10.1016/j.watres.2013.06.035 (2013).
54. Heisler, G. M. *et al.* Solar ultraviolet-B radiation in urban environments: the case of Baltimore, Maryland. *Photochemistry and Photobiology* **80**, 422–428. ISSN: 0031-8655. doi:10.1562/0031-8655(2004)080<0422:SURIUE>2.0.CO;2 (2004).
55. Beck, S. E. *et al.* Comparison of UV-Induced Inactivation and RNA Damage in MS2 Phage across the Germicidal UV Spectrum. *Applied and Environmental Microbiology* **82**, 1468–1474. ISSN: 0099-2240, 1098-5336. doi:10.1128/AEM.02773-15 (2016).
56. Lytle, C. D. & Sagripanti, J.-L. Predicted Inactivation of Viruses of Relevance to Biodefense by Solar Radiation. *Journal of Virology* **79**, 14244–14252. ISSN: 0022-538X. doi:10.1128/JVI.79.22.14244-14252.2005 (2005).
57. CDC. *42 CFR Part 84 Respiratory Protective Devices* <https://www.cdc.gov/niosh/nppt1/topics/respirators/pt84abs2.html>. Accessed: 2020-4-10. 1997.

58. Zhao, Z. *et al.* Germicidal Ultraviolet Light Does Not Damage or Impede Performance of N95 Masks Upon Multiple Uses. *Environmental Science & Technology Letters* **7**, 600–605. doi:10.1021/acs.estlett.0c00416 (2020).
59. Viscusi, D. J. *et al.* Evaluation of Five Decontamination Methods for Filtering Facepiece Respirators. *The Annals of Occupational Hygiene* **53**, 815–827. ISSN: 0003-4878. doi:10.1093/annhyg/mep070 (2009).
60. Ozog, D. *et al.* The importance of fit testing in decontamination of N95 respirators: A cautionary note. *Journal of the American Academy of Dermatology* **83**, 672–674. ISSN: 0190-9622. doi:10.1016/j.jaad.2020.05.008 (2020).
61. Lindsley, W. G. *et al.* Effects of Ultraviolet Germicidal Irradiation (UVGI) on N95 Respirator Filtration Performance and Structural Integrity. *Journal of Occupational and Environmental Hygiene* **12**, 509–517. ISSN: 1545-9624. doi:10.1080/15459624.2015.1018518 (2015).
62. CDC. *Filtering out Confusion: Frequently Asked Questions about Respiratory Protection* <https://doi.org/10.26616/NIOSH PUB2018130>. Accessed: 2020-4-10. 2018.
63. Bergman, M. S. *et al.* Impact of multiple consecutive donnings on filtering facepiece respirator fit. *Am. J. Infect. Control* **40**, 375–380. ISSN: 0196-6553, 1527-3296. doi:10.1016/j.ajic.2011.05.003 (2012).
64. CDC. *Recommended Guidance for Extended Use and Limited Reuse of N95 Filtering Facepiece Respirators in Healthcare Settings* <https://www.cdc.gov/niosh/topics/hcwcontrols/RecommendedGuidanceExtUse.html#ref16>. Accessed: 2020-4-21. 2020.
65. Battelle. *Instructions for Healthcare Personnel: Preparation of Compatible N95 Respirators for Decontamination by the Battelle Memorial Institute Using the Battelle Decontamination System* <https://www.fda.gov/media/136532/download>. Accessed: 2020-4-22. 2020.
66. Marra, A. R., Schweizer, M. L. & Edmond, M. B. No-Touch Disinfection Methods to Decrease Multidrug-Resistant Organism Infections: A Systematic Review and Meta-analysis. *Infection Control & Hospital Epidemiology* **39**, 20–31. ISSN: 0899-823X, 1559-6834. doi:10.1017/ice.2017.226 (2018).
67. *Environmental Control for Tuberculosis: Basic Upper-Room Ultraviolet Germicidal Irradiation Guidelines for Healthcare Settings* tech. rep. (U.S. Department of Health et al., 2009).
68. Beam, B. L. & Hayes, A. K. *N95 Respirator Limited Reuse - Healthcare Professionals Providing Clinical Care* <https://app1.unmc.edu/nursing/heroes/mpv.cfm?updateindex=132&src=yt> (2021).
69. Ontiveros, C. C. *et al.* Characterization of a commercially-available, low-pressure UV lamp as a disinfection system for decontamination of common nosocomial pathogens on N95 filtering facepiece respirator (FFR) material. *Environmental Science: Water Research & Technology* **6**, 2089–2102. ISSN: 2053-1419. doi:10.1039/DOEW00404A (2020).

70. Purschke, M. *et al.* Construction and validation of UV-C decontamination cabinets for filtering facepiece respirators. *Applied Optics* **59**. doi:<https://doi.org/10.1364/AO.401602> (2020).
71. Wilde, J. P., Baer, T. M. & Hesselink, L. Modeling UV-C irradiation chambers for mask decontamination using Zemax OpticStudio. *Applied Optics* **59**, 7596. ISSN: 1559-128X, 2155-3165. doi:10.1364/AO.402603 (2020).
72. Bentancor, M. & Vidal, S. Programmable and low-cost ultraviolet room disinfection device. *HardwareX* **4**, e00046. ISSN: 24680672. doi:10.1016/j.ohx.2018.e00046 (2018).
73. Rutala, W. A. *et al.* Room decontamination using an ultraviolet-C device with short ultraviolet exposure time. *Infect. Control Hosp. Epidemiol.* **35**, 1070–1072. ISSN: 0899-823X, 1559-6834. doi:10.1086/677149 (2014).
74. International Ultraviolet Association. *UV FAQs* <http://www.iuva.org/UV-FAQs>. Accessed: 2020-4-18.
75. Khazova, M. *et al.* Survey of Home-Use UV Disinfection Products. *Photochemistry and Photobiology* **97**, 560–565. ISSN: 1751-1097. doi:<https://doi.org/10.1111/php.13423> (2021).
76. Viscusi, D. J., King, W. P. & Shaffer, R. E. Effect of Decontamination on the Filtration Efficiency of Two Filtering Facepiece Respirator Models. *J Int Soc Resp Prot* **24**, 15 (2007).

## Chapter 4

# Best practices for germicidal ultraviolet-C dose measurement for N95 respirator decontamination

Reproduced with permission from: A. Geldert\*, H. B. Balch\*, A. Gopal, A. Su, S. M. Grist, & A. E. Herr, "Best practices for germicidal ultraviolet-C dose measurement for N95 respirator decontamination", *Journal of Research of the National Institute of Standards and Technology*, accepted, 2021.

\*contributed equally.

### 4.1 Introduction

The coronavirus disease 2019 (COVID-19) pandemic caused severe shortages of N95 filtering facepiece respirators, which are essential personal protective equipment (PPE) for healthcare professionals worldwide<sup>1</sup>. In response to the global shortage, the U.S. Centers for Disease Control and Prevention (CDC) issued guidelines for decontamination and reuse of N95 respirators as a crisis capacity strategy and identified ultraviolet-C (UV-C) germicidal irradiation as one of the most promising methods for primary decontamination [1]. UV-C plays an important role in infection control across the medical industry but, due to the complex geometry and material properties of N95 respirators (which differ between N95 respirator models), the UV-C measurement considerations for N95 decontamination differ substantially from the more established applications of germicidal UV-C. Safe and effective UV-C decontamination depends critically on (1) the spectral overlap between the emission spectrum of the UV-C source and the wavelengths capable of inactivating the pathogen (i.e., the action

---

<sup>1</sup>“N95” is a filter class designation of the U.S. National Institute of Occupational Safety and Health (NIOSH). It is applied to respirators that are at least 95% efficient at filtering NaCl aerosols with particle sizes of mean diameter  $75 \text{ nm} \pm 20 \text{ nm}$  (NIOSH Procedure No. TEB-APR-STP-0059, 13 December 2019).

spectrum), and (2) how much energy is delivered to the pathogen (fluence, often described as dose<sup>2</sup>). However, accurately measuring and reporting these characteristics for UV-C N95 decontamination systems is complicated, and measurement standards targeting the unique challenges of complex, multi-material N95 respirators remain in development.

Accurate measurements of UV-C dose are central both for verifying that decontamination systems are operating within specification and for reproducible reporting. UV-C dose measurements provide a key link in the translation of effective and reproducible decontamination protocols across different communities: from UV-C device manufacturers and researchers, to infection control staff implementing UV-C N95 decontamination. In this paper, we highlight key measurement considerations for researchers, engineers, and clinical staff who are evaluating and implementing UV-C-based decontamination of N95 respirators. First, we highlight the technical and regulatory context for UV-C N95 decontamination; second, we discuss the science behind UV-C decontamination, highlighting the central importance of both wavelength and dose in viral inactivation; third, we examine techniques and common pitfalls in UV-C dose measurement; and finally, we outline best practices that help avoid these pitfalls.

## UV-C for N95 Decontamination

UV-C radiation is widely used as a secondary technique for decontamination of air [3], water [4], and non-porous surfaces [5]. Until April 2021, CDC guidance [1] and hospital protocols [6] indicated that UV-C was used during the COVID-19 pandemic as a primary and standalone decontamination method for N95 respirators under crisis capacity conditions [7]. As a primary decontamination technique, the application of UV-C to N95 respirators requires specific consideration of the complex geometry, porous multi-material electret layers, and filtration central to N95 respirator function. For example, UV-C radiation is heavily attenuated when passing through non-UV-C-transparent and scattering materials; dose received at interior layers may be orders of magnitude lower than the applied dose at the outer surface of the N95 (Figure 4.1A) [8]. UV-C attenuation through the porous layers requires special consideration to ensure that the dose received at all contaminated layers within the respirator is sufficient for decontamination [8]. Consequently, decontamination of porous materials can require 100× higher applied dose at the surface than that required for non-porous surfaces with low surface roughness [9, 10], but excessive doses can reduce respirator function [11]. The electrostatic respirator filter material is also damaged by chemical disinfectants such as

---

<sup>2</sup>Not all the energy incident on a substrate is absorbed. While dose is almost always used in the germicidal UV-C literature to describe the energy incident on the material being decontaminated, dose can also refer to the total amount of absorbed (not incident) energy in other contexts. The most accurate technical term to describe the total incident UV-C energy (in units of J/cm<sup>2</sup>) on a surface is fluence [2]. However, to align with the germicidal UV-C literature, here we choose to use the term “dose” to describe total incident energy on an N95. Similarly, while fluence rate is a more technically accurate term to describe the radiant power (in units of W/cm<sup>2</sup>) irradiating a sample from all directions [2], here we use the term irradiance to align with the decontamination literature.

ethanol [12], limiting the use of some primary healthcare surface disinfectants. Furthermore, the complex three-dimensional geometry of N95 respirators can result in the received dose varying several-fold across a single N95 respirator [13, 14] and about twenty-fold across different N95 respirators within one decontamination system [14], with received dose strongly dependent on the incident angle of UV-C irradiation (Figure 4.1(A-B)) [15].

Due to the technical challenges and additional considerations required to implement UV-C decontamination for N95 respirators, federal guidelines for UV-C decontamination of N95 respirators remain in development [16]. For example, the CDC has assessed the impact of several UV-C N95 decontamination systems on the fit and filtration of specific N95 respirator models, but the assessment “is not to determine the effectiveness of the decontamination procedure at killing the pathogenic microorganism” [17]. The U.S. Food & Drug Administration (FDA) guidelines emphasize that while the FDA regulates UV-C sources, the lack of clear and standardized manufacturer data on wavelength, duration, and associated UV-C dose required to inactivate severe acute respiratory syndrome coronavirus 2 (SARS-CoV-2), the strain of coronavirus that causes COVID-19, presents an outstanding challenge [18]. In addition, the FDA allows previously approved devices to extend to SARS-CoV-2 inactivation [19]. However, the FDA requires previously approved devices to submit Emergency Use Authorizations (EUAs) and 510(k) when adapted to new applications including decontamination of N95 respirators and other single-use PPE [16]. A 510(k) is a premarket submission made to the FDA to demonstrate that a proposed device is as safe and effective as a legally marketed device. For example, a steam sterilization device with prior 510(k) clearance for sterilization of other materials in healthcare settings required an FDA-issued EUA before it was approved for N95 respirator decontamination [20]. While the FDA has issued numerous EUAs for devices implementing the other two PPE decontamination methods (moist heat and vaporous hydrogen peroxide) [20, 21] identified as promising by the CDC for crisis-capacity conditions, as of January 2021, only one limited EUA has been issued for the use of UV-C to reduce bioburden on one N95 respirator model [22].

Despite this context, the accessibility and relatively low cost of UV-C sources has led to widespread implementation of UV-C for N95 decontamination in both research [12, 23, 24] and medical [6] environments. Decontamination system specifications depend on technical measurement factors, such as the wavelengths emitted, the wavelengths detected, the type and position of UV-C detector, and the method of analysis. Reports of UV-C-based decontamination of N95 respirators often fail to report the parameters necessary to ensure validation and reproducibility despite using diverse types of UV-C sources and different measurement devices. To accurately describe, evaluate, and reproduce UV-C decontamination protocols, parameters such as type, number, and location of UV-C sources, orientation and position of both N95(s) and UV-C detector(s) relative to UV-C source(s), models of N95 respirator and UV-C detector, decontamination chamber specifications (e.g., reflectivity), and other details of dose quantification are needed. Omitting these parameters for the source, target, or detector when reporting decontamination procedures substantially limits validation and reproducibility. In addition, standards for measurement are currently limited, which impedes comparison of UV-C sources and detectors [25]. In particular, minimum report-

ing standards for systems claiming UV-C decontamination of N95 respirators are urgently needed to facilitate comparison and critical evaluation. Here, we provide an overview of UV-C measurement fundamentals to inform the development of measurement and reporting standards for UV-C N95 respirator decontamination systems.

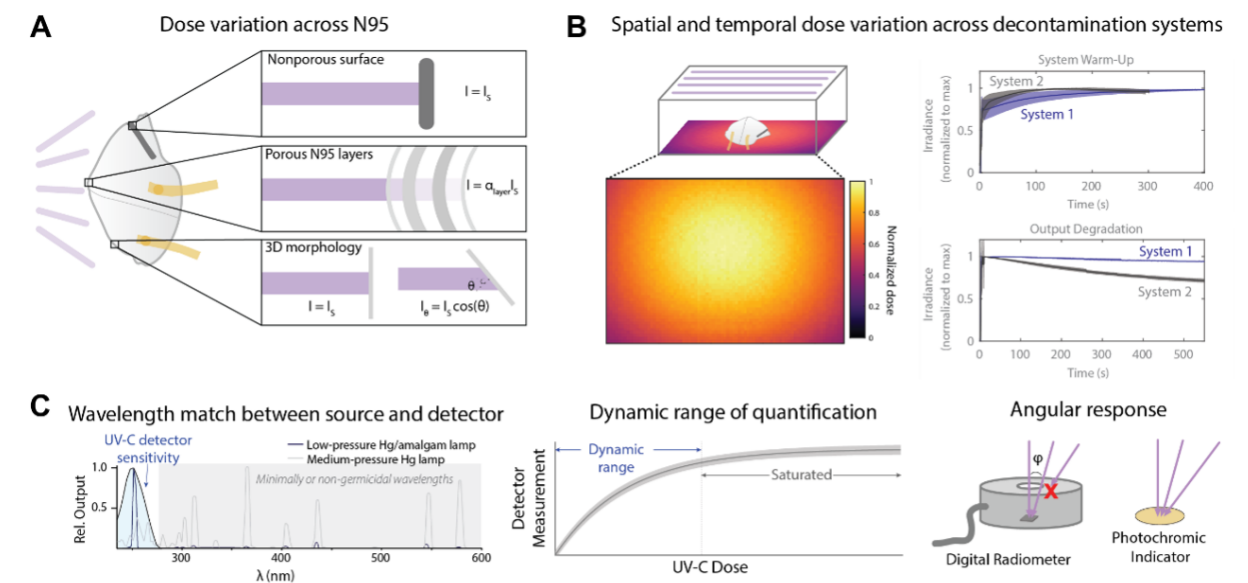


Figure 4.1: Factors influencing UV-C dose distribution and measurement for N95 decontamination. (A) Factors affecting UV-C dose applied to the N95 respirator. Sloped surfaces and attenuation by the N95 layers reduce received UV-C dose. Received UV-C intensity ( $I$ ) is reduced from the intensity normally incident on the top surface ( $I_s$ ) by a layer-dependent attenuator factor ( $\alpha_{layer}$ ) and by a factor of the cosine of the angle of incidence ( $\theta$ ). (B) Factors affecting UV-C dose distribution within a decontamination system. UV-C irradiance can vary spatially and temporally. (C) Key specifications of UV-C detectors, including wavelength specificity, dynamic range, and angular response ( $\phi$  denotes the radiometer field-of-view angle). Figure adapted with permission from Su & Grist, et al. [14].

## Key Germicidal UV-C Specifications: Wavelength and Dose

Not all wavelengths of UV radiation offer sufficient germicidal efficacy for N95 respirator decontamination. Absorbed germicidal UV-C radiation (200 nm to 280 nm) inactivates pathogens by promoting photochemical reactions that damage proteins and genomic material [26, 27]. Distinct wavelengths have different microbe-specific germicidal efficacy, a relationship represented in what is known as the action spectrum of a microbe. The overlap between the action spectrum and the UV-C source emission spectrum will determine the efficiency of germicidal action, with higher efficiency when the overlap is greater. For many pathogens, there is a peak in the action spectrum at the absorption maximum of



genomic material, around 260 nm. While research into the germicidal action spectrum of SARS-CoV-2 is ongoing, a working assumption is that the action spectrum will be similar to that of viral analogues with similar structure that exhibit a peak near 260 nm [27, 28]. Germicidal UV-C radiation sources emit close to this maximum, such as the narrow emission around 254 nm from low-pressure mercury (Hg) lamps commonly used as germicidal sources. The relative efficacy of emerging monochromatic and polychromatic UV-C sources is also an area of active research, highlighting the importance of rigorous measurement and reporting to facilitate accurate comparison of sources with different emission spectra. While shorter wavelengths within the UV-C range ( $\sim 200$  nm to 220 nm) can have higher germicidal efficacy [27], these wavelengths may be more strongly attenuated by the multiple N95 layers, requiring confirmation of dose and viral inactivation on interior layers. Longer-wavelength UV radiation ( $>280$  nm), such as UV-B and UV-A in sunlight at the earth's surface, has substantially lower germicidal activity [29] and has not been shown to decontaminate porous materials such as N95 respirators. While UV-B (280 nm to 320 nm) can photochemically damage nucleic acids, UV-B is orders of magnitude less efficient than UV-C wavelengths [29] due to reduced overlap with the absorption spectrum of nucleic acids. While UV-A (320 nm to 400 nm) can generate reactive oxygen species to contribute to pathogen inactivation (particularly in water) [30, 31], UV-A is generally not considered germicidal [27]. Because absorption by the multiple porous N95 layers causes N95 decontamination to require about  $100\times$  higher applied dose [8] as compared to more common applications (e.g., air, water, non-porous surface decontamination), UV-A and UV-B likely have insufficient germicidal efficacy to be feasible for N95 respirator decontamination.

Efficacy of germicidal UV-C also depends critically on dose. Studies on other coronaviruses and influenzas indicate that 254 nm UV-C doses (from a low-pressure Hg UV-C source) of at least  $1.0$  J/cm<sup>2</sup> at the N95 respirator surface can lead to  $\geq 99.9\%$  viral inactivation on most N95 models [9, 32]. Preliminary studies using both UV-C light-emitting diodes (LEDs) and mercury lamps have found that UV-C doses of at least  $1.5$  J/cm<sup>2</sup> are required to yield  $\geq 99.9\%$  inactivation of SARS-CoV-2 on some N95 respirator models [12, 24], and research on SARS-CoV-2 inactivation on N95 respirators is ongoing. On the other hand, studies indicate that doses over  $120$  J/cm<sup>2</sup> can cause respirator degradation [11]. Because it is infeasible to measure UV-C dose delivered to viral particles embedded in the interior layers of the respirator during a decontamination cycle, the dose required for pathogen inactivation or degradation is typically reported in terms of dose applied at the respirator surface. However, because UV-C transmission through N95 respirator layers is dependent on the N95 model [8], the minimum dose applied at the N95 surface for pathogen inactivation throughout all N95 layers will differ from model to model. These examples underscore the importance of accurate measurement and reporting of UV-C wavelength and dose when using germicidal UV-C for effective and reproducible decontamination of N95 respirators.

## Critical UV-C Source and Detector Metrics

Applying sufficient UV-C dose to N95 respirators can make – or break – effective decontamination [33]. While measurement of pathogen inactivation is the most direct way of verifying decontamination efficacy on N95 respirators, this approach is time- and resource-intensive. It is largely infeasible to perform pathogen inactivation assays at the frequency necessary to validate the ongoing efficacy of UV-C decontamination systems, especially in healthcare settings. UV-C decontamination systems must be regularly validated because the irradiance reaching an N95 respirator can vary with UV-C source age, environmental factors such as temperature, and setup-dependent shadowing or reflections. In particular, the material properties of nearby surfaces, such as UV-C reflectivity, have a substantial influence on the spatial pattern and magnitude of UV-C dose delivered to N95 respirators [34, 35]. Thus, even if the UV-C output or pathogen inactivation efficacy of a particular UV-C lamp or decontamination system has been rigorously characterized by the manufacturer, frequent UV-C dose measurements are a more scalable, reliable, and cost-effective method (as compared to pathogen inactivation testing) for end users to ensure the system continues to operate within specification in the particular user environment.

Despite its critical role, UV-C dose is not always calculated or reported in a standardized way [25]. Dose (energy, in  $\text{J}/\text{cm}^2$ ) is the integrated irradiance measured on a surface ( $\text{W}/\text{cm}^2$ ) over the exposure time (s). Germicidal efficacy is wavelength dependent. Thus, to compare UV-C sources with different emission spectra and to evaluate overlap between a UV-C source and the pathogen action spectrum, dose reported from polychromatic sources should weight each wavelength by its respective, relative germicidal efficacy [2, 36]. Unless a detector is omnidirectional, measured UV-C dose will depend on the location and orientation of the UV-C detector with respect to the source. As a result, to ensure reproducibility, it is critical to measure and report UV-C dose along with parameters such as UV-C source, distance from and position with respect to the source, measured irradiance, and exposure time.

Accurate dose measurements depend on the selection of an appropriate UV-C sensor. Detectors such as radiometers, dosimeters, and dose indicator strips are all used to measure and/or calculate UV-C dose. Characteristics of UV-C sensors, such as the sensor wavelength sensitivity spectrum, dynamic range, and angular response strongly affect measured values [37]. As a result, it is important to consider the working principle of the sensor when matching a sensor to a given application. For example, radiometers can provide quantitative measurements appropriate for research or validation environments, but radiometers that do not have an ideal cosine response (e.g., those that are designed for collimated sources) will not accurately report UV-C doses from non-normal incident radiation. Additionally, angular response of UV-C sensors is often not characterized or provided. Spherical actinometric detectors relate the detector quantum yield to the dose on a surface, are widely used to calibrate physical sensors, and accurately measure dose on complex geometries. However, actinometry can be labor intensive, and the diversity of chemical transitions used in actinometry require careful reporting for accurate measurement and reproducibility [2, 38]. Low-cost photochromic dose indicator strips can offer a straightforward colorimetric indicator of dose

range, are commonly used in healthcare settings, and may facilitate implementation of UV-C decontamination across both low- and high-resource environments. However, these qualitative indicators are subject to potential pitfalls: dose indicator strips are commonly sensitive to both UV-B and UV-C, and those designed for non-porous or low-dose applications frequently have insufficient dynamic range, saturating below the  $1.0 \text{ J/cm}^2$  dose required for decontamination of many N95 models [14, 39]. Thus, even when the goal is simply to verify that a decontamination system is operating within specification, understanding the specificity and dynamic range of qualitative UV-C dose indicators is critical. The ability to perform reproducible UV-C decontamination, whether in the lab or the clinic, requires applied dose to be measured with a UV-C-specific sensor capable of measuring at least  $1.0 \text{ J/cm}^2$  and with maximum sensitivity aligned with the pathogen action spectrum (e.g., 260 nm). If the detector has a non-ideal angular response, the beam divergence at the detector should be identical to the conditions under which the sensor was calibrated, without which measurement errors are common (Figure 4.1C).

## Common Measurement Pitfalls

Several common pitfalls hinder accurate measurements of UV-C wavelength and dose, some of which are listed in Table 4.1. One common source of error is a mismatch between the source and detector. For example, dose measurements with a broadband sensor will collect not only germicidal UV-C but also minimally or nongermicidal wavelengths such as UV-A/B, visible, and infrared radiation, often with even greater sensitivity. Unless UV-C is specifically isolated at the sensor (e.g., with a bandpass filter), this mismatch will yield artificially high readings of UV-C dose. While different standards define different acceptable wavelength ranges of sensor sensitivity for different applications [2, 40, 41], sensors specifically used to measure UV-C should only be responsive to UV-C wavelengths between 200-300 nm and with peak response at the emission peak of the UV-C source (e.g., 254 nm for low-pressure Hg lamps) [40]. Methods to calculate a correction factor to account for the wavelength-dependence of a sensor are further described by Bolton & Linden [2]. Another common mistake is in mapping measurements of power or irradiance to dose. Since the irradiation of a UV-C source can vary over both space and time (Figure 4.1B), calculations of dose determined by multiplying a single irradiance measurement by exposure time can result in overestimates or underestimates of the dose applied (as shown in Table 4.2). Instead, applied dose is more accurately determined by integrating irradiance measured throughout the entire exposure time, to account for fluctuations in applied irradiance.

Many of the risks associated with over- or underestimating applied dose can be managed with an understanding of the working principles of the UV-C source and detector and through adequate reporting. However, the implications of over- or under-reporting UV-C dose applied to N95 respirators are wide-ranging and user-dependent, as demonstrated in Table 2. For example, if researchers studying viral inactivation overestimate the UV-C dose required to decontaminate N95 respirators (e.g., reported dose is higher than true delivered dose), then this can provide a margin of safety; however, if clinical staff overestimate the UV-C

Table 4.1: Common pitfalls in UV-C dose measurement for N95 decontamination

Pitfall	Examples
Wavelength mismatch between UV-C source and sensor	<ul style="list-style-type: none"> <li>• Sensor does not detect the UV-C germicidal wavelengths because sensor is specific for UV-A/UV-B wavelengths (280-400 nm).</li> <li>• Sensor is broadband and measures a range of wavelengths across the UV, visible, or infrared spectrum, making it impossible to determine the UV-C specific contribution to irradiance or dose without additional filters.</li> </ul>
Dose indicators or sensors with insufficient dynamic range	<ul style="list-style-type: none"> <li>• Photochromic dose indicator does not change color beyond 100 mJ/cm<sup>2</sup>.</li> <li>• Incident irradiance is not matched to the sensor dynamic range (e.g., irradiance is lower than the sensor noise floor or higher than the sensor saturation limit).</li> </ul>
Dose calculated using a single measured irradiance value	<ul style="list-style-type: none"> <li>• Irradiance is measured at a single time point but does not remain constant throughout the exposure period due to system-dependent variation in lamp output.</li> <li>• Irradiance measured at a single N95 location does not represent irradiance received across all surfaces of N95s located closer/farther from the UV-C source or closer/farther from reflective surfaces.</li> </ul>
Sensor with limited angular response	<ul style="list-style-type: none"> <li>• Incident UV-C is only partially collected by the radiometer (e.g., due to sensor housing or sensor field of view that is narrower than the UV-C source output).</li> </ul>
Dose calculated using rated UV-C lamp power	<ul style="list-style-type: none"> <li>• Identical UV-C lamp bulbs with identical make, model, and power ratings may have differing output efficiencies.</li> </ul>

dose delivered to N95 respirators during a decontamination cycle, then this could result in incomplete decontamination and create a transmission risk. Understanding the best practices in UV-C dose measurement can help users choose the most conservative UV-C measurement approach for their application.

Table 4.2: Importance of considering over- and under-reporting of UV-C dose

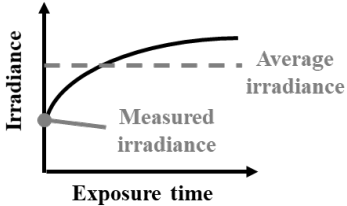
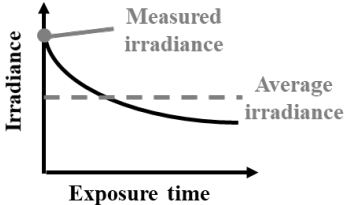
Problem		Underreporting UV-C dose <i>Measured or reported dose is lower than true delivered dose</i>	Overreporting UV-C dose <i>Measured or reported dose is higher than true delivered dose</i>
<p>How? <i>Example case listed; see Table 4.1 for additional pitfalls</i></p>		<p>Dose is calculated from a single irradiance measurement made at the start of the exposure period, but <b>lamp output increases throughout the exposure period as the lamp warms up</b>. The irradiance measurement underestimates the average irradiance over the exposure period, and thus reported (calculated) UV-C dose is lower than the true delivered dose.</p> 	<p>Dose is calculated from a single irradiance measurement made at the start of the exposure period, but <b>lamp output decreases throughout the exposure period due to air temperature changes</b>. The irradiance measurement overestimates the average irradiance over the exposure period, and thus reported (calculated) UV-C dose is higher than the true delivered dose.</p> 
<p>Implications <i>User is a...</i></p>	<p>Researcher studying the impact of UV-C on N95 viral inactivation</p>	<p>The researcher attributes measured viral inactivation to an artificially low UV-C dose.</p> <ul style="list-style-type: none"> <li>• Protocols based on these reported results can yield insufficient decontamination.</li> </ul>	<p>The researcher attributes measured viral inactivation to an artificially high UV-C dose.</p> <ul style="list-style-type: none"> <li>• Protocols based on these reported results may recommend unnecessarily high dose and unnecessarily increase decontamination time.</li> <li>• If insufficient viral inactivation was observed, report may incorrectly claim that reported dose is ineffective for N95 decontamination, potentially conflicting with other publications in which UV-C dose was measured accurately.</li> </ul>

Table 4.2: Importance of considering over- and under-reporting of UV-C dose

	<p>Researcher studying the impact of UV-C on N95 fit &amp; filtration</p>	<p>The researcher attributes measured N95 respirator damage to an artificially low UV-C dose.</p> <ul style="list-style-type: none"> <li>• The number of decontamination cycles an N95 can withstand prior to degradation is underestimated, leading to premature disposal of scarce resources.</li> </ul>	<p>The researcher attributes measured N95 respirator damage to an artificially high UV-C dose.</p> <ul style="list-style-type: none"> <li>• The UV-C dose (and number of decontamination cycles) N95s can withstand prior to degradation is overestimated, which may lead to application of damaging levels of UV-C to N95 respirators.</li> </ul>
	<p>Clinical staff implementing UV-C decontamination of N95s</p>	<p>Clinical staff underestimate the delivered dose during N95 decontamination treatments, exceeding the target dose for decontamination.</p> <ul style="list-style-type: none"> <li>• Inaccurate decontamination protocols are perpetuated.</li> <li>• N95 respirator may be damaged (if reported UV-C dose is severely underestimated).</li> </ul>	<p>Clinical staff overestimate the UV-C dose delivered to N95 respirators during a decontamination cycle.</p> <ul style="list-style-type: none"> <li>• Virus may persist due to insufficient UV-C dose delivery.</li> </ul>

Cell color indicates the level of safety risk posed by inaccurate UV-C dose measurements in different scenarios, where yellow denotes lower risk than red.

## Best Practices for UV-C Measurements and Methods

Because UV-C dose is the key metric used to link research to implementation, understanding the best practices for characterizing and reporting UV-C decontamination systems is critical for both the research and clinical communities. The measurement needs differ among communities (e.g., precise, quantitative UV-C dose readout may be valuable for researchers studying the effect of UV-C on pathogen inactivation or N95 respirator function, while clinical staff may solely need to verify that the UV-C dose applied to N95 respirators is within a specified range). However, a shared understanding of the factors impacting UV-C dose measurements is critical to allow users to accurately evaluate and implement UV-C methods for N95 respirator decontamination, in the context of current federal guidelines. Here, we outline key considerations for multiple user groups when studying, evaluating, or implementing UV-C N95 decontamination.

### **In Research**

Researchers developing or studying UV-C N95 respirator decontamination systems can support safe and effective UV-C N95 respirator decontamination both in the way they perform and report UV-C measurements. In making UV-C measurements, consider the implications of over- and under-estimating dose and choose the most conservative option (yellow cells in Table 4.2). For clinical staff to evaluate and reproducibly implement UV-C for N95 respirator decontamination, researchers and device manufacturers also must report in sufficient detail the way in which UV-C measurements were made [25]. Best practices, or “minimum reporting standards”, are common across scientific disciplines [42, 43]. These standards would be valuable for UV-C decontamination of N95 respirators. Standards should include physical specifications for both the UV source and the optical detector, along with necessary optical elements such as filters, diffusers, or cosine correctors. Data acquisition and analysis should also be explicitly reported, describing how dose was measured and calculated and how (or if) viral inactivation was verified. A list of suggested reporting parameters can be found in Appendix B. Thorough and standardized reporting provides a path to sidestep common pitfalls and realize the potential for UV-C to dramatically mitigate crisis-capacity conditions.

### **In Clinical Implementation**

In evaluating UV-C decontamination systems: When reading and interpreting research, it is important for users to understand how UV-C dose was measured and to critically evaluate the accuracy of reported UV-C dose. To ensure N95 respirator decontamination, data should establish UV-C-induced viral inactivation on the specific N95 model and in an enclosure that is comparable to that available at the workplace. To ensure that UV-C treatment does not reduce N95 respirator function, users should also assess whether preservation of respirator fit and filtration was evaluated, and they should consider how the applied UV-C dose compares to the maximum dose at which respirator integrity is expected to be maintained [11].

In implementing UV-C N95 decontamination protocols: UV-C decontamination should be used only during critical N95 shortages when in accordance with federal guidelines. UV-C dose should be regularly measured, particularly at locations receiving the highest and lowest dose, as the range of applied dose impacts decontamination efficacy and the number of times N95 respirators can be safely decontaminated prior to material degradation. The calibrated sensors used for these measurements should have narrow-band UV-C detection. Other factors that are important to consider when implementing N95 decontamination and reuse:

1. High UV-C exposure, whether through a single high-dose treatment or many UV-C cycles, can degrade respirator materials and reduce filtration efficacy [11]. Due to differences in material construction, the maximum dose that an N95 can withstand may be model-dependent.
2. Decontamination and multiple donning and doffing cycles can affect fit [44].

3. Shadowing and irradiation of surfaces non-perpendicular to the incident UV-C angle decrease the received dose and increase dose non-uniformity. For example, the lower viral inactivation efficacy observed on N95 facepieces with ridges has been attributed to shadowing [9]. The irradiance reaching shadowed surfaces will depend on the absorbance of the material in the optical path between the UV-C source and shadowed surface. Additionally, because irradiance depends on the angle of incident radiation [15], N95 respirator surfaces that are steeply sloped with respect to the incident UV-C will generally receive a lower UV-C dose (Figure 4.1A).
4. Soiling agents (saliva, oils) can modulate pathogen inactivation efficacy by reducing UV-C penetration into the respirator material [45, 46].
5. Viral inactivation can be N95 respirator model-dependent [9].
6. Other pathogens with lower UV-C susceptibility, especially bacterial spores, may remain active on N95 respirators even if the applied UV-C dose achieves viral inactivation [47–49].
7. Elastic straps may require a secondary decontamination method [9, 45].

## 4.2 Conclusions

Application of the appropriate UV-C wavelength and dose are critical metrics for reproducible UV-C N95 decontamination protocols under crisis-capacity conditions. Engaging vertically integrated teams with engineering, infection control/sterile-processing, and clinical expertise promotes technical validation and safe processing workflows. Full consideration of the technical and practical considerations of UV-C respirator N95 decontamination is key to more safely weathering pandemic-induced crisis capacity conditions.



# Bibliography

1. Centers for Disease Control and Prevention. *Decontamination and Reuse of Filtering Facepiece Respirators* <https://www.cdc.gov/coronavirus/2019-ncov/hcp/ppe-strategy/decontamination-reuse-respirators.html> (2020).
2. Bolton, J. R. & Linden, K. G. Standardization of Methods for Fluence (UV Dose) Determination in Bench-Scale UV Experiments. *Journal of Environmental Engineering* **129**, 209–215. ISSN: 0733-9372, 1943-7870. doi:10.1061/(ASCE)0733-9372(2003)129:3(209) (2003).
3. Memarzadeh, F., Olmsted, R. N. & Bartley, J. M. Applications of ultraviolet germicidal irradiation disinfection in health care facilities: effective adjunct, but not stand-alone technology. *American Journal of Infection Control* **38**, S13–24. ISSN: 1527-3296. doi:10.1016/j.ajic.2010.04.208 (2010).
4. U.S. Environmental Protection Agency & C. *Ultraviolet Disinfection Guidance Manual for the Final Long Term 2 Enhanced Surface Water Treatment Rule* tech. rep. EPA 815-R-06-007 (U.S. Environmental Protection Agency Office of Water, Washington, DC, 2006), 436.
5. U.S. Food & Drug Administration. *Code of Federal Regulations Title 21* tech. rep. 21CFR880.6600 (U.S. Food & Drug Administration, 2020).
6. Lowe, J. J. *et al.* *N95 Filtering Facepiece Respirator Ultraviolet Germicidal Irradiation (UVGI) Process for Decontamination and Reuse* tech. rep. (2020).
7. Centers for Disease Control. *Strategies for Optimizing the Supply of N95 Respirators* <https://www.cdc.gov/coronavirus/2019-ncov/hcp/respirators-strategy/index.html> (2021).
8. Fisher, E. & Shaffer, R. A method to determine the available UV-C dose for the decontamination of filtering facepiece respirators: UV-C decontamination of respirators. *Journal of Applied Microbiology* **110**, 287–295. ISSN: 13645072. doi:10.1111/j.1365-2672.2010.04881.x (2011).
9. Mills, D. *et al.* Ultraviolet germicidal irradiation of influenza-contaminated N95 filtering facepiece respirators. *American Journal of Infection Control* **46**, e49–e55. ISSN: 01966553. doi:10.1016/j.ajic.2018.02.018 (2018).

10. Tseng, C.-C. & Li, C.-S. Inactivation of Viruses on Surfaces by Ultraviolet Germicidal Irradiation. *Journal of Occupational and Environmental Hygiene* **4**, 400–405. ISSN: 1545-9624, 1545-9632. doi:10.1080/15459620701329012 (2007).
11. Lindsley, W. G. *et al.* Effects of Ultraviolet Germicidal Irradiation (UVGI) on N95 Respirator Filtration Performance and Structural Integrity. *Journal of Occupational and Environmental Hygiene* **12**, 509–517. ISSN: 1545-9624. doi:10.1080/15459624.2015.1018518 (2015).
12. Fischer, R. J. *et al.* Effectiveness of N95 Respirator Decontamination and Reuse against SARS-CoV-2 Virus. *Emerging Infectious Diseases* **26**. ISSN: 1080-6059. doi:10.3201/eid2609.201524 (2020).
13. Kohli, I. *et al.* UVC Germicidal Units: Determination of Dose Received and Parameters to be Considered for N95 Respirator Decontamination and Reuse. *Photochemistry and Photobiology* **96**, 1083–1087. ISSN: 1751-1097. doi:10.1111/php.13322 (2020).
14. Su, A. *et al.* Quantitative UV-C dose validation with photochromic indicators for informed N95 emergency decontamination. *PLOS ONE* **16**, e0243554. ISSN: 1932-6203. doi:10.1371/journal.pone.0243554 (2021).
15. Reifsnyder, W. E. Radiation geometry in the measurement and interpretation of radiation balance. *Agricultural Meteorology* **4**, 255–265. ISSN: 00021571. doi:10.1016/0002-1571(67)90026-X (1967).
16. Center for Devices and Radiological Health. *Recommendations for Sponsors Requesting EUAs for Decontamination and Bioburden Reduction Systems for Face Masks and Respirators During the Coronavirus Disease 2019 (COVID-19) Public Health Emergency* tech. rep. FDA-2020-D-1138 (Center for Devices and Radiological Health, 2020).
17. The National Personal Protective Technology Laboratory. *NPPTL Respirator Assessments to Support the COVID-19 Response* tech. rep. (The National Personal Protective Technology Laboratory, 2021).
18. Center for Devices and Radiological Health. *UV Lights and Lamps: Ultraviolet-C Radiation, Disinfection, and Coronavirus* Publisher: FDA. <https://www.fda.gov/medical-devices/coronavirus-covid-19-and-medical-devices/uv-lights-and-lamps-ultraviolet-c-radiation-disinfection-and-coronavirus> (2021).
19. Center for Devices and Radiological Health. *Enforcement Policy for Sterilizers, Disinfectant Devices, and Air Purifiers During the Coronavirus Disease 2019 (COVID-19) Public Health Emergency* tech. rep. FDA-2020-D-1138. Publisher: FDA (Food and Drug Administration, 2020).
20. Hinton, D. M. *STERIS STEAM DECON Cycle in AMSCO Medium Steam Sterilizers - Letter of Authorization* Letter of Authorization (Food and Drug Administration, 2020).
21. Hinton, D. M. *Battelle Decontamination System - Letter of Authorization*. Letter of Authorization (Food and Drug Administration, 2021).

22. Hinton, D. M. *Lumin LM3000 Bioburden Reduction UV System: Emergency Use Authorization Letter* Letter of Authorization (Food and Drug Administration, 2020).
23. Smith, J. S. *et al.* Effect of various decontamination procedures on disposable N95 mask integrity and SARS-CoV-2 infectivity. *Journal of Clinical and Translational Science* **5**. ISSN: 2059-8661. doi:10.1017/cts.2020.494 (2020).
24. Ozog, D. M. *et al.* The Effect of Ultraviolet C Radiation Against Different N95 Respirators Inoculated with SARS-CoV-2. *International Journal of Infectious Diseases*, 224–229. ISSN: 12019712. doi:10.1016/j.ijid.2020.08.077 (2020).
25. Poster, D. L. *et al.* Innovative Approaches to Combat Healthcare-Associated Infections Using Efficacy Standards Developed Through Industry and Federal Collaboration. *Proceedings of SPIE—the International Society for Optical Engineering* **10730**. ISSN: 0277-786X. doi:10.1117/12.2500431 (2018).
26. Kowalski, W. *Ultraviolet Germicidal Irradiation Handbook: UVGI for Air and Surface Disinfection* ISBN: 978-3-642-01999-9 (Springer Science & Business Media, Berlin, Heidelberg, 2010).
27. Beck, S. E. *et al.* Action spectra for validation of pathogen disinfection in medium-pressure ultraviolet (UV) systems. *Water Research* **70**, 27–37. ISSN: 1879-2448. doi:10.1016/j.watres.2014.11.028 (2015).
28. Blatchley III, E. R., Petri, B. & Sun, W. *SARS-CoV-2 UV Dose-Response Behavior* 2020.
29. Lytle, C. D. & Sagripanti, J.-L. Predicted Inactivation of Viruses of Relevance to Biodefense by Solar Radiation. *Journal of Virology* **79**, 14244–14252. ISSN: 0022-538X. doi:10.1128/JVI.79.22.14244-14252.2005 (2005).
30. McGuigan, K. G. *et al.* Solar water disinfection (SODIS): a review from bench-top to roof-top. *Journal of Hazardous Materials* **235-236**, 29–46. ISSN: 1873-3336. doi:10.1016/j.jhazmat.2012.07.053 (2012).
31. Horton, L. *et al.* Spectrum of virucidal activity from ultraviolet to infrared radiation. *Photochemical & Photobiological Sciences* **19**. Publisher: The Royal Society of Chemistry, 1262–1270. ISSN: 1474-9092. doi:10.1039/D0PP00221F (2020).
32. Lore, M. B. *et al.* Effectiveness of Three Decontamination Treatments against Influenza Virus Applied to Filtering Facepiece Respirators. *The Annals of Occupational Hygiene* **56**, 92–101. ISSN: 0003-4878. doi:10.1093/annhyg/mer054 (2011).
33. Narla, S. *et al.* The importance of the minimum dosage necessary for UVC decontamination of N95 respirators during the COVID-19 pandemic. *Photodermatology, Photoimmunology & Photomedicine*, phpp.12562. ISSN: 0905-4383, 1600-0781. doi:10.1111/phpp.12562 (2020).

34. Rutala, W. A. *et al.* Room decontamination using an ultraviolet-C device with short ultraviolet exposure time. *Infection Control and Hospital Epidemiology* **35**, 1070–1072. ISSN: 1559-6834. doi:10.1086/677149 (2014).
35. Rutala, W. A. *et al.* Rapid hospital room decontamination using ultraviolet (UV) light with a nanostructured UV-reflective wall coating. *Infection Control and Hospital Epidemiology* **34**, 527–529. ISSN: 1559-6834. doi:10.1086/670211 (2013).
36. Meulemans, C. C. E. The Basic Principles of UV-Disinfection of Water. *Ozone: Science & Engineering* **9**, 299–313. ISSN: 0191-9512. doi:10.1080/01919518708552146 (1987).
37. Reed, N. G., Wengraitis, S. & Sliney, D. H. Intercomparison of Instruments Used for Safety and Performance Measurements of Ultraviolet Germicidal Irradiation Lamps. *Journal of Occupational and Environmental Hygiene* **6**, 289–297. ISSN: 1545-9624, 1545-9632. doi:10.1080/15459620902801041 (2009).
38. Rahn, R. O., Xu, P. & Miller, S. L. Dosimetry of room-air germicidal (254 nm) radiation using spherical actinometry. *Photochemistry and Photobiology* **70**, 314–318. ISSN: 0031-8655 (1999).
39. tesa® 54140 UV Strips: Product Information <https://www.tesa.com/da-dk/files/download/2605120,1,tesa-54140-uv-strips-en-us.pdf>.
40. *Method Of Testing Ultraviolet Lamps For Use In HVAC And R Units Or Air Ducts To Inactivate Microorganisms On Irradiated Surfaces* tech. rep. ANSI/ASHRAE Standard 185.2-2014 (ANSI/ASHRAE).
41. ASTM International. *Standard Test Method for Determining Antimicrobial Efficacy of Ultraviolet Germicidal Irradiation against Influenza Virus on Fabric Carriers with Simulated Soil* ASTM standard E3179 - 18 (ASTM International, 2018).
42. Scrutinizing lasers. *Nature Photonics* **11**, 139–139. ISSN: 1749-4893. doi:10.1038/nphoton.2017.28 (2017).
43. A solar checklist. *Nature Photonics* **9**, 703–703. ISSN: 1749-4893. doi:10.1038/nphoton.2015.233 (2015).
44. Bergman, M. S. *et al.* Impact of multiple consecutive donnings on filtering facepiece respirator fit. *American Journal of Infection Control* **40**, 375–380. ISSN: 1527-3296. doi:10.1016/j.ajic.2011.05.003 (2012).
45. Heimbuch, B. & Harnish, D. *Research to Mitigate a Shortage of Respiratory Protection Devices During Public Health Emergencies* tech. rep. HHSF223201400158C (Applied Research Associates, Inc., 2019).
46. Fisher, E. M., Williams, J. & Shaffer, R. E. The Effect of Soil Accumulation on Multiple Decontamination Processing of N95 Filtering Facepiece Respirator Coupons Using Physical Methods. **27**, 11 (2010).

47. Lin, T.-H. *et al.* Relative survival of *Bacillus subtilis* spores loaded on filtering facepiece respirators after five decontamination methods. *Indoor Air*. ISSN: 1600-0668. doi:10.1111/ina.12475 (2018).
48. Rutala, W. A., Weber, D. J. & the Healthcare Infection Control Practices Committee (HICPAC). *Guideline for Disinfection and Sterilization in Healthcare Facilities, 2008* tech. rep. (Centers for Disease Control, 2019), 163.
49. Malayeri, A. H. *et al.* Fluence (UV Dose) Required to Achieve Incremental Log Inactivation of Bacteria, Protozoa, Viruses and Algae. *UV Solutions Magazine* **18** (2016).

## Chapter 5

# Quantitative UV-C dose validation with photochromic indicators for informed N95 emergency decontamination

Reproduced with permission from: A. Su\*, S. M. Grist\*, A. Geldert, A. Gopal, and A. E. Herr, "Quantitative UV-C dose validation with photochromic indicators for informed N95 emergency decontamination", *PLoS ONE*, 2021.

\*contributed equally.

### 5.1 Introduction

Ultraviolet (UV) light in the UV-C wavelength range is one of three promising methods identified by the United States Centers for Disease Control and Prevention (CDC) for N95 respirator (N95) decontamination as a shortage mitigation strategy during the COVID-19 pandemic [1]. Building upon years of literature evidence demonstrating that specific UV-C doses inactivate viruses while preserving respirator fit and filtration [2–5], UV-C decontamination of N95 respirators has become a rapidly expanding area of interest for both research and implementation [6]. However, effective UV-C bioburden reduction (while appearing straightforward) requires exquisite attention to detail in both treatment design and validation of treatment parameters. Challenges and intricacies of UV-C measurements can stymie study translation when UV-C dose measurements reporting viral inactivation are not robustly characterized. Innovation is urgently needed to introduce new measurement workflows that are both quantitatively robust and translatable across UV-C systems and facilities.

UV-C pathogen inactivation critically depends on two physical properties: wavelength

and dose (or fluence), where dose is defined as integrated irradiance over the exposure time. Longer UV-C wavelengths (240-280 nm) inactivate pathogens like SARS-CoV-2 by damaging their genetic material (absorption peak near 260 nm) [7] (Figure 5.1a); far (short-wavelength) UV-C also damages proteins [8]. Because UV-C decontamination relies upon pathogen interaction with electromagnetic radiation, efficacy depends on direct line-of-sight between the UV-C source and target surface. As is well established in the literature, UV-C irradiance, and therefore integrated dose, is attenuated throughout the thickness of an N95 respirator due to reflection, absorption, and scattering of UV-C photons as light passes through each porous N95 material layer (Figure 5.1b) [9]. Thus, in contrast to nonporous surfaces, effective decontamination of N95 respirators requires that the minimally acceptable UV-C dose is delivered not just to viral particles on the exterior surface, but also to those that may be embedded in interior N95 layers. Because integrating dosimeters into intact respirators is infeasible, decontamination efficacy throughout the N95 layers is typically measured in the peer-reviewed literature as a function of UV-C dose applied to the N95 surface. The established approach to quantify the minimum surface UV-C dose for N95 decontamination is to directly assess active virus recovered from throughout the N95 layers (e.g., using the TCID<sub>50</sub> assay) vs. surface dose [3, 10, 11]. On the majority of N95 models, studies (almost all of which used 254 nm low-pressure mercury light) support  $\geq 1.0 \text{ J/cm}^2$  UV-C dose across the entire N95 surface for  $\geq 3$ -log reduction of SARS-CoV-2 analogues [2, 4, 12]: a 100–1000 $\times$  higher dose than that required for non-porous surface decontamination [13].

Researchers have also used an augmented approach to measure UV-C attenuation through the N95 layers, then used this attenuation to scale the surface dose and quantify the inner-layer UV-C dose delivered to embedded viral particles [9]. Critically, measured attenuation varied by a factor of  $>100$  between N95 models [9]; furthermore, the wide variation in N95 morphology enhances inter-model differences in applied UV-C dose because irradiance depends on the incident angle following Lambert’s cosine law (Figure 5.1b) [15]. Likely because of the impact of both model-dependent attenuation and morphology on UV-C dose reaching the N95’s inner layers, UV-C viral inactivation efficacy on N95s varies between models [3, 4, 9].

UV-C measurement challenges are further exacerbated by radiometer complexities [16]. The accuracy and relative uncertainty of digital UV-C radiometers are established through calibration to a known standard (e.g., from the National Institute of Standards and Technology, NIST) [17]; however, accuracy is dependent on sensor linearity, spectral sensitivity, and angular response [16, 18] (Figure 5.1c). Though some countries have adopted standards for comparison between sensors [19], no universal standards exist [20]. Consequently, there is large variability between sensors in environments differing from the calibration setup, compromising replicability when detailed reporting is omitted. Furthermore, radiometers are costly, limited, low-throughput, and bulky, precluding measurements on complex 3D surfaces (which require fine spatial resolution and ideal angular response). As a result, UV-C dose is often not robustly characterized, and relative doses over a 3D N95 surface have not yet been empirically quantified using sensors rigorously validated for this application.

Photochromic, color-changing UV-C indicators (PCIs) for evaluating surface decontami-

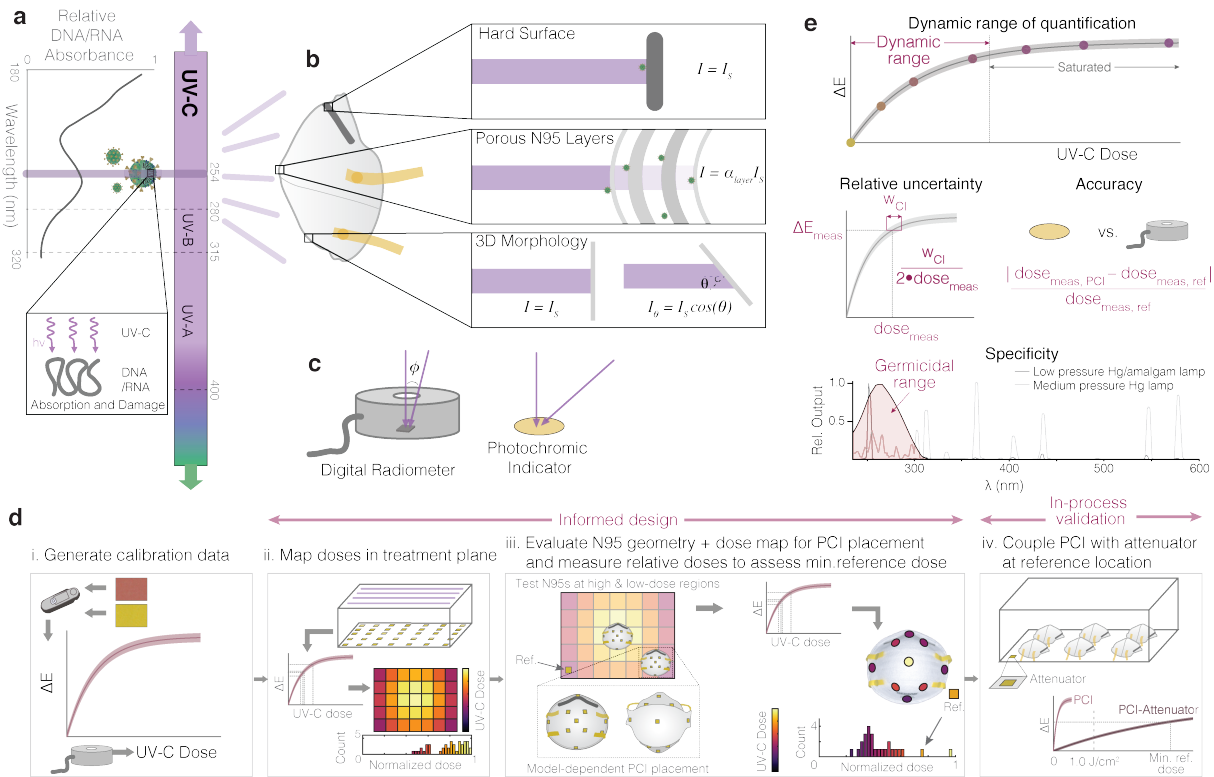


Figure 5.1: Mechanism and challenges of UV-C for N95 decontamination. (a) UV-C at 254 nm primarily inactivates pathogens by damaging genomic material (absorption peak near 260 nm). (b) The multilayer porous N95 materials and 3D morphology reduce the irradiance (and thus dose) available for pathogen inactivation compared to the irradiance that reaches nonporous surfaces ( $I_S$ ), like the metal nosepiece ( $\alpha_{layer}$  represents the layer-dependent attenuation factor). (c) UV-C detectors often have angle-dependent responses that differ from the ideal cosine response expected from a surface such as flat photochromic indicators. (d) The introduced workflow allows end users to both design and validate their UV-C systems, reducing source- and sensor-specific inaccuracies. Critically, assessment of treatment area dose nonuniformity informs N95 placement during on-N95 measurements; on-N95 measurements in turn determine minimum reference PCI doses that yield  $\geq 1.0 \text{ J/cm}^2$  to all N95 surfaces. On-N95 measurements are designed to specifically measure steep-angled or potentially shadowed N95 regions. (e) Robust UV-C measurements must meet key specifications, including dynamic range of quantification, relative measurement uncertainty (determined from error propagation from the confidence intervals on the calibration curve fit), measurement accuracy compared to a calibrated standard sensor, and specificity of the PCI response to the germicidal wavelength range (in order to accurately report germicidal activity). Nucleic acid absorbance spectrum modified from Voet *et al.* [14]. SARS-CoV-2 diagrams adapted from an image by Maya Peters Kostman for the Innovative Genomics Institute.



nation are commercially available and address challenges presented by digital sensors. Due to their low cost and small, flexible form factor, PCIs are ideal for characterizing UV-C uniformity and have been applied for this characterization in hospital rooms [21]. PCIs are intended for qualitative validation; however, there has been effort to quantify color change (a topic of broader interest [22–27]) to characterize water sterilization reactors [28].

In this work, we introduce a novel PCI-based dose quantification workflow (Figure 5.1a) for informed design and validation of UV-C N95 decontamination systems, and outline the steps below:

Step 1 (Figure 5.1d(i)): The first step of the workflow is to create a robust calibration curve of PCI color change as a function of dose, using a calibrated, NIST-traceable (or traceable to similar standards organization) radiometer. The tested doses should cover the full range of the PCI with sufficient data points to yield a well-defined calibration curve fit (we typically acquired data at 7-10 doses), with replicate indicators run at each dose. Color measurements of the PCIs exposed to each dose, along with unexposed and saturated reference indicators, should be acquired immediately (PCI color is often unstable after exposure) with a color measurement tool like a spectrophotometer or spectroradiometer. A more widely available imaging tool can also be used as long as (1) acquisition parameters are tightly controlled and held constant, (2) raw images are acquired, with the exposed PCI and reference within the same image, (3) the PCIs are isolated from ambient illumination, (4) images are not saturated, and (5) the measurement uncertainty on the color change ( $\Delta E$ ) has been quantified. Color differences between each PCI and the unexposed reference, as a function of measured UV-C dose, are calculated and fitted to a calibration curve as described in the Methods and “PCI quantification using colorimetry”. This calibration curve can then be applied to estimate UV-C dose from PCI color change in future experiments. Calibration should be confirmed after changes in condition (e.g., temperature, humidity) and after change in PCI shipment/lot.

Step 2 (Figure 5.1d(ii)): After the calibration curve is generated, relative exposures can be mapped across the UV-C treatment plane using either a single exposure of spatially arrayed PCIs or multiple exposures of a radiometer moved to each position in order to select the best representative N95 and reference positions for on-N95 measurements. To make these measurements, PCIs are placed in defined regions of the treatment plane and exposed to a quantifiable UV-C dose (as determined from the calibration curve of Step 1). UV-C dose at each location is estimated from the calibration curve based on the color difference between each exposed PCI and an unexposed reference PCI using the same acquisition criteria as described in Step 1. Variability around the treatment plane as well as the lowest- and highest-dose regions should be identified at this step, as demonstrated in Figure 5.14 of the main text. The active area of the treatment plane (area where N95s will ultimately be placed), as well as a reference location within the treatment plane (low-dose region that will not be shadowed by N95s during treatment), should be defined in this step. The inclusion of the reference facilitates translation from informed design to in-process validation in Step

4, when dose may be monitored using only a PCI at the reference location.

Step 3 (Figure 5.1d(iii)): 3D structure adds additional and significant variability to the UV-C dose delivered to N95 surfaces. Steep or shadowed surfaces will receive the lowest dose on a given object, so these regions should be identified on each model of N95 to be decontaminated. PCIs should be placed on these regions as well as regions expected to receive high doses (e.g., N95 apex). Note that the 3D structure, and therefore optimal PCI placement, is expected to be model-dependent (e.g., some models may have pleats that cause shadowing while others may have steeper morphology). To assess the full degree of variability in irradiance to which N95 surfaces may be exposed, representative N95s with PCIs affixed in the expected high and low-dose regions should be placed in the active regions of the treatment plane expected to have (1) the highest dose, and (2) the lowest dose (informed from Step 2). A PCI placed at the reference location during on-N95 measurement enables relative doses delivered to all N95 surfaces to be compared to those at the reference location. PCIs at all locations should be exposed to a UV-C dose within the indicator's quantifiable range. Using the color quantification workflow and calibration curve, relative doses delivered to N95 surfaces in the high and low-dose regions of the treatment plane can then be computed with respect to the dose at the reference location. From this relative dose information, the configuration of N95s within the treatment plane can be optimized to minimize on-N95 dose variation. Any adjustments to the N95 layout should be reanalyzed to determine the relative dose quantification in the adjusted setup. The minimum dose required at the reference location to ensure all N95 surfaces receive  $\geq 1.0$  J/cm<sup>2</sup> should also be assessed. For example, if the lowest-dose N95 region receives 25% of the dose delivered to the reference location, the reference indicator must receive  $\geq 4.0$  J/cm<sup>2</sup> in order for all N95 surfaces to receive at least the marginally effective dose of 1.0 J/cm<sup>2</sup>. This reference position and minimum dose can then be used for in-process validation of UV-C treatment.

Step 4 (Figure 5.1d(iv)): After identifying the reference indicator location and minimum dose the reference must receive to ensure all surfaces of the N95s receive  $\geq 1.0$  J/cm<sup>2</sup>, an indicator with sufficient dynamic range should be placed at that reference location during each and every UV-C treatment cycle to validate that the minimum reference dose is delivered to the reference location. To extend PCI dynamic range, optical attenuation can be coupled with PCIs (to reduce light reaching the PCI by a known factor, stretching the dynamic range of response to include the minimum reference dose).

We first demonstrate that PCI color quantification can yield UV-C-specific quantitative dose measurements with high accuracy (Figure 5.1d(i)). We then use this relationship between color change and UV-C dose to show how PCIs can be implemented by end users: high throughput dose mapping within the treatment plane (Figure 5.1d(ii)), combined with assessment of dose distribution across the N95 surface (Figure 5.1d(iii)) allow PCIs to highlight critical locations to monitor (both on-respirator and on the treatment plane) for informed design. Relative dose measurements using PCIs can then be made on N95s positioned in

the identified treatment locations (Figure 5.1d(iii)) in order to establish the minimum color change that reference PCIs on the treatment plane must undergo for all N95 surfaces to receive  $\geq 1.0$  J/cm<sup>2</sup>. Finally, we study how the addition of optical attenuator materials in front of the PCIs can extend the quantifiable UV-C dose range to  $\geq 1.0$  J/cm<sup>2</sup> (Figure 5.1d(iv)), enabling the final critical step of the workflow: in-process dose validation at a characterized reference location during every decontamination cycle.

## 5.2 Materials and Methods

### UV-C sensors

A Model 308 data-logging UV radiometer equipped with a 254 nm sensor (Optical Associates, Inc., OAI) was used for all irradiance measurements. An ILT1254/TD UV-C (International Light Technologies, ILT) radiometer with a near-ideal cosine angular response was used for secondary validation of irradiance measurements. Both radiometers are NIST-traceable and were calibrated within 2 months of data collection. Dose was calculated from irradiance data measured by the OAI radiometer and data logging software over the exposure time:

$$\text{dose} = \sum_{t_{\text{exposure}}} (\text{Irradiance} \cdot \Delta t)$$

### UV-C sources

Two different Spectroline UV treatment systems (same dimensions) were used as the UV-C source for all experiments. The XL-1500 Spectrolinker (“System 2”) was equipped with six low-pressure mercury bulbs (BLE-1T155, uvebay.com). In order to record the dose delivered in this enclosure using the radiometer, the OAI meter was wrapped in UV-C blocking material (PVC) and placed along the back wall of the chamber. This meter was plugged into a Microsoft Surface Pro tablet wrapped in multiple layers of UV-C blocking materials positioned on the left-hand side of the chamber floor. The tablet was controlled remotely using TeamViewer to record irradiance values over time. All PCI dose-response curves were measured near the center of the chamber, beside the Surface tablet. In addition, a Spectroline HCL-1500 (with the same chamber materials and dimensions as System 2, referred to as “System 1”) equipped with six low pressure amalgam bulbs (BLE-1T155, Spectroline) was generously donated by Spectroline with a small notch in the door to accommodate a sensor cable. With this modified instrument, data logging could be performed with the meter and tablet outside of the UV-C chamber.

### UV-C dose-response of PCIs

Commercial PCIs marketed for UV-C detection from two different companies were assessed: UVC 100 Dosimeter Dots from Intellego (‘PCI1’) and Control-Cure<sup>®</sup> UV-C Intensity Labels (N010-004) from UV Process Supply (‘PCI2’). Dose measurements were quantified by

integrating irradiance measurements logged by the OAI radiometer over time using a custom Python script. PCIs were placed on a plastic container of similar height to the sensor (16 mm). The irradiance at the PCI location was verified to be within 0.01 mW/cm<sup>2</sup> of the irradiance at the radiometer location prior to measurements. PCIs were cut into pieces and a single sample was placed on either the digital sensor or plastic container and exposed during bulb warm-up to serve as a saturated reference. D65/10° L\*a\*b\* measurements of both saturated and unsaturated reference PCIs were recorded using an RM200QC spectrophotometer (X-Rite). After bulb warm-up, sample PCIs were irradiated for a set amount of time using the “time” operating mode of the UV-C treatment system. After UV-C exposure, the color of the exposed PCI was immediately (within 5 min) assessed using the RM200QC spectrophotometer (set to report the average of three measurements of each sample).

## Quantifying dose-response curves of PCIs

D65 L\*a\*b\* measurements of PCI color assessed using the RM200QC spectrophotometer, along with UV-C doses (integrated from irradiance measurement logs of the radiometer readings) were compiled into a spreadsheet format using custom Python scripts, and then analyzed in MATLAB<sup>®</sup> using scripts custom-written for this application. In order to minimize the impact of imaging/measurement conditions on the PCI color measurement, color difference from an unexposed PCI was assessed in all cases, rather than absolute PCI color. There are a range of color difference metrics [29], and for this work we quantified and compared several.

CIELAB (1976) color difference was computed as the Euclidean distance between the L\*a\*b\* values of the exposed (E) and reference (unexposed, R) PCIs:

$$CIELAB \Delta C = \sqrt{(\Delta L^*)^2 + (\Delta a^*)^2 + (\Delta b^*)^2}$$

$\Delta L^*$ ,  $\Delta a^*$ , and  $\Delta b^*$  are the differences between the exposed and reference sensor L\*a\*b\* coordinates. Similarly, the L\*a\*b\* colors were converted to the RGB color space using built-in MATLAB functions and the Euclidean RGB color difference was computed as:

$$RGB \Delta C = \sqrt{(\Delta R)^2 + (\Delta G)^2 + (\Delta B)^2}$$

Similar to the L\*a\*b\* color space,  $\Delta R$ ,  $\Delta G$ , and  $\Delta B$  are the differences between the exposed and reference RGB coordinates. We also plotted, as a function of exposure dose, the differences in individual components  $\Delta R$ ,  $\Delta G$ , and  $\Delta B$ , as well as differences in lightness ( $\Delta L^* = L^*_E - L^*_R$ ), chroma ( $\Delta C^* = C^*_E - C^*_R$ ), and the CIE 1976 Metric Hue Difference ( $\Delta H^* = s\sqrt{2 \cdot (C^*_E C^*_R - a^*_E a^*_R - b^*_E b^*_R)}$ ), where  $s = 1$  if  $a^*_R b^*_E > a^*_E b^*_R$  and -1 otherwise [29].

We compute red, green, and blue channel colorimetric absorbance as [25]:

$$Abs_{RGB} = -\gamma \log(I_{RGB}/I_{RGB,0})$$

where  $\gamma$  is the device-dependent gamma correction factor,  $I_{RGB}$  is the red, green, or blue channel intensity of the exposed sensor and  $I_{RGB,0}$  is the respective channel intensity of the unexposed reference sensor.  $I_{RGB}$  was computed from the RM200QC-measured  $L^*a^*b^*$  values using the ‘lab2rgb’ MATLAB function with  $\gamma$  assumed to be 1. Finally, we computed the sets of equations for the CIEDE2000  $\Delta E$  color difference, as defined by Luo, Cui, and Rigg [30]. Our MATLAB implementation of CIEDE2000 was tested using the example color pairs presented by Luo, Cui, and Rigg [30], and found to yield the reported  $\Delta E$  values for the 10 sample-reference pairs.

## Extending the dynamic range of PCI

In order to assess the amount by which the dynamic range of the PCIs could be extended, two different filter materials were studied: a mounted 1.3 OD neutral density filter (NDUV13A, Thorlabs) and 1.10 mm-thick Borofloat<sup>®</sup> glass specified with 80/50 scratch/dig (Precision Glass & Optics). PCIs were placed on the plastic container underneath the filter material while the radiometer recorded unfiltered irradiance over time. UV-C transmission was measured using the OAI digital radiometer and calculated as the peak irradiance through the filtering material divided by the peak irradiance in the absence of filtering material.

## Characterizing variability across the treatment plane

A 279.4 mm  $\times$  431.8 mm paper grid with 63.5 mm-spaced markings was centered on the floor of the treatment plane. After bulb warm-up, the digital UV-C radiometer was placed at specified grid locations and peak irradiance was recorded over 15–20 s. The irradiance at the center of the treatment plane was verified to remain constant every 3–6 measurements to minimize variability caused by bulb output changes. The irradiances at all designated spatial locations were measured in triplicate. For PCI measurements (performed in duplicate), indicators were secured to the spatial locations on a copy of the 63.5 mm grid using double-sided tape. The grid was then inserted into the treatment system atop the master grid. The digital radiometer was placed in its designated location for data logging (offset from center). After exposure, PCIs were transferred to a consolidated layout for RM200QC analysis and measured within  $\sim$ 15 min.

## Quantifying unknown doses using PCIs

In order to quantify unknown UV-C doses (e.g. across the treatment plane of the UV-C exposure system, or across the surface of an N95 respirator), color measurements from the RM200QC were read in from a spreadsheet into a custom MATLAB script. Previously generated calibration datasets (CIEDE2000  $\Delta E$  measured with the same instrument vs. known UV-C dose, as described in “Quantifying dose-response curves of PCIs” above) were read in and fitted with the calibration functions described. For each measurement, the  $L^*a^*b^*$  color values for the exposed PCI and unexposed PCI reference (measured on the

same day with the same instrument) were read in and the CIEDE2000  $\Delta E$  between this pair was computed as previously described. The UV-C exposure dose was predicted from the CIEDE2000  $\Delta E$  using the calibration curve. First, the inverse of the fit function was used to predict the dose from the color change. For the fit function corresponding to first-order reaction kinetics:

$$\text{dose}(\Delta E) = -b \cdot \ln(1 - \Delta E/a)$$

For the fit function corresponding to second-order reaction kinetics:

$$\text{dose}(\Delta E) = \frac{\Delta E}{1/2 \cdot a^2 \cdot b - a \cdot b \cdot \Delta E}$$

To estimate the uncertainty on the predicted dose measurement ( $u_{\text{dose}}$ ), methods for estimating uncertainties of calibrated values via propagation of error, along with uncertainties on the fitted parameters (standard deviations  $s_a$  and  $s_b$ ) and  $\Delta E$  measurement (standard deviation  $s_{\Delta E}$ ), were used to estimate the variance of the measured value  $u_{\text{dose}}^2$  [31]:

$$u_{\text{dose}}^2 = \left(\frac{\delta \text{dose}}{\delta a}\right)^2 s_a^2 + \left(\frac{\delta \text{dose}}{\delta b}\right)^2 s_b^2 + \left(\frac{\delta \text{dose}}{\delta \Delta E}\right)^2 s_{\Delta E}^2 + 2 \left(\frac{\delta \text{dose}}{\delta a}\right) \left(\frac{\delta \text{dose}}{\delta b}\right) s_{ab}$$

where  $s_{ab}$  denotes the covariance between  $a$  and  $b$ . To complete this computation,  $s_a$ ,  $s_b$ , and  $s_{ab}$  were computed from the curve fit covariance matrix, and the partial derivatives of the inverse fit functions used in the computation are as described in Table 5.1.

Table 5.1: Fit functions, inverse fit functions, and partial derivatives used in uncertainty calculations for calibrated measurements.

Fit type	First-order	Second-order
Fit function	$\Delta E = a \left\{ 1 - e^{-\frac{\text{dose}}{b}} \right\}$ .	$\Delta E = \frac{\frac{1}{2} a^2 \cdot b \cdot \text{dose}}{1 + a \cdot b \cdot \text{dose}}$
Inverse fit function	$\text{dose}(\Delta E) = -b \cdot \ln(1 - \Delta E/a)$	$\text{dose}(\Delta E) = \frac{\Delta E}{1/2 \cdot a^2 \cdot b - a \cdot b \cdot \Delta E}$
$\frac{\delta \text{dose}}{\delta a}$	$\frac{-b \cdot \Delta E}{a^2 - a \cdot \Delta E}$	$\frac{4 \Delta E (\Delta E - a)}{b \cdot a^2 (a - 2 \cdot \Delta E)^2}$
$\frac{\delta \text{dose}}{\delta b}$	$-\ln(1 - \Delta E/a)$	$\frac{-2 \cdot \Delta E}{a \cdot b^2 \cdot (a - 2 \cdot \Delta E)}$
$\frac{\delta \text{dose}}{\delta \Delta E}$	$\frac{b}{a - \Delta E}$	$\frac{2}{b \cdot (a - 2 \cdot \Delta E)^2}$

The  $\Delta E$  measurement uncertainty  $s_{\Delta E}$  was measured from the standard deviation of 15 replicate measurements of unexposed PCI1 or PCI2 using the RM200QC, each compared to the same measurement of an exposed (saturated) PCI1 or PCI2, respectively. To understand the uncertainty on each type of color quantification, this standard deviation was calculated for color quantification via CIEDE2000  $\Delta E$ , CIELAB 1976  $\Delta C$ , RGB  $\Delta C$ ,  $\Delta R$ ,  $\Delta G$ ,  $\Delta B$ ,  $\Delta L$ ,  $\Delta C$ ,  $\Delta H$ , and colorimetric absorbances  $Abs_R$ ,  $Abs_G$ , and  $Abs_B$ . The resulting uncertainties are presented in Table 5.2.

Table 5.2: RM200QC measurement uncertainties  $s_{\Delta E}$  for various metrics of color quantification and two PCI models. Each uncertainty reports the standard deviation of  $N = 15$  measurements of replicate unexposed PCIs. We observe higher measurement uncertainty for unexposed PCI1, which we attribute to heterogeneity (dots and striations) in the colored PCI coating.

Model	CIEDE2000	$\Delta C_{CIELAB}$	$\Delta C_{RGB}$	$\Delta R$	$\Delta G$	$\Delta B$	$\Delta L$	$\Delta C$	$\Delta H$	$Abs_R$	$Abs_G$	$Abs_B$
PCI1	0.273	1.215	0.010	0.0063	0.0029	0.011	0.263	1.443	1.227	0.0029	0.0015	0.012
PCI2	0.083	0.397	0.0020	0.0015	0.0015	0.0071	0.106	0.450	0.495	$6.66 \times 10^{-4}$	$7.13 \times 10^{-4}$	0.014

Ninety-five percent confidence intervals (CIs) for predicted doses from each curve fit ( $\alpha = 0.05$ ) were predicted from the estimated variance ( $u_{dose}^2$ ) as [32]:

$$CI = \text{dose}_{\text{meas}} \pm \sqrt{u_{dose}^2} \cdot t_{1-\alpha/2, \nu}$$

where  $t_{1-\alpha/2, \nu}$  is the student's t-inverse cumulative distribution (tinv in MATLAB<sup>®</sup>), and  $\nu$  is the degrees of freedom for the calibration curve fit. The relative widths of these 95% CIs (normalized to the measured dose) are thus:

$$CI_{\text{rel}} = \frac{2(\sqrt{u_{dose}^2} t_{1-\alpha/2, \nu})}{\text{dose}_{\text{meas}}}$$

In experiments where triplicate PCI measurements of unknown doses were acquired and quantified using the calibration curve process described above, the measured doses were first equalized by correcting with a factor related to the dose logged by the radiometer during each exposure to correct for differences in the exposure time/dose between replicate measurements. To perform this correction, the doses measured from the PCI color change (as well as the confidence intervals and standard deviation of the measured value  $\sqrt{u_{dose}^2}$ ) were multiplied by a target dose (constant across the replicate datasets) and divided by the logged OAI radiometer dose. After correcting for differences in the dose to which the PCIs were exposed, the uncertainty estimated from the standard deviation of the replicate measurements was combined with the uncertainty from the calibration fit measurements by root sum of squares:

$$u_{\text{total}} = \sqrt{u_{dose}^2 + u_{rep}^2}$$

where  $u_{dose}^2$  is as described above, and  $u_{rep}^2$  is the squared standard deviation of replicate measurements. For several datasets, dose measurement data are presented as relative doses ( $dose_{norm}$ ), normalized to measurements at a different location or in a different experimental setup:

$$dose_{norm} = \frac{dose_{meas}}{dose_{ref}}$$

For these normalized measurements, the uncertainty is calculated from the uncertainties on both the measured and reference estimated doses via propagation of error as follows:

$$u_{norm} = |dose_{norm}| \sqrt{\left(\frac{u_{total,meas}}{dose_{meas}}\right)^2 + \left(\frac{u_{total,ref}}{dose_{ref}}\right)^2}$$

Measured doses were plotted as heatmaps and histograms using the ‘inferno’ perceptually uniform, colorblind-friendly colormap, which was created by Stéfan van der Walt and Nathaniel Smith and adapted from Python’s matplotlib for use in MATLAB<sup>®</sup> by Ander Biguri [33].

## PCI response to non-germicidal light

A 300 nm longpass filter (#46-417, Edmund Optics) was used to assess the reactivity of the PCIs to wavelengths longer than the germicidal (200–280 nm) UV-C range. For each experiment, one PCI was placed beneath the longpass filter on top of the plastic container and one PCI was placed on the digital sensor as an unfiltered control. Post-exposure color was measured using the RM200QC. In order to assess the reactivity of the PCIs to sunlight, both models of commercial PCI were taped to the same white background using double-sided tape and covered with black cardstock during transport outside. The exposure to sunlight began at 17:50 on May 30<sup>th</sup>, 2020 in Berkeley, CA, USA, when the UV index [34] was reported as 1 by Apple Weather. The color change was recorded over 5 min via iPhone 8 video. Both pre- and post-exposure PCIs were imaged using a Nikon D5500 and quantified using the RM200QC.

## Measuring dose received by N95 respirator surface

PCIs were affixed to the appropriate location on the surface of a NIOSH-approved Gerson 1730 N95 respirator using double-sided tape. Due to the limited dose range of the PCIs, preliminary experiments were conducted to determine an exposure time that caused all PCIs to change color within the dynamic range of the color calibration curves. For all but one condition, the exposure time was set for 8 s. For two exposures using PCI2 to quantify dose on a peripheral N95, the time was set for 19 s to take advantage of more of the PCI2 indicators’ range. These differences in exposure were compensated for in the analysis workflow described in “Quantifying unknown doses using PCIs” above. The respirator was positioned in its marked location within the UV-C source (either center or periphery). In



the center, the straps were spread away from the respirator to minimize shadowing. For measurements of the respirator on the periphery of the treatment plane, the straps were taped together and tucked under the respirator. The OAI radiometer, with a corresponding PCI on top, was placed in its designated location for irradiance logging. The color of all PCIs after exposure was recorded using the RM200QC.

## Assessing alternative imaging systems (iPhone, flatbed scanner, and digital SLR)

After each PCI exposure, the exposed indicator was imaged between unexposed and saturated references with the iPhone and Nikon D5500 within a FotodioX LED Studio-in-a-Box (FOSIAB2424, B&H) with the grey background installed. A platform was frequently inserted underneath the grey background to raise the PCIs closer to the cameras. The included diffuser sheet was cut and installed to cover the LED lights but not the top hatch. Within the Studio-in-a-Box, raw images of the PCIs were acquired using a Nikon D5500 equipped with a 40 mm macro lens or using Halide on an iPhone X at 2× optical zoom. The settings for both cameras were set manually and kept consistent within each experiment. At the conclusion of each experiment, the PCIs were scanned using VueScan, set to acquire raw images, on a flatbed scanner (LiDE 400, Canon).

## Color quantification from different imaging systems

In order to compare color quantification from the RM200QC spectrophotometer ‘gold standard’ tool with that from more widely available imaging devices, images of the PCIs acquired with multiple imaging devices were compared. For iPhone and DSLR images, a set of images (one for each exposed PCI) was acquired, each containing the exposed PCI between an unexposed and saturated PCI, with nearby white-balance region and Pantone<sup>®</sup> color match to the exposed PCI. For the flatbed scanner images, a single image of all of the exposed PCIs from a dose-response experiment, along with a single unexposed and single saturated PCI, was acquired on a white background. iPhone and DSLR images were acquired after each PCI exposure; scanner images were acquired once all PCI exposures in an experiment were complete. Raw images (.DNG for iPhone X, .NEF for DSLR, .TIF for flatbed scanner) were acquired and converted to .TIF format to be read into MATLAB<sup>®</sup> and analyzed using custom scripts.

In the image analysis script, each image was read in sequentially and the user prompted to draw rectangular areas over (a) the exposed PCI, (b) the Pantone<sup>®</sup> match to the PCI, (c) the white region proximal to the PCI(s), (d) the unexposed PCI, and (e) the saturated PCI. In all cases, care was taken to draw a region encompassing only the region of interest (i.e., not edges, dust, or shadowed regions). For the camera images (an image for each PCI), all 5 regions were denoted on each image (for each exposed PCI). For the scanner images (a single image for all PCIs), a single region was denoted for the white, unexposed, and saturated regions, respectively, and used in the analysis for all exposed PCIs in one experiment, with

only the PCI region denoted for each exposure dose (Pantone<sup>®</sup> matches were not scanned). After all regions on each image were selected, the average RGB value for the white region was used to white-balance and exposure-correct the image before computing the average RGB values for the other region types. The RGB value for each region was then converted to the L\*a\*b\* color space using MATLAB<sup>®</sup>'s built-in `rgb2lab` function. RGB and L\*a\*b\* values from the processed images were then subjected to the same processing for color difference calculations as described above for the measured RM200QC L\*a\*b\* values in "Quantifying dose-response curves of PCIs".

CIEDE2000 color differences from an unexposed PCI, computed from each image type as well as the RM200QC measurements of the same set of PCIs, were fitted to the appropriate calibration function and plotted (along with 95% prediction intervals) as a function of exposure dose, in order to compare the relative dose-responses and calibration uncertainties measured with each tool. The squared sum of the residuals from the curve fit (SSE) for each dataset was computed and compared as a metric of calibration robustness for each color readout method.

## Visualizing reduced UV-C transmission through permanent marker ink

To demonstrate spatially resolved measurement, we visualized the UV-C shadowing abilities of permanent marker ink. The "Cal" university logo was drawn with Sharpie<sup>®</sup> permanent marker on a UV-C-transmissive ( $\sim 82\%$  transmittance) plastic plate sealer adhesive film. The plastic film with permanent marker logo was then placed atop a PCI1 indicator within the UV-C treatment plane and exposed to UV-C for  $\sim 10$  s (applied UV-C not precisely controlled for this qualitative test). After exposure, the film and exposed PCI were imaged using the flatbed scanner.

## Assessing temporal fluctuations in irradiance

Irradiances over time logged using the OAI radiometer either during system warm-up or during long-exposures after warm-up were parsed from the output .txt files using a custom Python script and read into MATLAB<sup>®</sup>. Warm-up datasets approximated the variance that would be present in applied conditions because the time since previous use was not controlled (the datasets began with the lamps in varying states of warm-cool). Each dataset was analyzed to automatically detect the iteration ( $i_{end}$ ) at which lamp shutoff occurred (from the change from the previous measurement). The irradiance data were plotted until 2 measurements prior to that measurement iteration ( $i_{end-2}$ ). For the system warm-up datasets, warm-up rise time was computed as the time for the irradiance to rise from 10% of the maximum recorded value to 90% of the maximum recorded value. For the long exposure datasets, the output degradation was assessed by extracting the irradiance degradation slope from linear least-squares curve fitting.

The estimated time to reach  $1.0 \text{ J/cm}^2$  from each exposure was computed as the target dose ( $1.0 \text{ J/cm}^2$ ) divided by the mean irradiance. To assess the effects of temporal instability of the lamp output, this calculation was computed for both a mean irradiance at the beginning of each exposure (taking the mean irradiance over the 10<sup>th</sup> to 20<sup>th</sup> iterations of the data logger) and a mean irradiance at the end of each exposure (taking the mean irradiance over the last 11 iterations prior to the detected end point ( $i_{end}$ , automatically detected from lamp shutoff as described above)).

## Optical simulation

To determine the spatially dependent Rad1 correction factor, colleagues at NIST modelled our specific UV-C source and sensor in Zemax OpticStudio Pro (Version 19.4 SP2). The UV-C bulbs were simulated using known radiation patterns of T8 bulbs. The radiometer was simulated using known physical characteristics of the actual sensor such as the height of the aperture and the angular response of the photodetector, which were furnished by the manufacturer. Monochromatic spectral bandpass at 254 nm was assumed. Since the angular response was only measured up to an angle of incidence of  $55^\circ$  by the manufacturer, the response to angles  $>55^\circ$  was extrapolated using a Gaussian fit in Labview.

## Radiometer correction factor validation using mask/aperture setup

To validate the correction factor determined using optical simulations, a black cardstock-lined cardboard insert was used to block all emitted UV-C light within the treatment system except for a precisely positioned 6.35 mm diameter aperture. The virtual calibration was repeated with only one source bulb. Within the simulation, a mask containing a 6.35 mm diameter aperture was positioned directly below and centered on the virtual bulb. This mask/aperture setup for the experimental setup was mimicked using cardboard, black cardstock, and an Iris Diaphragm (M-ID-1.0, Newport) with aperture set to  $\sim 6.35$  mm diameter. All but 2 bulbs were removed from the physical UV-C source (2 bulbs were required for operation). The mask/aperture was arranged in the UV-C treatment system such that the aperture was centered directly below one bulb and the mask bolstered using popsicle sticks kept vertical using sticky tack. In order to minimize contributions of the second bulb to the irradiance measurements, a strip of black cardstock was vertically affixed to the side of the aperture in between the two bulbs. Minimal crosstalk was validated as  $\leq 0.01 \text{ mW/cm}^2$  difference in irradiance measured at equidistant offsets from the sensor position below the aperture perpendicular to the long axis of the bulbs.

### 5.3 Results and Discussion

UV-C dose measurements are frequently the only link between viral inactivation studies and implementation of each decontamination cycle. Decontamination efficacy and safety consequently depend on robust UV-C measurements, defined by several critical metrics (Figure 5.1e) for which we establish and describe marginal and ideal values (Table 5.3).

Table 5.3: Specifications for robust UV-C measurements

Number	Metric	Units	Marginal Value	Ideal value
1	Dose measurement range (in-process validation)	J/cm <sup>2</sup>	≥1.0	> 3.0
2	Dose measurement range (informed design)	J/cm <sup>2</sup>	> 0.1	> 0.3
3	Relative uncertainty on dose measurement (CI)	%	<20	< 10
4	Accuracy	%	> 80	> 90
5	Sensitivity to non-germicidal longer wavelengths	%	< 5	< 1

1. The marginal dose measurement dynamic range for in-process validation ( $\geq 1.0$  J/cm<sup>2</sup>) is based upon the marginally acceptable dose to be delivered to each and every N95 surface for  $\geq 3$ -log inactivation of enveloped viruses [2, 4, 12]. Ideally, the measurement range would be higher ( $> 3.0$  J/cm<sup>2</sup>) as the reference sensor will likely receive a higher dose than the lowest N95 surface surface dose due to shadowing and model-dependent angles of the N95 surfaces.
2. The necessary dose measurement dynamic range for informed design, which uses relative dose measurements, can be lower than that for in-process validation. The marginal value of  $> 0.1$  J/cm<sup>2</sup> was chosen to ensure that the UV-C exposure times for informed design  $> 1/10^{\text{th}}$  those for in-process validation. As the same UV-C exposure system is used for both informed design and actual decontamination, low dynamic range PCIs would require very short exposure times because the systems are designed to deliver  $\geq 1.0$  J/cm<sup>2</sup> during a reasonable exposure time. These short exposure times during informed design may (1) not be feasible or (2) introduce unacceptable run-to-run variability.
3. The calibration uncertainty for very well characterized UV-C radiometers is  $\sim 5\%$  [35], although many radiometers will not reach this level due to sources of error in UV-C measurements [36]. As measurement solutions like PCIs have advantages over even the best calibrated radiometers (e.g., form factor), we identified a marginal and ideal target for PCIs of 4 and 2 times the radiometer value, respectively. These values (20% and 10%, respectively) allow reasonable ‘safety factors’ of  $< 50\%$  to be implemented to ensure minimally acceptable doses are reached. Safety factors are multipliers on the target dose to take into account measurement uncertainty (e.g., for 20% total propagated uncertainty, a safety factor of 1.5 would ensure at least 1.5 J/cm<sup>2</sup> was delivered to all N95 surfaces).

4. Accuracy values (how well measurements align with a calibrated, NIST-traceable reference measurement) were chosen to align with target relative uncertainty.
5. Ideally, UV-C measurements for characterizing and validating decontamination should only report irradiance or dose within the germicidal range (UV-C extends to 280 nm; germicidal efficacy at 300 nm is <10% of that at 254 nm [37]). We selected marginal and ideal values such that the measurement response to >300 nm was 1-2 orders of magnitude less than that to <300 nm light from a commonly employed low-pressure mercury/amalgam source.

Here, we introduce a new technique using PCIs to address three critical challenges hindering UV-C decontamination processes: (1) accurate and high-throughput characterization of the UV-C treatment plane (Figure 5.1d(ii)), (2) spatially resolved dose quantification across complex 3D structures placed within the treatment plane (Figure 5.1d(iii)), and (3) translatable and reproducible in-process measurements to validate the dose of 1.0 J/cm<sup>2</sup> delivered to all N95 surfaces during every UV-C treatment cycle (Figure 5.1d(iv)).

## PCI quantification using colorimetry

PCIs have the potential to fill three urgent gaps in UV-C dose validation; however, a quantitative rather than qualitative readout strategy is required. To assess the indicators' suitability for contributing to informed design of UV-C treatment processes, we introduce a novel quantification workflow and demonstrate the capability to measure spatial heterogeneity within a UV-C treatment system from a single exposure. We first assessed whether UV-C dose could be quantified from the color change of commercially available PCIs; quantification relies upon distinct, reproducible color change that follows a known, predictable relationship. Measurement of color differences between the sample and a reference (rather than absolute colors) improves quantification robustness as the difference between two colors measured under the same conditions is less sensitive to many confounding effects [23, 29]. To test whether two models of commercial PCIs (Intellego UVC 100 Dosimeter Dots: 'PCI1', and UV Process Supply UV-C Intensity Labels: 'PCI2') could meet the specifications of Table 5.3, we exposed them to UV-C doses measured with a calibrated radiometer, quantified their endpoint color using an RM200QC spectrophotometer (outputting a single L\*a\*b\* color per PCI), and computed the CIEDE2000 [30] industry-standard color difference ( $\Delta E$ ) from an unexposed indicator as a function of UV-C dose (Figure 5.2a). Both PCI models showed visually discernable color change up to  $\sim 0.15$  J/cm<sup>2</sup>. PCI1 has a higher maximum  $\Delta E$  of  $\sim 45$  compared to  $\sim 25$  for PCI2 (Figure 5.2a). Higher maximum  $\Delta E$  will lead to lower relative uncertainty for a constant color difference measurement uncertainty. Additionally, we observe good reproducibility between batches of PCI1 (Figure 5.3).

We also scrutinized other metrics of color difference outlined in ASTM D2244-16 [29] and observed comparable dose-response data (Figure 5.4). The RGB and CIELAB  $\Delta C$ , as well as the CIE 1976 Metric Hue Difference ( $\Delta H$ ), showed strong dose-dependent response suggesting that any of these established metrics could be employed for PCI calibration. A previous

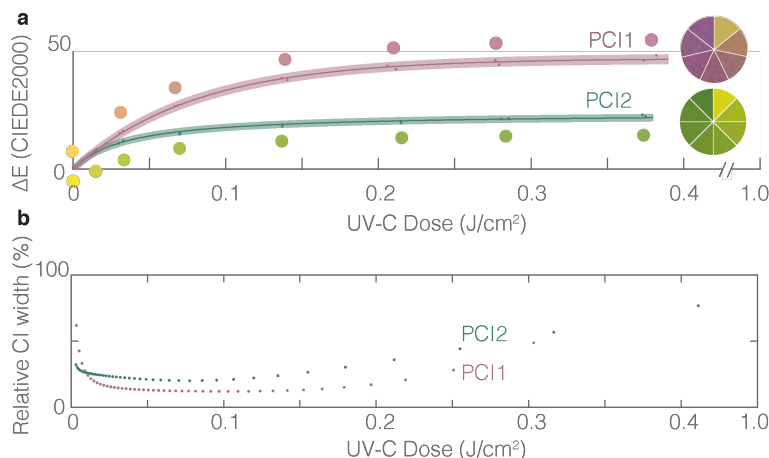


Figure 5.2: Robust color measurement facilitates UV-C dose quantification from two PCI models. (a) CIEDE2000 color difference between exposed and unexposed Intellego UVC Dosimeter Dot (PCI1, pink) and UV Process Supply UVC Intensity Label (PCI2, green) as a function of UV-C dose. Dose-responses for PCI1 and PCI2 were fit with a calibration function corresponding to first-order reaction kinetics (Eq. 5.1:  $R^2 = 0.998$ ;  $a = 47.1$  (46.1, 48.1);  $b = 80.4$  (74.6, 86.3); 95% confidence interval on fit parameters reported in parentheses) and second-order reaction kinetics (Eq. 5.2:  $R^2 = 0.992$ ;  $a = 47.7$  (45.9, 49.5);  $b = 0.00060$  (0.00049, 0.00072), respectively. PCI color depicted by the RM200QC-measured color values (circles) and digital SLR camera (DSLR) image swatches in the comparison wheels. Datapoints within the shaded region denote individual PCI measurements, line denotes best fit, and shaded region denotes 95% prediction interval on prediction of color change from observation of UV-C dose. (b) Relative quantification uncertainties using the PCI calibration workflow. Plots depict quantified 95% confidence intervals on UV-C dose measurements from CIEDE2000 color difference between exposed and unexposed PCIs, normalized to and as a function of UV-C dose.

study characterized an unspecified model of UV Process Supply PCI and defined a color difference metric as  $\Delta R + \Delta G$ ; these previous characterization data appeared to have higher variability than our measurements but with qualitatively similar saturation [28]. Our more robust quantification is likely due to (1) our use of a dedicated, contact color measurement tool instead of a camera [23, 38] and (2) our direct, logged measurements of UV-C dose to generate the calibration curve rather than modelled irradiance. As the CIEDE2000 metric [30] showed comparable dose-response to the other metrics and has been found to better correlate with perceptible color difference and outperform other color difference standards [39, 40], we chose to employ CIEDE2000  $\Delta E$  as the color difference metric for subsequent calibration and measurement in our characterization and application of the PCIs.

We next scrutinized whether fitting the  $\Delta E$  vs. dose data to a calibration function could predict UV-C dose from  $\Delta E$  with relative dose measurement uncertainty below the 10–20% thresholds of Table 5.3. We endeavored to define a calibration function mapping the color

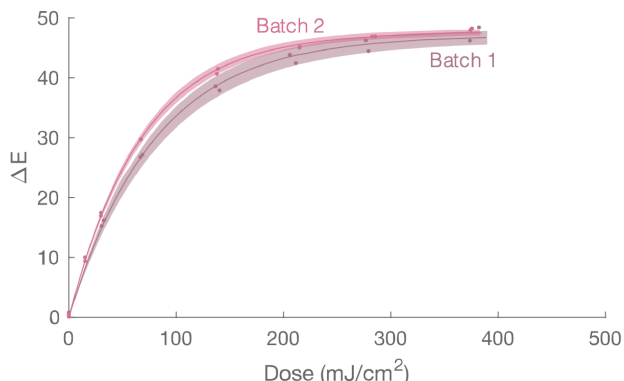


Figure 5.3: Comparison dose-response curves of two different batches of PCI1. For batch 1,  $R^2 = 0.9976$ ,  $a = 47.1$  (46.1, 48.1),  $b = 74.6$  (74.6, 86.3). For batch 2,  $R^2 = 0.9994$ ,  $a = 47.7$  (47.3, 48.2),  $b = 68.6$  (66.3, 70.8). Slight differences in dose-response data may be due to different batches of indicator, different environmental conditions, systems for UV-C exposure (all batch 2 sensors were exposed in System 1 whereas half of the batch 1 data were exposed in System 2), and potentially indicator color change during storage.

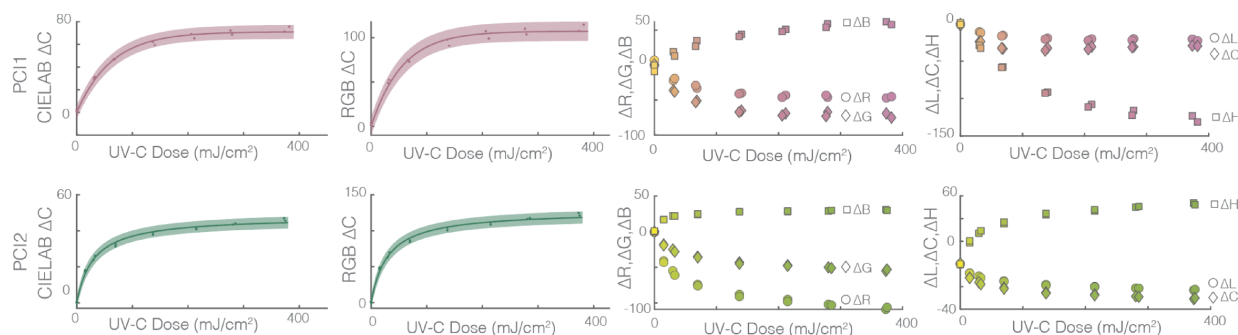
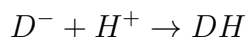
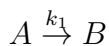


Figure 5.4: Comparison of alternative color difference metrics. Plots of alternate color difference metrics for PCI1 and PCI2, as a function of UV-C exposure dose. From left, the CIELAB 1976  $\Delta C$  (Euclidean), RGB Euclidean  $\Delta C$ , differences in each RGB component, and differences in each LCH component, are plotted for each PCI type. Differences in RGB and LCH components are plotted in the measured sensor color; 95% prediction intervals are plotted as the shaded regions on CIELAB and RGB  $\Delta C$ .

change of photochromic UV-C indicators to quantitative UV-C dose (fluence). For some types of UV indicator [41], the sensing mechanism involves one molecule (acid-release agent, ARAH) that is triggered by UV light to release a proton ( $H^+$ ), which then protonates another dye molecule ( $D^-$ ), resulting in a color change:



To design an appropriate calibration function to which to fit color change data (CIEDE2000 [30] color differences from an unexposed sensor) as a function of UV dose (dose), we hypothesized that, depending on the rate-limiting step of the reaction, one might be able to use functions based on expected product concentration from first- or second-order reaction kinetics. For first-order reaction kinetics [42]:



$$[B] = [A]_0(1 - e^{-k_1 t})$$

Assuming the color change is proportional to the concentration of product, and using the relationship that  $dose = irradiance \cdot t$ :

$$\Delta E \approx a \left\{ 1 - e^{-\frac{dose}{b}} \right\}$$

where  $b \equiv irradiance/k_1$ . We found that this first-order kinetics fit function fit the PCI1 color change data well. However, the fit was poorer for PCI2, with lower goodness-of-fit and poor visual agreement (Figure 5.5).

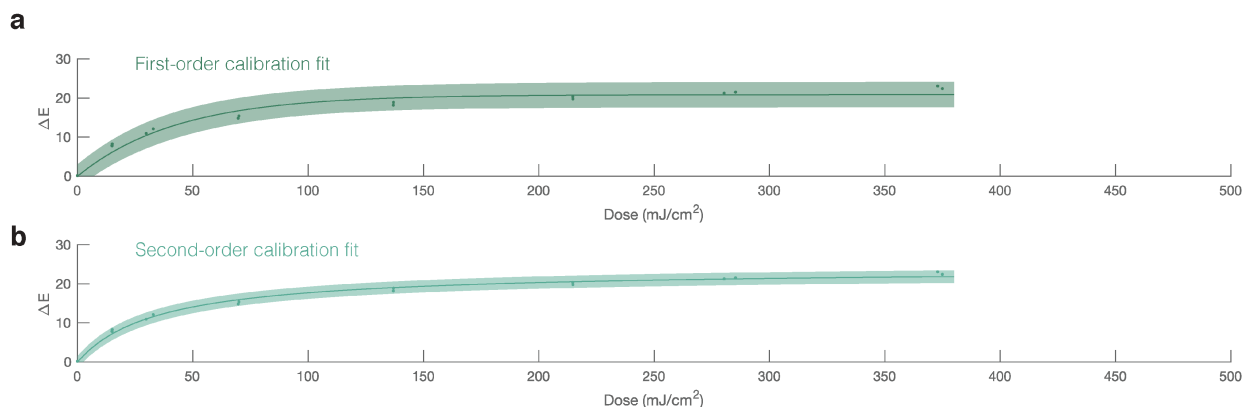


Figure 5.5: Comparison of calibration fit functions for PCI2 based on (a) first-order reaction kinetics and (b) second-order reaction kinetics for PCI2. Using the fit function corresponding to second-order reaction kinetics results in better fit and smaller prediction intervals. For the first-order fit (a),  $R^2 = 0.967$ ,  $a = 20.9$  (19.7, 22.0),  $b = 43.0$  (33.5, 52.6). For the second-order fit (b),  $R^2 = 0.992$ ,  $a = 47.7$  (45.9, 49.5),  $b = 0.00060$  (0.00049, 0.00072). In each plot, fitted data are represented as points, best fit lines are represented as solid lines, and 95% prediction intervals are plotted as shaded regions on each plot.

We hypothesized that a fit function derived from second-order reaction kinetics might yield better fit performance for PCI2. We first assessed the simplest type of second-order



reaction [42]:

$$\begin{aligned}
 A + A &\xrightarrow{k_2} B \\
 \frac{1}{[A]} &= \frac{1}{[A]_0} + k_2 t \\
 [A] &= \frac{[A]_0}{1 + [A]_0 k_2 t} \\
 [B] &= \frac{[A]_0 - [A]}{2} = \frac{[A]_0 \left\{ 1 - \frac{1}{1 + [A]_0 k_2 t} \right\}}{2} = \frac{\frac{1}{2} [A]_0^2 \cdot k_2 t}{1 + [A]_0 k_2 t} \\
 \Delta E &\approx \frac{\frac{1}{2} a^2 \cdot b \cdot \text{dose}}{1 + a \cdot b \cdot \text{dose}}
 \end{aligned}$$

This function based on second-order reaction kinetics better fits the PCI2 data (Figure 5.5).

Due to the two-stage reaction described by Mills, *et al.* [41], it may be more relevant to use an equation derived from consecutive first-order reactions [42]:

$$\begin{aligned}
 A &\xrightarrow{k_1} B \xrightarrow{k_2} C \\
 [C] &= [A]_0 \left\{ 1 + \frac{1}{k_1 - k_2} [k_2 e^{-k_1 t} - k_1 e^{-k_2 t}] \right\} \\
 \Delta E &\approx c \left\{ 1 + \frac{1}{a - b} [b e^{-a \cdot \text{dose}} - a e^{-b \cdot \text{dose}}] \right\}
 \end{aligned}$$

However, when this equation was applied to data from PCI1, the fitting algorithm could not robustly quantify all three fit parameters (with 10 points fitted and  $R^2=0.9993$ ; the 95% CI on fit parameter  $b$  extended from  $-1.3E+08$  to  $1.3E+08$ ). This was likely because fit parameter  $a$  (0.001398) was found to be much smaller than fit parameter  $b$  (2328), suggesting that the color change is limited by one of the constituent reactions (and thus may be approximated as a single first-order reaction). Similarly, when the fit for a consecutive first-order reaction was applied to PCI2, the second fit parameter was again poorly defined and the goodness-of-fit similar to that for the equation based on a single first-order reaction. Thus, for PCI1, we used the fit function corresponding to first-order reaction kinetics ( $a, b$  are fit parameters):

$$\Delta E = a \left\{ 1 - e^{-\frac{\text{dose}}{b}} \right\} \tag{5.1}$$

while for PCI2 used the fit function corresponding to second-order reaction kinetics:

$$\Delta E = \frac{\frac{1}{2} a^2 \cdot b \cdot \text{dose}}{1 + a \cdot b \cdot \text{dose}} \tag{5.2}$$

After fitting the calibration function to the CIEDE2000 vs. UV-C dose data, 95% prediction intervals on the fit were generated using the MATLAB ‘predint’ function, generating non-simultaneous observation bounds. The upper bound of this prediction interval, with the

addition of a safety factor, could be used to generate a color change threshold to determine whether a given UV-C dose (e.g.,  $1.0 \text{ J/cm}^2$ ) has been surpassed.

We note that although these fit functions serve as effective calibration functions with high goodness-of-fit, the current implementation does not facilitate extraction of reaction parameters (e.g., reaction order, reaction rate) from the curve fit because the relationship between CIEDE2000 and colored reaction product concentration is not known. While colorimetric absorbance data from commercial PCIs also show a UV-C dose response (Figure 5.6), the unknown chemical composition of the commercial PCIs confounds determination of reaction parameters. Colorimetric absorbance of dye on paper has been found to deviate from Beer’s Law [25], so careful calibration of colorimetric absorbance over a range of known dye concentrations is required to quantify concentrations or reaction kinetics from colorimetric absorbance on paper [43]. Nevertheless, adoption of colorimetric absorbance approaches will be useful to inform design of new optimized chemistries for PCI materials.

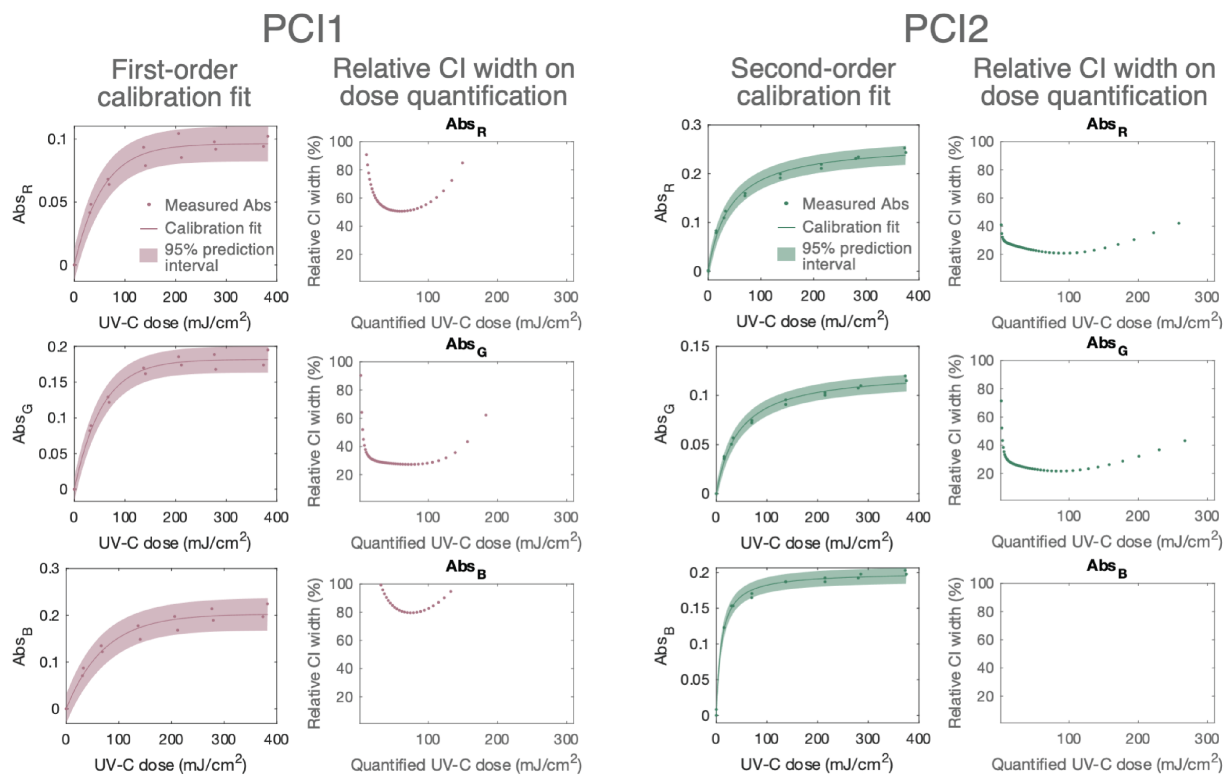


Figure 5.6: Calibration curve fit and relative uncertainty on measurements using red, green, and blue colorimetric absorbance. RGB colorimetric absorbances ( $Abs_R$ ,  $Abs_G$ ,  $Abs_B$ ) of PCIs computed from RM200QC spectroradiometer measurements show UV-C dose-response behavior. Relative CI widths, a measure of quantification uncertainty, vary depending on color channel and PCI model.

We assessed the precision of the measurement by comparing the width of the dose mea-

surement confidence intervals (CIs) to the respective dose values (Figure 5.2b). The relative 95% CIs on UV-C doses measured with the calibration function from known CIEDE2000 color differences were considerably larger for PCI2 than for PCI1, suggesting that PCI1 is better-suited to robust UV-C quantification using CIEDE2000. Dose quantification uncertainties are dependent on the  $\Delta E$  uncertainty, encompassing both the uncertainty of the measurement tool and the variability in PCI coating color. Using an experimentally determined  $\Delta E$  uncertainty of 0.273 for PCI1 and 0.083 for PCI2 (see Methods), we find that the two PCI models yield disparate relative uncertainties on the dose measurements. At a dose of  $\sim 0.1 \text{ J/cm}^2$ , the relative CI width (width of the CI divided by the measured dose) of PCI1 is 12.1%, equivalent to 6.05% relative uncertainty and meeting the  $<10\%$  ideal relative uncertainty target. At the same dose, the relative CI width of PCI2 is 21.2%, equivalent to 10.6% relative uncertainty. PCI2 thus does not meet the ideal relative uncertainty target but does meet the marginally acceptable 20% relative uncertainty target. PCI1 relative uncertainty remains  $<10\%$  up to  $\sim 0.20 \text{ J/cm}^2$ . We also quantify how the relative CI width on the PCI dose measurement varies with both measured dose and uncertainty on  $\Delta E$  (Figure 5.7). These results highlight the importance of quantifying the  $\Delta E$  measurement uncertainty in order to accurately predict PCI dose quantification uncertainty. The relative quantification uncertainty of PCI1, while higher than that established for calibration of UV-C radiometers under ideal conditions [35], should still facilitate dose quantification as long as appropriate safety factors on applied dose (i.e., a multiplier  $>1$ ) are included in the N95 treatment protocol to account for the propagated relative uncertainty in the dose measurement and ensure minimum doses are met.

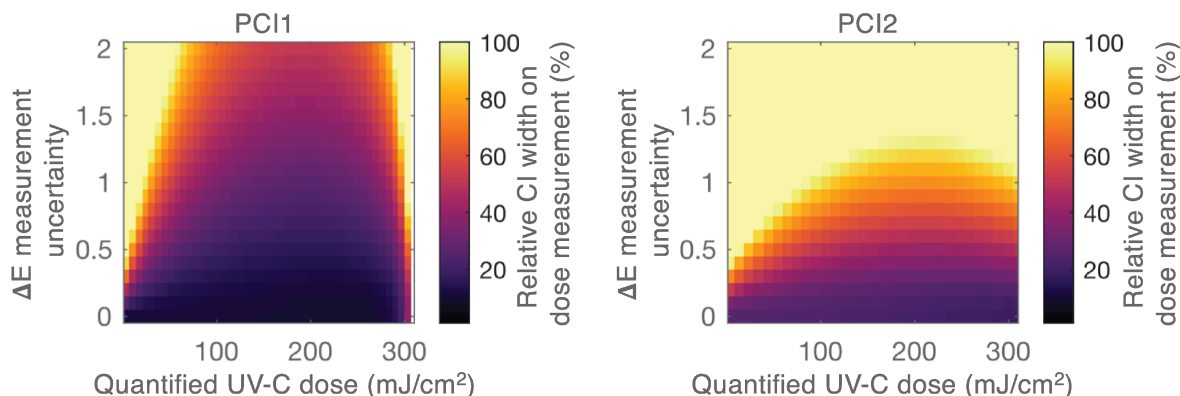


Figure 5.7: Relative PCI dose quantification uncertainty as a function of both UV-C dose and uncertainty on measured  $\Delta E$ . Both the quantified UV-C dose and the 95% confidence interval on that quantified dose were calculated using the PCI calibration functions for a range of simulated  $\Delta E$  measurements and  $\Delta E$  measurement uncertainties. Quantification uncertainty is high at low doses (where  $\Delta E$  uncertainty dominates) and at high doses (where the calibration curve saturates), with a minimum at intermediate doses. The upper limit of the color scale was set to 100%, although some regions exceed this level of uncertainty.

Robust color quantification metrics that are well-suited to calibration should vary with applied UV-C dose in a reproducible and quantifiable manner with low relative quantification uncertainty. To better understand the calibration capacity of other standard metrics of color quantification, we scrutinized the relative quantification uncertainty on alternate color difference/color distance formulae: CIELAB 1976 (Euclidean  $\Delta C$ ) and Euclidean RGB  $\Delta C$  (Figure 5.8). To isolate specific color components well-suited to calibration, we also compared absolute differences in the red, green, and blue ( $\Delta R$ ,  $\Delta G$ ,  $\Delta B$ ) components and lightness, chroma, and hue ( $\Delta L$ ,  $\Delta C$ ,  $\Delta H$ ) components between exposed and unexposed PCIs (Figure 5.8). We fit each metric to the same calibration functions defined in the Methods (Eq. 5.1 for PCI1; Eq. 5.2 for PCI2). Relative CI widths for each of these 9 color metrics were computed by comparing the PCI dose measurement CI widths to the respective dose values. Not surprisingly, the most favorable color difference metrics were dependent on PCI type. Given the benefits of CIEDE2000 for robust color difference determination across the full color space of different potential PCI colors [30], we chose to use CIEDE2000 for all subsequent quantification of both PCI models used in this study. We acknowledge, however, that different color metrics may be optimal for characterizing a single specific PCI model. For PCI1, the difference in hue angle ( $\Delta H$ ) yielded low quantification uncertainty (<10% up to the highest tested dose of 0.25 J/cm<sup>2</sup>) and may be an avenue for future research to improve quantification robustness compared to CIEDE2000 for certain PCI models. Additionally, measurements of the PCI material optical spectra as a function of exposure dose may help developers of new PCI chemistries identify the most promising color metrics for dose quantification.

We note that the PCI color changes are governed by reaction kinetics; thus, environmental factors (e.g., temperature and humidity) are expected to affect the rate of color change with dose [42, 44]. Additionally, we have observed PCI color instability after exposure; thus, PCIs should be quantified immediately (within 10–20 min of exposure for these models). Although the PCI1 quantifiable dynamic range of <0.2 J/cm<sup>2</sup> is not sufficient for in-process validation ( $\geq 1.0$  J/cm<sup>2</sup> to all N95 surfaces [2–4]), it meets the  $\geq 0.1$  J/cm<sup>2</sup> marginal threshold to assess relative doses for informed design of UV-C treatment systems.

## PCIs vary in specificity to germicidal UV-C

Given that ultraviolet decontamination efficacy depends on wavelength, it is critical that PCIs used for UV-C decontamination are not only sensitive, but also specific to germicidal UV-C wavelengths (200–280 nm) [7]. We used the quantification workflow to start to investigate PCI specificity to UV-C wavelengths (Figure 5.9). Specificity of the measurement tool to UV-C light is important because many UV-C sources (e.g., medium-pressure mercury or xenon arc lamps) emit wavelengths outside of the germicidal UV-C range [7]. Even near-monochromatic UV-C sources such as low-pressure mercury and amalgam lamps emit wavelengths >300 nm (Figure 5.1e) [45] that could lead to overestimation of UV-C dose without UV-C-specificity. We asked two questions: (1) how much of the PCI color change from low-pressure amalgam bulbs is due to non-germicidal wavelengths, and (2) how suscep-

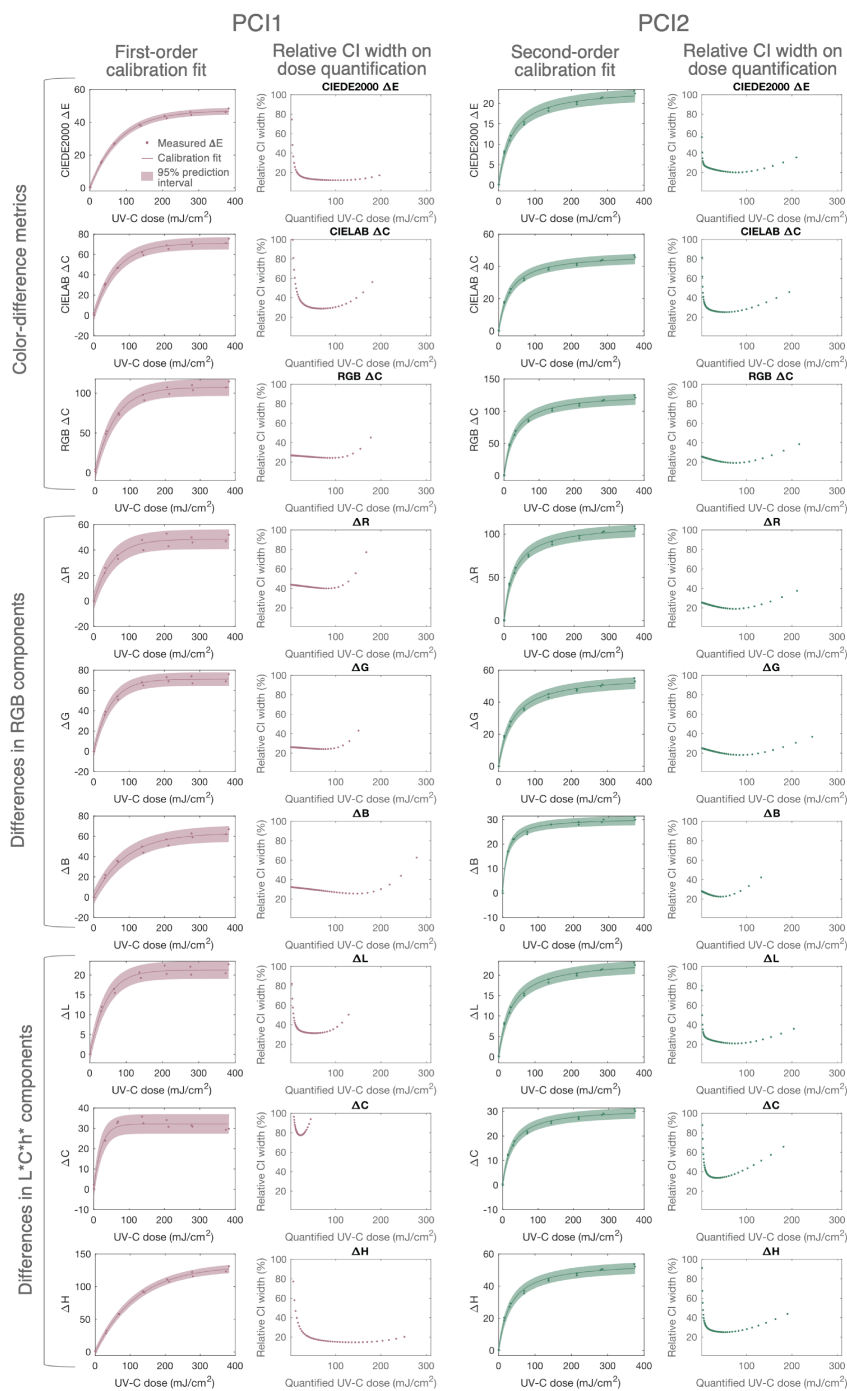


Figure 5.8: Calibration curve fits and relative width of 95% confidence intervals on quantified PCI UV-C doses using alternate color change metrics as a function of UV-C dose. Color difference metrics reporting the lowest relative uncertainty vary by PCI model. Here, difference in hue angle ( $\Delta H$ ) and overall color difference (CIEDE2000  $\Delta E$ , Euclidean CIELAB 1976  $\Delta C$ , and Euclidean RGB  $\Delta C$ ) appear suitable for dose quantification.

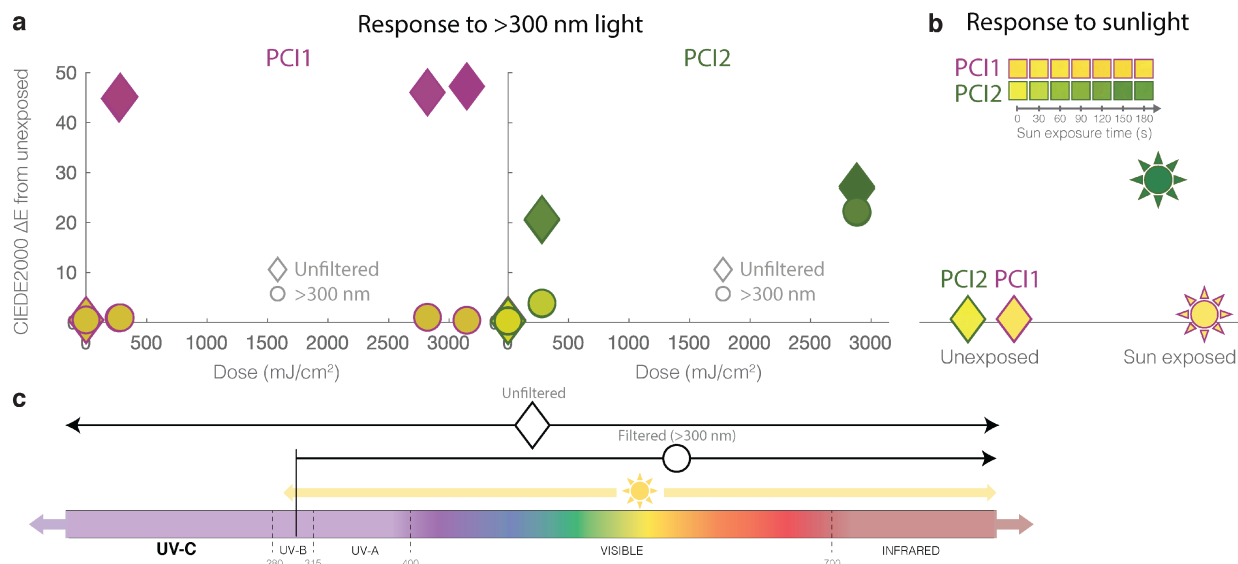


Figure 5.9: Model-dependent PCI specificity to germicidal UV-C. (a) Comparing responses from bare, unfiltered PCIs (diamonds) to those underneath a longpass filter (circles; blocking light  $<300$  nm) quantifies the sensitivity to  $>300$  nm light. Dose axis denotes unfiltered 254 nm UV-C dose measured with the radiometer.  $N = 2$  replicates are plotted. (b) Quantified color change after sun exposure of the PCIs outdoors assesses indicator sensitivity to sunlight. Pink symbol outlines correspond to PCI1, green symbol outlines refer to PCI2. Symbol fill color depicts the sensor color of each measurement (yellow shows minimal color change; pink or green shows color change). Inset shows the white-balanced PCI color recorded over time using iPhone 8 video (not raw). Plot shows a representative replicate of  $N = 2$  PCIs. (c) Schematic showing the relevant portion of the electromagnetic spectrum and the relevant wavelengths associated with the filtered and unfiltered measurements and sunlight.

tible are PCIs to perturbation by spurious solar exposure during transport or storage. We compared the PCI color change after exposure through a longpass ( $>300$  nm) optical filter to that of an unfiltered PCI when exposed to low-pressure amalgam illumination. At an unfiltered dose of  $0.28 \text{ J/cm}^2$ , one PCI (PCI1) showed negligible color change, thus meeting the  $<5\%$  specification (Figure 5.9a). In another PCI model (PCI2), the same longer-wavelength, non-germicidal components of the emission generated  $\sim 19\%$  of the total color change resulting from  $0.28 \text{ J/cm}^2$  measured from the unfiltered source (Figure 5.9a), highlighting how specificity to the germicidal range is PCI model-dependent. Natural sunlight (which contains UV-A and UV-B, but no longer contains UV-C at the earth’s surface [46]) also induced rapid color change of PCI2 ( $\Delta E \sim 28$  in 5 min), while PCI1 only marginally changed ( $\Delta E \sim 1.5$ ) (Figure 5.9b). These results demonstrate the importance of UV-C specificity characterization when assessing PCIs, as common UV-C sources (e.g., low and medium pressure mercury bulbs, LEDs) vary in their proportional outputs within the germicidal UV-C range

[7] and misreporting the germicidal dose could have wide-ranging negative consequences. We see quantitative assessment and reporting of PCI color change in response to well-controlled, known non-germicidal wavelengths as beneficial to PCI development. Specifically, PCI color change arising from exposure to common UV sources including low, medium, and high-pressure mercury lamps, xenon arc lamps, and solar simulators would inform both end users and future PCI design iterations.

### **Non-ideal angular response of radiometer requires correction**

The accuracy and reproducibility of UV-C measurements is hindered by a lack of standardization of critical sensor properties such as angular response, which can drastically impact readings [18, 36] (with system-dependent impact). In the absence of a calibration reference, the sensor angular response can be obtained (either through measurement [18] or through the manufacturer) and used with optical modeling to estimate spatially dependent system- and sensor-specific correction factors.

The OAI radiometer ('Rad1') was calibrated by the manufacturer using a collimated source such that the sensor is situated a specified distance from the source, at normal geometry (i.e., perpendicular to the optical axis). In this study, however, the sensor is used to measure UV-C that is uncollimated and at non-normal geometric configuration. Since the sensor assembly consists of a cylindrical case where optical elements such as diffusers, filters, and apertures are stacked in front of the photosensing element, the offset distance from the front aperture to the photosensing element causes positional sensitivity when the sensor is used to measure uncollimated beams. UV-C rays with a high angle of incidence may be blocked from reaching the sensing element. Therefore, we anticipate that the irradiance reported by the photosensing element may be lower than the actual irradiance at the sensor's front surface, and correction or calibration needs to be performed to compensate for the sensor's nonideal (non-cosine) angular response.

The inaccuracy in irradiance measurement can be corrected experimentally by calibrating the sensor in the exact conditions for which it will be used; however, in the absence of a reference sensor with an ideal cosine angular response and a photosensing element at the same height as the inaccurate radiometer's photosensing element, this is not possible. Furthermore, because this calibration must be conducted within each specific UV-C system (since systems are frequently sold separate from radiometers), this experimental approach is not practical to the majority of users. Instead of performing this calibration experimentally, this sensor 'calibration' can be performed virtually with the use of optical modeling software to determine spatially dependent 'correction factors' that quantify the amount by which the sensor underestimates true irradiance. The sensor's irradiance readings can then be multiplied by the appropriate correction factor to more accurately reflect the true irradiance.

Colleagues at NIST modelled our specific UV-C source and sensor in Zemax OpticStudio Pro. The virtual sensor was validated by first comparing its angular response to a simulated collimated light beam at different angles of incidence to the normalized angular response provided by the manufacturer of the radiometer, and then comparing the spatially resolved

normalized virtual irradiance estimates with those of the physical sensor (Figure 5.10a). As shown in Figure 5.10, the ratios of the normalized irradiances detected by the virtual and physical sensors are close to one, as expected.

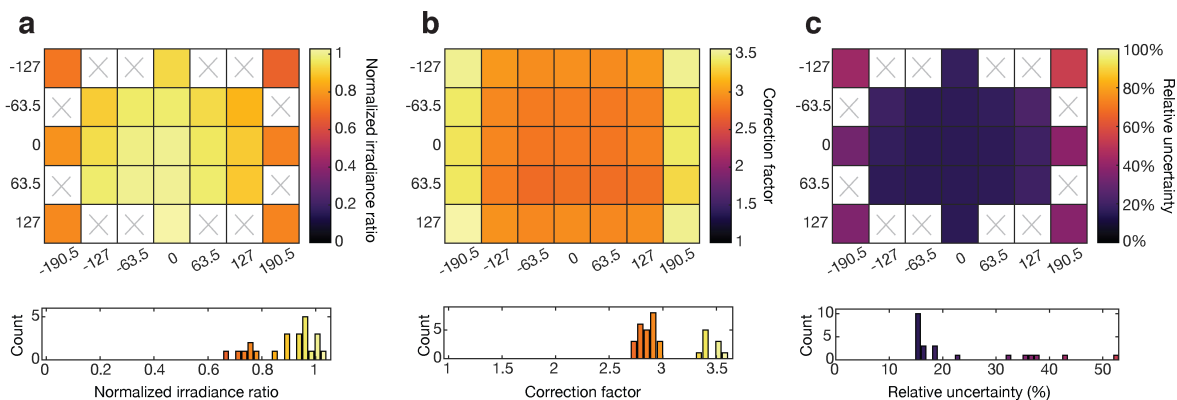


Figure 5.10: Spatially dependent correction factor improves accuracy of radiometer. Heatmaps depicting the (a) ratio between normalized (to the maximum value) irradiance readings of the radiometer and the virtual sensor, (b) spatially varying radiometer correction factor, and (c) the spatially dependent relative uncertainty associated with the correction factor. White regions with ‘x’s were not measured.

The correction factor was then calculated as the ratio of the total irradiance incident upon the front surface of the sensor to the irradiance reported by the physical sensor. The total irradiance from the six bulbs at the plane of the radiometer sensor front surface was mapped across the simulation treatment plane. The virtual sensor was then positioned at various points on that same plane to map what the actual sensor readings would be. The resulting correction factor map is shown in Figure 5.10b). The values of the correction factor vary from 2.72-3.57 and are spatially dependent, with larger correction factors required around the periphery of the treatment plane.

The spatially resolved relative uncertainty was calculated as the square root of the sums of the squared relative uncertainties on (1) the OAI calibration (reported by the manufacturer as 3%), (2) the UV-C treatment system’s irradiance ray trace standard uncertainty (standard deviation of  $N = 4$  ray traces), (3) the solid angle uncertainty, represented as the relative difference between the virtual and physical sensor readings (similar error is depicted in Figure 5.8), and (4) the detector area. This spatially resolved relative uncertainty is shown in Figure 5.10c). The relative error on the detector area was estimated as the relative error on the differences between the virtual and physical OAI sensor readings during a validation experiment using a mask/aperture setup designed such that the small aperture limited the angles of incidence to near-normal.

The corrected and uncorrected Rad1 readings were also compared to readings from another radiometer with near-ideal (cosine) angular response (‘Rad2’), as well as simulation. Absolute irradiance readings between the corrected first radiometer and near-ideal cosine second radiometer agreed within 11% (Figure 5.11a). Differences between the normalized



corrected Rad1 and simulations (Figure 5.11b) reveal that simulations underestimate nonuniformity in irradiance by up to 22% (Figure 5.11c). However, even though the simulated irradiance map underestimates the extent of nonuniformity present in the treatment plane, the relative nonuniformities measured by the virtually corrected radiometer agreed within 3% with those measured by the radiometer with near-ideal cosine response (Figure 5.11c).

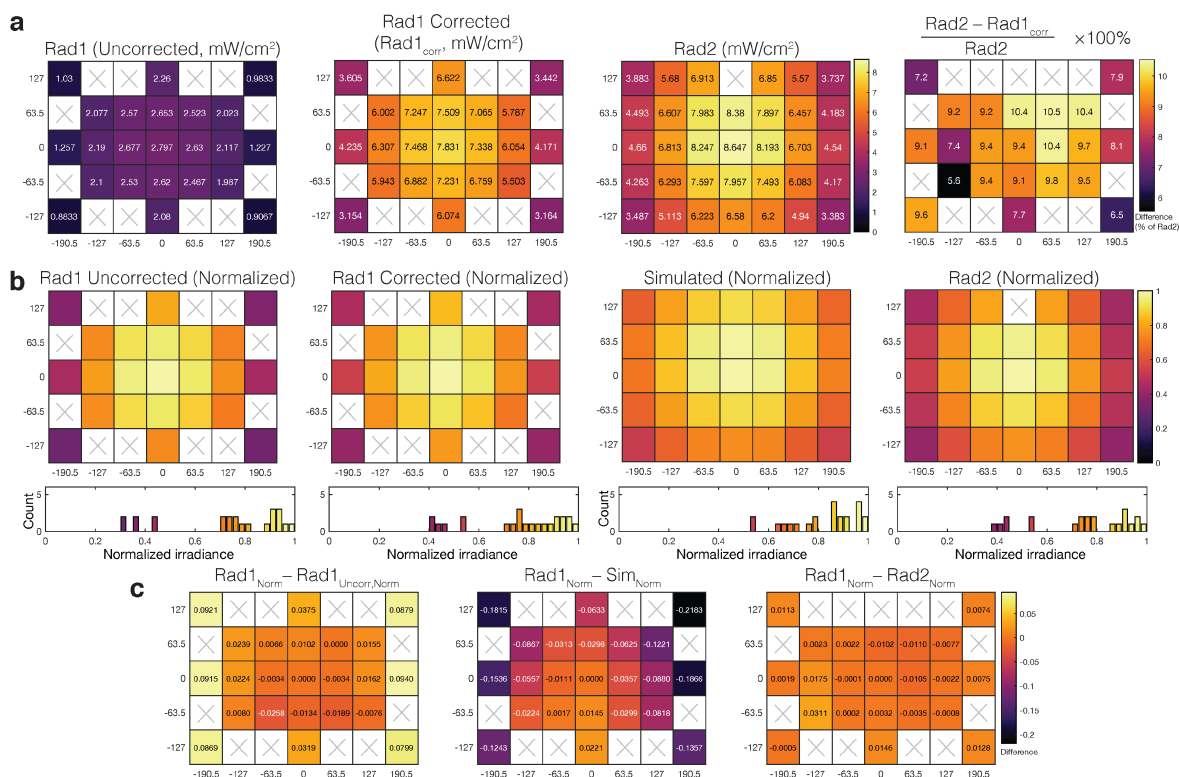


Figure 5.11: Angular response affects spatial nonuniformity quantification. (a) Two UV-C sensors report  $\sim 3\times$  difference in irradiance within the exposure system due angular response discrepancies (Rad1 has nonideal angular response; Rad2 has near ideal cosine angular response). Correction of Rad1’s angular response with a virtual calibration factor yields irradiance profile in good agreement with Rad2. (b) Normalized corrected Rad1 measurements agree well with normalized Rad2 measurements and optical simulations of the treatment system, although simulations underestimate irradiance nonuniformity. Each plot shows a heatmap of irradiance values normalized to the center location above a histogram of normalized irradiances (showing mean of  $N = 3$  measurements for experimental (Rad1/Rad2) measurements). (c) Differences between normalized corrected Rad1 measurements and uncorrected Rad1 measurements (left), simulation values (middle), and Rad2 measurements (right). All heatmaps in (c) are plotted on the same scale. White regions with ‘x’ were not measured. Each experimental (Rad1 or Rad2) plot depicts mean of  $N = 3$  measurements.

Two orthogonal approaches were taken to validate the computed correction factors. First, a mask/aperture setup was used to limit the angular distribution of rays that reach the

sensor to verify that the virtual sensor matches the actual sensor in positional sensitivity. Measurements were made of irradiance detected by the physical sensor both directly normal to the aperture and laterally offset (parallel to the long axis of the bulbs) by 25.4 mm at several known heights below the bulb. The ratio of these measurements was compared to those predicted by running the equivalent optical simulation, and good agreement was observed (Figure 5.12).

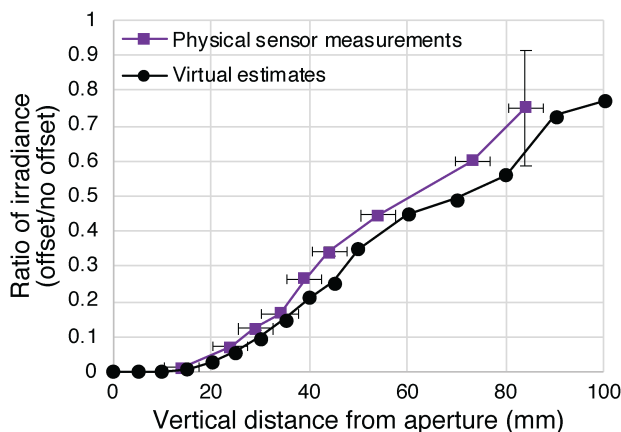


Figure 5.12: Correction factor validation using mask/aperture setup. One method of validation of the virtual calibration factor compared modelled and measured irradiances at varying distances from the aperture. Vertical error bars show error-propagated standard deviation of  $N = 3$  measurements. Horizontal error bars depict propagated error in height measurements.

Second, to further validate the correction factor, PCIs were exposed in the modified mask/aperture setup (in which the correction factor is approximately 1), and the dose-response curve was compared to the curve generated in the original UV-C setup (Figure 5.13). While we do not observe perfect agreement between the dose-responses, some variation is expected due to the drastically different irradiances ( $\sim 0.10 \text{ mW/cm}^2$  under the aperture;  $\sim 7.5\text{-}12 \text{ mW/cm}^2$  without the aperture) measured in the two setups (PCI response as characterized by the manufacturer has some dependence on irradiance [47]).

We note that the reported correction factors are only accurate for the specific conditions assumed for this virtual sensor calibration. Changes to the physical chamber, sensor or bulb properties, as well as changes to the height and/or angle of the sensor within the treatment system require revised simulations that account for these new conditions. In addition, changes to the sensor such as blockage of the effective aperture or insertion of optical elements are significant changes not accounted for in the simulation and require recalculation of the correction factors. However, changes to the lamp irradiance as lamps age or are replaced are expected; sensor readings will reflect such changes and the calculated correction factors should still apply.

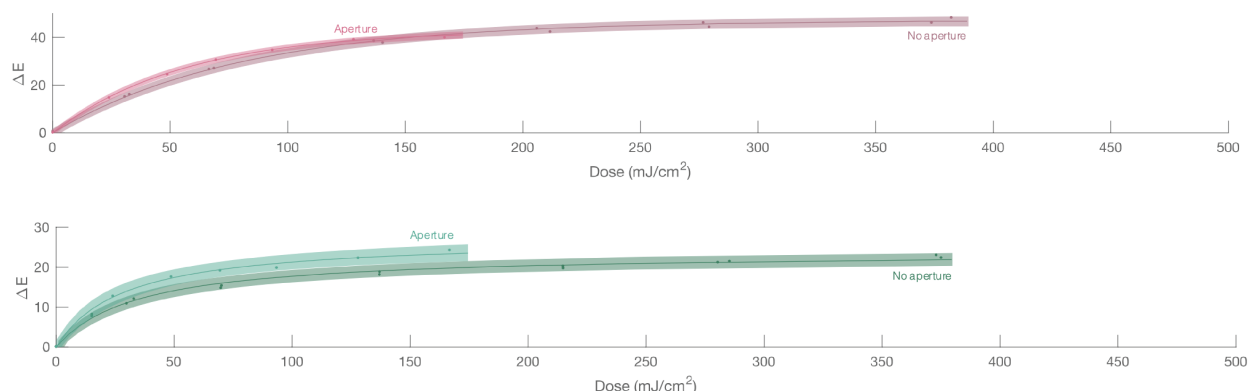


Figure 5.13: Correction factor validation using PCIs. Comparison of PCI dose response with correction factor (‘no aperture’) to through the aperture (‘aperture’), where the estimated correction factor for the OAI radiometer would be 1. Dose-responses for PCI1 and PCI2 are shown in the top and bottom plots, respectively.  $R^2$  and fit parameters: (PCI1 no aperture)  $R^2 = 0.998$ ,  $a = 47.1$  (46.1, 48.1),  $b = 80.4$  (74.6, 86.3); (PCI1 aperture)  $R^2 = 0.999$ ,  $a = 42.8$  (41.3, 44.2),  $b = 55.8$  (50.9, 60.6); (PCI2 no aperture)  $R^2 = 0.992$ ,  $a = 47.7$  (45.9, 49.5),  $b = 0.00060$  (0.00049, 0.00072); (PCI2 aperture)  $R^2 = 0.994$ ,  $a = 55.0$  (49.9, 60.0),  $b = 0.00090$  (0.00037, 0.00090). In each plot, fitted data are represented as points, best fit lines are represented as solid lines, and 95% prediction intervals are plotted as shaded regions.

## Novel PCI quantification accurately assesses spatial nonuniformities in UV-C treatment systems

Having established a novel PCI quantification workflow and spatially dependent correction factor for the OAI 308 radiometer, we next asked whether PCI measurements could scrutinize spatial dose uniformity within a UV-C treatment system as the first step towards informed design of N95 decontamination (Figure 5.1d(ii)). Guiding principles of optics dictate that irradiance nonuniformities will be present in nearly any UV-C treatment system. We first mapped UV-C dose within a Spectroline HCL-1500 UV-C source using simulation (Figure 5.14a) and 23 individual OAI 308 radiometer measurements post-correction (Figure 5.14b). After correction, the irradiance measured near the corners of the treatment plane is  $\sim 40\%$  of that measured at the center.

We leveraged the nonuniform treatment plane irradiance to validate our quantification workflow by comparing PCI-measured doses (Figure 5.14(c-d), quantified using the appropriate calibration curve depicted in Figure 5.2a) to corrected radiometer measurements (Figure 5.14b). The relative quantification error ( $\frac{|\text{dose}_{PCI} - \text{dose}_{radiometer}|}{\text{dose}_{radiometer}}$ ) for PCI1 is  $7\% \pm 7\%$  (mean  $\pm$  standard deviation of  $N = 23$  spatial measurements averaged across  $N = 2$  replicates), meeting the  $>90\%$  accuracy target. In contrast, the relative quantification error for PCI2 is  $28\% \pm 10\%$ , failing to meet the marginal  $>80\%$  accuracy target. While it is unclear why PCI2 performs so discordantly in this test, the good agreement between PCI1 and the radiometer

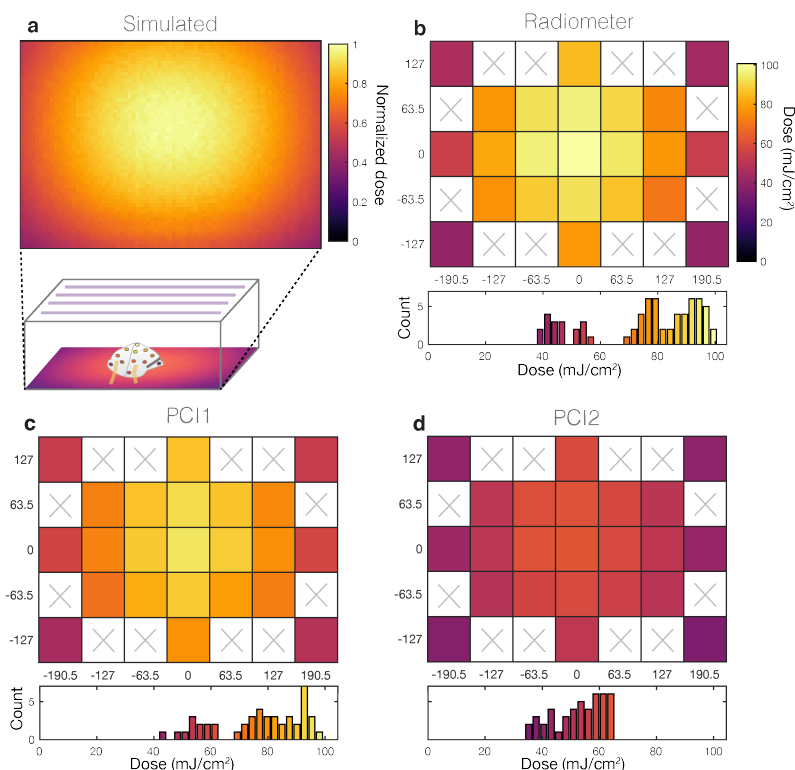


Figure 5.14: UV-C dose delivered across the treatment plane, quantified with (a) optical simulations (plot depicts relative dose), (b) digital radiometer (with correction factor, mean of  $N = 3$  measurements/location), (c) PCI1 (mean of  $N = 2$  measurements/location), and (d) PCI2 (mean of  $N = 2$  measurements/location). The PCI2 model appears to underestimate both dose and nonuniformity. Heatmaps in (b-d) are plotted on the same color scale (up to the radiometer maximum measured dose), while heatmap in (a) depicts dose normalized to the highest value observed. White regions with ‘x’ in (b-d) were not measured.

suggests not only that our PCI quantification workflow can capture nonuniformities in a single UV-C exposure (compared with 23 radiometer exposures), but also that color difference quantification should facilitate new classes of measurements not feasible with radiometers.

### PCI quantification facilitates new types of measurements for informed design of UV-C treatment

PCI quantification facilitates measurements not possible with bulky radiometers (Figure 5.15), such as dose mapping across complex 3D morphologies. To highlight the impact of our workflow, we mapped relative UV-C doses across the 3D morphology of a Gerson 1730 N95 respirator in three orientations (Figure 5.16a) informed by the treatment area dose mapping (Figure 5.14(a-d)). We exposed PCI1 indicators located on exterior and interior N95 surfaces to sub-saturating UV-C treatments (Figure 5.16(b-d)). Limited by PCI dynamic range, the



Figure 5.15: Image of physical sensor comparison. From left to right: UVPS photochromic indicator (PCI2), Intellego photochromic indicator (PCI1), ILT1254 digital radiometer (Rad2), OAI 254 nm sensor (Rad1). PCIs, false-colored for contrast, are notably smaller than radiometers, permitting measurement over complex 3D geometries.

exposure times were insufficient for N95 decontamination, but did measure relative dose delivered to different respirator regions (informed design, Figure 5.1d(iii)). We observe that while nonuniformities in the system alone suggest  $\sim 2.5\times$  irradiance nonuniformity across the treatment plane (Figure 5.14(a-d)), on-N95 measurements show that nearly  $20\times$  disparity exists across multiple N95s in the same treatment system (Figure 5.16(b-d) and Table 5.4).

The respirator morphology has a striking impact on delivered dose: even in the center of the treatment plane there are regions on the exterior (convex) N95 surface that receive only  $\sim 25\%$  of the dose at the apex (Figure 5.16b). There is similar but less dramatic nonuniformity present on the respirator interior (exposed concave side-up) (Figure 5.16c). Perhaps most strikingly, there are regions of a respirator in the treatment plane periphery (Figure 5.16d) that receive only 6% of the dose at the apex of the central N95 (Figure 5.16b). Due to the angular dependence of irradiance [15] as well as respirator self-shadowing stemming from the 3D morphology with respect to the UV-C source, the entire N95 surface must be considered when estimating UV-C dose for decontamination; measuring the irradiance in an empty system does not sufficiently predict irradiance on the N95 surface. Scientific evidence suggests that all N95 surfaces must receive  $\geq 1.0 \text{ J/cm}^2$  UV-C dose for 3-log bioburden reduction of several enveloped viruses [2–4]; however, our results show that  $1.0 \text{ J/cm}^2$  delivered to the apex of the central N95 in this system would result in only  $0.06 \text{ J/cm}^2$  applied to the side of an N95 placed in the periphery of the treatment plane. While this dose heterogeneity is certainly system- and N95 model-specific, it underscores the challenges of N95 decontamination and the critical importance of considering complex 3D geometries when designing and validating UV-C decontamination workflows.

In contrast with single-point radiometers, each PCI also records spatially resolved doses (Figure 5.17). As many N95 decontamination implementations track N95s using permanent marker labelling, we assessed whether such labels might shadow underlying respirator layers by positioning a pattern (‘Cal’) drawn on UV-C-transmitting film overtop a PCI1 indicator during exposure. We observe pattern transfer onto the indicator (Figure 5.17), suggesting that material underneath marker labels may not be as effectively decontaminated as unmarked regions. These examples of on-respirator dose quantification and spatially resolved measurement illustrate the novel, robust measurements PCIs can provide when combined

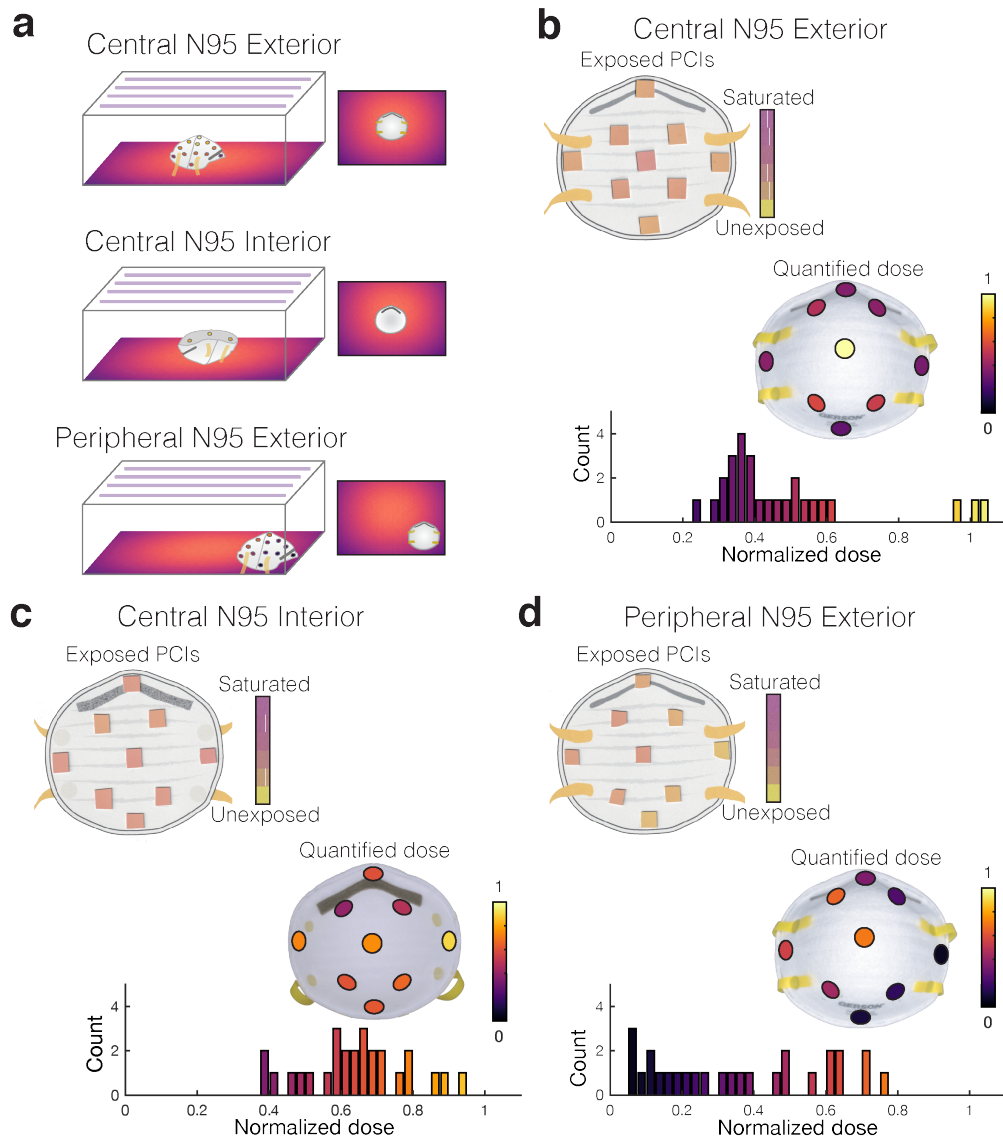
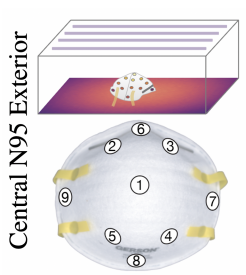
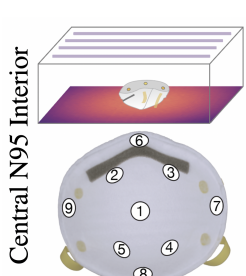
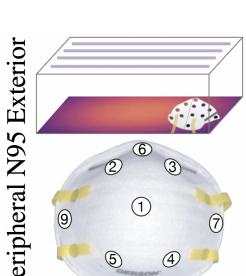


Figure 5.16: (a) Illustration of the three sets of on-N95 measurements, mapping dose across: (1) the exterior of an N95 placed in the treatment plane center (highest-dose region), (2) the interior of an N95 placed in the treatment plane center, (3) the exterior of an N95 placed in the treatment plane periphery (lowest-dose region). (b-d) Scanned PCI1 images and corresponding UV-C dose quantified from PCI1 at various respirator surface locations. Although PCI color differences can appear subtle, quantification reveals substantial dose variation. Each relative dose measurement is normalized to the measurement at the apex of the central ‘convex-up’-oriented (exterior) respirator. Scanned images show a representative replicate, on-N95 heatmaps plot the mean of  $N = 3$  measurements, while the histograms below each measurement plot all individual measurements. (b) Exterior of central respirator. (c) Interior of central respirator. (d) Exterior of peripheral respirator.

Table 5.4: Quantified on-N95 relative doses (normalized to the apex location 1 of the exterior of the central respirator) measured with PCI1 as depicted in Figure 5.16. Errors are reported as one standard deviation propagated uncertainty encompassing both the standard deviation of 3 replicate measurements (measured across  $\geq 2$  separate days) and the uncertainty on the dose measurement from the calibration curve. Schematics in the left column depict measurement location for each configuration.

Configuration	Location	Norm. Dose (PCI1)
Central N95 Exterior 	1	$1.00 \pm 0.07$
	2	$0.47 \pm 0.06$
	3	$0.38 \pm 0.05$
	4	$0.53 \pm 0.07$
	5	$0.57 \pm 0.06$
	6	$0.36 \pm 0.02$
	7	$0.33 \pm 0.02$
	8	$0.28 \pm 0.04$
	9	$0.38 \pm 0.03$
Central N95 Interior 	1	$0.75 \pm 0.06$
	2	$0.40 \pm 0.03$
	3	$0.48 \pm 0.04$
	4	$0.66 \pm 0.06$
	5	$0.61 \pm 0.05$
	6	$0.60 \pm 0.06$
	7	$0.90 \pm 0.06$
	8	$0.62 \pm 0.04$
	9	$0.73 \pm 0.06$
Peripheral N95 Exterior 	1	$0.71 \pm 0.07$
	2	$0.65 \pm 0.07$
	3	$0.24 \pm 0.03$
	4	$0.16 \pm 0.02$
	5	$0.43 \pm 0.06$
	6	$0.34 \pm 0.04$
	7	$0.063 \pm 0.011$
	8	$0.104 \pm 0.015$
	9	$0.55 \pm 0.06$



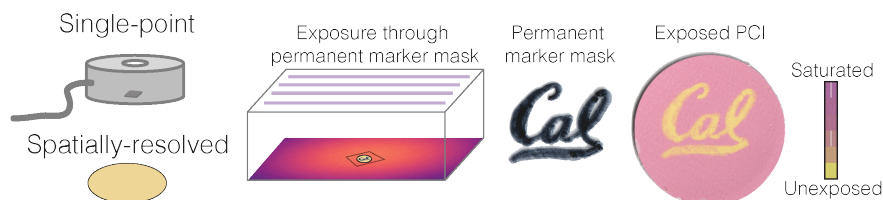


Figure 5.17: PCIs are 2D surface-like sensors that facilitate spatially resolved measurements. We leveraged this characteristic to show that permanent marker (‘Cal’ pattern) on a UV-C-transmissive film placed atop PCI1 can mask UV-C exposure, suggesting that markings on respirators should be minimized. PCI1 changes from yellow to pink as it is exposed to higher UV-C doses; yellow regions correspond to areas shadowed by the marker.

with suitable, spatially resolved readout tools (vs. the single-measurement spectrophotometer), better informing UV-C treatment design.

## Device-specific calibration facilitates quantification using widely available imaging tools

To overcome spectrophotometer limitations (e.g., cost, availability, and throughput) as well as work towards capturing spatial information already recorded in the PCIs, we generated and assessed device-specific calibration curves using widely available imaging tools under controlled lighting conditions (Figure 5.18). The calibration curves were generated from images of PCIs acquired using a flatbed scanner (Canon LiDE-400), a digital SLR camera (DSLR, Nikon D5500), and a smartphone (iPhone X) (DSLR and iPhone images were acquired in a light box to minimize the impact of ambient illumination). All tools captured raw images of the entire surface of both the exposed PCI as well as an unexposed reference PCI. The resulting calibration curves were then compared to those generated with data from the RM200QC (Figure 5.18a). The CIEDE2000  $\Delta E$  measurement uncertainty for each imaging tool was calculated from the standard deviation of measurements comparing measured color of unexposed PCIs to a saturated reference PCI. The resulting  $\Delta E$  measurement uncertainties for PCI1 and PCI2 were 0.273 and 0.083 for the RM200QC, 0.624 and 0.413 for the iPhone, 0.161 and 0.046 for the DSLR, and 0.293 and 0.113 for the scanner, respectively. We observe the highest CIEDE2000  $\Delta E$  values from measurement with the cameras. Though the flatbed scanner measures the lowest  $\Delta E$  values, its measurements trend with those of the RM200QC and conveniently do not require a light box. We further assessed the squared sums of the residuals (SSE) for all fits as a measure of calibration accuracy (Figure 5.18b) as well as the dose measurement relative uncertainty (using the  $\Delta E$  measurement uncertainties in the error propagation) (Figure 5.19). We measure relative CI widths on a measurement of  $\sim 0.1 \text{ J/cm}^2$  UV-C dose using PCI1 of 8.8% for the RM200QC, 16.9% for the iPhone, 6.7% for the DSLR, and 14.0% for the scanner (relative measurement uncertainties of 4.4%, 8.5%, 3.4%, and 7.0%, respectively). Thus, we observe the lowest SSE for the RM200QC, but all imaging approaches yield PCI1 quantification meeting the 10% ideal target relative uncer-



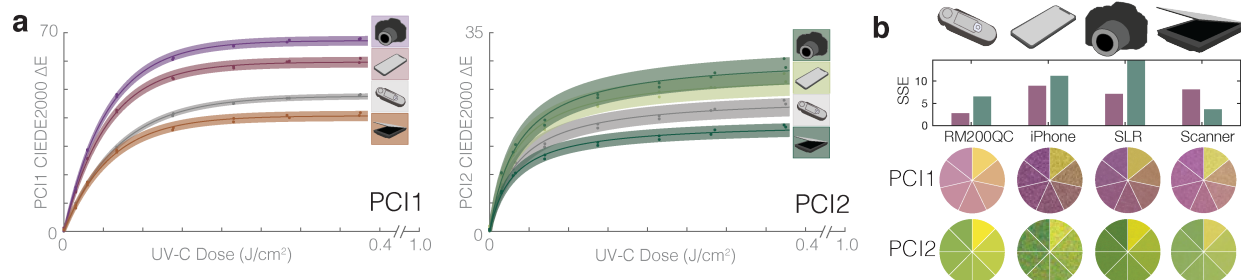


Figure 5.18: The potential applications for UV-C quantification from PCIs could be broadened using widely available color measurement tools. (a) Comparison of calibration curve fits of CIEDE2000  $\Delta E$  from an unexposed sensor vs. UV-C dose, for PCI1 and PCI2 colors quantified using the digital SLR and iPhone X in a light box, RM200QC spectroradiometer, and flatbed scanner. Datapoints within the shaded region denote individual PCI measurements, line denotes best fit, and shaded region denotes 95% prediction interval on prediction of color change from observation of UV-C dose. (b) Squared sum of the residuals (SSE) for each curve fit in (a), along with color comparison wheels showing indicator color at various doses as captured by the different imaging devices.

tainty for a  $\sim 0.10 \text{ J/cm}^2$  dose. Relative CI widths on a measurement of  $\sim 0.1 \text{ J/cm}^2$  UV-C dose using PCI2 are 20.5% for the RM200QC, 39.4% for the iPhone, 22.0% for the DSLR, and 24.3% for the scanner (relative measurement uncertainties of 10.3%, 19.7%, 11.0%, and 12.2%, respectively); thus, no PCI2 quantification met the ideal target, consistent with the model’s higher relative uncertainty (Figure 5.2). Color measurement literature stresses that careful control of lighting conditions (e.g., using an enclosed light box or contact measurement) is critical in order to minimize variation induced by changes in ambient lighting [23, 38]. Even under identical lighting conditions with tight control of acquisition parameters, different imaging devices have different spectral sensitivities and color processing. For this reason, device-specific calibration (using a stringent color reference chart with a range of known colors) has been proposed as an essential step for image-based color quantification for several applications [24, 25, 38, 48]. A smartphone algorithm has been generated for this purpose [27], and flatbed scanners may be a promising, accessible approach provided raw images are acquired (e.g., with third-party software). Overall, these results suggest that with rigorous characterization and proper implementation, widely available imaging tools are appealing for spatially resolved PCI quantification.

### Optical engineering extends the quantifiable dose range for in-process validation of UV-C dose during N95 decontamination

The commercial market for UV-C PCIs has focused on hard surface UV-C decontamination processes requiring orders-of-magnitude lower doses than required for N95 decontamina-

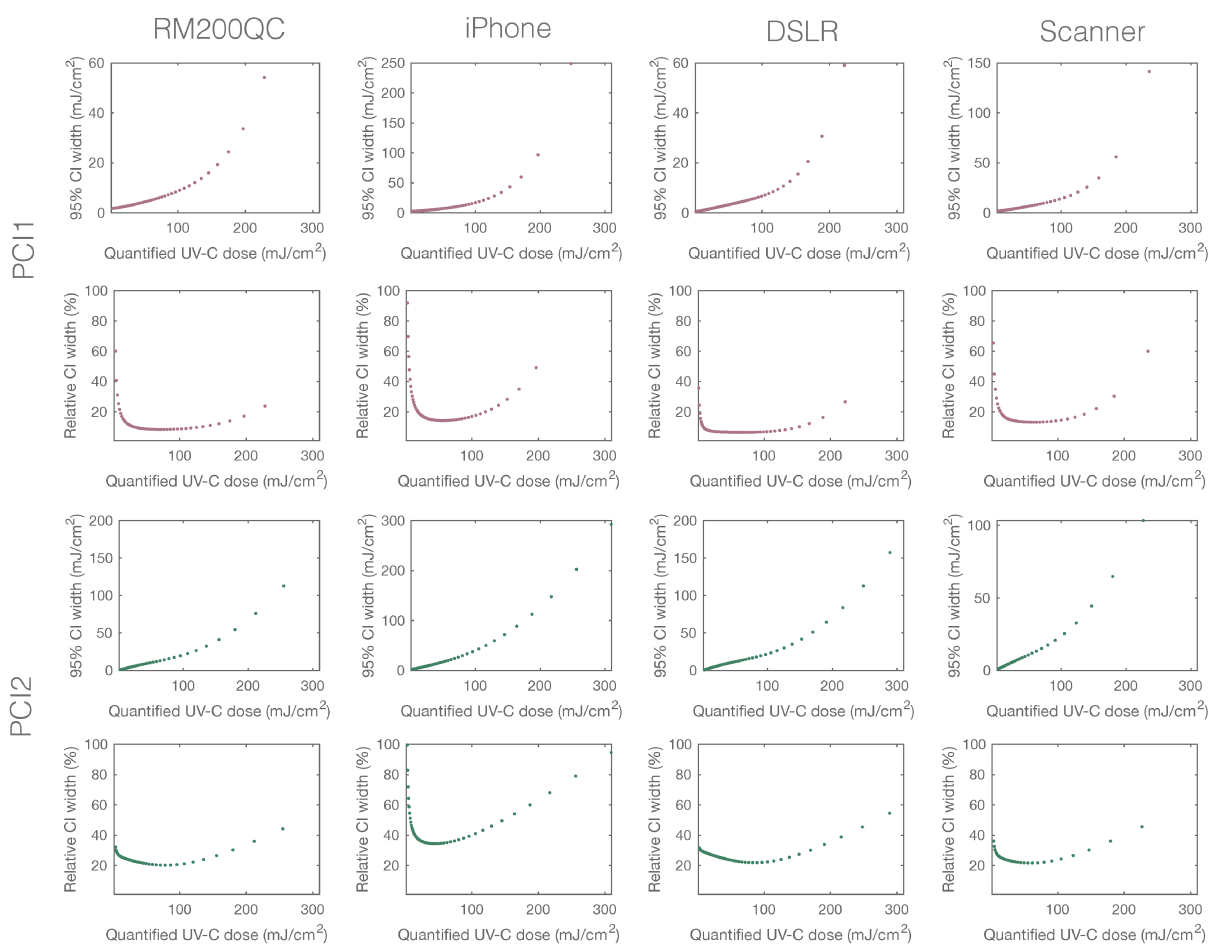


Figure 5.19: Absolute and relative widths of 95% confidence intervals on dose measurements from calibration data for PCI1 (pink, top) and PCI2 (green, bottom) generated from CIEDE2000 color differences quantified by widely available imaging tools. The CIEDE2000  $\Delta E$  measurement uncertainty was calculated from the standard deviation of  $N = 15$  (RM200QC),  $N = 4$  (iPhone, SLR), and  $N = 3$  (scanner)  $\Delta E$  measurements comparing measured color of unexposed PCIs to a saturated reference PCI.

tion, and thus, at this time of this study, we determined that there were no commercially available PCIs that met the dose-range requirements for in-process validation of N95 decontamination. Given the benefits of PCIs over radiometers, we next assessed whether a single ‘snap-shot’ dose/irradiance measurement could be extrapolated to accurately estimate the time required to deliver the minimally acceptable dose for N95 decontamination (i.e., is irradiance constant?). As irradiance is dependent on myriad factors (e.g., UV-C source and surrounding physical environment, operating temperature, bulb conversion efficiency and warm-up status [17, 29]), we hypothesized that irradiance variability within and between

UV-C treatment systems would necessitate full in-process (vs. snap-shot) validation. To test this hypothesis, we studied two UV-C systems with the same specifications: a Spectroline HCL-1500 with BLE-1T155 15W 254 nm low-pressure amalgam bulbs (System 1), and a Spectroline Spectrolinker XL-1500 with third-party BLE-1T155 15W 254 nm low-pressure mercury bulbs (System 2) (Figure 5.20).

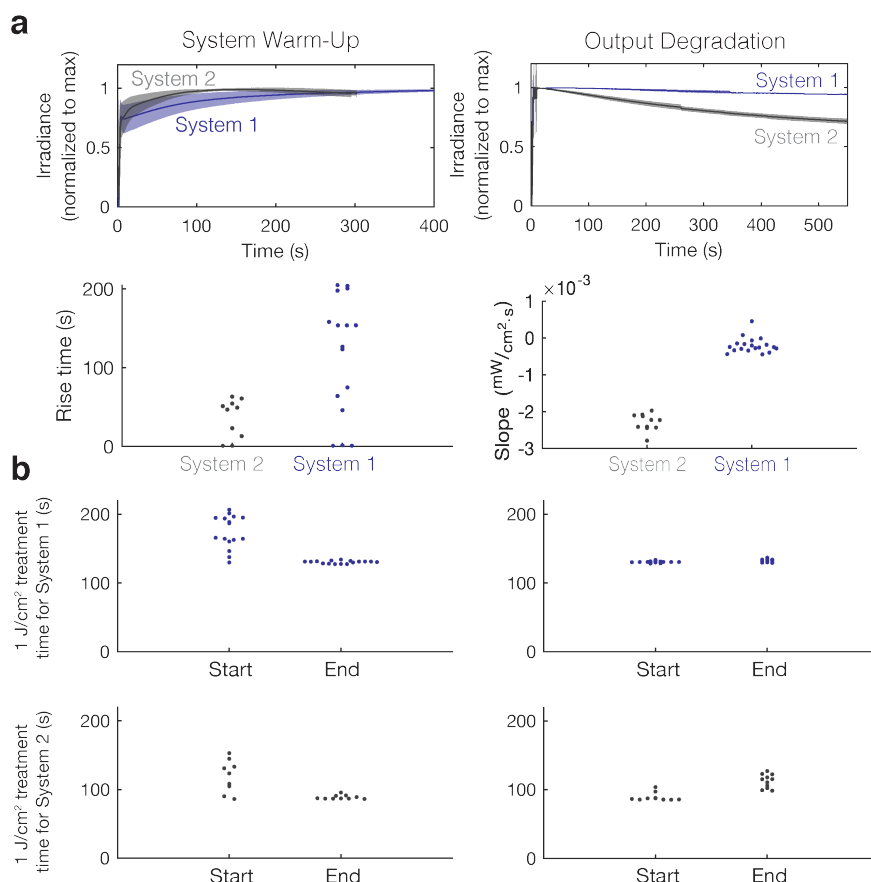


Figure 5.20: Validation of delivered UV-C dose in every treatment cycle is critical due to temporal variations in UV-C output. (a) Measured irradiance rises with time during warm-up (left) and falls with time during long exposure (right). Shaded regions depict one standard deviation of the replicate measurements:  $N = 16$  (System 1 warm-up);  $N = 10$  (System 2 warm-up);  $N = 19$  (System 1 long exposure);  $N = 11$  (System 2 long exposure). (b) Quantification of 10-90% rise time (left) and output degradation slope (right) for multiple exposures in both systems. (c) 1.0 J/cm<sup>2</sup> treatment time estimated from the starting irradiance or ending irradiance for both System 1 (top row) and System 2 (bottom row) in each condition (warm-up or long exposure after warm-up). For each system, the left minimum treatment time plot corresponds to treatment time computations from an uncontrolled (not necessarily warmed-up) start; right plot corresponds to treatment time computations from a warmed-up system.

We observed distinct temporal irradiance variation as well as different maximum output ( $\sim 11$  mW/cm<sup>2</sup> vs.  $\sim 7.7$  mW/cm<sup>2</sup>), despite these systems having the same specifications (Figure 5.20a). These irradiance variations propagate to the exposure time required to reach the critical UV-C dose. To extrapolate the effect these irradiance differences would have on N95 decontamination protocols, exposure times required to reach the marginally acceptable 1.0 J/cm<sup>2</sup> dose at the center of the treatment plane were calculated for (i) the two near-identical systems, (ii) whether the bulbs are warmed-up prior to measurement, and (iii) whether the calculation is performed from measurements at the beginning or end of the exposure (Figure 5.20b). For System 1 after sufficient bulb warm-up, the average times required to deliver 1.0 J/cm<sup>2</sup> dose only differed by 1.5% if calculated from the irradiance measured at the start and end of the exposure, indicative of relatively stable output over the treatment period. In contrast, the calculated average times to deliver the same dose in the same system without sufficient bulb warm-up differed by 29% (Figure 5.20b, top row), highlighting the importance of rigorously controlled bulb warm-up protocols. Following a similar trend, the calculated average times to deliver 1.0 J/cm<sup>2</sup> without sufficient bulb warm-up for System 2 also differed by 29%. However, the absolute time required for System 2 to deliver 1.0 J/cm<sup>2</sup> dose is far less than System 1 due to higher absolute irradiance. In contrast to System 1, the average times calculated to deliver 1.0 J/cm<sup>2</sup> dose from the irradiance measured at the start and end of the exposure in System 2 after sufficient bulb warm-up still differed by 23% (Figure 5.20b, bottom row). This difference is due to an observed decline in irradiance over time, which we hypothesize is caused by the increased sensitivity to temperature of low-pressure mercury bulbs compared to low-pressure amalgam bulbs [49]. The observed substantial dependence of irradiance on UV-C system, warm-up status, and duration of exposure challenges use of ‘snap-shot’ approaches and necessitates innovation to extend the quantifiable PCI dose range for in-process validation of UV-C N95 decontamination.

There are two potential solutions to extend the PCI dose range: (1) engineer the indicator (e.g., modified chemistry), or (2) engineer the system surrounding the indicator. Towards (2), we assessed the capacity of several materials to attenuate the UV-C irradiance reaching the indicator to a sufficient degree to facilitate dose quantification beyond 1.0 J/cm<sup>2</sup> (Figure 5.21). We observe that commercial UV neutral density filters (1.3 OD) extend the quantifiable dose (<10% relative measurement uncertainty on the PCI1 measurements) from 0.2 J/cm<sup>2</sup> to at least 5.0 J/cm<sup>2</sup> to meet the in-process validation dose specification (Figure 5.21(a,c)). After confirming that the quantifiable dose range could be extended beyond 1.0 J/cm<sup>2</sup> with attenuation, we investigated a less expensive, widely available glass option. Although standard borosilicate or soda-lime glass slides and coverslips block UV-C and are thus not appropriate filter options, 1.1 mm-thick Borofloat glass offers much higher UV-C transmittance [50] and is available in a range of sizes and shapes from multiple suppliers. The Borofloat glass filters extended the quantifiable range of both PCIs beyond 1.0 J/cm<sup>2</sup> (Figure 5.21(a-d)), with the PCI1 measurement uncertainty remaining below 10% up to 2.0 J/cm<sup>2</sup> (below 20% up to the highest tested dose of 2.5 J/cm<sup>2</sup>).

The dose-response curves presented in Figure 5.21(a-b) illustrate how optical attenuators

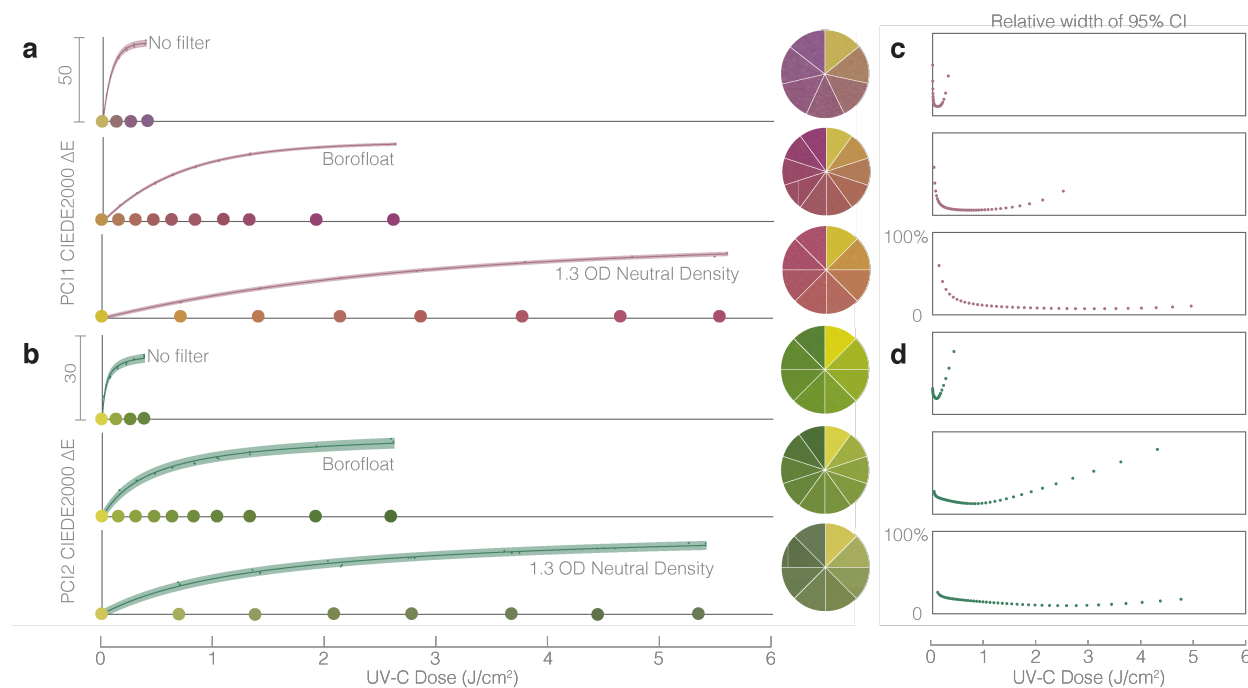


Figure 5.21: Quantitative in-process UV-C dose validation of N95 decontamination cycles using PCIs could be feasible using optical attenuation to extend the dynamic range beyond  $1.0 \text{ J/cm}^2$ . (a-b) 1.1 mm-thick Borofloat glass and 1.3 OD neutral density filters extend the dynamic range of (a) PCI1 and (b) PCI2 sensors. PCI1 no filter  $R^2 = 0.998$ ,  $a = 47.1$ ,  $b = 80.4$ . PCI1 with Borofloat filter  $R^2 = 0.999$ ,  $a = 47.3$ ,  $b = 699$ . PCI1 with 1.3 OD neutral density filter  $R^2 = 0.998$ ,  $a = 44.2$ ,  $b = 2728$ . PCI2 no filter  $R^2 = 0.992$ ,  $a = 47.7$ ,  $b = 0.00060$ . PCI2 with Borofloat filter  $R^2 = 0.990$ ,  $a = 61.8$ ,  $b = 3.63 \times 10^{-5}$ . PCI2 with 1.3 OD neutral density filter  $R^2 = 0.992$ ,  $a = 62.7$ ,  $b = 1.10 \times 10^{-5}$ . Color comparison wheels show PCI colors corresponding to doses marked along the x-axis, except in “No Filter” cases due to space constraints. Datapoints within the shaded region denote individual PCI measurements, line denotes best fit, and shaded region denotes 95% prediction interval on prediction of color change from observation of UV-C dose. (c-d) The relative width of quantified 95% confidence intervals on UV-C dose measurements from CIEDE2000 color difference between exposed and unexposed samples of (c) PCI1 and (d) PCI2, as a function of UV-C dose, plotted to the right of the corresponding dose-response curve.

can be coupled with PCIs to extend quantifiable dose range; however, the implementation of this type of approach requires careful characterization. First, before implementing any filter material, both the inter-filter transmittance variability and the transmittance change with UV-C exposure (e.g., due to solarization [51]) need to be characterized. Transmittance variability contributes to the uncertainty on any filtered dose measurement, while transmittance changes determine the usable lifetime of a filter (single-use vs. reuse). Second, the filter transmittance angular response needs to be assessed. Angular response can vary

from the ideal cosine response based on a number of factors, including the angle-dependent optical path length through the attenuator or the angle-dependent reflectance. For a glass filter, these can be modelled using the Beer-Lambert law coupled with the Fresnel equations and Snell's law [52]. Filter angular response could introduce similar measurement artefacts to those reported for the uncorrected radiometer previously and thus should be understood prior to implementation. Third, filter materials should either be combined with a validated UV-C-specific photochromic indicator or have well-controlled transmission spectra to avoid a filter-indicator pair that primarily detects non-germicidal UV-A or UV-B wavelengths [7, 37]. Many common materials such as glass and plastics have lower UV-C transmission than that at longer wavelengths [7], and thus may filter out the critical wavelength range to be measured. The ideal filter would block all non-germicidal light and attenuate UV-C; however, as solarization rapidly changes transmittance and translatability requires inexpensive, widely available materials, the ideal filter is not easily attainable. Neutral density filters or even filters that attenuate UV-C to a greater degree than longer wavelengths are acceptable when coupled with UV-C specific PCIs. Although important properties of the filter-indicator pair need to be characterized prior to implementation, the extension of quantifiable dose demonstrated in Figure 5.21(a-d) illustrates how Borofloat glass or other attenuating materials can help to address the urgent need for in-process UV-C validation, complementing future innovation in photochromic chemistry.

## 5.4 Conclusions

Quantifying color from PCIs addresses urgent needs in UV-C dose measurement for (and beyond) N95 respirator decontamination. By tailoring established color measurement protocols to PCIs, we designed and validated a photochromic quantification workflow and then applied it to conduct measurements not robustly quantifiable with existing tools. Novel aspects of our workflow include quantifying CIEDE2000 and a suite of alternate color difference metrics for PCIs, implementing calibration informed by chemical kinetics, and quantifying PCI dose measurement uncertainty. Our workflow quantified performance specifications and revealed that while performance was highly PCI model-dependent, one indicator model met all specifications for informed design of UV-C N95 treatment systems: UV-C dose measurement range up to  $0.2 \text{ J/cm}^2$  with relative measurement uncertainty of 6.05% at  $0.1 \text{ J/cm}^2$ ,  $<5\%$  response to UV-A/UV-B, and  $>90\%$  accuracy compared to a calibrated digital radiometer. Our workflow enabled on-respirator dose quantification using PCIs, identifying nearly  $20\times$  dose nonuniformity across different N95 surface regions within a treatment system. As a result, the target dose delivered to the treatment plane within the UV-C system may need to be much higher than  $1.0 \text{ J/cm}^2$  to ensure that all N95 surfaces are exposed to  $\geq 1.0 \text{ J/cm}^2$ . Because these dose nonuniformities across the N95 surface are model- and configuration-dependent, each treatment system should be characterized with the N95 models *in situ* for informed design of UV-C N95 treatment processes. PCI calibration curves for widely available imaging tools like flatbed scanners, iPhones, and DSLRs also meet minimum

performance specifications and facilitate accessible, spatially resolved dose measurements. In future work, intercalation of PCIs between each N95 material layer would quantify spatially resolved UV-C attenuation in the interstices of each porous layer, improving our understanding of complex multi-layer materials. Finally, PCI dynamic range can be extended by coupling with optical attenuators of known transmittance. Although important open questions remain for these attenuators (such as optical transmission stability and angular response), filter-coupled PCIs are promising for high-throughput in-process dose validation for UV-C N95 decontamination. We anticipate that the PCI quantification workflow will be widely applied to meet the current urgent validation need, facilitating (1) informed design of UV-C treatment protocols to ensure that all N95 surfaces are exposed to the minimum dose, (2) in-process dose validation of each cycle, and (3) characterization of the robustness of new PCI materials.

# Bibliography

1. Center for Devices and Radiological Health. *Recommendations for Sponsors Requesting EUAs for Decontamination and Bioburden Reduction Systems for Face Masks and Respirators During the Coronavirus Disease 2019 (COVID-19) Public Health Emergency* tech. rep. FDA-2020-D-1138 (Center for Devices and Radiological Health, 2020).
2. Lore, M. B. *et al.* Effectiveness of Three Decontamination Treatments against Influenza Virus Applied to Filtering Facepiece Respirators. *The Annals of Occupational Hygiene* **56**, 92–101. ISSN: 0003-4878. doi:10.1093/annhyg/mer054 (2011).
3. Mills, D. *et al.* Ultraviolet germicidal irradiation of influenza-contaminated N95 filtering facepiece respirators. *American Journal of Infection Control* **46**, e49–e55. ISSN: 01966553. doi:10.1016/j.ajic.2018.02.018 (2018).
4. Heimbuch, B. & Harnish, D. *Research to Mitigate a Shortage of Respiratory Protection Devices During Public Health Emergencies* tech. rep. HHSF223201400158C (Applied Research Associates, Inc., 2019).
5. Lindsley, W. G. *et al.* Effects of Ultraviolet Germicidal Irradiation (UVGI) on N95 Respirator Filtration Performance and Structural Integrity. *Journal of Occupational and Environmental Hygiene* **12**, 509–517. ISSN: 1545-9624. doi:10.1080/15459624.2015.1018518 (2015).
6. Lowe, J. J. *et al.* *N95 Filtering Facepiece Respirator Ultraviolet Germicidal Irradiation (UVGI) Process for Decontamination and Reuse* tech. rep. (2020).
7. Kowalski, W. *Ultraviolet Germicidal Irradiation Handbook: UVGI for Air and Surface Disinfection* ISBN: 978-3-642-01999-9 (Springer Science & Business Media, Berlin, Heidelberg, 2010).
8. Beck, S. E. *et al.* Wavelength-Dependent Damage to Adenoviral Proteins Across the Germicidal UV Spectrum. *Environmental Science & Technology* **52**, 223–229. ISSN: 0013-936X, 1520-5851. doi:10.1021/acs.est.7b04602 (2018).
9. Fisher, E. & Shaffer, R. A method to determine the available UV-C dose for the decontamination of filtering facepiece respirators: UV-C decontamination of respirators. *Journal of Applied Microbiology* **110**, 287–295. ISSN: 13645072. doi:10.1111/j.1365-2672.2010.04881.x (2011).



10. Ozog, D. M. *et al.* The Effect of Ultraviolet C Radiation Against Different N95 Respirators Inoculated with SARS-CoV-2. *International Journal of Infectious Diseases*, 224–229. ISSN: 12019712. doi:10.1016/j.ijid.2020.08.077 (2020).
11. Cadnum, J. L. *et al.* Effectiveness of Ultraviolet-C Light and a High-Level Disinfection Cabinet for Decontamination of N95 Respirators. *Pathogens and Immunity* **5**. Number: 1, 52–67. ISSN: 2469-2964. doi:10.20411/pai.v5i1.372 (2020).
12. Heimbuch, B. K. *et al.* A pandemic influenza preparedness study: Use of energetic methods to decontaminate filtering facepiece respirators contaminated with H1N1 aerosols and droplets. *American Journal of Infection Control* **39**, e1–e9. ISSN: 0196-6553. doi:10.1016/j.ajic.2010.07.004 (2011).
13. Tseng, C.-C. & Li, C.-S. Inactivation of Viruses on Surfaces by Ultraviolet Germicidal Irradiation. *Journal of Occupational and Environmental Hygiene* **4**, 400–405. ISSN: 1545-9624, 1545-9632. doi:10.1080/15459620701329012 (2007).
14. Voet, D. *et al.* Absorption spectra of nucleotides, polynucleotides, and nucleic acids in the far ultraviolet. *Biopolymers* **1**, 193–208. ISSN: 1097-0282. doi:10.1002/bip.360010302 (1963).
15. Reifsnnyder, W. E. Radiation geometry in the measurement and interpretation of radiation balance. *Agricultural Meteorology* **4**, 255–265. ISSN: 00021571. doi:10.1016/0002-1571(67)90026-X (1967).
16. Bolton, J. R. & Linden, K. G. Standardization of Methods for Fluence (UV Dose) Determination in Bench-Scale UV Experiments. *Journal of Environmental Engineering* **129**, 209–215. ISSN: 0733-9372, 1943-7870. doi:10.1061/(ASCE)0733-9372(2003)129:3(209) (2003).
17. Lawal, O. *et al.* Method for the Measurement of the Output of Monochromatic (254 nm) Low-Pressure UV Lamps. *IUVA News* **19**, 9–16 (2017).
18. Reed, N. G., Wengraitis, S. & Sliney, D. H. Intercomparison of Instruments Used for Safety and Performance Measurements of Ultraviolet Germicidal Irradiation Lamps. *Journal of Occupational and Environmental Hygiene* **6**, 289–297. ISSN: 1545-9624, 1545-9632. doi:10.1080/15459620902801041 (2009).
19. Schmalwieser, A. W. *et al.* Aging of low-pressure amalgam lamps and UV dose delivery. *Journal of Environmental Engineering and Science* **9**, 113–124. ISSN: 1496-2551, 1496-256X. doi:10.1680/jees.13.00009 (2014).
20. Poster, D. L. *et al.* Innovative Approaches to Combat Healthcare-Associated Infections Using Efficacy Standards Developed Through Industry and Federal Collaboration. *Proceedings of SPIE—the International Society for Optical Engineering* **10730**. ISSN: 0277-786X. doi:10.1117/12.2500431 (2018).
21. Lindblad, M. *et al.* Ultraviolet-C decontamination of a hospital room: Amount of UV light needed. *Burns* **46**, 842–849. ISSN: 03054179. doi:10.1016/j.burns.2019.10.004 (2020).

22. ASTM International. *Standard Test Method for Determining Antimicrobial Efficacy of Ultraviolet Germicidal Irradiation against Influenza Virus on Fabric Carriers with Simulated Soil* ASTM standard E3179 - 18 (ASTM International, 2018).
23. Cui, G. *et al.* Grading textile fastness. Part 1; Using a digital camera system. *Coloration Technology* **119**, 212–218. ISSN: 1472-3581, 1478-4408. doi:10.1111/j.1478-4408.2003.tb00174.x (2003).
24. Carpenter, K. & Farnand, S. Assessing the use of smartphones to determine crop ripeness. *Electronic Imaging*. ISSN: 2470-1173. doi:10.2352/ISSN.2470-1173.2020.12.FAIS-173 (2020).
25. Soda, Y. & Bakker, E. Quantification of Colorimetric Data for Paper-Based Analytical Devices. *ACS Sensors* **4**, 3093–3101. ISSN: 2379-3694, 2379-3694. doi:10.1021/acssensors.9b01802 (2019).
26. Singh, G. *et al.* Colorimetric detection and ratiometric quantification of mercury(II) using azophenol dye: ‘dip & read’ based handheld prototype device development. *Journal of Materials Chemistry C* **6**, 12728–12738. ISSN: 2050-7526, 2050-7534. doi:10.1039/C8TC04720K (2018).
27. Yetisen, A. K. *et al.* A smartphone algorithm with inter-phone repeatability for the analysis of colorimetric tests. *Sensors and Actuators B: Chemical* **196**, 156–160. ISSN: 09254005. doi:10.1016/j.snb.2014.01.077 (2014).
28. Solari, F. *et al.* A New Method for the Validation of Ultraviolet Reactors by Means of Photochromic Materials. *Food and Bioprocess Technology* **8**, 2192–2211. ISSN: 1935-5130, 1935-5149. doi:10.1007/s11947-015-1581-1 (2015).
29. ASTM International. *Standard Practice for Calculation of Color Tolerances and Color Differences from Instrumentally Measured Color Coordinates* ASTM standard D2244 - 16 (ASTM International, 2016).
30. Luo, M. R., Cui, G. & Rigg, B. The development of the CIE 2000 colour-difference formula: CIEDE2000. *Color Research & Application* **26**, 340–350. ISSN: 0361-2317, 1520-6378. doi:10.1002/co1.1049 (2001).
31. NIST/SEMATECH. *Uncertainty for quadratic calibration using propagation of error in e-Handbook of Statistical Methods* (2003).
32. NIST/SEMATECH. *Single-Use Calibration Intervals in NIST/SEMATECH e-Handbook of Statistical Methods* (2003).
33. Biguri, A. *Perceptually uniform colormaps* <https://www.mathworks.com/matlabcentral/fileexchange/51986-perceptually-uniform-colormaps> (2020).
34. World Health Organization *et al.* *Global solar UV index: a practical guide* ISBN: 3-9804789-0-4 (World Health Organization, Geneva, Switzerland, 2002).

35. Larason, T. & Ohno, Y. Calibration and characterization of UV sensors for water disinfection. *Metrologia* **43**, S151–S156. ISSN: 0026-1394, 1681-7575. doi:10.1088/0026-1394/43/2/S30 (2006).
36. Larason, T. & Cromer, C. Sources of error in UV radiation measurements. *Journal of Research of the National Institute of Standards and Technology* **106**, 649. ISSN: 1044677X. doi:10.6028/jres.106.030 (2001).
37. Lytle, C. D. & Sagripanti, J.-L. Predicted Inactivation of Viruses of Relevance to Biodefense by Solar Radiation. *Journal of Virology* **79**, 14244–14252. ISSN: 0022-538X. doi:10.1128/JVI.79.22.14244-14252.2005 (2005).
38. Nixon, M. *et al.* The importance of a device specific calibration for smartphone colorimetry. *Color and Imaging Conference* **2019**, 49–54. ISSN: 2166-9635. doi:10.2352/issn.2169-2629.2019.27.10 (2019).
39. Gómez-Polo, C. *et al.* Comparison of the CIELab and CIEDE2000 color difference formulas. *The Journal of Prosthetic Dentistry* **115**, 65–70. ISSN: 00223913. doi:10.1016/j.prosdent.2015.07.001 (2016).
40. Luo, M. R. *CIEDE2000, History, Use, and Performance* in *Encyclopedia of Color Science and Technology* (ed Luo, M. R.) 202–207 (Springer New York, New York, NY, 2016). ISBN: 978-1-4419-8071-7. doi:10.1007/978-1-4419-8071-7\_7.
41. Mills, A. *et al.* Flagging up sunburn: a printable, multicomponent, UV-indicator that warns of the approach of erythema. *Chemical Communications*, 1345–1346. ISSN: 1359-7345, 1364-548X. doi:10.1039/b900569b (2009).
42. El Seoud, O. A., Baader, W. J. & Bastos, E. L. *Practical Chemical Kinetics in Solution* in *Encyclopedia of Physical Organic Chemistry, 5 Volume Set* (ed Wang, Z.) 1–68 (John Wiley & Sons, Inc., Hoboken, NJ, USA, 2016). ISBN: 978-1-118-46858-6. doi:10.1002/9781118468586.epoc1012.
43. Soda, Y. *et al.* Colorimetric absorbance mapping and quantitation on paper-based analytical devices. *Lab on a Chip* **20**, 1441–1448. ISSN: 1473-0197, 1473-0189. doi:10.1039/D0LC00028K (2020).
44. Abdel-Fattah, A. A., El-Kelany, M. & Abdel-Rehim, F. Development of a radiation-sensitive indicator. *Radiation Physics and Chemistry* **48**, 497–503. ISSN: 0969-806X. doi:10.1016/0969-806X(96)00014-X (1996).
45. Schmid, J. *et al.* UV-C inactivation of *Legionella rubrilucens*. *GMS hygiene and infection control* **12**, 1–6. ISSN: 2196-5226. doi:10.3205/dgkh000291 (2017).
46. Centers for Disease Control and Prevention. *Ultraviolet Radiation* <https://www.cdc.gov/nceh/radiation/ultraviolet.htm> (2020).
47. Stefan Källberg. *UVC exposure (254 nm) of UV sensitive material at different irradiation levels* tech. rep. MTt7P06268-3 (RISE Research Institutes of Sweden, Borås, Sweden, 2017).

48. Martinez, A. W. *et al.* Simple Telemedicine for Developing Regions: Camera Phones and Paper-Based Microfluidic Devices for Real-Time, Off-Site Diagnosis. *Analytical Chemistry* **80**, 3699–3707. ISSN: 0003-2700, 1520-6882. doi:10.1021/ac800112r (2008).
49. Lister, G. *et al.* The physics of discharge lamps. *Reviews of Modern Physics* **76**, 541–598. ISSN: 0034-6861, 1539-0756. doi:10.1103/RevModPhys.76.541 (2004).
50. SCHOTT Technical Glass Solutions GmbH. *BOROFLOAT® 33 – Optical Properties* [https://www.schott.com/d/borofloat/bde16ad3-70e5-48a0-b8ac-9146fcd34511/1.0/borofloat33\\_opt\\_en\\_web.pdf](https://www.schott.com/d/borofloat/bde16ad3-70e5-48a0-b8ac-9146fcd34511/1.0/borofloat33_opt_en_web.pdf) (2020).
51. Natura, U., Ehrt, D. & Naumann, K. Formation of radiation defects in high-purity silicate glasses in dependence on dopants and UV radiation sources. *Glastech. Ber. Glass Science and Technology* **74**, 23–31 (2001).
52. Furler, R. A. Angular Dependence of Optical Properties of Homogeneous Glasses. *ASHRAE Transactions* **97**, 1–9 (1991).

## Chapter 6

# Mapping of UV-C dose and SARS-CoV-2 viral inactivation across N95 respirators during decontamination

Reproduced with permission from: A. Geldert\*, A. Su\*, A. W. Roberts, G. Golovkine, S. M. Grist, S. A. Stanley, & Amy E. Herr. "Mapping of UV-C dose and SARS-CoV-2 viral inactivation across N95 respirators during decontamination", *posted on medRxiv and under peer review*, 2021.

\*contributed equally.

### 6.1 Introduction

The global shortages of N95 respirators during the COVID-19 pandemic has required crisis capacity strategies for decontamination and reuse of these complex, multilayered, made-for-single-use protective textiles. With established applications in water [1, 2], air [3, 4], and non-porous surface [5] disinfection, ultraviolet-C (UV-C) germicidal (200-280 nm) irradiation was identified as a promising and accessible method for N95 decontamination [6]. Upon sufficient absorption by nucleic acids, UV-C inactivates pathogens by damaging their genetic material [5]; thus, UV-C decontamination efficacy is critically dependent on total received dose (integrated irradiance over time). The U.S. Food & Drug Administration (FDA) definition of tier 3 "bioburden reduction" requires sufficient UV-C dose to be applied across the N95 to yield  $\geq 3\text{-log}_{10}$  inactivation of non-enveloped virus [7] ("log<sub>10</sub>" subsequently referred to as "log").

N95s present distinct challenges for UV-C decontamination: the applied surface dose required to decontaminate all N95 layers is orders of magnitude higher than the dose required

on non-porous surfaces [8, 9], and varies between N95 models [10, 11] due to substantial differences in material composition. UV-C decontamination protocols must ensure that all N95 surfaces receive sufficient dose for pathogen inactivation, while also not exceeding the exposure threshold for material degradation, as high cumulative doses of UV-C degrade N95 material [12]. Additionally, UV-C dose is nonuniformly distributed across the complex, 3D N95 surface due to Lambert's cosine law [13] and self-shadowing. Thus, UV-C distribution across N95 surfaces is highly dependent on N95 morphology, as well as the decontamination system and N95 positioning. Together, these characteristics complicate determination of the UV-C dose applied to all N95 surfaces in a decontamination system, impacting both research and implementation [14, 15].

Effective implementation requires translation of robust research studies linking on-N95 surface dose to viral inactivation for a given UV-C source emission spectrum and N95 model. However, coincident on-N95 dose and viral inactivation measurements are infeasible as the measurement sensor would shadow the pathogen. Furthermore, most UV-C dosimetry tools lack sufficient spatial resolution, throughput, and angular response for on-N95 measurements. As a result, UV-C dose for N95 decontamination is typically characterized indirectly. For example, to circumvent challenges associated with making UV-C dose measurements on non-planar surfaces, many studies, including a recent study of SARS-CoV-2 [16], assess UV-C dose and viral inactivation on flat coupons of N95 material. N95 coupon studies determine the UV-C dose required for viral inactivation throughout the porous N95 material layers, but fail to capture the impact of the 3D facepiece shape on the received UV-C dose across the N95 surface. Other approaches use optical modeling to estimate the UV-C distribution across N95 surfaces from the UV-C dose measured in a single location, in order to relate approximate UV-C dose to SARS-CoV-2 inactivation [17]. Optical modeling is an attractive approach to study UV-C distribution, as it can recapitulate nearly any UV-C system to provide a high-resolution map of irradiance distribution [18] via entirely user-defined system parameters. However, optical models alone cannot capture non-idealities such as irradiance fluctuations, bulb-to-bulb differences in power output, and environmental and material changes over time [5, 14, 19, 20]. Additionally, while the modularity of optical modeling is advantageous for broad applicability, the model accuracy depends on both the optics expertise of the user and the accuracy of user-defined parameters such as the reflective and scattering properties of all materials. Thus, the high resolution and rapid iteration capabilities of optical simulations would be most valuable when coupled with *in situ* validation measurements.

To this end, a promising *in situ* method has recently been developed to quantify on-N95 dose using UV-C photochromic indicators (PCIs) [14]. PCIs complement simulation results by providing absolute dose measurements and empirical validation. Planar, paper-like dosimeters similar to PCIs have been shown to have ideal angular detection response [21], though the angular response of UV-C PCIs has not been quantified. The low cost and small, flexible form factor of PCIs supports quantitative, spatially resolved and high-throughput on-N95 PCI dosimetry in the same exposure and in nearly the same on-N95 location as inoculated pathogens, minimizing confounding factors such as temporal or spatial variation [14] and angular dependence of UV-C irradiance [13]. Thus, PCIs may comprise

a cornerstone to better inform safe and effective UV-C decontamination, especially when corroborated by further study to confirm PCI angular response and suitability for readout by diverse, lower-cost color readers.

Here, to investigate the impact of UV-C dose variation on SARS-CoV-2 inactivation on N95s, we introduce a method to simultaneously map UV-C dose and SARS-CoV-2 viral inactivation across N95 respirator facepieces. We integrate two approaches for high-spatial-resolution on-N95 dosimetry: PCI quantification and optical modeling. We develop an optical modeling workflow to characterize UV-C dose distribution across N95s within a decontamination chamber to rapidly iterate on experimental design, and simultaneously inform and validate this model using *in-situ* PCI dose quantification. From the high-resolution simulated N95 dose maps, we identify pairs of proximal measurement sites receiving equivalent UV-C dose in order to measure UV-C dose at SARS-CoV-2 inoculation sites within the same UV-C exposure. For the first time, we apply quantitative *in-situ* PCI dosimetry to simultaneously quantify UV-C dose and SARS-CoV-2 inactivation across a model N95 facepiece (intra-N95) at multiple locations (intra-chamber), providing new, practical insight into how N95 facepiece shape impacts decontamination efficacy.

## 6.2 Materials and Methods

### Inter-UV-C chamber and radiometer assessment

All UV-C decontamination experiments were performed with Spectronics XL-1000 UV-C chambers with BLE-8T254 low pressure amalgam bulbs. Irradiance was measured using calibrated, NIST-traceable ILT 1254/TD UV-C radiometers (International Light Technologies, ILT) and corresponding ILT DataLight III meter software. A custom notch in the UV-C chamber doors allowed a cable to pass through for *in-situ* radiometer measurements. One chamber and radiometer were used exclusively in a biosafety level 3 (BSL-3) laboratory for SARS-CoV-2 inactivation experiments, while another set was used for all experiments outside BSL-3. The UV-C irradiance over time and space within the two chambers were concordant (Figure 6.1), as were measurements from the two radiometers (Figure 6.2).

### PCI measurements

For UV-C dose measurements, PCIs (UVC 100 Dosimeter dots, American Ultraviolet; 25.4 mm diameter) were cut into quarters prior to use. D65/10° L\*a\*b\* PCI color was measured using an RM200QC spectrophotometer (X-Rite, large aperture setting) and/or Color Muse colorimeter (Variable, Inc, with Variable color app). PCI quantification was performed as described previously [14]. Briefly, calibration curves relating PCI color change (CIEDE2000  $\Delta E$ ) to received dose were established by placing a radiometer and a PCI at two locations of equal irradiance within the UV-C chamber. PCIs were placed on a platform of similar height to the radiometer sensor (34 mm). The dose (calculated by integrating recorded radiometer

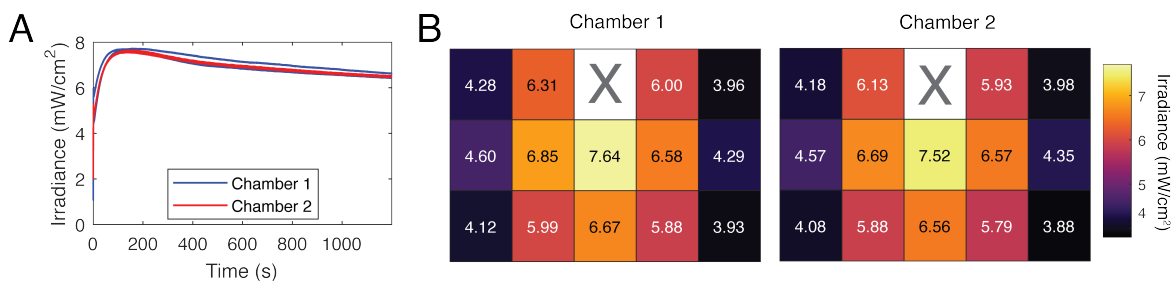


Figure 6.1: Two UV-C chambers have similar irradiance profiles over time and space. (A) Irradiance at the center of the chamber during the first 20 min of exposure after turning on the UV-C bulbs ( $N = 2$  for each chamber). Note decrease in output over time after bulb warm-up. (B) Heatmaps of spatial irradiance distribution within each chamber (average of 3 replicate measurements at each location).

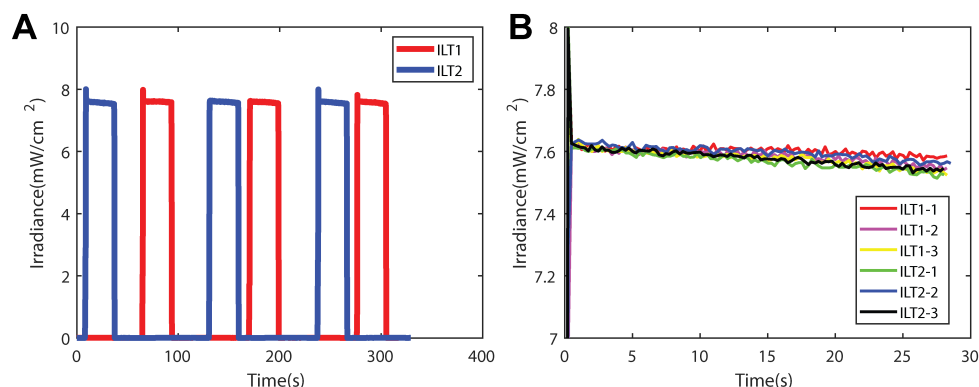


Figure 6.2: Equivalent performance of two ILT1254 radiometers. (A) Irradiance recorded by each radiometer (labeled ILT1, ILT2) when placed in the same location at the center of a UV-C chamber and exposed for 30 s in alternating fashion. (B) The irradiance data from (A) overlaid on top of one another, where  $t = 0$  represents the start of each exposure.

irradiance over time) and CIEDE2000  $\Delta E$  measured after 9 different exposure lengths were fit to a function based on first-order reaction kinetics ( $a$  and  $b$  are fit parameters):  $\Delta E = a \left( 1 - e^{-\frac{\text{dose}}{b}} \right)$  (Figure 6.3(A,C)). Ninety-five percent confidence intervals (CIs) on UV-C dose measurements were calculated via propagation of error from standard deviations of the fit parameters and the standard deviation of replicate  $\Delta E$  measurements of unexposed PCIs ( $N = 10$  and  $11$  for RM200QC measurement of PCI batches 1 and 2, respectively;  $N = 6$  and  $5$  for Color Muse measurement of PCI batches 1 and 2, respectively). Relative uncertainty was defined as  $\frac{\text{CI width}}{2 \times \text{estimated dose}}$  (Figure 6.3(B,D)). Batch-specific calibration curves were generated due to batch-to-batch variability (Figure 6.4). The PCI dynamic range was quantified as the dose range over which the relative uncertainty was  $<10\%$ . Custom MATLAB scripts performed PCI dosimetry analyses.



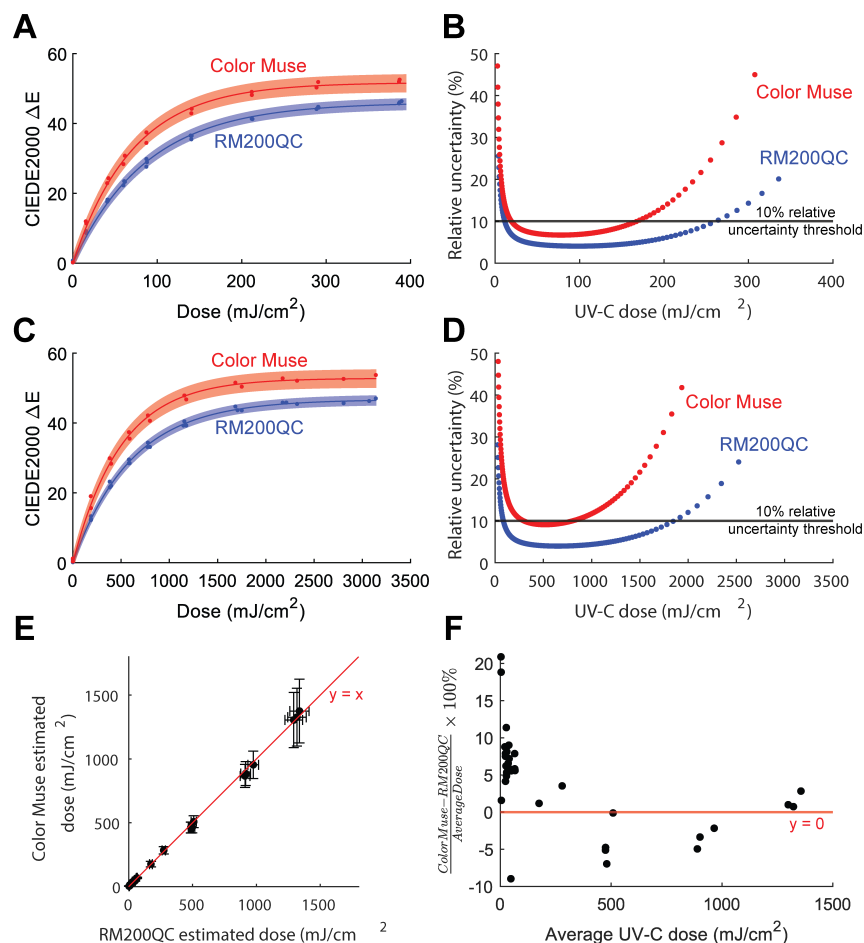


Figure 6.3: UV-C dose quantification from PCI color change. (A) Calibration curve relating UV-C dose to PCI color change (CIEDE2000  $\Delta E$ ) measured with either the RM200QC spectrophotometer ( $N = 3$  replicate data sets) or the Color Muse colorimeter ( $N = 2$  replicates). Shaded regions represent the 95% prediction interval on PCI color change predicted from measured UV-C dose. RM200QC:  $R^2 = 0.9976$ ,  $a = 46.0$  (45.3, 46.7),  $b = 87.4$  (83.6, 91.2). Color Muse:  $R^2 = 0.9963$ ,  $a = 51.7$  (52.8, 50.6),  $b = 71.2$  (66.5, 75.9). (B) Relative uncertainty of dose measurement.  $<10\%$  relative uncertainty from 11.3–261.4 mJ/cm<sup>2</sup> (RM200QC) or 19.2–168.1 mJ/cm<sup>2</sup> (Color Muse). (C) Calibration curve of Borofloat-covered PCI. RM200QC:  $R^2 = 0.9982$ ,  $a = 46.7$  (46.2, 47.3),  $b = 605.9$  (584.3, 627.5). Color Muse:  $R^2 = 0.9960$ ,  $a = 52.8$  (51.7, 53.9),  $b = 495.6$  (462.9, 528.3). (D) Relative uncertainty of Borofloat-PCI dose measurements.  $<10\%$  relative uncertainty from 85.0–1853.2 mJ/cm<sup>2</sup> (RM200QC) or 295.6–802.6 mJ/cm<sup>2</sup> (Color Muse). (E) UV-C doses measured from the same PCI using either the RM200QC or Color Muse. Error bars represent uncertainty in the predicted dose due to uncertainty in the calibration fit parameters and the  $\Delta E$  measurement. (F) Difference in dose measured by the Color Muse and RM200QC.  $N = 34$  PCIs.

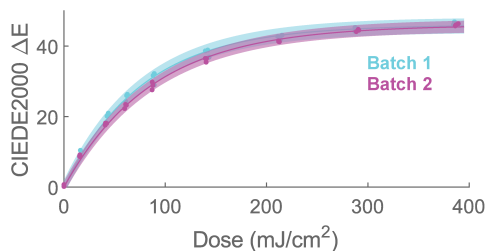


Figure 6.4: PCI calibration curve is batch-dependent. Each curve consists of 3 replicate datasets and was fit to the function based on first-order reaction kinetics [14]. For batch 1,  $R^2 = 0.9964$ ,  $a = 46.0$  (45.2, 46.8),  $b = 77.6$  (73.5, 81.6). For batch 2,  $R^2 = 0.9976$ ,  $a = 46.0$  (45.3, 46.7),  $b = 87.4$  (83.6, 91.2). Batch to batch variation may be due to changes in PCI starting color or variation in indicator reaction kinetics.

To measure doses beyond the PCI dynamic range on planar surfaces, a 1.1 mm-thick Borofloat glass attenuator (25.4 mm width and length, 80/50 scratch/dig quality, Precision Glass & Optics 0025-0025-0011-GE-CA) was placed over the PCI. A single batch of Borofloat had  $12.4\% \pm 0.4\%$  UV-C transmittance measured using a Spectroline XL-1500 chamber with BLE-1T155 bulbs and Model 308 data-logging radiometer with a 254 nm sensor (Optical Associates, Inc., OAI). We generated calibration curves specific to the PCI batch, attenuator, and colorimeter to quantify UV-C dose from PCI color change (CIEDE2000  $\Delta E$ ) with respect to an unexposed reference (Figure 6.3, Figure 6.4).

For all ratios of two PCI measurements (e.g., fold difference in on-N95 dose), other than cases where PCI measurements are normalized to a maximum PCI reading, we report total error: the root sum square of standard deviations associated with both replicate variation and propagated uncertainty in PCI dose estimation. All other error values report the standard deviation of replicate measurements.

## Angular response measurements

PCI angular response was characterized by measuring the RM200QC-measured dose quantified from PCIs exposed to a UV-C point source at different angles of incidence (Figure 6.5). To determine where UV-C output power is independent of distance, irradiance was measured at several distances from a UV-C source (Spectroline E-Series handheld UV lamp with a BLE-2537S bulb and custom-built 2.54 cm diameter aperture) using a radiometer. UV-C output power at each distance was calculated from the Keitz equation using the average ( $N = 3$ ) irradiance measured at different distances from the UV-C source [19]. The distance from the UV-C source at which output power changes by  $<5\%$  between measurements (determined here to be  $\geq 10.2$  cm) was considered to be the point at which UV-C output power is independent of distance, which indicates that UV-C is near-normally incident to a PCI perpendicular to the optical axis. Each PCI was affixed with double-sided tape to a glass microscope slide in a filter holder (Thorlabs FH2) mounted on a rotation platform

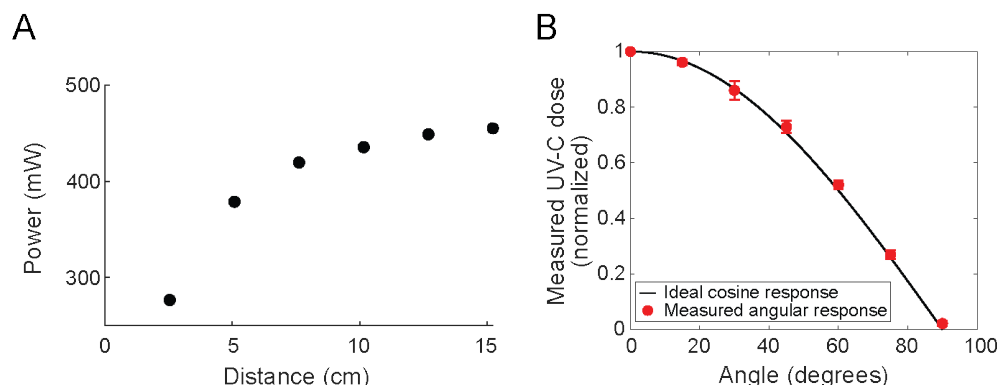


Figure 6.5: Measuring the angular response of PCIs. A) Irradiance was measured at several distances from the UV-C source using a radiometer to determine distance at which output power changes by  $<5\%$  between measurements (determined here to be  $\geq 10.2$  cm). B) PCIs have near-ideal cosine angular response. UV-C dose measured by a PCI with differing angles of incidence from a UV-C point source, normalized to the measured dose at  $0^\circ$ . The mean of 3 replicates is plotted (error bars indicate standard deviation of the replicates).

(Thorlabs QRP02). PCIs were placed 10.2 cm away from a UV-C lamp. Angular response was measured between  $0^\circ$ - $90^\circ$  in  $15^\circ$  increments, in accordance with the range of angles used to characterize the angular response of other dosimeters [22]. To ensure consistent UV-C output between exposures, a radiometer was used to monitor dose during each exposure; all PCIs within an experiment were exposed to the same dose, as measured by the radiometer. To avoid shadowing, the radiometer was placed behind the PCI and at an offset such that the PCI/glass slide did not shadow the radiometer.

## Optical model

To create a model of the respirator compatible with the optical modeling software, a 3M 1860 N95 with straps removed was scanned using a Creaform Go!SCAN 3D. After additional pre-processing, the N95 was positioned within a CAD model of the UV-C chamber (Figure 6.6). The entire assembly was then imported into non-sequential mode in Zemax OpticStudio Pro (Version: 20.3) and exploded into individual parts. Parts not essential to the optical model (e.g., screws, hinges, etc.) were ignored during simulations. UV-C source and surface parameters are listed in Table 6.1.

The N95 CAD object was converted to an absorbing detector, consistent with a previous study that approximated on-N95 UV-C distribution using an absorbing spherical detector [18], and positioned and/or duplicated to match *in-situ* chamber locations. All simulations were performed with “Use Polarization”, “Scatter NSC Rays”, “Split NSC Rays” and “Ignore Errors” engaged. Detector data were exported and analyzed using custom MATLAB scripts. Because the optical model may not accurately predict absolute dose due to environmental

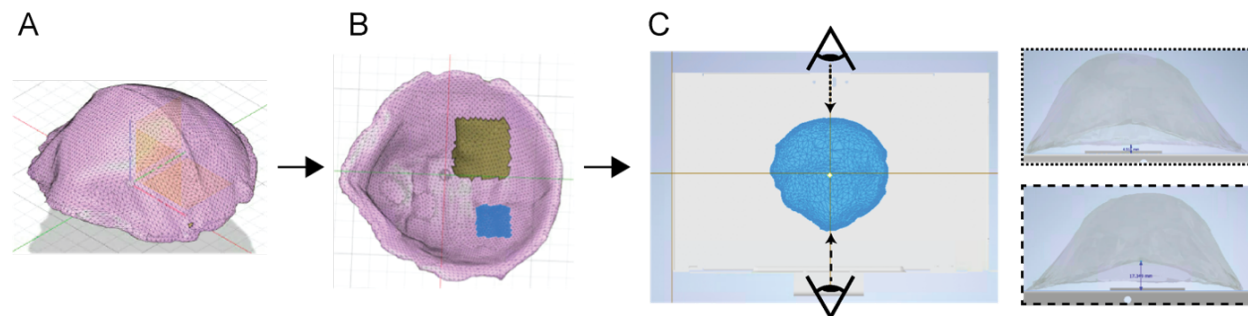


Figure 6.6: Preprocessing of scanned N95 for optical model. A) Scanned 3M 1860 N95 mesh model is roughly aligned to X-Y plane in Autodesk Fusion 360. B) The inner mesh layer facing the wearer was manually removed prior to converting the model to a solid and exporting as a .STEP file. C) A CAD model of the Spectronics XL-1000 and modified N95 .STEP file were imported into an Autodesk Inventor assembly. The Spectrolinker-1000 was positioned to align the bottom of the back-left chamber corner with the origin. The model N95 was aligned close to the center of the top surface of the chamber floor. The N95 pitch angle was adjusted so that the height of the nosepiece and the chin piece approximated values measured *in situ*. The entire assembly was then imported into the optical modeling software for use.

Table 6.1: Additional optical model specifications

UV-C source information		
Emission	254 nm, monochromatic	
Number of UV-C bulbs	5	
Filament-to-filament length	230 mm	
Diameter	3 mm	
Rays/source tube during simulations	$5 \times 10^7$	
Reflective properties applied to chamber surfaces		
Component	% reflective	% diffuse scattering
Top reflector	86	100
Rear panel	20	90
Front door	5	100
Sides and bottom panel	20	90

fluctuations, simulation results were normalized to the maximum value within the analyzed domain (e.g., entire chamber and/or N95(s)).

## UV-C dose distribution on chamber floor

UV-C dose distribution across the chamber floor was characterized *in situ* at 15 evenly spaced locations (Figure 6.7) using PCIs as described previously [14]; briefly, all 15 PCIs were simultaneously exposed to  $\sim 100$  mJ/cm<sup>2</sup>, then read with the RM200QC within 600

s. Peak UV-C irradiance within a 15 s exposure was also measured at 14 of these locations sequentially using a radiometer (the built-in chamber sensor obstructed placement at one location). Simulated UV-C dose at each location was extracted from the optical model using custom MATLAB scripts.

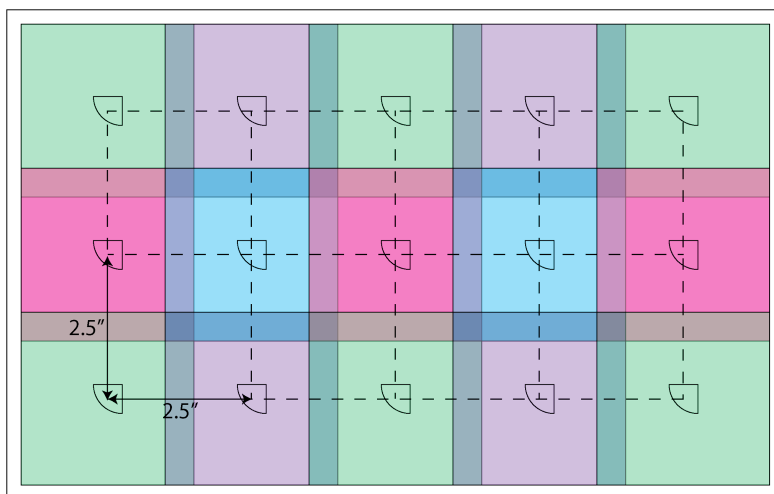


Figure 6.7: Map for *in-situ* measurements on chamber floor. Irradiance and dose were measured at 14 or 15 locations with a radiometer (colored squares) and PCIs (quarter-circles), respectively.

## UV-C dose distribution across N95 facepieces

*In situ:* To empirically measure on-N95 UV-C dose, PCIs with backing removed were adhered to the N95 facepiece, exposed, and subsequently removed for color quantification. To facilitate comparison to simulation, each PCI location on the N95 was recorded by measuring the PCI: 1) corner height ( $C$ ), 2) highest point height if not corner height (lowest point height if corner is highest) ( $h$ ), 3) rotation along the N95 surface ( $\phi$ , Figure 6.8), and 4) lateral distance from either the nosepiece-to-chin midline or side-to-side seam. N95 straps were removed to minimize shadowing and variability in N95 tilt. A printed floor map ensured reproducible N95 positioning in the chamber, with nosepieces toward the door (Figure 6.9).

*Optical model:* To characterize on-N95 UV-C dose from simulations, average values at specific *in-situ* PCI locations were extracted from the N95 detector simulation data using a custom MATLAB script. Briefly, N95 detector data were imported into MATLAB. The outline of each PCI was plotted on top of the simulated N95 dose map using the spatial parameters described above. The vertical height of the PCI ( $d$ ) was then defined as  $|C - h|$ . The angle of rotation toward the N95 surface ( $\alpha$ , Figure 6.8) of the PCI was calculated based on geometry.



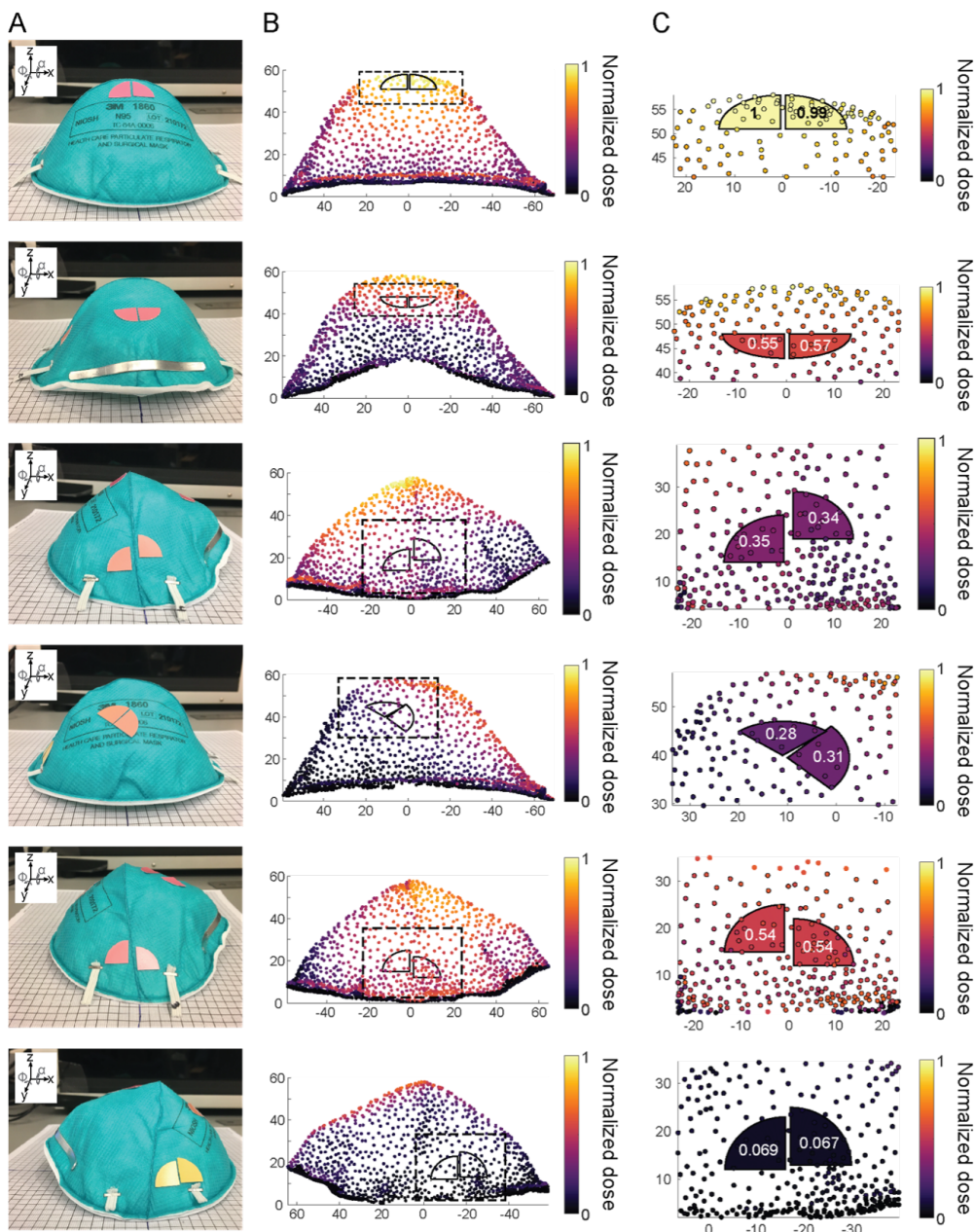


Figure 6.8: Optical model identifies paired measurement sites for *in-situ* PCI measurements. A) Images of exposed PCIs on N95s. Rotational angles  $\alpha$  and  $\phi$  are defined relative to the view angle. B) Scatterplots of simulation output overlaid with outlines of PCIs estimated to receive similar doses to identify measurement sites. C) High resolution plots of B (dashed rectangle) projected onto 2D plane. PCIs colored by average dose normalized to maximum average PCI-measured dose (also indicated in overlying text). Axes in B) and C) show distance in mm. Due to N95 curvature, the 2D-projected PCI outline may differ slightly from the true PCI footprint on an N95 *in situ*. We assume these differences are minimal.

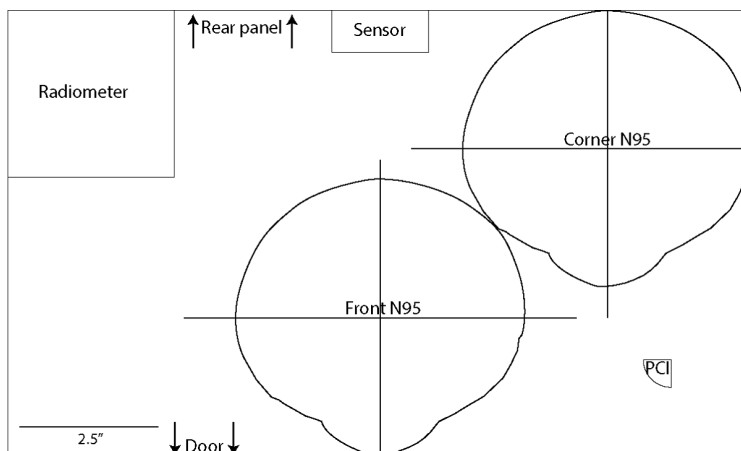


Figure 6.9: Chamber floor map to ensure reproducible placement of all physical components for on-N95 measurements. “Sensor” indicates location of built-in chamber sensor.

When the corner is either the highest or lowest part of the PCI:

$$\alpha = \cos^{-1} \frac{d}{r} \quad (6.1)$$

where  $r$  is the radius of the PCI. When corner is not the highest or lowest point of the PCI,

$$\alpha = \cos^{-1} \frac{d}{r \cdot \sin(\phi)} \quad (6.2)$$

where  $\phi$  is defined as the angle between the horizontal axis and highest PCI point.

The average on-N95 value from simulation was calculated as the mean value of the data points contained within the PCI perimeter, determined using the “inpolygon” function on a 2D projection of N95 data points and PCI outlines (Figure 6.8).

## Heatmap plots

All heatmaps of UV-C dose or irradiance were generated with the ‘inferno’ perceptually uniform, colorblind-friendly colormap, which was created by Stéfan van der Walt and Nathaniel Smith and adapted from Python’s matplotlib for use in MATLAB by Ander Biguri [23].

## SARS-CoV-2 preparation and handling

*Virus preparation and stock titration:* SARS-CoV-2 stocks of the strain USA-WA1/2020 were obtained from the Biodefense and Emerging Infections (BEI) Research Resources Repository. Dulbecco’s Modified Eagle Medium (DMEM, Sigma-Aldrich) containing 10% fetal bovine serum (FBS), 100 U/mL penicillin, and 100 µg/mL streptomycin was used for all cell culture. To produce virus passage 1, SARS-CoV-2 stocks were amplified in Vero-E6

cells (ATCC<sup>®</sup> CRL-1586<sup>™</sup>). In brief, to generate passage 1, 50  $\mu\text{L}$  of the BEI stock was inoculated onto confluent T-175 flasks of Vero-E6 cells and allowed to propagate until 50% cytopathic effect (CPE) was achieved ( $\sim 48$  h post infection) at which time cells were lysed through 1 round of freeze and thaw. CPE was defined as any virus-induced cell death or change in cell morphology observed using brightfield microscopy. Supernatants were collected and clarified by spinning at 1500 rpm for 300 s. The clarified viral supernatant was aliquoted and frozen at  $-80^\circ\text{C}$ . Aliquots were thawed for production of virus passage 2, which was performed as above except using Calu-3 human lung epithelial cells (UC Berkeley Cell Culture Facility). The concentration of virus passage 2 stocks was assessed by 50% tissue culture infectious dose ( $\text{TCID}_{50}$ ) assay using Vero-E6 cells and was determined to be  $8 \times 10^7$   $\text{TCID}_{50}/\text{mL}$ . Passage 2 cells were used for all experiments.

*N95 facepiece/coupon inoculation:* All coupons or N95 facepiece viral measurement sites were inoculated by pipetting 3 aliquots of 16.67  $\mu\text{L}$ , for a total of 50  $\mu\text{L}$ , of passage 2 virus stock at  $8 \times 10^7$   $\text{TCID}_{50}/\text{mL}$  onto the N95 material. While most locations on the N95 facepiece can be inoculated, for the hydrophobic N95 model used in this study, we observed that beaded inoculation droplets would roll off of steeply sloped surfaces (e.g., base of the facepiece near the chin or nosepiece), precluding inoculation at some locations. Alternate droplet sizes or N95 orientations during drying may mitigate this challenge. The SARS-CoV-2 inoculation volume was selected to balance drying time and assay sensitivity. Inoculation sites were left to dry at room temperature for 3.5 h in a biosafety cabinet. For paired on-N95 UV-C dose and SARS-CoV-2 inactivation measurements, where the PCIs were placed on the N95 prior to inoculation, we also verified that the N95s were not exposed to UV-C during the drying process. To do so, a PCI was positioned in the biosafety cabinet next to the N95 respirators while the inoculation sites dried, and the PCI color was measured using the RM200QC spectrophotometer before and after the 3.5 h drying period to verify no change in color.

*Virus titration:* After irradiation, inoculated coupons or N95 facepiece measurement sites were extracted using 12 mm biopsy punches. N95 facepiece punches were incubated in stationary 24-well plates containing cell culture media for  $\geq 30$  min. Viable SARS-CoV-2 virus was quantified by  $\text{TCID}_{50}$  assay by incubating confluent Vero E6 cells in 96 well plates with 10-fold serial dilutions of viral extraction sample at  $37^\circ\text{C}/5\% \text{CO}_2$ . Eight replicate wells were assessed per dilution. Five days after inoculation, CPE was scored visually under bright-field illumination using a  $4\times/0.13$  NA objective. Wells with CPE exhibited either complete destruction of the cell monolayer, or large areas of cell lysis/cell debris.  $\text{TCID}_{50}$  was calculated using the Reed-Muench method [24]. The limit of detection of the assay is 3.16  $\text{TCID}_{50}/\text{mL}$ , which was determined by calculating the  $\text{TCID}_{50}$  at which no CPE is observed in any replicate wells.

All study procedures were approved by the UC Berkeley Committee for Laboratory and Environmental Biosafety and conducted in agreement with BSL-3 requirements.



### SARS-CoV-2 dose response on N95 coupons

The UV-C dose response of SARS-CoV-2 was assessed by measuring viral inactivation on 3M 1860 N95 coupons inoculated with SARS-CoV-2 and exposed to different UV-C doses. By mapping UV-C irradiance across the chamber floor, we identified 5 locations of equivalent irradiance at which to place a radiometer, PCI, and 3 inoculated N95 coupons (Figure 6.10, Figure 6.11). PCIs and coupons were placed on custom-built platforms to match the height of the radiometer sensor.

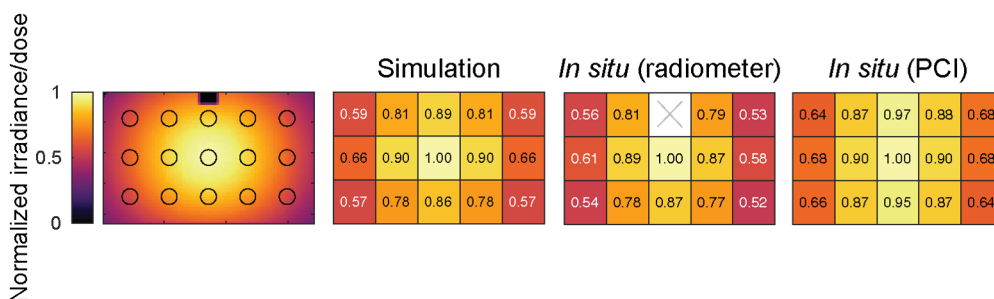


Figure 6.10: Spatial measurements across chamber floor estimated from simulation and measured *in situ* with a radiometer and PCIs. Leftmost heatmap shows simulation locations from which values were averaged to compare to *in-situ* measurements. To map UV-C dose distribution on the chamber floor within the optical model, a rectangular detector with the surface area of the chamber floor was positioned at approximately the base height of the diffuser of the physical radiometer (35.175 mm). Small fiducials were introduced in the back left corner and above the built-in chamber sensor to assist with orientation during data post-processing. The average value within a 25.4 mm diameter circle (diameter of radiometer diffuser) at each *in-situ* position was determined using a custom MATLAB script.

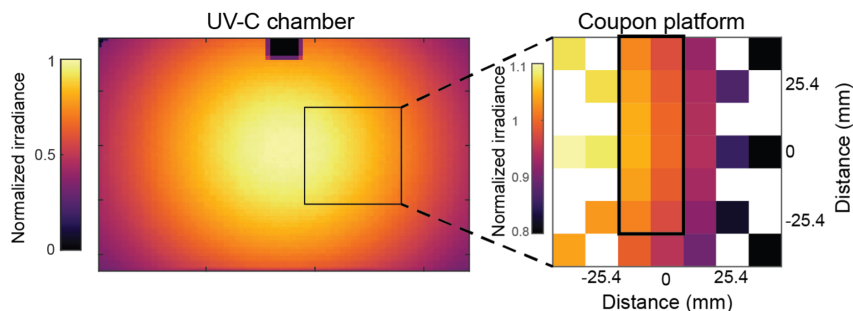


Figure 6.11: *In-situ* irradiance mapping using the radiometer at the coupon platform location identifies a 25.4 mm  $\times$  63.5 mm region (black outline) where irradiance varies  $<10\%$ . Within this area, 3 N95 coupons can fit for simultaneous exposure. Irradiance on the chamber heatmap is normalized to the maximum chamber irradiance. Irradiance on the coupon platform heatmap is normalized to the center irradiance (0 mm, 0 mm) position.

Platforms were built from laser-cut (HL40-5G-110, Full Spectrum Laser) pieces of 3.175 mm-thick acrylic (McMaster Carr 85635K421), joined with epoxy (J-B Weld 50176). Printed maps on the chamber floor and platforms ensured consistent positioning from run-to-run (Figure 6.12).

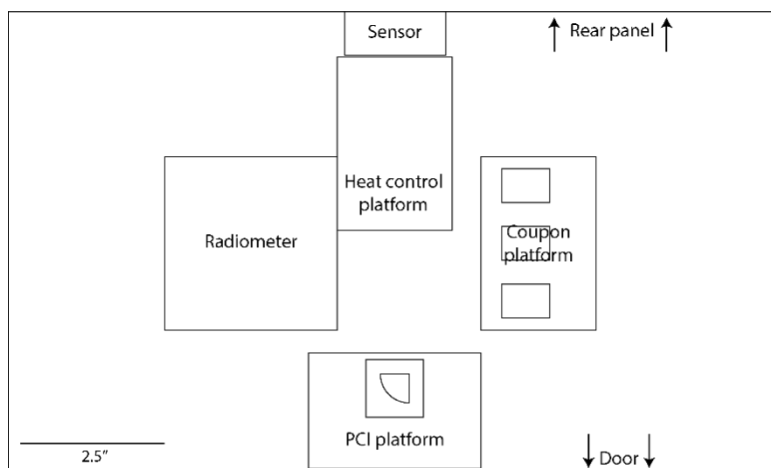


Figure 6.12: Map positioned on chamber floor to ensure reproducible placement of all physical components involved in coupon study.

For SARS-CoV-2 inactivation experiments, 3 replicate inoculated coupons were simultaneously irradiated with a given UV-C dose. Given the minimal impact of expiration status on UV-C decontamination efficacy (Figure 6.13), expired (i.e., past the manufacturer-recommended shelf life) N95s were used for experiments, to preserve non-expired N95s for healthcare workers. Coupons (15 mm  $\times$  20 mm) were cut from the edge of N95s to include the raised, sealed seam to minimize layer separation. The seam did not prevent the coupons from lying flat during UV-C exposure. Both a radiometer and PCI (with Borofloat attenuator for doses beyond the PCI upper limit of quantification) were used to quantify *in-situ* UV-C dose applied during each exposure. Exposure time was estimated by dividing the target dose by the irradiance at the coupon platform ( $\sim 6.4$  mW/cm<sup>2</sup> after bulb warm-up). To account for output degradation [14] (Figure 6.1A), exposure time was optimized by comparing the dose measured by the radiometer during a test exposure to the target dose.

After each exposure, PCI(s) were measured with both the RM200QC and the Color Muse. Biopsies were excised from all irradiated coupons, as well as one unexposed control coupon stored at room temperature outside the UV-C chamber. A TCID<sub>50</sub> assay was performed to assess SARS-CoV-2 viability.

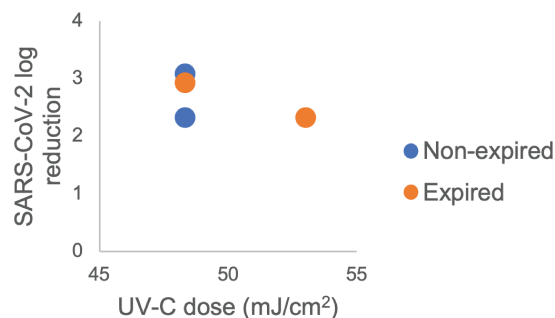


Figure 6.13: No difference in SARS-CoV-2 UV-C response was observed between non-expired and expired 3M 1860 N95 material coupons used in this study (N = 2 replicates/condition).

### Paired measurements of UV-C dose and SARS-CoV-2 inactivation on N95s

To simultaneously measure UV-C dose and SARS-CoV-2 inactivation on 3M 1860 N95 facepieces, PCIs (without attenuator) were affixed to N95s at each chosen dose measurement site, and accompanying SARS-CoV-2 inoculation sites outlined in advance to facilitate accurate viral deposition. SARS-CoV-2 was inoculated at each paired inoculation site. After drying, two N95s (‘corner’ and ‘front’ N95s) were placed in a UV-C chamber after bulb warm-up. To monitor dose during each exposure, a radiometer and PCI were also placed at their respective positions near the two corners of the chamber floor (Figure 6.9). After a 10 s UV-C exposure, PCIs were removed from the N95s and measured with both the RM200QC and the Color Muse. SARS-CoV-2 inoculation sites as well as an unexposed room temperature control coupon were excised following each UV-C exposure.

## 6.3 Results and Discussion

### Measuring UV-C dose and SARS-CoV-2 inactivation on and across N95s

In this study, we sought to understand the impact of N95 shape and placement on SARS-CoV-2 inactivation and how variation in inactivation relates to UV-C dose received across the N95 surfaces (Figure 6.14A). Building upon previous work quantitatively relating PCI color change to received UV-C dose [14], we introduce simultaneous measurement of SARS-CoV-2 inactivation and UV-C dose on N95 facepieces. We extend characterization of the quantitative PCI dosimetry method [14] in two ways. First, we measured the angular response of PCIs and verified a near-ideal response (Figure 6.5), confirming that PCIs are suitable to measure UV-C dose on non-planar surfaces. Second, to increase accessibility of the PCI dosimetry method, we compared the performance of a substantially lower-cost colorimeter to the previously reported spectrophotometer (Figure 6.3). Applying this PCI dosimetry

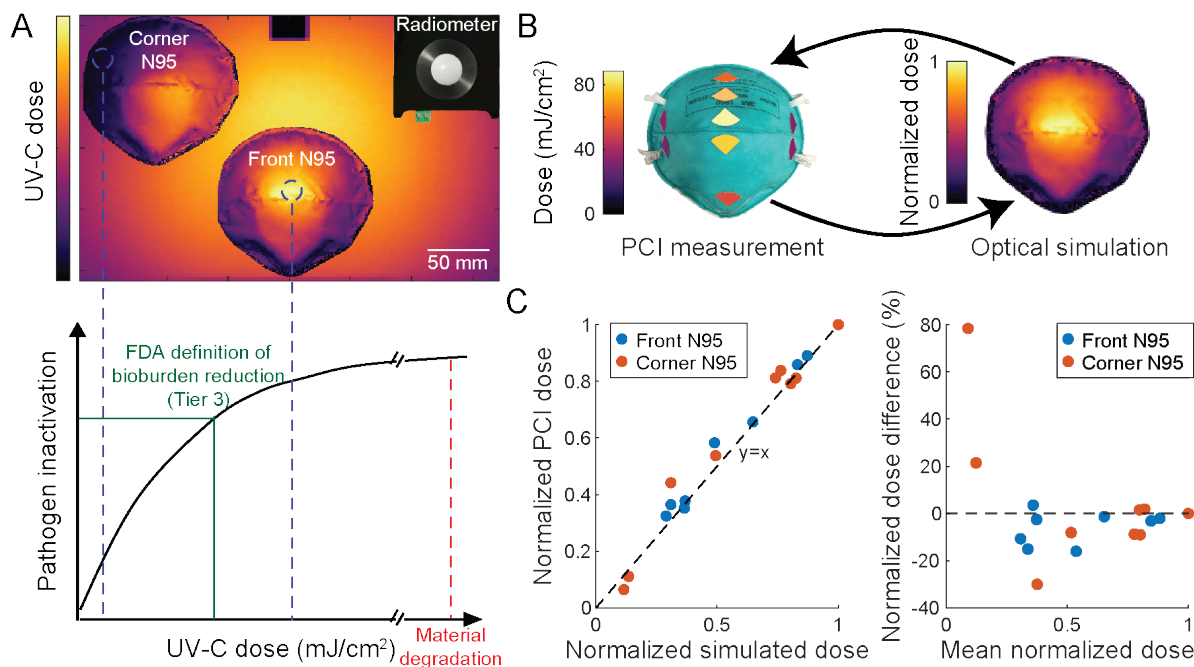


Figure 6.14: Integrated optical modeling and *in-situ* PCI measurement pipeline for simultaneous and near-coincident on-N95 UV-C dose and viral inactivation measurements. (A) Schematic highlighting how UV-C dose received across complex N95 surfaces can vary substantially, creating a narrow range of UV-C doses sufficient for pathogen inactivation while not exceeding the exposure threshold for material degradation. (B) *In-situ* PCI measurements and optical simulation results were used in tandem to inform and rapidly iterate on experimental design. (C) Comparison of normalized *in-situ* PCI and simulated doses at 7 discrete locations on N95s in 2 different chamber positions. Normalized dose difference was calculated as (simulation-PCI)/PCI. Dashed black lines ( $y = x$  on left,  $y = 0$  on right) indicate where the data would lie if PCI and simulation measurements were equal. Simulation tends to overestimate normalized *in-situ* PCI dose at low doses and underestimate *in-situ* PCI dose at high doses.

method, we paired PCI UV-C dose measurements with SARS-CoV-2 inactivation measurements to characterize the received dose and resulting viral inactivation variation across N95 facepiece surfaces.

Towards the study goal of assessing impact of N95 shape and placement on received UV-C dose and SARS-CoV-2 inactivation, we first identified the dynamic range of the UV-C dose-response curve. Only doses within this range will elucidate the variable relationship between UV-C dose and viral inactivation. The physical setup and exposure time of N95s in a decontamination chamber and the SARS-CoV-2 inoculation sites were then optimized to receive doses spanning that dynamic range. To perform this non-trivial optimization, we implemented both *in silico* optical ray-trace modeling and *in-situ* experimental PCI quan-

tification. We iterated between high-resolution modeling predictions and the more accurate on-N95 PCI-based UV-C dose measurements (Figure 6.14B).

## Building and validating optical model of a UV-C decontamination system

After optically modeling the UV-C decontamination chamber, we observed normalized simulation dose measurements differ from normalized *in-situ* radiometer measurements by an average of  $4.7\% \pm 4.5\%$  at 14 unique locations across the chamber floor (Figure 6.10). Assuming spatially invariant fluctuations, the normalized irradiance and normalized dose distribution within the system are equal. Therefore, the terms “normalized irradiance” and “normalized dose” are used interchangeably to compare to *in-situ* results, depending on the *in-situ* measurement approach (i.e., radiometer or PCI). From a 3D scan of a 3M 1860 N95 imported into the virtual UV-C chamber, normalized simulation measurements differ from normalized *in-situ* PCI measurements by an average of  $6.0 \pm 6.2\%$  across the facepiece centrally positioned near the chamber door (‘front N95’) (Figure 6.14C). The largest discrepancy on the door-facing N95 surface saw simulation underestimate the normalized PCI dose by  $\sim 16\%$ . For an N95 positioned in the chamber rear corner (‘corner N95’), simulation differed from *in-situ* PCI measurements by an average of  $18 \pm 25\%$ , with the largest discrepancies again occurring on the wall-facing N95 surfaces (Figure 6.14C and Figure 6.15). Differences between the simulation and *in-situ* measurements may arise due to N95-to-N95

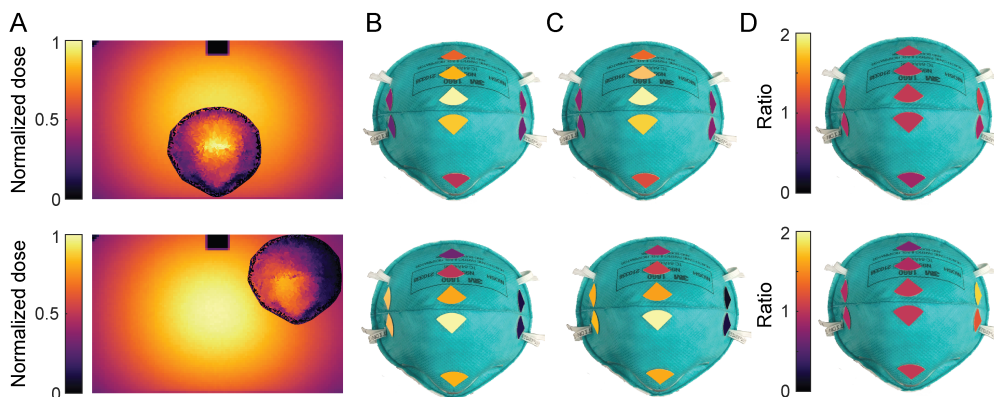


Figure 6.15: Correspondence between simulated and *in-situ* measured on-N95 UV-C dose distribution using PCIs. A) High resolution optical model output (generated using delaunayTriangulation in Matlab) represented as UV-C dose heatmaps across the front (top) and corner (bottom) N95s. B) Normalized dose at PCI locations extracted from simulation results. C) *In-situ* normalized dose measured using PCIs (average of  $N = 3$  replicates). D) Ratio of simulated to *in-situ* dose. All values were normalized to the highest on-N95 value, and on-N95 PCIs were false-colored to match color-mapped value. For PCI measurements, exposure times were chosen such that the on-N95 dose was within the PCI dynamic range.

shape variability (Figure 6.16), differences between true and modeled surface properties, and higher relative uncertainty of low-dose PCI measurements. Overall, however, on-N95 dose measurements correlate with simulation measurements at corresponding locations (Figure 6.14C). Thus, after validating the agreement between the simulation and *in-situ* measurements across both the chamber floor and an N95 in multiple chamber locations, we coupled the two measurement tools to design and optimize paired UV-C dose and SARS-CoV-2 inactivation experiments, leading to the first demonstration of simultaneous on-N95 viral inactivation and UV-C dose measurements to date.

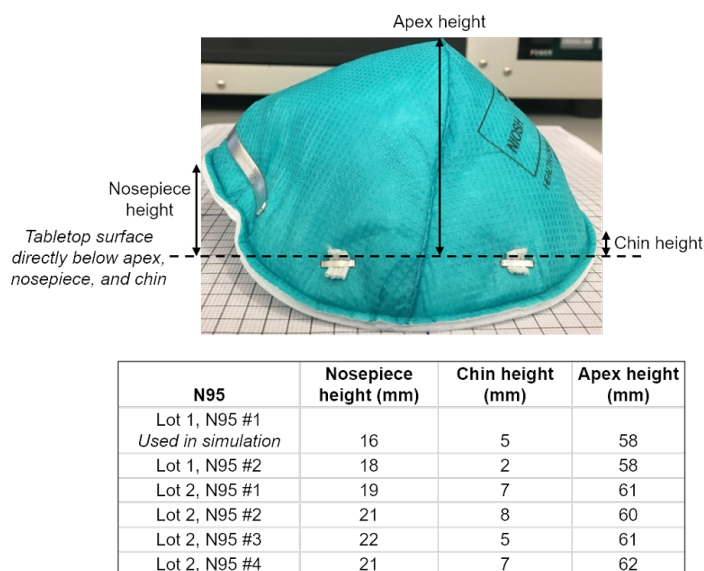


Figure 6.16: N95-to-N95 variation in morphology. Vertical heights from the tabletop to the seam on the nosepiece and chin seam of the N95, as well as to the apex. Heights are measured as the vertical distance from the nosepiece, apex, or chin to the tabletop directly below.

## Establishing dose-response for SARS-CoV-2 viral inactivation by UV-C

In order to quantify the UV-C dose dependence of SARS-CoV-2 viral inactivation without the added complexity of the N95 facepiece shape, we first considered SARS-CoV-2 viral inactivation using UV-C on coupons of N95 material. Simulation and *in-situ* measurements identified and validated five locations in a UV-C decontamination chamber that receive equivalent UV-C irradiance (<5% variation, Figure 6.17A) for location-paired UV-C dose and SARS-CoV-2 inactivation measurements on N95 coupons. We simultaneously exposed triplicate coupons inoculated with SARS-CoV-2 while recording the applied dose using both a radiometer and a PCI (Figure 6.18).



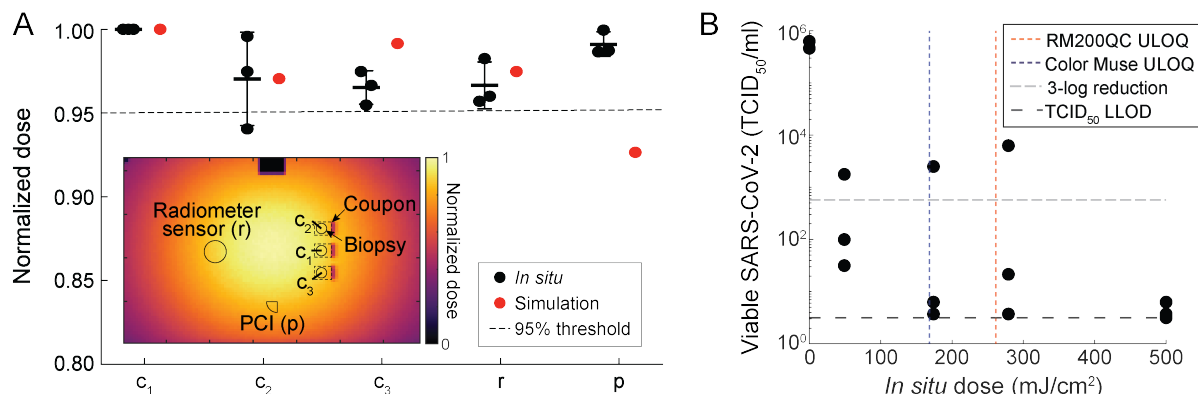


Figure 6.17: Measurement of UV-C dose required for SARS-CoV-2 inactivation on N95 coupons is informed by optical modeling and *in-situ* PCI dose measurements. (A) The optical model and *in situ* validation identified 5 locations receiving similar UV-C doses (<5% variation between mean *in-situ* dose measurements at each location). To inform biopsy location, the optical model also assessed the impact of each coupon seam (modeled as 15 mm-wide $\times$ 2.5 mm-tall $\times$ 1 mm-thick absorbing rectangular volumes at the right-hand side of each coupon) on UV-C distribution. *In-situ* PCI measurements simultaneously measure dose received at the PCI and 3 coupon locations while simultaneously recording irradiance with the radiometer. Mean and standard deviation are indicated for the *in-situ* measurements. (B) SARS-CoV-2 recovery on N95 coupons is dependent on *in-situ* UV-C dose, measured using a radiometer. During UV-C exposure, the radiometer, PCI, and triplicate N95 coupons were each placed as shown in (A). A Borofloat attenuator was placed on top of PCIs to measure doses  $>168$  mJ/cm<sup>2</sup> due to the limited PCI ULOQ. N=3 replicates per dose. ULOQ = upper limit of quantification. LLOD = lower limit of detection.

As the dynamic range of the PCIs measured with either color reader was insufficient to measure UV-C doses  $\gtrsim 260$  mJ/cm<sup>2</sup> (Figure 6.17B), for these higher doses we placed 1.1 mm-thick Borofloat glass over the PCI on the flat PCI platform to attenuate incident UV-C irradiance and extend the PCI dynamic detection range. We observed an extended upper limit of quantification (ULOQ) of 1853.2 mJ/cm<sup>2</sup> for the Borofloat-PCI pair when PCI color is measured with the spectrophotometer, compared to 261.4 mJ/cm<sup>2</sup> without the attenuator (Figure 6.3). When using the lower-cost colorimeter, Borofloat extended the ULOQ from 168.1 mJ/cm<sup>2</sup> to 802.6 mJ/cm<sup>2</sup> (Figure 6.3). While the ULOQ of the Borofloat-PCI pair when using the lower-cost colorimeter was lower than some of the UV-C doses included in the SARS-CoV-2 dose-response measurements, we observed good agreement in estimated dose using both color readers to measure all PCIs in SARS-CoV-2 experiments (Figure 6.3). Borofloat was only paired with PCIs on planar surfaces (not on-N95), as Borofloat transmittance may depend on incident angle, yielding non-ideal angular response [25].

To elucidate the SARS-CoV-2 dose-response curve, we measured SARS-CoV-2 viral activity from N95 coupons after exposure to applied UV-C doses ranging from 500-1500 mJ/cm<sup>2</sup>.

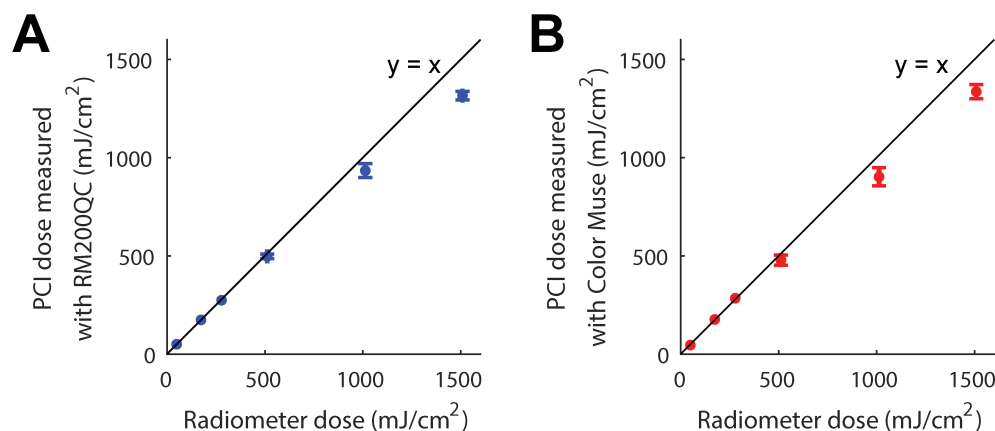


Figure 6.18: Correspondence between radiometer and PCI-measured UV-C doses during coupon experiments. PCI color change was measured with both the (A) RM200QC spectrophotometer, and (B) Color Muse colorimeter. For both color readers,  $N = 1$  for radiometer doses  $< 500$  mJ/cm<sup>2</sup> and  $N = 3$  for radiometer doses  $> 500$  mJ/cm<sup>2</sup>. For dose measurements  $> 168$  mJ/cm<sup>2</sup>, PCIs were coupled to a 1.1 mm-thick Borofloat attenuator. Vertical and horizontal error bars are the standard deviation of the estimated dose measurements. At UV-C doses  $< 1000$  mJ/cm<sup>2</sup>, PCI UV-C dose measurements were within 10% of radiometer measurements. PCIs underestimated dose (compared to the radiometer) up to 13% at  $\sim 1500$  mJ/cm<sup>2</sup>, which may be due to higher relative uncertainty in this dose range. Differences in temperature, humidity, and other environmental factors may cause the PCI response to differ between the BSL-3 environment and the non-BSL-3 location where PCI calibration curves were generated. Additionally, radiometer measurements were either made by integrating dose every 1 s in real-time or recording irradiance every 0.25 s and calculating integrated dose downstream; systematic differences between the two radiometer dose measurement methods may also contribute to differences between PCI and radiometer dose measurements.

The applied UV-C range was selected based on previous results demonstrating that  $\geq 1000$  mJ/cm<sup>2</sup> UV-C dose is required for 3-log inactivation of SARS-CoV-2 analogs on the majority of N95 models tested [10, 11, 26]. For all replicates exposed to 500-1500 mJ/cm<sup>2</sup>, we observed  $> 5$ -log SARS-CoV-2 reduction on N95 coupons (Figure 6.19). Furthermore, any remaining virus was below the limit of detection of the TCID<sub>50</sub> assay for all but one replicate, signifying that lower doses are required to identify the dynamic range of the dose-response curve of our assay.

We next assessed an applied UV-C dose range of 50-500 mJ/cm<sup>2</sup>. For these lower UV-C doses, we observed an average of  $> 3$ -log reduction of viable SARS-CoV-2 virus at all doses (Figure 6.17B), with no significant differences observed between non-zero UV-C dose conditions ( $N = 3$  replicates, Kruskal-Wallis test with Dunn's multiple comparison test). To investigate whether heating within the chamber during treatment contributes to SARS-CoV-2 inactivation, we first monitored the chamber temperature during UV-C exposures.



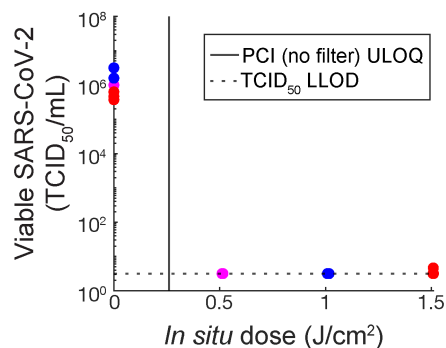


Figure 6.19: SARS-CoV-2 is inactivated by  $>3$ -log on N95 coupons when exposed to 0.5-1.5 J/cm<sup>2</sup> UV-C. ULOQ = upper limit of quantification. LLOD = lower limit of detection. Colors highlight temporally matched data (control coupons processed at the same time as exposed coupons). N = 3 replicates/condition.

Temperature in the UV-C chamber was recorded in preliminary experiments (outside of BSL-3) over time using a USB temperature/RH datalogger placed at the center of the chamber (Digi-Sense UX-20250-42). After UV-C bulb warm-up, we measured a chamber temperature of  $\sim 27^\circ\text{C}$ . Over an exposure time of 200 s, we observe a temperature increase of  $0.016 \pm 0.001^\circ\text{C/s}$  (N = 3 exposures), which corresponds to  $<3.3^\circ\text{C}$  increase over the total cumulative exposure time of all replicates (183 s). Thus, we did not anticipate the total temperature increase to contribute to SARS-CoV-2 inactivation, as equivalent SARS-CoV-2 survival after 30 min at  $22^\circ\text{C}$  and  $37^\circ\text{C}$  has been observed [27].

Furthermore, to directly verify that heating in the UV-C chamber did not contribute to SARS-CoV-2 inactivation, we measured SARS-CoV-2 inactivation on inoculated N95 coupons shielded from UV-C inside the chamber during exposures. An additional inoculated ‘heating control’ coupon was included in the chamber under UV-C-blocking material during the 175, 300, and 500 mJ/cm<sup>2</sup> exposures of the dose-response characterization on N95 coupons. Like the exposed and room-temperature unexposed control coupons, the inoculation site on the heating control coupon was excised and processed immediately after each exposure. Compared to control coupons kept outside of the chamber during exposures, we observed no significant difference in viable SARS-CoV-2 TCID<sub>50</sub>/mL (N = 3 replicates,  $p > 0.9999$ , Wilcoxon matched-pairs signed rank test, Figure 6.20). These observations suggest that chamber heating does not contribute to SARS-CoV-2 inactivation, as supported by literature on SARS-CoV-2 stability at measured chamber temperatures.

We postulate that the  $> 20\times$  higher SARS-CoV-2 UV-C susceptibility observed in this study as compared to previous literature is likely attributable to two factors. First, SARS-CoV-2 was inoculated without a soiling agent (e.g., sweat or sebum surrogates); soiling agents can decrease UV-C inactivation by 1-2 logs [11, 28]. Second, the 3M 1860 N95 material was very hydrophobic (water contact angle  $> 90^\circ$ , Figure 6.21), and deposited viral samples ‘beaded’ on the facepiece surface. Greater UV-C decontamination efficacy has generally been observed on hydrophobic N95 models [11], which we hypothesize may

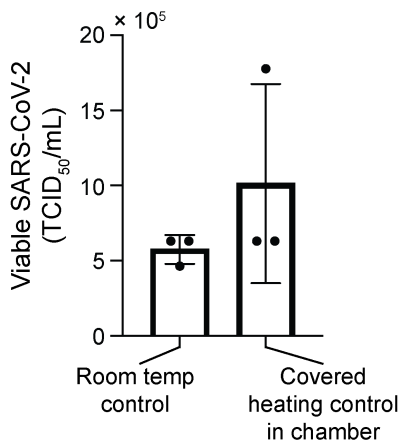


Figure 6.20: Comparison of SARS-CoV-2 survival on N95 coupons at room temperature and within the chamber shielded from UV-C during illumination. The inoculated heating control coupon was placed on a platform of the same height receiving approximately the same irradiance as the coupon and PCI platforms. An UV-C blocking acrylic cover was placed on top of the heating control coupon so that the coupon would be exposed to the temperature rise in the chamber but not to UV-C. A PCI placed under the acrylic cover near the heating control coupon verified that the heating control coupon was not irradiated with UV-C.  $p > 0.9999$ , Wilcoxon matched-pairs signed rank test.

be due to the greater proportion of virus inoculated on the outer N95 layers. Because the outer N95 layers receive more UV-C dose than inner layers [9], inactivation on hydrophobic N95s may more closely resemble nonporous surface decontamination, on which lower UV-C doses ( $\sim 4.3 \text{ mJ/cm}^2$ ) have been shown to yield  $>3$ -log reduction of SARS-CoV-2 [27]. Droplet imbibition into porous matrices is a complex process that depends on properties of the fluid and substrate [29], differences in inoculation volume and solution, and N95 material, all of which may influence the proportion of virus which penetrates into inner N95 layers. Thus, the system scrutinized here is an idealized model system and the SARS-CoV-2 dose response behavior observed is not anticipated to represent SARS-CoV-2 inactivation in clinical settings, where different N95 models and soiling are expected to substantially increase the UV-C dose necessary.

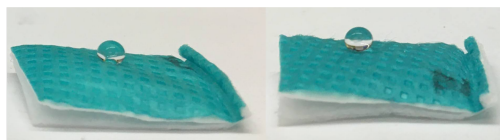


Figure 6.21: 3M 1860 N95 coupons are hydrophobic. A  $\sim 10 \text{ }\mu\text{L}$  water droplet on expired (right) and non-expired (left) N95 coupons has a contact angle  $>90^\circ$ , indicating high hydrophobicity. Additionally, the separation of the layers along the three sides without a seam may cause variable slope with respect to the UV-C source between coupons.

Given the results and precision of the TCID<sub>50</sub> assay (Figure 6.17B), and the anticipated single- or two-stage exponential inactivation of virus with increasing dose [5, 16, 30], we expect the dynamic range of our measured dose-response curve to exist between 0-50 mJ/cm<sup>2</sup>. Thus, we aimed to deliver UV-C doses within this range to map SARS-CoV-2 inactivation differences and UV-C dose nonuniformity to the complex 3D geometry of N95 facepieces (i.e., comparing among facepiece locations).

## On-N95 UV-C mapping informs design of near-coincident UV-C dose and SARS-CoV-2 inactivation measurements

Having established the UV-C dose response of SARS-CoV-2 on flat N95 coupons, we next investigated the magnitude of N95 shape-induced UV-C dose variation, as received UV-C is dependent on incident angle and distance from the UV-C source. Concomitantly, we sought to understand how the nonuniform on-N95 UV-C dose translated to SARS-CoV-2 viral inactivation efficacy. We aimed to map SARS-CoV-2 inactivation differences and UV-C dose nonuniformity across the N95 facepiece by simultaneously quantifying on-N95 dose with *in-situ* PCI measurements and SARS-CoV-2 inactivation via TCID<sub>50</sub>. The tandem approach allowed simultaneous measurement at multiple locations on intact N95 facepieces: a measurement not feasible with radiometers or viral inactivation measurements alone.

Because a PCI placed at the SARS-CoV-2 inoculation site would shadow the virus inoculum, we used optical simulation to identify pairs of adjacent measurement sites on-N95 which receive equal dose. With paired measurement sites, the UV-C dose received by a SARS-CoV-2 inoculation site can be monitored using a PCI placed at the proximal equivalent-dose site. Optical simulation rapidly reports the irradiance distribution across easily tunable N95 configurations with high spatial resolution, facilitating identification of: (1) locations to make on-N95 measurements that sample the range of delivered UV-C doses, and (2) measurement sites within each location receiving the same dose. Each location must be large enough to house two proximal measurement sites each  $\sim 13$  mm in diameter.

We first used optical simulation to characterize the UV-C dose distribution across the surface of multiple N95s within the chamber. To increase decontamination system throughput, multiple N95s are often irradiated simultaneously [31, 32], but care must be taken to ensure all N95s receive sufficient dose. Additionally, N95s must be separated to prevent cross-contamination. In the studied decontamination system, three N95s can be staggered within the chamber (e.g., two in the back, one in the front). Given the lateral symmetry in dose distribution within the chamber (Figure 6.1, Figure 6.10), we characterized UV-C dose distribution across two N95s in the unique positions in this ‘maximal-throughput’ layout, which we call ‘front’ and ‘corner’ (Figure 6.22A). From the simulated UV-C dose map across these N95s, we identified six discrete locations (a-f in Figure 6.22A) which sample the dose range. At locations a, b, d, and e, UV-C dose measured with PCIs *in situ* was  $3.3\% \pm 7.6\%$  greater than simulated dose (Figure 6.22A). At location f, *in-situ* UV-C dose was  $46.4\% \pm 7.6\%$  lower than simulated dose, in line with our previous findings that simulation

overestimated *in-situ* dose by 78% near that location (Figure 6.15). Similarly, the largest difference between simulated and *in-situ* UV-C dose was at location c, where simulated dose was  $26\% \pm 3\%$  lower than the *in-situ* dose, consistent with our previous finding that simulation underestimated the *in-situ* dose by 16% near the nosepiece of the front N95 (Figure 6.15). The discrepancy between simulation and *in-situ* UV-C dose measurements at select on-N95 locations highlights the importance of complementary *in-situ* measurements.

Within each location, the high-spatial-resolution map of simulated dose was used to identify two proposed measurement sites; dose at each site was then measured *in situ* using PCIs. Note that while measurement sites were often proximal to one another, the high-resolution simulation results established that some measurement sites receive the most similar dose when slightly offset (e.g., the sites at location b) due to the irregular N95 facepiece geometry and the off-center positioning of the N95s in the chamber. We observed that for locations receiving normalized UV-C doses  $>0.34$  (normalized to the maximum on-N95 dose), the doses across each proximal pair of PCI and inoculation sites were within 6.0% of each other, both in simulation and when measured *in situ*. For normalized UV-C doses  $\leq 0.34$  (at more steeply sloped and/or shadowed locations), the simulated doses at each pair of measurement sites were within 11.1% of each other and the doses measured *in situ* were within  $11.8\% \pm 6.0\%$  of each other (Figure 6.22B). Differences between paired sites may be larger at locations with greater curvature (e.g., location e), where PCI angle (and thus, received UV-C dose) is more sensitive to run-to-run variation in PCI placement as well as N95 morphology. At locations with normalized UV-C doses  $\leq 0.34$ , the higher relative uncertainty of PCI quantification at low doses may also contribute to a greater difference in dose at proximal sites. We quantified a relative uncertainty of  $\sim 20\%$  at the lowest-dose ( $\sim 5$  mJ/cm<sup>2</sup>) location, compared to a relative uncertainty of  $\sim 5\%$  at all other locations when PCIs are measured with the RM200QC (Figure 6.3B).

## Intra-chamber variation in UV-C dose and SARS-CoV-2 inactivation

Having identified paired on-N95 measurement sites receiving equivalent dose, simultaneous measurements of UV-C dose and SARS-CoV-2 inactivation on intact N95s could be performed. We assessed N95s placed at the front and corner positions in the decontamination chamber and chose an exposure time such that dose received across the N95 surfaces would span the dynamic range of 0-50 mJ/cm<sup>2</sup> determined from the coupon study (Figure 6.17B). For analysis, both UV-C dose and SARS-CoV-2 log reduction were normalized to the respective maximum value measured in the system within each replicate UV-C exposure.

UV-C dose and SARS-CoV-2 log reduction correspond well (Figure 6.22C) and are positively and linearly correlated ( $r^2 = 0.7016$ ;  $p = 1.4428 \times 10^{-5}$ ) (Figure 6.22D). SARS-CoV-2 dose response is still being investigated, but is expected to be primarily log-linear [30, 33–35] in agreement with other pathogens. While the dose response curve likely has shoulder and/or tailing behavior at the lower and upper ends [5], these nonlinear regions may not

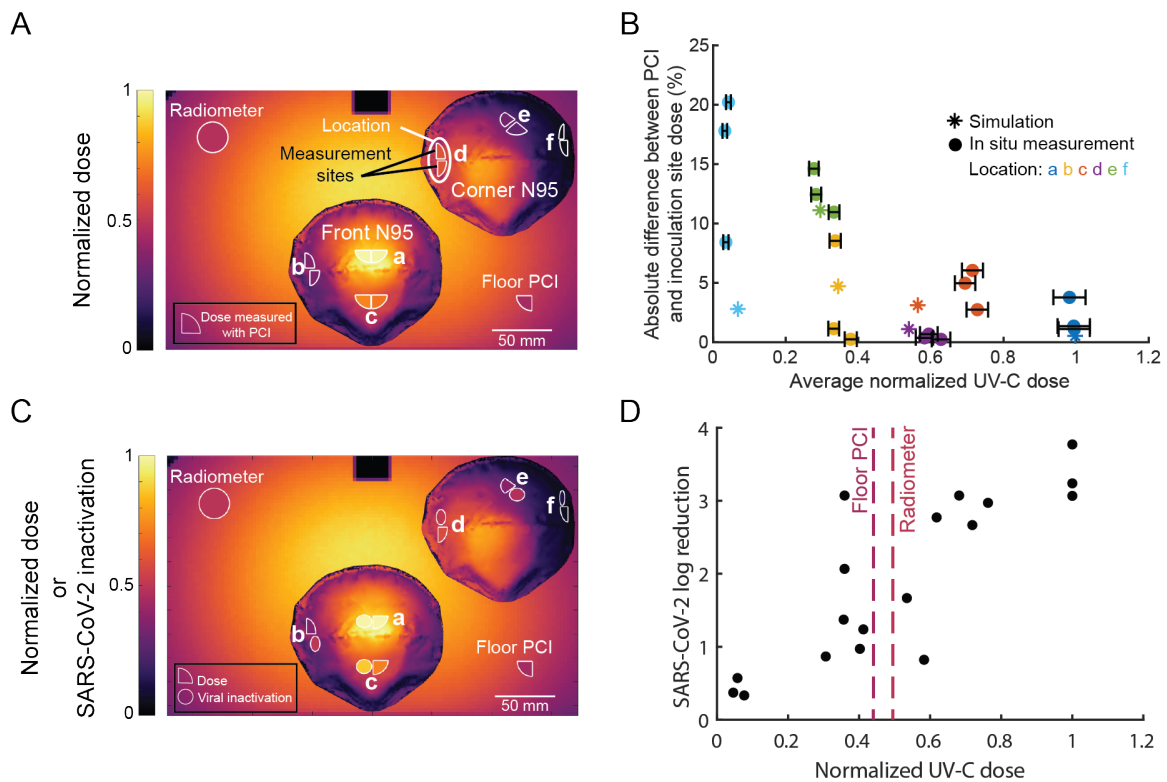


Figure 6.22: Paired on-N95 measurements of UV-C dose and SARS-CoV-2 inactivation show correlated, several-fold variation in dose and inactivation across one decontamination chamber. (A) Optical simulation of UV-C dose distribution over two 3M 1860 N95 facepieces in the UV-C chamber, overlaid with PCIs at paired measurement sites for viral inactivation and dose measurement. Heatmap shows simulated UV-C dose (normalized to the maximum dose in the chamber). PCI fill color represents the mean dose measured with PCIs *in situ* across triplicate measurements. (B) Comparison of dose differences within paired measurement sites. Data are colored by on-N95 location. Horizontal error bars on measured values represent the error in estimated dose. (C) Average normalized UV-C dose (quarter-circles) and SARS-CoV-2 inactivation (circles) at measured locations on front and corner N95, colored by the normalized value. Values are normalized to measurements at the apex of the front N95. Surrounding heatmap shows simulated UV-C dose. (D) SARS-CoV-2 inactivation on N95 facepieces is proportional to UV-C dose received. Selected locations on two N95 facepieces in the Spectronics XL-1000 UV-C chamber receive a  $17.4 \pm 5.0$ -fold difference in UV-C dose, which yields an  $8.2 \pm 1.4$ -fold difference in SARS-CoV-2 log reduction.

be captured with the range and resolution of UV-C doses tested here. The dose required for 90% inactivation ( $D_{90}$ ) estimated from a linear regression on the dose-response curve ( $r^2 = 0.78$ ) is  $\sim 19$  mJ/cm<sup>2</sup>, higher than the  $D_{90}$  of  $\sim 1.4$  mJ/cm<sup>2</sup> for dried SARS-CoV-2 on a nonporous surface [33], as expected (Figure 6.23).

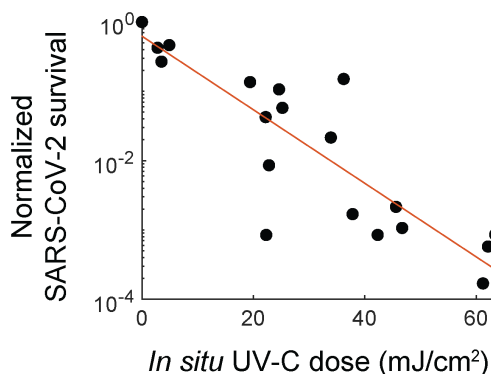


Figure 6.23: Normalized on-N95 SARS-CoV-2 dose-response curve for 2 N95 facepieces. Normalized SARS-CoV-2 survival is calculated as  $TCID_{50}/mL$  divided by the time-matched negative control  $TCID_{50}/mL$ . Red line illustrates the linear regression on *in-situ* UV-C dose and  $\log(\text{survival})$  with equation:  $y = -0.0531*x - 0.2045$  ( $R^2 = 0.78$ ). Based on linear regression, the estimated  $D_{90}$  dose is between 18.83 - 19.03 mJ/cm<sup>2</sup>, depending on whether the y-intercept value is ignored or considered, respectively.

Similar to the coupon study, we observe varying SARS-CoV-2 inactivation among replicate inoculation sites receiving similar UV-C dose ( $1.1 \pm 0.8$ -log difference in inactivation between replicates), which we hypothesize may be due to: (1) the quantal nature of the  $TCID_{50}$  assay [36, 37], and/or (2) variability in the slope of the coupon surface caused by separation of N95 layers along the three sides without a seam (Figure 6.21). Slight variations in the amount of virus inoculated, viral extraction efficiency, and excision area may also contribute to technical variation in measured  $TCID_{50}/mL$ . To characterize intra-chamber variation, we quantified the fold difference in UV-C dose and SARS-CoV-2 log reduction across both N95 facepieces in the chamber. Simulation predicted a 14.9-fold difference in UV-C dose across both N95 facepieces in the chamber, and we measured *in situ* a dose difference of  $17.4 \pm 5.0$ -fold. This UV-C dose range yielded an  $8.2 \pm 1.4$ -fold difference in SARS-CoV-2 log reduction (from  $0.4 \pm 0.1$ -log reduction at location f to  $3.4 \pm 0.4$ -log reduction at location a). The observed  $2.9 \pm 0.2$ -log difference in SARS-CoV-2 survival across N95s within one chamber is substantial, given the FDA definition of “bioburden reduction” on N95 respirators that requires  $\geq 3$ -log reduction of non-enveloped pathogens [7]. To our knowledge, this is the first study to rigorously quantify both UV-C dose and viral inactivation at paired locations on intact N95s, to understand how UV-C dose distribution and resulting decontamination efficacy depend on N95 facepiece shape.

Because *in-situ* dose is often monitored at an off-N95 location in decontamination proto-

cols [38], we characterized the relationship between on-N95 dose and the dose measured on at a specific low-irradiance location on the chamber floor. *In-situ* dose is often monitored at an off-N95 location in decontamination protocols [38], as on-N95 dose measurements would shadow the underlying N95 region from irradiation. To test whether UV-C dose monitoring on the chamber floor could serve as a proxy for the lowest dose received by N95s in the chamber, we compared the dose received in two of the lowest-dose locations on the chamber floor to the lowest dose measured on-N95. Based on the simulation of UV-C dose distribution across the chamber floor (Figure 6.22(A,C)), we anticipated that the UV-C chamber corners receive the lowest on-floor dose, and thus we chose to measure dose at two corners using a radiometer and PCI. Compared to the maximum on-N95 dose measured, the doses on the floor in the chamber corners were  $49.5\% \pm 1.6\%$  (radiometer location) and  $44.0\% \pm 0.7\%$  (floor PCI location) of the maximum on-N95 dose, whereas the lowest on-N95 dose measured was  $6.0\% \pm 1.6\%$  of the maximum on-N95 dose (Figure 6.22(C-D)). Thus, in the UV-C chamber tested here, dose monitoring on the chamber floor cannot serve as a proxy for the lowest on-N95 UV-C dose, even if on-floor dose is monitored in the lowest-irradiance locations. As can be seen in the heatmaps and values reported in Figure 6.22(C-D), steeply sloped regions (particularly on the corner N95) receive several-fold lower UV-C dose than the lowest-irradiance location on the chamber floor. If a protocol is tuned only to ensure the on-floor monitoring location receives sufficient dose for decontamination, the N95s will not be fully decontaminated. Instead, care must be taken to quantify the relationship between the lowest on-N95 UV-C dose and the dose received at any *in-situ* monitoring point. This relationship can then be used to ensure that all N95 surfaces receive at least the on-N95 target dose, as described previously [14].

### Intra-N95 variation in UV-C dose and SARS-CoV-2 inactivation

In addition to characterizing intra-chamber variation, we also analyzed UV-C dose and SARS-CoV-2 inactivation variation across each individual N95. On the front N95, the apex (location a) receives the highest dose while the more steeply sloped regions near the base of the sides of the N95 (location b) receive some of the lowest doses that can be measured with our approach, given the footprint of the PCI and SARS-CoV-2 inoculation site. Across the locations sampled on the front N95, simulation predicted a 3.0-fold difference in UV-C dose, and we measured a  $2.8 \pm 0.4$ -fold difference in UV-C dose using PCIs *in situ*. This variation in UV-C dose yielded a  $2.8 \pm 1.5$ -fold difference in SARS-CoV-2 log reduction (from  $1.6 \pm 1.2$ -log reduction at location b to  $3.4 \pm 0.4$ -log reduction at location a). While placing the N95 directly in the center of the UV-C chamber rather than offset toward the door would increase UV-C dose uniformity, throughput may be reduced, as the number of N95s that could fit in the chamber without contacting each other would be reduced from three to one.

Across the 3 measured locations on the facepiece of the corner N95, simulation predicted an 8.1-fold difference in UV-C dose and we measured a  $10.2 \pm 3.3$ -fold difference in dose. This variation in UV-C dose yielded a  $4.9 \pm 1.3$ -fold difference in SARS-CoV-2 inactivation (from  $0.4 \pm 0.1$ -log reduction at location f to  $2.1 \pm 0.7$ -log reduction at the maximum-dose

location on the corner N95, which was either location d or e depending on the replicate). However, because the measurement locations were chosen to evenly sample the range of UV-C doses applied across both (front and corner) N95s, the measured locations on the corner N95 did not capture the maximum corner N95 dose near the apex (Figure 6.22(A,C)). Thus, we expect that the total variation in UV-C dose and resulting viral inactivation on the corner N95 would be even higher than measured here.

We also compared the magnitude of variation in UV-C dose and SARS-CoV-2 inactivation on the front and corner N95s. As compared to the front N95, the corner N95 had greater intra-N95 variation in both UV-C dose and SARS-CoV-2 inactivation. In contrast to the front N95, which had an equal amount of variation (2.8-fold) in UV-C dose and SARS-CoV-2 inactivation, the corner N95 had a difference in UV-C dose (10.2-fold) greater than the difference in SARS-CoV-2 inactivation (4.9-fold). We hypothesize that the corner N95 receives UV-C doses which may be in the shoulder of the SARS-CoV-2 survival curve, where SARS-CoV-2 inactivation is not fully log-linear with dose [5]. If the corner N95 receives UV-C doses in this shoulder region, the magnitude of intra-N95 UV-C dose variation will be larger than the amount of variation in SARS-CoV-2 inactivation.

Characterization of UV-C dose distribution across N95s within a decontamination system is crucial for informing decontamination protocols and evaluating throughput. In our system, we observed substantially lower variation in UV-C dose and SARS-CoV-2 inactivation across a single N95, as compared to across both N95s in the chamber, which suggests that approaches to increase decontamination throughput should be carefully considered. Including more N95s in the chamber each cycle may not necessarily increase throughput as compared to a single N95 in the center of the chamber, as multiple N95s likely have more nonuniform on-N95 dose because they are more spread out and can shadow each other. Additionally, greater UV-C dose nonuniformity increases the exposure time needed for all N95 surfaces to reach the minimally acceptable UV-C dose, which in turn affects the total number of safe reprocessing cycles prior to N95 material degradation (Figure 6.14A) [12]. The simulation and *in-situ* dose measurement workflows we demonstrate here help inform N95 positioning within decontamination systems to optimize decontamination cycle time, pathogen inactivation, and the maximum number of safe reuses.

## 6.4 Conclusions

In summary, we have demonstrated that the N95 facepiece shape and position within a UV-C decontamination system have substantial influence on the on-N95 UV-C dose distribution and concomitant decontamination efficacy. We introduce a workflow to combine optical modeling and *in-situ* quantitative PCI dosimetry to characterize on-N95 UV-C dose with high spatial resolution, high throughput, and near-ideal angular response. For the first time, we combined simultaneous and robust quantitative UV-C dose measurements with SARS-CoV-2 inactivation measurements at specific locations on N95 respirators to probe the relationship between on-N95 dose and pathogen inactivation within each UV-C exposure.



The substantial variation in on-N95 UV-C dose and SARS-CoV-2 inactivation we observed in a single decontamination chamber highlights how nonuniform UV-C dose distribution impacts pathogen inactivation and total UV-C exposure (which influences N95 material degradation and the safe number of decontamination cycles). We further demonstrated that a lower-cost colorimeter accurately quantifies dose from PCIs, making the PCI quantification workflow more accessible. Additional investigation into alternative color metrics may extend the dynamic range of PCIs measured with lower-cost color readers. Future studies are needed to characterize SARS-CoV-2 dose response in more clinically relevant conditions, such as with the addition of soiling agents and on varying N95 models. Extending the dynamic range of PCIs, while maintaining a near-ideal angular response, is also critical for measurement of  $\gtrsim 200$  mJ/cm<sup>2</sup> UV-C dose on-N95. Overall, given the diversity of UV-C systems and setups, the on-N95 UV-C dosimetry approach here facilitates characterization of decontamination protocols of any UV-C system, supporting system-specific validation that is critical to ensuring safe and effective N95 decontamination.

# Bibliography

1. U.S. Environmental Protection Agency & C. *Ultraviolet Disinfection Guidance Manual for the Final Long Term 2 Enhanced Surface Water Treatment Rule* tech. rep. EPA 815-R-06-007 (U.S. Environmental Protection Agency Office of Water, Washington, DC, 2006), 436.
2. Sun, Z. *et al.* Using Algal Virus *Paramecium bursaria* Chlorella Virus as a Human Adenovirus Surrogate for Validation of UV Treatment Systems. *Environmental Science & Technology* **54**. Publisher: American Chemical Society, 15507–15515. ISSN: 0013-936X. doi:10.1021/acs.est.0c06354 (2020).
3. Memarzadeh, F., Olmsted, R. N. & Bartley, J. M. Applications of ultraviolet germicidal irradiation disinfection in health care facilities: effective adjunct, but not stand-alone technology. *American Journal of Infection Control* **38**, S13–24. ISSN: 1527-3296. doi:10.1016/j.ajic.2010.04.208 (2010).
4. Qiao, Y. *et al.* Greater than 3-Log Reduction in Viable Coronavirus Aerosol Concentration in Ducted Ultraviolet-C (UV-C) Systems. *Environmental Science & Technology* **55**. Publisher: American Chemical Society, 4174–4182. ISSN: 0013-936X. doi:10.1021/acs.est.0c05763 (2021).
5. Kowalski, W. *Ultraviolet Germicidal Irradiation Handbook: UVGI for Air and Surface Disinfection* ISBN: 978-3-642-01999-9 (Springer Science & Business Media, Berlin, Heidelberg, 2010).
6. Centers for Disease Control and Prevention. *Decontamination and Reuse of Filtering Facepiece Respirators* <https://www.cdc.gov/coronavirus/2019-ncov/hcp/ppe-strategy/decontamination-reuse-respirators.html> (2020).
7. Center for Devices and Radiological Health. *Recommendations for Sponsors Requesting EUAs for Decontamination and Bioburden Reduction Systems for Face Masks and Respirators During the Coronavirus Disease 2019 (COVID-19) Public Health Emergency* tech. rep. FDA-2020-D-1138 (Center for Devices and Radiological Health, 2020).
8. Tseng, C.-C. & Li, C.-S. Inactivation of Viruses on Surfaces by Ultraviolet Germicidal Irradiation. *Journal of Occupational and Environmental Hygiene* **4**, 400–405. ISSN: 1545-9624, 1545-9632. doi:10.1080/15459620701329012 (2007).

9. Fisher, E. & Shaffer, R. A method to determine the available UV-C dose for the decontamination of filtering facepiece respirators: UV-C decontamination of respirators. *Journal of Applied Microbiology* **110**, 287–295. ISSN: 13645072. doi:10.1111/j.1365-2672.2010.04881.x (2011).
10. Mills, D. *et al.* Ultraviolet germicidal irradiation of influenza-contaminated N95 filtering facepiece respirators. *American Journal of Infection Control* **46**, e49–e55. ISSN: 01966553. doi:10.1016/j.ajic.2018.02.018 (2018).
11. Heimbuch, B. & Harnish, D. *Research to Mitigate a Shortage of Respiratory Protection Devices During Public Health Emergencies* tech. rep. HHSF223201400158C (Applied Research Associates, Inc., 2019).
12. Lindsley, W. G. *et al.* Effects of Ultraviolet Germicidal Irradiation (UVGI) on N95 Respirator Filtration Performance and Structural Integrity. *Journal of Occupational and Environmental Hygiene* **12**, 509–517. ISSN: 1545-9624. doi:10.1080/15459624.2015.1018518 (2015).
13. Reifsnnyder, W. E. Radiation geometry in the measurement and interpretation of radiation balance. *Agricultural Meteorology* **4**, 255–265. ISSN: 00021571. doi:10.1016/0002-1571(67)90026-X (1967).
14. Su, A. *et al.* Quantitative UV-C dose validation with photochromic indicators for informed N95 emergency decontamination. *PLOS ONE* **16**, e0243554. ISSN: 1932-6203. doi:10.1371/journal.pone.0243554 (2021).
15. Grist, S. M. *et al.* Current Understanding of Ultraviolet-C Decontamination of N95 Filtering Facepiece Respirators. *Applied Biosafety*. ISSN: 1535-6760. doi:10.1089/apb.20.0051 (2021).
16. Fischer, R. J. *et al.* Effectiveness of N95 Respirator Decontamination and Reuse against SARS-CoV-2 Virus. *Emerging Infectious Diseases* **26**. ISSN: 1080-6059. doi:10.3201/eid2609.201524 (2020).
17. Ozog, D. M. *et al.* The Effect of Ultraviolet C Radiation Against Different N95 Respirators Inoculated with SARS-CoV-2. *International Journal of Infectious Diseases*, 224–229. ISSN: 12019712. doi:10.1016/j.ijid.2020.08.077 (2020).
18. Wilde, J. P., Baer, T. M. & Hesselink, L. Modeling UV-C irradiation chambers for mask decontamination using Zemax OpticStudio. *Applied Optics* **59**, 7596. ISSN: 1559-128X, 2155-3165. doi:10.1364/AO.402603 (2020).
19. Lawal, O. *et al.* Method for the Measurement of the Output of Monochromatic (254 nm) Low-Pressure UV Lamps. *IUVA News* **19**, 9–16 (2017).
20. Masse, V. *et al.* Comparing and optimizing ultraviolet germicidal irradiation systems use for patient room terminal disinfection: an exploratory study using radiometry and commercial test cards. *Antimicrobial Resistance & Infection Control* **7**, 29. ISSN: 2047-2994. doi:10.1186/s13756-018-0317-1 (2018).

21. Lester, R. A. *et al.* Optical properties of poly(2,6-dimethyl-1,4-phenylene oxide) film and its potential for a long-term solar ultraviolet dosimeter. *Physics in Medicine and Biology* **48**, 3685–3698. ISSN: 0031-9155, 1361-6560. doi:10.1088/0031-9155/48/22/005 (2003).
22. Quintern, L. E. *et al.* A Biofilm Used as Ultraviolet-Dosimeter. *Photochemistry and Photobiology* **55**, 389–395. ISSN: 1751-1097. doi:<https://doi.org/10.1111/j.1751-1097.1992.tb04252.x> (1992).
23. Biguri, A. *Perceptually uniform colormaps* <https://www.mathworks.com/matlabcentral/fileexchange/51986-perceptually-uniform-colormaps> (2020).
24. Reed, L. & Muench, H. A simple method of estimating fifty per cent endpoints. *American Journal of Hygiene* **27**, 493–497. ISSN: 0002-9262. doi:10.1093/oxfordjournals.aje.a118408 (1938).
25. Furler, R. A. Angular Dependence of Optical Properties of Homogeneous Glasses. *ASHRAE Transactions* **97**, 1–9 (1991).
26. Lore, M. B. *et al.* Effectiveness of Three Decontamination Treatments against Influenza Virus Applied to Filtering Facepiece Respirators. *The Annals of Occupational Hygiene* **56**, 92–101. ISSN: 0003-4878. doi:10.1093/annhyg/mer054 (2011).
27. Chin, A. W. H. *et al.* Stability of SARS-CoV-2 in different environmental conditions. *The Lancet Microbe* **1**. Publisher: Elsevier, e10. ISSN: 2666-5247. doi:10.1016/S2666-5247(20)30003-3 (2020).
28. Fisher, E. M., Williams, J. & Shaffer, R. E. The Effect of Soil Accumulation on Multiple Decontamination Processing of N95 Filtering Facepiece Respirator Coupons Using Physical Methods. **27**, 11 (2010).
29. Das, S. *et al.* Droplet spreading and capillary imbibition in a porous medium: A coupled IB-VOF method based numerical study. *Physics of Fluids* **30**, 012112. ISSN: 1070-6631, 1089-7666. doi:10.1063/1.5010716 (2018).
30. Kariwa, H., Fujii, N. & Takashima, I. Inactivation of SARS coronavirus by means of povidone-iodine, physical conditions and chemical reagents. *Dermatology (Basel, Switzerland)* **212(suppl 1)**, 119–123. ISSN: 1018-8665. doi:10.1159/000089211 (2006).
31. Zunner-Keating, B. P. *et al.* Rapid implementation of ultraviolet germicidal irradiation and reuse processes for N95 respirators at a health system during the coronavirus disease 2019 (COVID-19) pandemic. *Infection Control and Hospital Epidemiology*, 1–3. ISSN: 1559-6834. doi:10.1017/ice.2020.1386 (2020).
32. Purschke, M. *et al.* Construction and validation of UV-C decontamination cabinets for filtering facepiece respirators. *Applied Optics* **59**. doi:<https://doi.org/10.1364/AO.401602> (2020).

33. Storm, N. *et al.* Rapid and complete inactivation of SARS-CoV-2 by ultraviolet-C irradiation. *Scientific Reports* **10**, 22421. ISSN: 2045-2322. doi:10.1038/s41598-020-79600-8 (2020).
34. Darnell, M. E. R. *et al.* Inactivation of the coronavirus that induces severe acute respiratory syndrome, SARS-CoV. *J. Virol. Methods* **121**, 85–91. ISSN: 0166-0934. doi:10.1016/j.jviromet.2004.06.006 (2004).
35. Blatchley III, E. R., Petri, B. & Sun, W. *SARS-CoV-2 UV Dose-Response Behavior* 2020.
36. Smither, S. J. *et al.* Comparison of the plaque assay and 50% tissue culture infectious dose assay as methods for measuring filovirus infectivity. *Journal of Virological Methods* **193**, 565–571. ISSN: 1879-0984. doi:10.1016/j.jviromet.2013.05.015 (2013).
37. Gustafsson, R. K. L., Engdahl, E. E. & Fogdell-Hahn, A. Development and validation of a Q-PCR based TCID<sub>50</sub> method for human herpesvirus 6. *Virology Journal* **9**, 311. ISSN: 1743-422X. doi:10.1186/1743-422X-9-311 (2012).
38. Lowe, J. J. *et al.* *N95 Filtering Facepiece Respirator Ultraviolet Germicidal Irradiation (UVGI) Process for Decontamination and Reuse* tech. rep. (2020).

## Chapter 7

# Optical attenuators extend dynamic range but alter angular response of planar ultraviolet-C dosimeters

Reproduced with permission from: A. Su\*, A. Geldert\*, S. M. Grist, and A. E. Herr, "Optical attenuators extend dynamic range but alter angular response of planar ultraviolet-C dosimeters", *posted on arXiv and under peer review*, 2021.

\*contributed equally.

### 7.1 Introduction

Ultraviolet-C (UV-C) radiation is a key germicidal technique regularly applied in healthcare settings to decontaminate air [1, 2], environmental surfaces [3, 4], and recently, N95 respirators to address the COVID-19 pandemic-induced shortages [5, 6]. UV-C photons inactivate pathogens by catalyzing photodegradation of proteins and genomic material; after sufficient cumulative photon absorption (UV-C dose), compromised pathogens are unable to replicate. The UV-C dose needed for decontamination depends on the pathogen, substrate, and other factors [7]. Additionally, porous and multilayered textiles such as N95 respirators, surgical masks, and surgical gowns require higher applied outer surface doses as compared to nonporous materials, to offset UV-C attenuation which reduces the amount of UV-C reaching pathogens embedded in the inner material layers [8, 9]. Given that decontamination efficacy is directly related to UV-C dose and UV-C dose measurements frequently serve as the only metric bridging laboratory viral inactivation studies to UV-C treatment implementation, accurate UV-C dose measurements are critical for protocol validation.

Validation of decontamination of N95s and other porous and/or nonplanar substrates poses unique UV-C measurement challenges. The  $100\times$  higher UV-C dose required to decontaminate porous materials as compared to nonporous surfaces [3, 8, 10] requires UV-

C sensors with sufficiently high dynamic range. Dose delivered by UV-C systems is often nonlinear with time [11, 12], precluding extrapolation from short exposure times. For N95s, studies support a minimum dose of  $1.0 \text{ J/cm}^2$  UV-C dose applied to the outer surface to achieve  $3\text{-log}_{10}$  (99.9%) inactivation of coronaviruses and influenzas on most N95 models [10, 13, 14]. Additionally, the complex N95 geometry complicates measurement accuracy, as the UV-C dose received by a surface at a given angle of incidence  $\theta$  is reduced by a factor of  $\cos(\theta)$  from the dose received at normal incidence (Lambert’s cosine law [15]). Thus, UV-C dose measurement accuracy depends on how proportional the sensor readout over angles of incidence  $0^\circ \leq \theta \leq 90^\circ$  (termed “angular response”) is to  $\cos(\theta)$  (termed “ideal response”). A sensor with an ideal response is critical for applications such as N95 decontamination, which involves both nonplanar targets and uncollimated UV-C. However, sensor housing, spectral filters, and other elements in the optical path often alter angular response [16] and sensor angular response is often non-ideal [17, 18], uncharacterized, or unreported.

UV-C photochromic indicators (PCIs), which change color in response to UV-C dose, overcome many challenges associated with measurements on N95s within UV-C decontamination systems. PCIs can have an ideal angular response [19] because PCI dose response and specificity are governed by chemistry [20] rather than additional physical elements within the optical path. Though PCI readout is traditionally qualitative or at-best semi-quantitative (if a reference relating color swatches to doses is provided), a recent study developed a robust workflow to quantify UV-C dose from PCI color change to map UV-C dose across N95 facepieces [11]. However, because PCIs were originally designed to validate nonporous surface decontamination, UV-C doses required for porous material decontamination typically exceed the PCI dynamic range. Thus, an extended PCI dynamic range spanning higher UV-C doses is urgently needed to validate decontamination of porous materials like N95s.

There are two approaches towards extending the PCI dynamic range: (1) altering the chemistry governing the PCI color change, (e.g., adding reagents to modify the reaction kinetics or equilibrium [20, 21]) or (2) attenuating UV-C incident on the PCI (without attenuating UV-C incident on the decontamination target) [22]. As a PCI-agnostic approach, attenuation lends itself to widespread adoption across diverse settings. However, objects within the optical path may alter the angular response of the PCI due to angle-dependent refraction, reflection, and absorption [16, 23]. A non-ideal angular response will cause angle-dependent dose measurement errors. In systems where the angle of incidence is known or constant, an angle-dependent correction factor can be determined [11, 24–26]. However, the flexible N95 facepiece shape combined with significant UV-C scattering and reflection render this correction-factor approach infeasible for N95 UV-C decontamination systems.

Here, we employ theoretical and empirical approaches to investigate whether readily available materials can serve as optical attenuators to extend PCI dynamic range while maintaining measurement accuracy for N95 decontamination protocol validation. We develop an analytical model based on fundamental optics principles and attenuator properties to predict attenuator transmittance as a function of angle of incidence. Analytically and empirically with a point-like UV-C source, we characterize the angular response of PCIs stacked directly behind (with respect to the optical axis) each of two model attenuator materials:

one non-diffuse and one diffuse. Finally, to mimic implementation in an N95 decontamination protocol, we evaluate the measurement accuracy of each PCI-attenuator stack on two differently sloped N95 facepiece locations in a UV-C decontamination chamber, where UV-C angles of incidence are unknown. We demonstrate that although attenuators with diffuse properties improve angular response as compared to non-diffuse attenuators, a model planar diffuse attenuator still alters angular response, which compromises measurement accuracy. In total, we develop frameworks to relate key material properties of optical attenuators to the dynamic range and angular response of the PCI-attenuator stack and assess model PCI-attenuator stacks on N95s in an example end-use case to highlight critical considerations when modifying planar dosimeters for measurements on nonplanar surfaces.

## 7.2 Materials and Methods

### Materials

The attenuators used were floated borosilicate (Borofloat<sup>®</sup>, 25.4 mm width  $\times$  25.4 mm length  $\times$  1.1 mm  $\pm$  0.1 mm thickness, 80/50 scratch/dig quality, Precision Glass & Optics #0025-0025-0011-GE-CA), referred to as “borosilicate”, and polytetrafluoroethylene film (brand name Teflon<sup>®</sup>, 0.51 mm thickness, cut into 25.4 mm squares, McMaster-Carr # 8569K23), referred to as “PTFE”. All radiometer measurements were collected using a calibrated ILT1254 UV-C radiometer with a Teflon dome diffuser (International Light Technologies). PCIs were UVC 100 Dosimeter dots (American Ultraviolet). For transmittance and angular response measurements, a modified UV-C lamp (EF-140) with one BLE-2537S amalgam bulb (254 nm emission) and a UV-C-blocking plate with a 25.4 mm-diameter aperture installed was used as a point-like UV-C source (Spectronics). PCI and PCI-attenuator stack calibration curves and on-N95 measurements were made in a commercial UV-C chamber (Spectronics XL-1000 UV-C with an array of 5 BLE-8T254 254 nm low-pressure amalgam bulbs along the top) with a small custom notch for the radiometer cord to pass through the door. All on-N95 measurements were made on one 3M 1860 N95 respirator.

All analytical modelling and analyses were performed in MATLAB<sup>®</sup> R2020b.

### Borosilicate transmittance measurement

In a PCI-borosilicate stack, borosilicate is larger than and placed directly in contact with the planar PCI. Thus, the proportion of UV-C incident on the PCI depends on the direct transmittance of borosilicate, with minimal contribution from scattered transmittance. Additionally, because borosilicate is a non-diffuse material [27, 28], we anticipate that direct transmittance of borosilicate approximates total transmittance. To measure direct transmittance of borosilicate, a radiometer placed normal to the point-like UV-C source at a distance of 127 mm recorded the irradiance with and without borosilicate in the optical path (Figure 7.1A). To ensure borosilicate is placed normal to the optical path and radiometer, borosili-



cate is mounted on a custom-made acrylic (McMaster-Carr 85635K421) platform with a 20 mm-diameter aperture centered over the radiometer sensor (borosilicate is placed  $\sim 9$  mm in front of the top of the radiometer diffuser dome). The acrylic blocks UV-C, so UV-C is incident only through the 20 mm aperture. To monitor UV-C source stability and ensure that the same nominal dose was applied in each condition, dose was monitored using a radiometer at an offset, non-shadowed location.

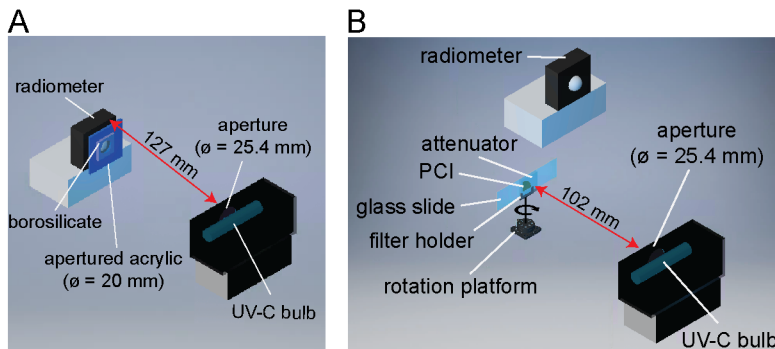


Figure 7.1: Schematics of measurement setups to characterize direct borosilicate transmittance and PCI-attenuator stack angular response. (A) Borosilicate direct transmittance at near-normal angles of incidence is measured by comparing irradiance measurements with and without borosilicate in the optical path (B) Angular response of PCI-attenuator stacks was measured by exposing the PCI-attenuator stack to UV-C from a point-like source at different angles of incidence. Arrow around optical post denotes axis of rotation.

## Analytical model

For homogeneous materials, the attenuation coefficient ( $\alpha$ ) can be calculated from the measured  $T_{\text{total}}$  and modeled  $T_{\text{int}}$  at  $0^\circ$ , and the attenuator thickness ( $d$ ) (Figure 7.1A):

$$\alpha = \frac{-\ln(T_{\text{total}}(0^\circ) / (T_{\text{int1}}(0^\circ) \cdot T_{\text{int2}}(0^\circ)))}{d} = \frac{-\ln(T_{\text{mat}}(0^\circ))}{d} \quad (7.1)$$

$\alpha$  of borosilicate in a PCI-borosilicate stack can be calculated from the measured  $T_{\text{direct}}$  (which approximates  $T_{\text{total}}$ ) measured at near-normal angles of incidence and used in the analytical model for borosilicate. We estimated the refractive index  $n_{\text{att}} \approx 1.50$  at 254 nm for borosilicate based on linear extrapolation of  $n$  for the two shortest wavelengths reported [29] ( $\sim 365$  nm and 405 nm). We estimated  $n_{\text{att}} \approx 1.38$  for PTFE, as reported by a manufacturer [30]. Integrated cosine error was calculated in MATLAB using the “cumtrapz” function.

## Angular response measurements with apertured UV-C source

To measure angular response, PCI-attenuator stacks were affixed to a glass microscope slide (VWR 48300-026) with double-sided tape (3M MMM137). The glass slide was held in a filter

holder (Thorlabs FH2) on an optical post attached to a rotation platform (Thorlabs QRP02). Angular responses of PCI-attenuator stacks were determined from the dose measured by PCIs at different rotation angles with respect to an apertured, point-like UV-C source ( $0^\circ$  -  $90^\circ$  in  $15^\circ$  increments) [31]. To approximate a point-like UV-C source, we determined the minimum distance between the optical post and apertured UV-C source at which UV-C output power was independent of distance ( $<5\%$  change between measurements) using the Keitz formula [12]. This distance was determined to be  $\sim 102$  mm, which meets the suggested criterion of  $>2\times$  the aperture diameter [12]. Though angular response measurements would ideally have been taken at a distance  $\geq 5\times$  the aperture diameter to represent true far field response [32], the low UV-C source irradiance at this distance (especially in the presence of an attenuator and at high angles of incidence) made angular response measurements infeasible, as PCI measurement uncertainty increases at low dose. The 102 mm distance is estimated to introduce a relative error of 1.53% compared to a true far-field measurement [32].

## PCI quantification

PCIs were quantified as previously described [11]. Briefly,  $D_{65}/10^\circ L^*a^*b^*$  values of PCIs were measured using an RM200QC spectrophotometer (X-rite<sup>®</sup>). Color change with respect to an unexposed PCI was quantified using the CIEDE2000  $\Delta E$  formula [11, 33]. To generate calibration curves, a radiometer and PCI were positioned within the UV-C chamber at planar locations of equal irradiance (Figure 7.2) to measure UV-C dose and CIEDE2000  $\Delta E$ , respectively. For PCI-attenuator stack calibration curves, the attenuator was placed directly on top of the PCI on the platform. CIEDE2000  $\Delta E$  values and corresponding UV-C doses were fit to a function based on first-order reaction kinetics [11]. Unless otherwise noted, reported errors are the root-sum-square of standard deviations corresponding to both replicate variation and PCI quantification uncertainty.

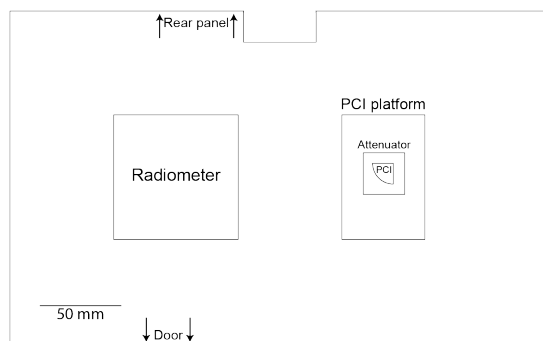


Figure 7.2: Chamber floor map for calibration curve measurements. PCIs were placed on a custom platform to match the radiometer’s diffuser base height. Irradiance at the radiometer and PCI locations was verified to be equivalent. Rectangular cut-out near the rear panel allows floor map to fit around a built-in raised component in the UV-C chamber.

## On-N95 dose measurements with PCI-attenuator pairs

On-N95 dose measurements were made at two N95 facepiece locations: near the apex where the N95 surface is nearly normal to the UV-C bulb array (“low-angle”), and near the base where the N95 surface is steeply sloped (“high-angle”). To measure on-N95 dose with PCI-attenuator stacks, PCIs were taped with the sensor side flush against the attenuator. The PCI-attenuator stack was then attached to the N95 facepiece using double-sided tape. Measured on-N95 dose was determined from PCI-attenuator calibration curves generated within the UV-C chamber. To compare to the bare PCI results, PCI-attenuator calibration curves were generated from the same locations in-chamber.

We evaluated the accuracy of on-N95 PCI-attenuator stack measurements by comparison to true on-N95 dose. To calculate the true UV-C dose applied at the N95 surface when either the dose exceeded the PCI upper limit of quantification or an attenuator was used, we first determined the ratio of dose at each on-N95 location to the dose measured using a radiometer positioned at a fixed location in the chamber ( $n = 3$  replicates). The radiometer recorded irradiance during UV-C exposure of an N95 with bare PCIs affixed at the low- and high-angle locations. Exposure time was chosen so that the dose applied to both PCIs was within the PCI dynamic range, because unmodified PCIs have an ideal angular response [19]. We refer to this ratio as the irradiance ratio, as we assume that the ratio of doses corresponds to the ratio of irradiance between the on-N95 and radiometer locations, regardless of exposure time. Then, in subsequent experiments, the *in situ* dose measured by the radiometer in the fixed location was multiplied by the predetermined irradiance ratio at each on-N95 location to estimate the true dose applied at each respective N95 location.

For consistent placement, high- and low-angle locations were marked on the N95, and facepiece deformation was minimized. During each exposure, the N95 was centered in the UV-C chamber, and a radiometer at a fixed location in the chamber recorded irradiance. A chamber floor map reduced positioning error (Figure 7.3).

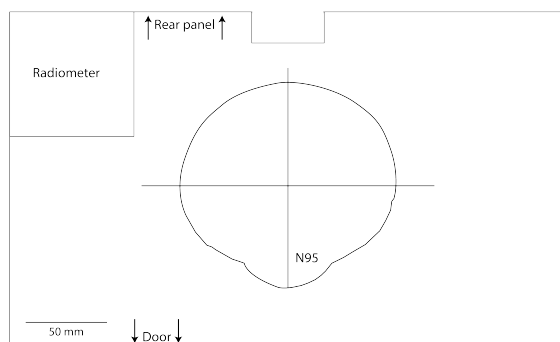


Figure 7.3: UV-C chamber floor map for on-N95 measurements.

## 7.3 Results and Discussion

### Design specifications relevant to pathogen inactivation

In this study, we sought to characterize the performance of PCIs stacked behind optical attenuators in measuring UV-C surface doses required for viral inactivation throughout porous surfaces. Because planar materials are accessible and scalable (can be cut to size from bulk material), we chose to study planar attenuators. We identified key performance specifications relevant to measurement accuracy: dynamic range and angular response (Figure 7.4A). We define the dynamic range of PCIs [11] as the UV-C doses between a lower and upper limit of quantification (LLOQ and ULOQ, respectively) where the relative PCI quantification uncertainty is  $<10\%$  (Figure 7.5). As studies support  $\geq 1.0 \text{ J/cm}^2$  for  $\geq 3\text{-log}_{10}$  inactivation of non-enveloped viruses on most N95 models [13, 14, 34] the PCI-attenuator stack ULOQ must exceed  $1.0 \text{ J/cm}^2$  for N95 decontamination protocol validation. However, pathogen- and model-specific efficacy of UV-C may require higher ULOQ and should be determined on a case-by-case basis. Additionally, on-N95 dose has been found to vary by  $\sim 20\times$  within a decontamination system [11]. To maximize the continuous measurement range in order to characterize the full range of nonuniform doses within a system, the PCI-attenuator stack LLOQ must remain below the bare PCI ULOQ ( $0.261 \text{ J/cm}^2$  for the PCI model and color-readout method used here [11]).

UV-C dose measurement accuracy on nonplanar surfaces depends on the angular response of the detector. Depending on attenuator material properties, transmittance may change with angle of incidence due to angle-dependent reflection, absorption, and degree of scattering (i.e., specular or diffuse reflectance and transmittance), leading to a non-ideal angular response. Because non-ideal angular response is infeasible to correct for without prior knowledge of the angle(s) of incidence, we sought to identify a PCI-attenuator stack with near-ideal angular response. At a given angle of incidence  $\theta$ , deviation from the ideal angular response is defined as the cosine error [35] (Eq. 7.2):

$$\text{Cosine error} = f_2(\theta) = \left( \frac{\text{response}(\theta)}{\text{response}(0^\circ) \cdot \cos(\theta)} - 1 \right) \times 100\% \quad (7.2)$$

To match the order of magnitude of bare PCI measurement error [11, 12] (average error of  $7\%$ ), PCI-attenuator stack cosine error magnitude must remain  $\leq 10\%$  over all angles of incidence ( $0^\circ \leq \theta < 90^\circ$ ). Integration of the cosine error between  $0^\circ$  and  $80^\circ$  (integrated cosine error, Eq. 7.3, defined [35] in ISO/CIE 19476) quantifies the overall deviation from the ideal angular response [36–38]:

$$\text{Integrated cosine error} = \int_0^{80^\circ} |f_2(\theta)| \cdot \sin(2\theta) d\theta \quad (7.3)$$

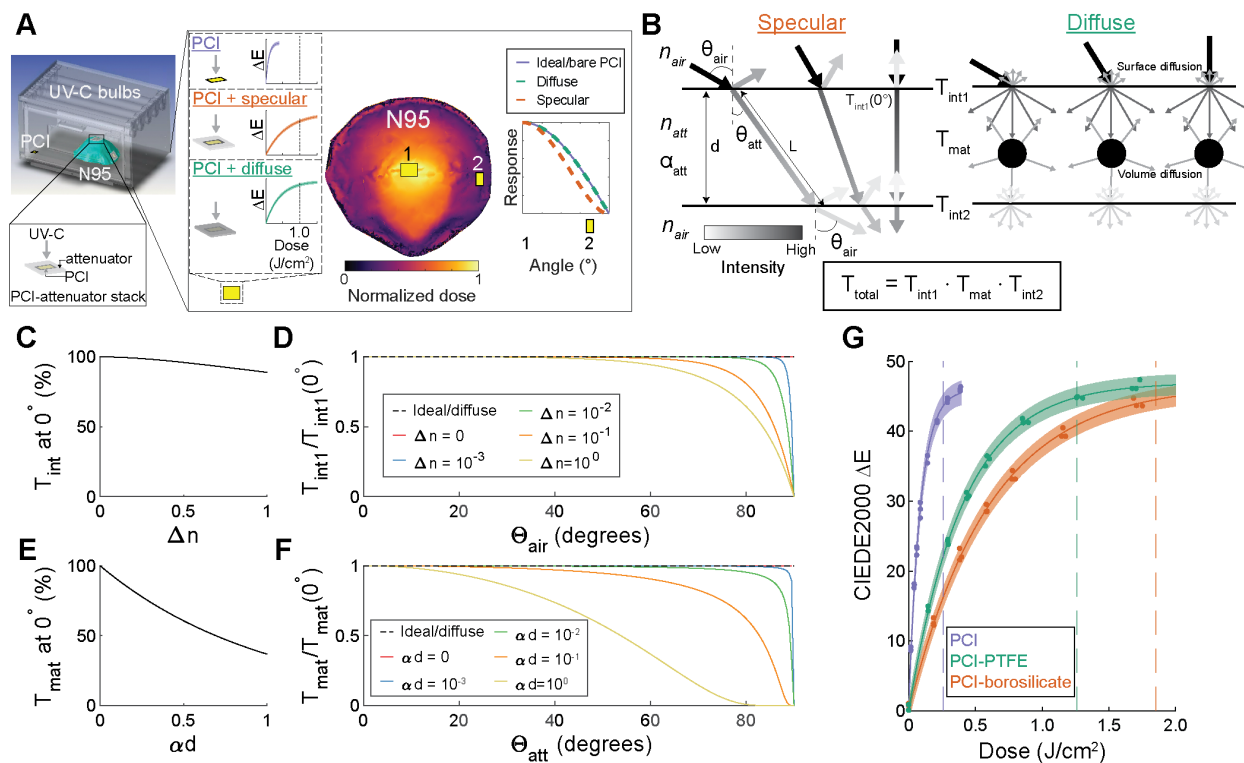


Figure 7.4: Attenuator material properties govern PCI-attenuator stack dynamic range and angular response. (A) 3D rendering of N95 UV-C decontamination system with 2D top-down view of chamber floor. Attenuators stacked in front of PCIs can extend PCI dynamic range to measure on-N95 dose variation (shown as heatmap), but measurement accuracy on non-planar surfaces like N95s requires an ideal PCI-attenuator angular response. (B) Schematic representation of UV-C transmittance through ideal specular and diffuse attenuators at varying angles of incidence: UV-C enters through the air-attenuator interface ( $T_{int1}$ ), traverses the attenuator ( $T_{mat}$ ), and exits via the attenuator-air interface ( $T_{int2}$ ). Arrow shade represents irradiance magnitude. In non-diffuse materials, reflection and attenuation increase with angle of incidence. In ideal diffusely transmitting materials, transmittance is independent of angle of incidence due to surface and volume diffuser behavior. (C-D) Non-zero  $\Delta n$  yields both decreased (C) and angle-dependent transmittance (D) at a specular interface. (E-F) Material thickness and attenuation coefficient yield both decreased (E) and angle-dependent (F) transmittance in non-diffuse material. (G) Two attenuator materials, borosilicate (specular) and PTFE (diffuse) extend the PCI upper limit of quantification (dashed vertical lines) beyond 1.0 J/cm<sup>2</sup>.

## Optical properties governing attenuator design for measurements on non-planar surfaces

To inform design of an attenuator that meets the required specifications, we first sought to identify and relate optical properties that affect attenuator transmittance through a planar material. Transmittance will affect both the dynamic range and angular response of a PCI-attenuator stack. Attenuators may exhibit entirely specular reflection and transmission (i.e., no scattering effects, ‘non-diffuse’), or diffuse scattering at the interface (‘surface diffusers’), within the material (‘volume diffusers’), or at both the interface and throughout the material. We developed an analytical model for total transmittance ( $T_{\text{total}}$ ) through materials based on two main interactions (Eq. 7.4): (1) reflection and refraction at air-attenuator interfaces, which govern the transmittance across the interfaces ( $T_{\text{int1}}$  and  $T_{\text{int2}}$ ) and (2) attenuation throughout the attenuator thickness, which governs the transmittance through the attenuator volume ( $T_{\text{mat}}$ ).

$$T_{\text{total}} = T_{\text{int1}} \cdot T_{\text{mat}} \cdot T_{\text{int2}} \quad (7.4)$$

At each air-attenuator interface, the Fresnel equations [23] (Eq. 7.5) for randomly polarized radiation describe the proportion of UV-C transmitted at the interface (interface transmittance,  $T_{\text{int}}$ ) based on the air and attenuator refractive indices ( $n_{\text{air}}$  and  $n_{\text{att}}$ ) and angle of incidence ( $\theta_{\text{air}}$ ). Snell’s law [39] (Eq. 7.6) governs the angle of refraction within the attenuator ( $n_{\text{att}}$ ) (Figure 7.4B).

$$T_{\text{int}} = 1 - \left\{ \frac{1}{2} \cdot \left[ \left( \frac{\eta_{\text{air}} \cos(\theta_{\text{air}}) - \eta_{\text{att}} \cos(\theta_{\text{att}})}{\eta_{\text{air}} \cos(\theta_{\text{air}}) + \eta_{\text{att}} \cos(\theta_{\text{att}})} \right)^2 + \left( \frac{\eta_{\text{air}} \cos(\theta_{\text{att}}) - \eta_{\text{att}} \cos(\theta_{\text{air}})}{\eta_{\text{air}} \cos(\theta_{\text{att}}) + \eta_{\text{att}} \cos(\theta_{\text{air}})} \right)^2 \right] \right\} \quad (7.5)$$

$$\eta_{\text{air}} \sin(\theta_{\text{air}}) = \eta_{\text{att}} \sin(\theta_{\text{att}}) \quad (7.6)$$

Note that the attenuator-to-air interface transmittance ( $T_{\text{int2}}$ ) calculation requires interchanging  $n_{\text{air}}$  and  $n_{\text{att}}$ , as well as  $\theta_{\text{att}}$  and  $\theta_{\text{air}}$  in Eq. 7.5. Specular reflectors have a microscopically flat interface, such that a collimated UV-C beam will strike the material at a single  $\theta_{\text{air}}$  that governs  $T_{\text{int}}$ . In contrast, due to interface roughness on surface diffusers, the surface normal varies randomly over distances much smaller than the length scale of interest (e.g., dimensions of the PCI) [16]. Thus, the textured interface causes collimated UV-C at any angle to actually strike the microscopically textured interface over a range of  $\theta_{\text{air}}$ . As a result, the proportion of UV-C transmitted across a surface diffuser interface does not depend on the angle of incidence (Figure 7.4B).

Using this analytical framework, we modeled specular and diffuse interface transmittance as a function of both the refractive index difference ( $\Delta n$ , Figure 7.4C) and the angle of incidence ( $\theta_{\text{air}}$ , Figure 7.4D). Increasing  $\Delta n$  decreases  $T_{\text{int1}}$ , thus extending the dynamic range of the PCI-attenuator stack (Eq. 7.5; Figure 7.4C). To characterize the effect of

$\Delta n$  on angular response, we evaluated  $T_{\text{int1}}$  normalized to  $T_{\text{int1}}(0^\circ)$  as a function of  $\theta_{\text{air}}$  over varying  $\Delta n$  values (Figure 7.4D). Because  $n$  of most materials [40] is  $\leq 2$  and  $n_{\text{air}} \approx 1$ , we evaluated  $\Delta n \leq 1$ . Surface diffusers exhibit angle-independent transmittance at the interface regardless of  $\Delta n$ . However, interfaces with specular reflection and transmission have increasingly angle-dependent transmittance as both  $\theta_{\text{air}}$  and  $\Delta n$  increase within the range of values modeled.

Internal transmittance through the attenuator thickness ( $d$ ) depends on two parameters: the material attenuation coefficient ( $\alpha$ ) and the optical path length through the material ( $L$ ). Bouguer's law [39] relates the internal transmittance ( $T_{\text{mat}}$ ) to the material attenuation coefficient ( $\alpha$ ) and the path length through the material ( $L$ ) (Eq. 7.7):

$$T_{\text{mat}} = e^{(-\alpha L)} \quad (7.7)$$

In non-diffuse materials and surface diffusers with no internal scattering,  $L$  is dependent on  $d$  and  $\theta_{\text{att}}$  (Eq. 7.8):

$$L = \frac{d}{\cos(\theta_{\text{att}})} \quad (7.8)$$

In volume diffusers, microstructures within the material scatter rays in random directions [41], decoupling  $L$  from  $\theta_{\text{att}}$ . Thus, in volume diffusers,  $T_{\text{mat}}$  is independent of angle of incidence (Figure 7.4B).

To elucidate contributions of attenuator properties ( $\alpha$  and  $d$ ) to the magnitude and angle-dependence of  $T_{\text{mat}}$ , we modeled  $T_{\text{mat}}$  as a function of a nondimensional parameter  $\alpha d$  (Figure 7.4E) and  $\theta_{\text{att}}$  (Figure 7.4F). Increasing  $\alpha d$  decreases transmittance via increased material attenuation, thereby extending the PCI dynamic range (Figure 7.4E). For UV-C transmittance through volume diffusers at any angle,  $T_{\text{mat}}/T_{\text{mat}}(0^\circ)$  is independent of angle of incidence regardless of  $\alpha d$ . However, increasing  $\alpha d$  for non-diffuse materials increases angular dependence of transmittance because 1) increasing  $d$  expands the range of optical path lengths  $d/\cos(\theta_{\text{att}})$  over which absorption occurs, and 2) increasing  $\alpha$  increases the sensitivity of  $T_{\text{mat}}$  on varying path lengths (Figure 7.4F).

Since the irradiance incident on the PCI-attenuator stack follows Lambert's cosine law [15], the irradiance ultimately incident on the PCI is proportional to  $T_{\text{total}} \cdot \cos(\theta_{\text{air}})$ . Thus, PCIs stacked directly behind planar attenuators (relative to the optical path) will maintain an ideal cosine response only if  $T_{\text{total}}$  remains constant over  $0^\circ \leq \theta_{\text{air}} < 90^\circ$ . However, the parameters ( $\Delta n$ ,  $d$ , and  $\alpha$ ) required to reduce attenuator transmittance and thus increase the dynamic range of the PCI-attenuator stack concomitantly introduce angle-dependent transmittance. Thus, unless the attenuator diffuses UV-C sufficiently to transmit UV-C independent of angle, there is a fundamental tradeoff between reducing transmittance to extend dynamic range and maintaining an ideal cosine angular response.

## Model diffuse and non-diffuse materials extend the PCI dynamic range beyond 1.0 J/cm<sup>2</sup>

To investigate how attenuator material properties UV-C dose quantification accuracy, we chose to characterize the performance of PCIs stacked behind one of two UV-C attenuators representative of widely accessible specular and diffuse materials. Floated borosilicate (“borosilicate”) has been demonstrated [11] to extend PCI dynamic range on planar surfaces by  $\sim 5\times$ , and thus was chosen as a model non-diffuse attenuator (i.e., exhibits specular reflection and transmission). Polytetrafluoroethylene (“PTFE”) was chosen as a model volume diffuser [42], as PTFE is commonly used to improve angular response of radiometers within the ultraviolet range [11, 43, 44]. We generated calibration curves for PCIs and PCI-attenuator stacks to verify that chosen attenuator thicknesses extend the PCI dynamic range beyond 1.0 J/cm<sup>2</sup> (Figure 7.4G, Figure 7.5). The bare PCI ULOQ was 0.261 J/cm<sup>2</sup>, below the 1.0 J/cm<sup>2</sup> design specification for on-N95 dose validation and in line with previous studies [11]. We found that 0.51 mm-thick PTFE and 1.1 mm-thick borosilicate increased the ULOQ to 1.259 J/cm<sup>2</sup> and 1.853 J/cm<sup>2</sup>, respectively, thus meeting the dynamic range specification. While we only studied one batch of each attenuator, transmittance may vary by batch and should be characterized prior to implementation.

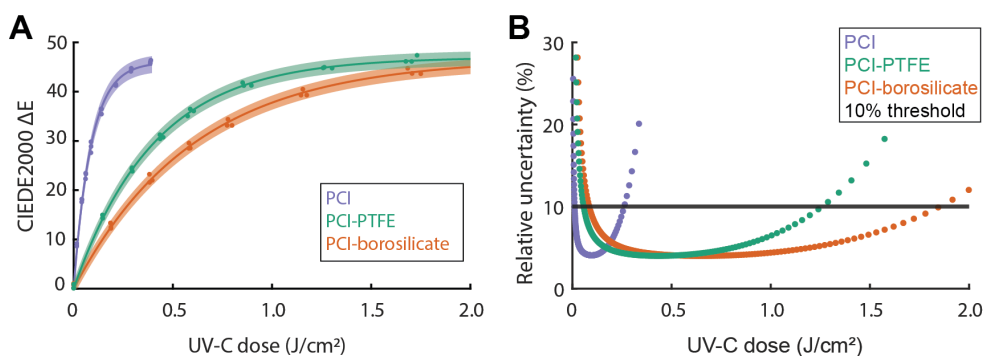


Figure 7.5: Attenuators extend PCI dynamic range. (A) Calibration curves relating UV-C dose to PCI color change (CIEDE2000  $\Delta E$ ). UV-C was applied to bare PCIs or PCIs stacked directly underneath an attenuator (PTFE or borosilicate). Each curve was fit to a fit function based on first-order reaction kinetics ( $\Delta E = a \left\{ 1 - e^{-\frac{dose}{b}} \right\}$ ). Shaded regions indicate the 95% prediction interval on prediction of PCI color change from measured UV-C dose. For bare PCIs,  $R^2 = 0.9976$ ,  $a = 46.0$  (45.3, 46.7),  $b = 87.4$  (83.6, 91.2). For PCI-PTFE,  $R^2 = 0.9982$ ,  $a = 47.0$  (46.5, 47.5),  $b = 407.3$  (393.2, 421.4). For PCI-borosilicate,  $R^2 = 0.9982$ ,  $a = 46.7$  (46.2, 47.3),  $b = 605.9$  (584.3, 627.5).  $N = 3$  replicates were measured at each dose. (B) The dynamic range is defined as the dose range over which relative dose measurement uncertainty (half the width of the 95% confidence interval divided by measured dose) is  $<10\%$ . UV-C dose measurements have  $<10\%$  relative uncertainty from 0.011 – 0.261 J/cm<sup>2</sup> (bare PCI), 0.057 – 1.259 J/cm<sup>2</sup> (PCI-PTFE), and 0.085 – 1.853 J/cm<sup>2</sup> (PCI-borosilicate).



## Analytical and empirical characterization demonstrate non-ideal angular response of a model specular attenuator

To assess quantification accuracy of the PCI-borosilicate stack at different angles of incidence, we compared both the analytical and empirical angular response of a PCI stacked behind 1.1 mm-thick borosilicate to an ideal response. Using an apertured UV-C lamp to achieve near-normal angles of incidence (Figure 7.6), we measured a direct transmittance ( $T_{\text{direct}}$ , which approximates  $T_{\text{total}}$  for borosilicate) of  $15.63\% \pm 0.06\%$  for 1.1 mm-thick borosilicate (standard deviation of 3 replicates). We used thickness and measured  $T_{\text{total}}$  to predict the PCI-borosilicate stack angular response analytically, and also measured angular response with the point-like UV-C source.

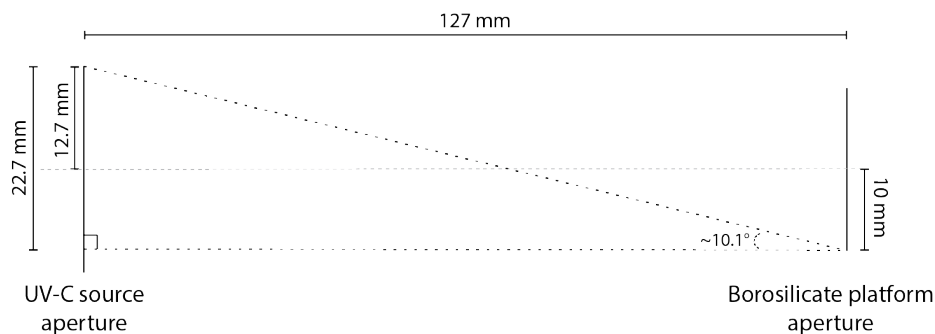


Figure 7.6: To measure the direct transmittance through borosilicate at near-normal incidence, the maximum angle incident on the borosilicate should be minimized. Borosilicate is placed on an apertured platform in front of the radiometer. In our setup, the maximum angle incident on the borosilicate from the apertured UV-C source is  $\sim 10.1^\circ$ .

As a non-diffuse material, we hypothesized that the PCI-borosilicate stack would readout lower UV-C doses than expected from Lambert's cosine law, with deviations from ideal increasing with angle of incidence due to angle-dependent reflection and absorption [23] (Figure 7.7A). We calculated the integrated cosine error (Eq. 7.3) using an upper integration limit of  $75^\circ$ , the last angle measured  $< 80^\circ$ . For the PCI-borosilicate stack, we predicted analytically and measured an integrated cosine error of 12.7% and 14.5%, respectively. Both analytically and empirically, we observed that the UV-C dose transmitted through borosilicate to the PCI underestimates an ideal angular response (Figure 7.7B). To quantify the amount of deviation from ideal cosine as a function of angle, we calculated the cosine error (Eq. 7.2, Figure 7.7C). At angles of incidence of  $15^\circ$  and  $75^\circ$ , our model predicted cosine errors of -2.7% and -64.8%, respectively, and we measured cosine errors of  $-8.2\% \pm 0.8\%$  and  $-82.9\% \pm 4.7\%$ , respectively. Thus, the PCI-borosilicate stack deviated more from an ideal response at higher angles of incidence (Figure 7.7C), as hypothesized. Importantly, PCI-borosilicate only meets the angular response design specification (i.e., magnitude of cosine error  $\leq 10\%$ ) at near-normal angles of incidence:  $0^\circ$  (due to normalization) and  $15^\circ$  empirically, and up to  $\sim 29^\circ$  analytically. While angle-specific correction factors have been determined and applied

in tightly controlled systems [26], this approach is not feasible for measurements on surfaces where the angle of incidence is not precisely known. For N95s in a UV-C chamber, both the 3D N95 facepiece morphology and uncollimated radiation confound application of an angle-specific correction factor to adjust inaccurate on-N95 UV-C dose measurements.

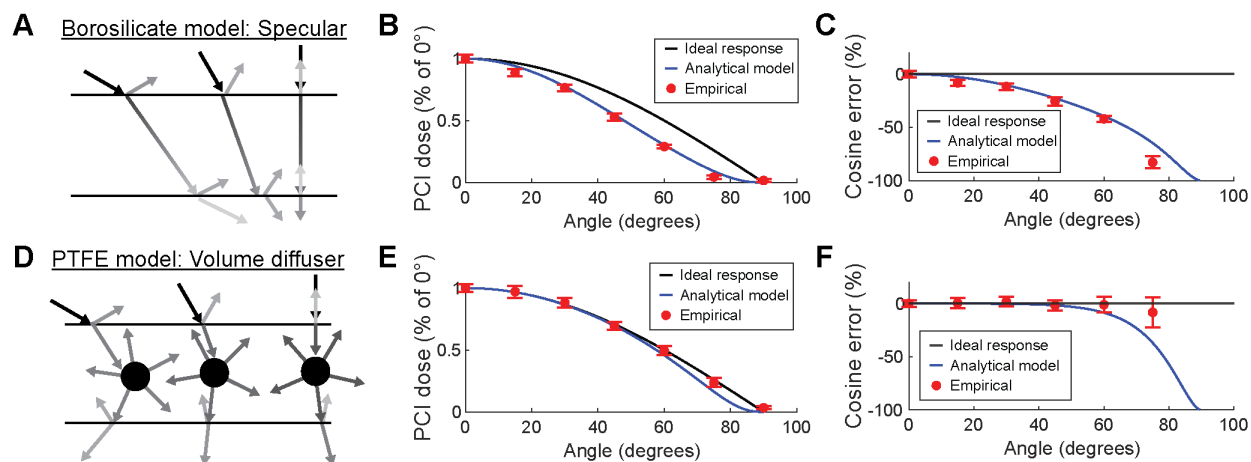


Figure 7.7: Concordance of analytical and empirical angular response of PCIs stacked with specular and diffuse attenuator materials. Analytical and empirical angular response and cosine error are compared for PCIs stacked behind (A-C) borosilicate, a model non-diffuse material, and (D-F) PTFE, a model volume diffuser. (A) Analytically, both reflection at the attenuator interfaces and path-length-dependent absorption through the material thickness contribute to the modeled angular response of non-diffuse materials. The (B) angular response and (C) cosine error of PCI-borosilicate stacks shows a non-ideal angular response at all angles of incidence. (D) The analytical model for PTFE as a volume diffuser includes specular reflection at interfaces, but assumes constant path length (and thus, absorption) through the material for all angles of incidence. The (E) angular response and (F) cosine error of PCI-PTFE stacks illustrate near-ideal response at low angles of incidence and non-ideal angular response at high angles of incidence. Error bars indicate total error, comprising both the standard deviation of replicates and the uncertainty of PCI measurements.

To evaluate the agreement between the analytical model and experiment, we compared the empirical angular response to model predictions. At 3 out of 6 non-normal angles measured, empirical angular response was within error (total propagated error of PCI quantification uncertainty and replicate variation) of model predictions (Figure 7.8(A-B)). The difference between empirical and analytical angular response was most substantial at 15° and 75° (Figure 7.8B), where the empirical normalized angular response was  $0.0531 \pm 0.0291$  and  $0.0469 \pm 0.0147$  below the model predictions, respectively. We hypothesize that the discrepancy between the empirical and analytical angular response arises from error in model parameters (e.g., refractive index,  $T_{\text{total}}$  at 0°), which will alter the predicted angular response (Figure 7.4(D,F)). Overall, however, analytical and empirical angular response measurements

for the PCI-borosilicate stack correspond well. Both show a nonideal angular response with cosine error magnitude  $>10\%$  for the majority of angles between  $0^\circ \leq \theta < 90^\circ$  and thus do not meet the angular response design specification. Negative cosine error at all non-normal angles of incidence means that the PCI-borosilicate stack underestimates UV-C dose, though to different amounts depending on angle.

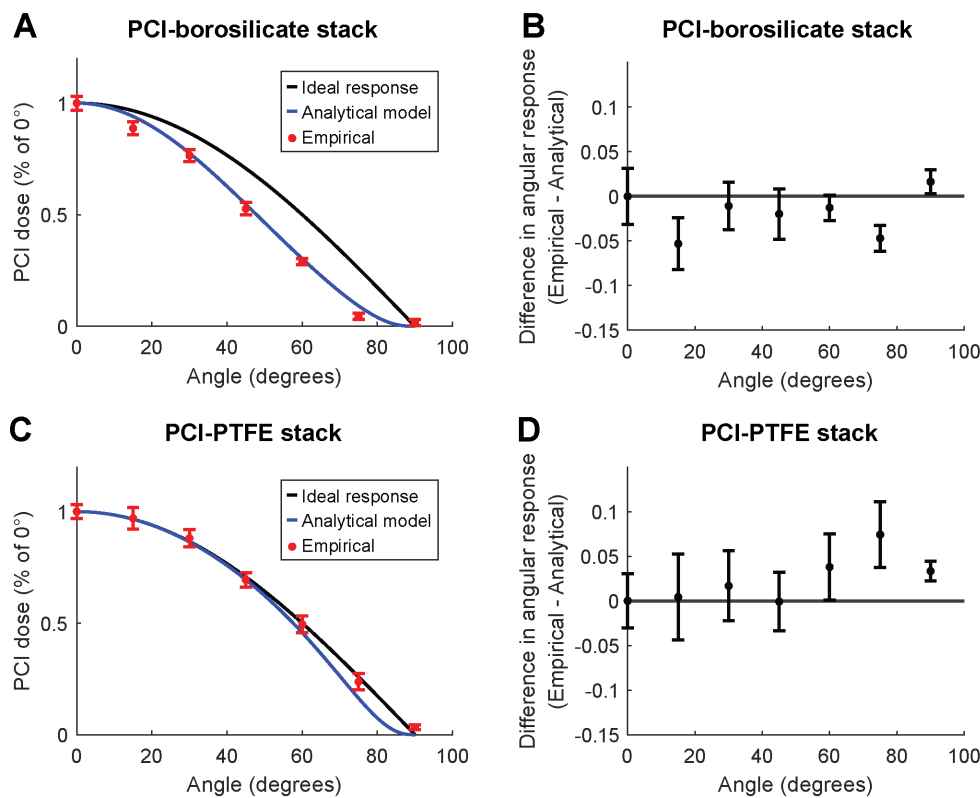


Figure 7.8: Analytical and empirical angular responses of PCI-attenuator pairs are concordant. (A) Analytical and empirical angular response of the PCI-borosilicate stack, along with ideal angular response ( $\cos(\theta)$ ). Error bars on empirical measurements indicate total propagated error (the root-sum-square combination of both PCI quantification uncertainty and standard deviation of 3 replicate measurements, as described previously [11]). (B) The difference between empirical and analytical angular response of the PCI-borosilicate stack at each angle of incidence measured. (C) Analytical and empirical angular response of the PCI-PTFE stack, along with ideal angular response. (D) The difference between empirical and analytical angular response of the PCI-PTFE stack at each angle of incidence measured.

## Diffuse attenuators cause less deviation from ideal angular response

Materials like borosilicate that exhibit specular reflection and transmittance highlight a fundamental tradeoff between extending the PCI dynamic range and minimizing cosine error. In contrast, diffuse materials are predicted to overcome this tradeoff by reducing angle-dependent reflectance (surface diffusers) and/or optical path length (volume diffusers). Available in numerous thicknesses and sizes at relatively low cost as compared to glass diffusers, PTFE is a readily available attenuator material appropriate to a wide range of environments. As a volume diffuser [42], we hypothesized that bulk scattering within PTFE would reduce path length dependence on angle of incidence. Due to unspecified surface roughness, we could not assume ideal surface diffuser behavior; thus, we modeled PTFE analytically as a volume diffuser with specular reflection and transmission at the interfaces (Figure 7.7D).

To assess the accuracy of the volume diffuser analytical model and characterize the extent to which PTFE alters PCI angular response, we compared both the analytical and empirical angular response of a PCI-PTFE stack to an ideal response (Figure 7.7(E-F)). For UV-C angles of incidence  $\leq 75^\circ$ , we predicted analytically and measured an integrated cosine error of 2.7% and 0.97%, respectively. Both the analytical and empirical integrated cosine errors of the PCI-PTFE stack are smaller in magnitude than observed for the PCI-borosilicate stack, as anticipated, and are lower than others have measured for 0.5 mm-thick PTFE [36, 38]. We hypothesize that the lower integrated cosine error observed here arises from differing limits of integration. Due to the limited number of angles of incidence characterized empirically, we integrate through  $75^\circ$ , while others integrate through  $85^\circ$  (past the ISO/CIE 19476 definition [35]), incorporating contributions from an additional  $10^\circ$  over which cosine error is typically large. At each rotation angle measured except  $90^\circ$ , PCI-PTFE angular response was within error of the ideal response (Figure 7.7F), suggesting a near-ideal angular response. Empirical angular response was within error of model predictions at  $<60^\circ$ ; at  $\geq 60^\circ$ , the empirical PCI-PTFE stack angular response was closer to an ideal response than model predictions (Figure 7.8(C-D)). We hypothesize that the empirical angular response of the PCI-PTFE stack was closer to ideal due to some surface diffuser behavior at the interface (not incorporated in the model), and/or slight curvature or non-negligible spacing between the deformable PTFE and PCI. Diffuser-sensor spacing and diffuser curvature have been shown to substantially alter the angular response of radiometers [38, 45, 46].

## Quantifying error in on-N95 UV-C dose measurements by PCI-attenuator stacks

Based on the modeled and measured angular response measurements from the point-like UV-C source, we hypothesized that a PCI-PTFE stack would measure on-N95 dose more accurately than a PCI-borosilicate stack, particularly at on-N95 locations with high angles of incidence. To test this hypothesis, we compared UV-C dose measured with PCIs and PCI-attenuator stacks to true applied dose at two locations on an N95 centered in a chamber

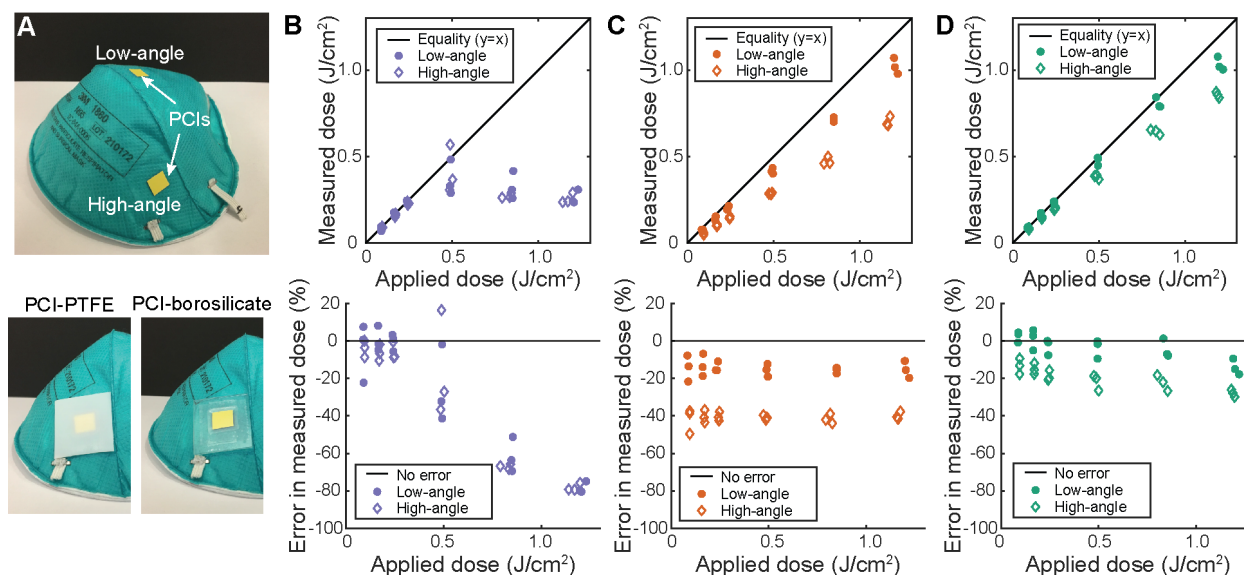


Figure 7.9: On-N95 UV-C dose measurement error depends on attenuator and on-N95 location. (A) UV-C dose was measured at two different on-N95 positions (top image): near the apex (“low-angle”), and on the steeply sloped side (“high-angle”). For PCI-attenuator stacks (PTFE or borosilicate), a PCI was placed directly underneath an attenuator (bottom image). On-N95 UV-C dose measurement accuracy of a (B) bare PCI, (C) PCI-borosilicate stack, or (D) PCI PTFE-stack was determined by comparing measured to true applied dose calculated from radiometer measurements and the predetermined ratio between the irradiance at the radiometer and at each on-N95 location. Measured dose (top) and percent error in measured dose (bottom) were plotted against true applied dose. UV-C dose measurements underestimate true applied dose, particularly at the high-angle location.

with 5 UV-C bulbs arrayed across the top. The presence of multiple UV-C bulbs, as well as scattering and reflection [47] in this and other commercial decontamination systems, stymie determination of angle of incidence distribution at any given location. We chose two on-N95 measurement locations which we hypothesized receive substantially different angles of incidence: (1) near the apex (“low-angle”; near-normal), and (2) near the base (“high-angle”; non-normal) (Figure 7.9A). Based on the analytical model and the point-like UV-C source measurements (Figure 7.7), we hypothesized that the PCI-borosilicate stack would underestimate UV-C dose at both N95 locations, with greater underestimation at the high angle location. In contrast, PCI-PTFE angular response had cosine error magnitudes  $<10\%$  at all angles of incidence measured empirically and at angles  $\leq 61^\circ$  analytically, so we hypothesized that the PCI-PTFE stack would measure on-N95 UV-C dose accurately, with some error introduced at the high-angle N95 location.

At both on-N95 locations, UV-C dose was measured from PCI color change using PCI-attenuator-specific calibration curves (Figure 7.4G). To evaluate the measurement accuracy, the true dose applied at each on-N95 location was determined based on the ratio of irradiance

at each on-N95 location to the irradiance measured by a radiometer positioned in the chamber corner. To evaluate the measurement accuracy, the true dose applied at each on-N95 location was determined by multiplying a radiometer measurement obtained in each exposure by the respective predetermined ratio of irradiances at each on-N95 location and at the radiometer ( $\frac{Irr_{low-angle}}{Irr_{radiometer}} = 2.27 \pm 0.06$ ;  $\frac{Irr_{high-angle}}{Irr_{radiometer}} = 0.93 \pm 0.03$ ). Based on the ULOQ of the two PCI-attenuator stacks, on-N95 UV-C dose measurements up to  $\sim 1.200 \text{ J/cm}^2$  were characterized and compared to the true dose to evaluate the on-N95 dynamic range and angular response of PCI, PCI-borosilicate, and PCI-PTFE (Figure 7.9(B-D)). In agreement with the dynamic ranges measured on a planar surface (Figure 7.4G), the measured UV-C dose of the PCI-attenuator stacks is linearly proportional to applied dose throughout the entire dose range tested at each on-N95 location ( $\sim 0.050$  to  $\sim 1.250 \text{ J/cm}^2$ , Figure 7.9(C-D), top row; Table 7.1). Thus, both borosilicate and PTFE meet the design specification of extending on-N95 PCI dynamic range to  $\geq 1.0 \text{ J/cm}^2$ . In contrast, UV-C dose measured by the bare PCI plateaus with measurement error greatly exceeding 10% at true doses above  $\sim 0.250 \text{ J/cm}^2$  (Figure 7.9B), in agreement with the PCI ULOQ (Figure 7.4G).

Table 7.1: Significance of linear correlation between true and measured dose for each attenuator and on-N95 location tested.

Attenuator on-N95 location	$r^2$	p
Bare PCI, low-angle	0.282	0.024
Bare PCI, high-angle	0.182	0.078
PCI-borosilicate stack, low-angle	0.997	4.76e-21
PCI-borosilicate stack, high-angle	0.997	8.21e-22
PCI-PTFE stack, low-angle	0.990	2.64e-17
PCI-PTFE stack, high-angle	0.995	1.68e-19

To evaluate overall measurement accuracy, we calculated the percent error of UV-C dose measurements (Figure 7.9(B-D), bottom). Doses measured with the PCI-borosilicate stack underestimate the true dose by  $14.7\% \pm 4.0\%$  and  $40.8\% \pm 3.0\%$  at the low-angle and high-angle on-N95 locations, respectively (errors are the standard deviation of 18 total dose measurements at a given location). Thus, in agreement with our hypothesis, we found that dose measured with the PCI-borosilicate stack underestimated true UV-C dose to a greater extent at the more steeply sloped, high-angle on-N95 location. Inaccuracy in measured dose also arises due to differences in the distribution of angles of incidence between the calibration curve and on-N95 measurements. As discussed, it is infeasible to generate calibration curves or correction factors specific to each on-N95 location in the chamber. In contrast, doses measured with the PCI-PTFE stack only underestimated the true dose by  $3.6\% \pm 6.7\%$  and  $19.8\% \pm 5.8\%$  at the low-angle and high-angle on-N95 locations, respectively. UV-C dose measurements by the PCI-PTFE stack were more accurate than those by the PCI-borosilicate stack, supporting our hypothesis and model predictions that PCIs stacked behind diffuse materials have an angular response nearer to an ideal response than when stacked

behind a non-diffuse material. Overall, PCI-PTFE dose measurements were within error of the true dose at the low-angle on-N95 location (measured dose underestimated true dose by  $3.6\% \pm 6.7\%$  over 18 measurements), in agreement with our hypothesis that PCI-PTFE has near-ideal angular response at low angles of incidence. We observe greater error in PCI-PTFE-measured dose at the high-angle on-N95 location than observed at all angles measured with the point-like UV-C source (Figure 7.7F). The larger error at the high-angle location on-N95 may indicate an average angle of incidence  $>75^\circ$  at that location, yielding a greater cosine error than measured with the point-like UV-C source at angles  $\leq 75^\circ$ . As discussed previously, geometrical factors such as slight variations in PTFE curvature, as well as the use of calibration curves not specific to each experimental measurement location, may have also contributed to angular response differences measured in the two systems. Additionally, while guidance on the acceptable source-to-detector distance for accurate angular response measurements varies [12, 48], insufficient distance can yield artificially high angular response [48]. This artifact may contribute to the near-ideal angular response measured with the point-like source, where the maximum source-to-detector distance was limited due to low source irradiance. On-N95, the PCI-PTFE attenuator stack underestimated dose to a greater extent with increasing dose, a phenomenon not observed with the PCI-borosilicate stack (Figure 7.9(C-D)). We hypothesize the dose-dependent error may arise from an increasing difference between the true and applied calibration curve at higher doses (Figure 7.10), and/or temperature-induced changes in PTFE transmittance [49] not captured in the PCI-PTFE calibration curve (generated off-N95) due to differences in heat dissipation on-N95.

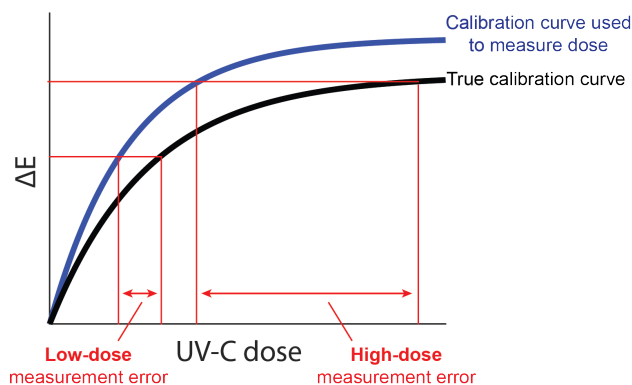


Figure 7.10: Use of incorrect calibration curve can yield dose-dependent measurement error. If the PCI-attenuator stack has a non-ideal angular response, and/or if PCI reaction kinetics depend on environmental conditions such as temperature or humidity, differences in UV-C angles of incidence and environmental factors may yield different calibration curve shapes. Because it is infeasible to generate calibration curves for every location and environmental condition within the UV-C chamber to exactly match the conditions of a given measurement, the calibration curve used to determine dose from a measured  $\Delta E$  may not represent the true calibration curve for the exact chamber location and environmental conditions present at the time the PCI was exposed and may lead to dose-dependent measurement error.

## 7.4 Conclusions

Overall, both modeling and measurements in two different UV-C systems demonstrate that diffuse attenuators such as PTFE alter the ideal angular response of PCIs less than non-diffuse materials such as borosilicate, but that both types of planar attenuators cause deviation from ideal at high angles of incidence. Unless the material is ideally diffuse, the factors which decrease attenuator transmittance (thus increasing PCI-attenuator ULOQ) also increase the angular dependence of transmittance, yielding a fundamental tradeoff between the two design requirements of increased dynamic range and minimal cosine error. Both attenuators increased the PCI ULOQ by  $>4\times$ , but the non-ideal angular response of PCI-attenuator stacks led to underestimation of measured on-N95 dose at one or both locations. The on-N95 results highlight a critical consideration for designing optical attenuators: materials that lead to measurements within error of the ideal angular response in a controlled setting may not accurately translate to user environments. Additionally, cumulative UV-C exposure also affects the transmission properties of some attenuators (e.g., solarization of glass [50, 51]), which limits reuse. Though relatively low-cost materials such as PTFE may be feasible for single-use applications, the stability of attenuator transmittance with increasing cumulative UV-C dose must be robustly characterized prior to implementation of any attenuator material. Future study could consider introducing surface roughness and/or curvature to volume diffusers to create PCI-attenuator stacks with smaller cosine error at higher angles of incidence. Alternative strategies to extend PCI dynamic range, such as the development of new PCI formulations, are also a promising approach that may be more robust than physically attenuating UV-C incident on the PCI.



# Bibliography

1. Memarzadeh, F., Olmsted, R. N. & Bartley, J. M. Applications of ultraviolet germicidal irradiation disinfection in health care facilities: effective adjunct, but not stand-alone technology. *American Journal of Infection Control* **38**, S13–24. ISSN: 1527-3296. doi:10.1016/j.ajic.2010.04.208 (2010).
2. Rutala, W. A., Weber, D. J. & the Healthcare Infection Control Practices Committee (HICPAC). *Guideline for Disinfection and Sterilization in Healthcare Facilities, 2008* tech. rep. (Centers for Disease Control, 2019), 163.
3. Tseng, C.-C. & Li, C.-S. Inactivation of Viruses on Surfaces by Ultraviolet Germicidal Irradiation. *Journal of Occupational and Environmental Hygiene* **4**, 400–405. ISSN: 1545-9624, 1545-9632. doi:10.1080/15459620701329012 (2007).
4. Cadnum, J. L. *et al.* Effect of Variation in Test Methods on Performance of Ultraviolet-C Radiation Room Decontamination. *Infection Control & Hospital Epidemiology* **37**, 555–560. ISSN: 0899-823X, 1559-6834. doi:10.1017/ice.2015.349 (2016).
5. Lowe, J. J. *et al.* *N95 Filtering Facepiece Respirator Ultraviolet Germicidal Irradiation (UVGI) Process for Decontamination and Reuse* tech. rep. (2020).
6. Ozog, D. M. *et al.* The Effect of Ultraviolet C Radiation Against Different N95 Respirators Inoculated with SARS-CoV-2. *International Journal of Infectious Diseases*, 224–229. ISSN: 12019712. doi:10.1016/j.ijid.2020.08.077 (2020).
7. Kowalski, W. *Ultraviolet Germicidal Irradiation Handbook: UVGI for Air and Surface Disinfection* ISBN: 978-3-642-01999-9 (Springer Science & Business Media, Berlin, Heidelberg, 2010).
8. Fisher, E. & Shaffer, R. A method to determine the available UV-C dose for the decontamination of filtering facepiece respirators: UV-C decontamination of respirators. *Journal of Applied Microbiology* **110**, 287–295. ISSN: 13645072. doi:10.1111/j.1365-2672.2010.04881.x (2011).
9. Huber, T. *et al.* Principles and practice for SARS-CoV-2 decontamination of N95 masks with UV-C. *Biophysical Journal*, S0006349521001971. ISSN: 00063495. doi:10.1016/j.bpj.2021.02.039 (2021).

10. Grist, S. M. *et al.* Current Understanding of Ultraviolet-C Decontamination of N95 Filtering Facepiece Respirators. *Applied Biosafety*. ISSN: 1535-6760. doi:10.1089/apb.20.0051 (2021).
11. Su, A. *et al.* Quantitative UV-C dose validation with photochromic indicators for informed N95 emergency decontamination. *PLOS ONE* **16**, e0243554. ISSN: 1932-6203. doi:10.1371/journal.pone.0243554 (2021).
12. Lawal, O. *et al.* Method for the Measurement of the Output of Monochromatic (254 nm) Low-Pressure UV Lamps. *IUVA News* **19**, 9–16 (2017).
13. Mills, D. *et al.* Ultraviolet germicidal irradiation of influenza-contaminated N95 filtering facepiece respirators. *American Journal of Infection Control* **46**, e49–e55. ISSN: 01966553. doi:10.1016/j.ajic.2018.02.018 (2018).
14. Heimbuch, B. & Harnish, D. *Research to Mitigate a Shortage of Respiratory Protection Devices During Public Health Emergencies* tech. rep. HHSF223201400158C (Applied Research Associates, Inc., 2019).
15. Reifsnnyder, W. E. Radiation geometry in the measurement and interpretation of radiation balance. *Agricultural Meteorology* **4**, 255–265. ISSN: 00021571. doi:10.1016/0002-1571(67)90026-X (1967).
16. McCluney, W. R. *Introduction to Radiometry and Photometry* Second. **4**, 159–163. ISBN: 9781608078332. doi:10.1108/sr.1998.08718dae.002 (1998).
17. Zorzano, M.-P., Martín-Soler, J. & Gómez-Elvira, J. *UV Photodiodes Response to Non-Normal, Non-Colimated and Diffusive Sources of Irradiance in Photodiodes - Communications, Bio-Sensings, Measurements and High-Energy Physics* (IntechOpen, 2011).
18. Larason, T. & Ohno, Y. Calibration and characterization of UV sensors for water disinfection. *Metrologia* **43**, S151–S156. ISSN: 0026-1394, 1681-7575. doi:10.1088/0026-1394/43/2/S30 (2006).
19. Geldert, A. *et al.* Nonuniform UV-C dose across N95 facepieces can cause 2.9-log variation in SARS-CoV-2 inactivation. *medRxiv*. doi:10.1101/2021.03.05.21253022 (2021).
20. Mills, A. *et al.* Flagging up sunburn: a printable, multicomponent, UV-indicator that warns of the approach of erythema. *Chemical Communications*, 1345–1346. ISSN: 1359-7345, 1364-548X. doi:10.1039/b900569b (2009).
21. Smith, A. T. *et al.* Multi-color Reversible Photochromisms via Tunable Light-Dependent Responses. *Matter* **2**, 680–696. ISSN: 2590-2385. doi:10.1016/j.matt.2019.12.006 (2020).
22. Khiabani, P. S. *et al.* Paper-Based Sensor for Monitoring Sun Exposure. *ACS Sensors* **1**, 775–780. doi:10.1021/acssensors.6b00244 (2016).
23. Furler, R. A. Angular Dependence of Optical Properties of Homogeneous Glasses. *ASHRAE Transactions* **97**, 1–9 (1991).

24. Lakkala, K. *et al.* Performance of the FMI cosine error correction method for the Brewer spectral UV measurements. *Atmospheric Measurement Techniques* **11**, 5167–5180. ISSN: 1867-8548. doi:10.5194/amt-11-5167-2018 (2018).
25. Seckmeyer, G. & Bernhard, G. Cosine error correction of spectral UV irradiance. *SPIE Proc.* **2049**. doi:10.1117/12.163505 (1993).
26. Severin, B. F. & Roessler, P. F. Resolving UV photometer outputs with modeled intensity profiles. *Water Research* **32**, 1718–1724. ISSN: 0043-1354. doi:10.1016/S0043-1354(97)00363-1 (1998).
27. Aytug, T. *et al.* Monolithic graded-refractive-index glass-based antireflective coatings: broadband/omnidirectional light harvesting and self-cleaning characteristics. *Journal of Materials Chemistry C* **3**. Publisher: The Royal Society of Chemistry, 5440–5449. ISSN: 2050-7534. doi:10.1039/C5TC00499C (2015).
28. Spitzer, M. B. & England, J. *Ion beam surface modification of solar module glass for reduced reflectance — IEEE Conference Publication — IEEE Xplore in 2010 35th IEEE Photovoltaic Specialists Conference* (IEEE, 2010), 002798–002801. doi:10.1109/PVSC.2010.5616751.
29. SCHOTT Technical Glass Solutions GmbH. *BOROFLOAT® 33 – Optical Properties* [https://www.schott.com/d/borofloat/bde16ad3-70e5-48a0-b8ac-9146fcd34511/1.0/borofloat33\\_opt\\_en\\_web.pdf](https://www.schott.com/d/borofloat/bde16ad3-70e5-48a0-b8ac-9146fcd34511/1.0/borofloat33_opt_en_web.pdf) (2020).
30. Lake Photonics. *Spectralex Optical Diffuser Films* <https://www.lake-photonics.com/wp-content/uploads/Spectralex-Optical-Diffuser-Films.pdf>.
31. Quintern, L. E. *et al.* A Biofilm Used as Ultraviolet-Dosimeter. *Photochemistry and Photobiology* **55**, 389–395. ISSN: 1751-1097. doi:<https://doi.org/10.1111/j.1751-1097.1992.tb04252.x> (1992).
32. Ohno, Y. *et al.* *Analyses of errors associated with photometric distance in goniophotometry* in *Proc., the 28th Session of CIE* **1** (Manchester, 2015), 458–468.
33. Luo, M. R. *CIEDE2000, History, Use, and Performance* in *Encyclopedia of Color Science and Technology* (ed Luo, M. R.) 202–207 (Springer New York, New York, NY, 2016). ISBN: 978-1-4419-8071-7. doi:10.1007/978-1-4419-8071-7\_7.
34. Lore, M. B. *et al.* Effectiveness of Three Decontamination Treatments against Influenza Virus Applied to Filtering Facepiece Respirators. *The Annals of Occupational Hygiene* **56**, 92–101. ISSN: 0003-4878. doi:10.1093/annhyg/mer054 (2011).
35. CIE Technical Committee 2-40. *Characterization of the performance of illuminance meters and luminance meters* BSI Standards Publication BS ISO/CIE 19476:2014 (The British Standards Institution 2014, Vienna, 2014).
36. Bernhard, G. & Seckmeyer, G. New Entrance Optics for Solar Spectral UV Measurements. *Photochemistry and Photobiology* **65**, 923–930. ISSN: 1751-1097. doi:<https://doi.org/10.1111/j.1751-1097.1997.tb07949.x> (1997).

37. Wu, H., Cheng, H. & Feng, Y. Design of a free-form diffuser for the entrance optic to correct the cosine error in the photometer. *Applied Optics* **58**, 5029–5039. ISSN: 2155-3165. doi:10.1364/AO.58.005029 (2019).
38. Pulli, T. *et al.* Improved diffusers for solar UV spectroradiometers in *AIP Conference Proceedings* **1531** (AIP Publishing LLC, 2013), 813–816. doi:10.1063/1.4804894.
39. Allen, D. W. *et al.* NIST measurement services: regular spectral transmittance tech. rep. NIST SP 250-69 (National Institute of Standards and Technology, Gaithersburg, MD, 2011). doi:10.6028/NIST.SP.250-69.
40. Miller, D. *et al.* Analysis of Transmitted Optical Spectrum Enabling Accelerated Testing of CPV Designs. *Proceedings of SPIE - The International Society for Optical Engineering* **7407**. doi:10.1117/12.826251 (2009).
41. Li, Q. *et al.* Light scattering of semitransparent sintered polytetrafluoroethylene films. *Journal of Biomedical Optics* **13**, 054064. ISSN: 10833668. doi:10.1117/1.2992485 (2008).
42. Lemaillet, P. *et al.* Goniometric and hemispherical reflectance and transmittance measurements of fused silica diffusers in *Proc. SPIE* **9961** (2016).
43. Pye, S. D. & Martin, C. J. A study of the directional response of ultraviolet radiometers: I. Practical evaluation and implications for ultraviolet measurement standards. *Physics in Medicine and Biology* **45**, 2701–2712. ISSN: 0031-9155, 1361-6560. doi:10.1088/0031-9155/45/9/319 (2000).
44. Sholtes, K. A. *et al.* Comparison of ultraviolet light-emitting diodes and low-pressure mercury-arc lamps for disinfection of water. *Environmental Technology* **37**, 2183–2188. ISSN: 1479-487X. doi:10.1080/09593330.2016.1144798 (2016).
45. Cahuantzi, R. & Buckley, A. Geometric optimisation of an accurate cosine correcting optic fibre coupler for solar spectral measurement. *The Review of Scientific Instruments* **88**, 095003. ISSN: 1089-7623. doi:10.1063/1.5003040 (2017).
46. Martínez, M. A., Andújar, J. M. & Enrique, J. M. A New and Inexpensive Pyranometer for the Visible Spectral Range. *Sensors (Basel, Switzerland)* **9**, 4615–4634. ISSN: 1424-8220. doi:10.3390/s90604615 (2009).
47. Gostein, M. & Stueve, B. Accurate measurement of UV irradiance in module-scale UV exposure chambers, including spectral angular response of sensor in *2016 IEEE 43rd Photovoltaic Specialists Conference (PVSC)* (2016), 0863–0866. doi:10.1109/PVSC.2016.7749731.
48. Schmalwieser, A. W. Fifteen years of experience with standardized reference radiometers for controlling low-pressure UV disinfection plants for drinking water. *Water Supply* **17**, 975–984. ISSN: 1606-9749, 1607-0798. doi:10.2166/ws.2016.197 (2017).
49. Ylianttila, L. & Schreder, J. Temperature effects of PTFE diffusers. *Optical Materials* **27**, 1811–1814. ISSN: 0925-3467. doi:10.1016/j.optmat.2004.11.008 (2005).

50. Natura, U., Ehrt, D. & Naumann, K. Formation of radiation defects in high-purity silicate glasses in dependence on dopants and UV radiation sources. *Glastech. Ber. Glass Science and Technology* **74**, 23–31 (2001).
51. Gatto, A. *et al.* Simulation of the degradation of optical glass substrates caused by UV irradiation while coating. *Optics Communications* **148**, 347–354. ISSN: 0030-4018. doi:10.1016/S0030-4018(97)00651-2 (1998).

## Chapter 8

# Conclusions and future directions

In this dissertation, we sought to design widely accessible workflows to both quantify and validate complex, spatially resolved measurements of three-dimensional nanoporous systems. First, we discussed how optical artefacts can confound quantification of solute partitioning in nanoporous hydrogel systems, and we introduced aberration-compensated laser scanning confocal microscopy (AC-LSCM) as a technique to quantify partitioning while minimizing and then subsequently characterizing remaining optical artefacts and their impact on  $K$ . Second, we discussed the underlying principles contributing to the existing UV-C measurement gap that stymies reproducibility and the development of safe, efficacious UV-C decontamination protocols, especially when multilayered, three-dimensional nanoporous N95 respirators serve as the decontamination target.

AC-LSCM takes advantage of the free solution surrounding the gel as an intrinsic control from which optical artefacts imparted by both the system and the gel can be quantified. We applied AC-LSCM to quantify how photoactivation of a protein capture moiety in the gel backbone or inclusion of progen molecules during gel polymerization alters solute partitioning compared to unmodified gels. We investigated the spatial distribution of solute throughout multilayered gel structures, which shed light on the internal gel architecture that could not be observed with other indirect  $K$  measurement methods. The imaging aspect of AC-LSCM is currently quite labor and time intensive due to the frequent manual repositioning required to image each gel and free solution region. Future work towards automated image acquisition (e.g., custom scripts compatible with the imaging software to locate regions of interest and minimize manual manipulation) would substantially increase throughput. Additionally, though confocal microscopy was chosen as a relatively accessible and common imaging instrument, newer microscopy approaches and instruments such as light sheet fluorescence microscopy may offer advantages over LSCM, such as increased imaging depth and speed, as well as reduced photobleaching [1, 2], but currently require additional and often times complex sample preparation and alignment [3].

In response to the global N95 respirator shortages caused by the COVID-19 pandemic, we turned to a different nanoporous system: N95 filtering facepiece respirators. we developed multiple new validation workflows for UV-C decontamination designed specifically to address

current gaps in the UV-C measurement field related to quantifying dose across complex, 3-D surfaces. Through N95DECON, we compiled and subsequently disseminated publicly multiple reviews highlighting these measurement gaps and potential associated consequences. Combining optics, colorimetry, and metrology fundamentals, we designed a method to quantify UV-C dose from color-changing photochromic indicators (PCIs), inexpensive surface-like sensors that previously provided qualitative (and thus subjective) visual readout. We leveraged optical simulations and PCI measurements in parallel and demonstrated how these two workflows can synergize to inform design of novel viral inactivation experiments that directly probe the relationship between SARS-CoV-2 inactivation and UV-C dose variation across N95 surfaces. Finally, we studied how planar optical attenuators stacked in front of PCIs impact measurement accuracy as a method to increase PCI dynamic range. Given the fundamental tradeoff observed between ideal angular response and attenuation for the two materials we investigated, further investigation into attenuator design (e.g., shaping the diffuse attenuator material [4]) or altered underlying PCI chemistry and reaction kinetics [5] is required prior to implementation. In depth characterization of the impact of environmental factors (e.g., temperature, humidity) on PCI response would also benefit future studies.

The COVID-19 pandemic has heightened interest in utilizing UV-C for applications spanning surface decontamination of personal devices to the interior of airplanes to upper room air treatment. As the market continues to grow, measurement standards to assess UV-C germicidal efficacy are urgently needed, as reports linking UV-C dose to pathogenic inactivation underpin safe and effective implementation. To this end, the International Ultraviolet Association (IUVA) and the National Institute of Standards and Technology (NIST) have partnered to develop UV-C efficacy measurement standards [6]. These standards should help bolster reproducibility and inter-study comparison at both the academic and industry levels, which in turn will underpin the development of safe and effective UV-C decontamination protocols.

Overall, robust, spatially resolved measurements of complex biological and material systems can illuminate heterogeneities otherwise masked by bulk measurements. These heterogeneities are an active and growing area of interest, as exemplified by the recent surge in measurement tools designed for resolving phenomena at the single-cell level. The work presented here focused on the development of measurement tools and workflows to study heterogeneities in two example three-dimensional nanoporous systems. Notably, the fundamental considerations for robust measurement design of each system varied substantially, highlighting the need for quantitative workflows grounded in measurement science and built using a multidisciplinary fundamental framework.

# Bibliography

1. Lazzari, G. *et al.* Light sheet fluorescence microscopy versus confocal microscopy: in quest of a suitable tool to assess drug and nanomedicine penetration into multicellular tumor spheroids. *European Journal of Pharmaceutics and Biopharmaceutics* **142**, 195–203. ISSN: 18733441. doi:10.1016/j.ejpb.2019.06.019 (2019).
2. Reynaud, E. G. *et al.* Light sheet-based fluorescence microscopy: More dimensions, more photons, and less photodamage. *HFSP Journal* **2**, 266–275. ISSN: 19552068. doi:10.2976/1.2974980 (2008).
3. Weber, M., Mickoleit, M. & Huisken, J. *Light sheet microscopy* in *Methods in Cell Biology* 193–215 (Academic Press Inc., 2014). doi:10.1016/B978-0-12-420138-5.00011-2.
4. Pulli, T. *et al.* Software for designing solar UV diffusers, 3 (2013).
5. Mills, A. *et al.* Flagging up sunburn: a printable, multicomponent, UV-indicator that warns of the approach of erythema. *Chemical Communications*, 1345–1346. ISSN: 1359-7345, 1364-548X. doi:10.1039/b900569b (2009).
6. Poster, D. L. *et al.* Innovative Approaches to Combat Healthcare-Associated Infections Using Efficacy Standards Developed Through Industry and Federal Collaboration. *Proceedings of SPIE—the International Society for Optical Engineering* **10730**. ISSN: 0277-786X. doi:10.1117/12.2500431 (2018).



# Appendix A

## Chambered coverslip silanization

**Purpose:** To silanize chambered coverslips to facilitate bonding of polyacrylamide gels on the chambered coverglass surface.

**Materials:**

- Chambered coverslips (ibidi, cat. no. 80427)
- Acetic acid (ACS grade,  $\geq 99.7\%$ , Sigma-Aldrich, cat. no. 695092)
- 3-(Trimethoxysilyl)propyl methacrylate (98%, Sigma-Aldrich, cat. no. 440159)
- Methanol (ACS grade,  $\geq 99.7\%$ ; Sigma-Aldrich, cat. no. 179337)
- Distilled water
- Clean silanization glassware

**Protocol:**

1. Make one batch of silane solution in 250 mL Erlenmeyer flask
  - 50 mL should be enough for 700  $\mu\text{L}$ /well for 16 4-well chambers
  - Use 20 mL syringe to extract 10 mL of silane from stock bottle

Original volumes (mL)	Volumes for small batch silanization (mL)	Component
60	10	3-(Trimethoxysilyl)propyl methacrylate
90	15	Acetic acid
150	25	Deionized water
300	50	Total

2. Degas precursor solution for 10 min in sonicator, connected to the vacuum.
3. Use pipette to add 700  $\mu\text{L}$ /well. Incubate (with lids) for 30 min.
4. Fill 2 glass wash containers with methanol. Fill 2 glass wash containers with deionized water.
5. Remove silane solution from each well using 1 ml pipette and dispose in waste container
6. To wash, shake vigorously in 1) methanol, 2) water, 3) methanol, 4) water. Avoid cross-transfer of wash solutions by shaking chambers lightly and tilting to remove excess liquid before transferring. Wafers can be handled using wafer tweezers to grip the non-chambered ends of the device. After wash is completed, transfer chambers to clean dish of DI water for drying.
7. Dry chambered coverslips using nitrogen stream. If you see a chamber that is dirty and has residual silane, place the chamber back into methanol and water. Dry the chamber again.
8. If important for notekeeping, note the lot number associated with these chambered coverslips and label them accordingly.
9. At the end of the silanization, dispose of MeOH in hazardous waste and rinse all glassware 3 $\times$  with deionized water before taking to the glasswash.
10. Clean all used glassware in glasswash (rooms B227, 235, 430).
  - Do not put the non-glass lids or funnels into the glasswash. Rinse with water.

## Appendix B

# Recommended reporting summary for studies using UV-C

Recommended reporting summary for authors sharing research on UV-C decontamination of N95 respirators to support dissemination of accurate and reproducible UV-C decontamination protocols.

## UV-C Author Reporting Summary

This form provides structure for reproducibility and transparency in reporting on studies of viral inactivation by UV-C irradiation. Because equipment for UV-C based decontamination is not standardized and actual UV-C dose depends on numerous factors, it is important for accuracy and reproducibility to report the physical parameters as outlined below. There are additional factors that may affect the efficacy of this technique, such as N95 style, layout, and N95 model. This checklist also does not evaluate filtration efficiency or N95 degradation from the decontamination process.

### Hardware

#### 1. UV Source

Make (brand) and model number  Yes  No

*State where this information is in the text*

*Explain why this information is not reported/not relevant*

Type of source  Yes  No

*State where this information is in the text*

*For instance: mercury lamp, xenon lamp, LED, etc.*

*Explain why this information is not reported/not relevant*

Dimensions of the source  Yes  No

*State where this information is in the text*

*Dimensions of emission source can be important for determining the angular variation in UV-C illumination. For instance: mercury lamp arc length (m) from electrode tip to electrode tip.*

*Explain why this information is not reported/not relevant*

State wavelengths emitted, and either show or reference an emission spectrum  Yes  No

*State where this information is in the text*

*Explain why this information is not reported/not relevant*

#### 2. Optical Detector

Radiometer and sensor probe: make and model, wavelength range, calibration  Yes  No

*State where this information is in the text*

*Explain why this information is not reported/not relevant*

*For instance: "An ILT-1254 radiometer (International Light Technologies), which measures 254 nm wavelengths, was used to measure UV-C irradiance. The radiometer is calibrated annually according to manufacturer's instructions."*

Any filters, diffusers, cosine correctors, or other optical elements attached to the sensor; brand and model number; specifications (e.g., wavelength range); purpose  Yes  No

*State where this information is in the text*

*Explain why this information is not reported/not relevant.*

*For instance: "To specifically quantify UV-C irradiance, the spectroradiometer was fitted with a 254 nm shortpass filter (Newport HG-SC-OEM) to block out wavelengths above 254 nm."*

**Data and Reporting**

3. The authors report:

Confirmed	n/a	
<input type="checkbox"/>	<input type="checkbox"/>	Distance between UV-C source and UV-C detector
<input type="checkbox"/>	<input type="checkbox"/>	Exposure time
<input type="checkbox"/>	<input type="checkbox"/>	Measurement of UV-C dose at the treated substrate
<input type="checkbox"/>	<input type="checkbox"/>	Calculations of UV-C dose (J/cm <sup>2</sup> ) at the treated substrate, using measured irradiance and exposure time <i>If UV-C dose was calculated from measured irradiance and time, please describe in the manuscript what irradiance measurements were used and any assumptions involved in the dose calculation (e.g., irradiance measurements collected throughout the exposure time, or a single irradiance measurement which was assumed to stay constant throughout exposure). Please discuss whether the calculated dose may be an over- or under-estimate, in light of any assumptions made. Because the output of a UV-C source can vary over time [ASTM E3179-18], best practice is to measure irradiance throughout the exposure period.</i>
<input type="checkbox"/>	<input type="checkbox"/>	Details about setup and methods: spatial arrangement of N95 respirators relative to UV-C source, any chamber/room reflectivity, and characterization of UV-C dose distribution across entire area in which respirators are placed
<input type="checkbox"/>	<input type="checkbox"/>	Is the minimally-acceptable dose applied to both sides of the respirator?

4. Terminology

Confirmed	n/a	
<input type="checkbox"/>	<input type="checkbox"/>	Irradiance measurements (W/cm <sup>2</sup> ) are described as <i>irradiance</i> or <i>fluence rate</i>
<input type="checkbox"/>	<input type="checkbox"/>	Dose measurements (J/cm <sup>2</sup> ) are described as <i>dose</i> or <i>fluence</i> <i>Please note that "dosage" is a redundant term for "dose" that should be avoided [IUVA].</i>

5. Measurement of viral inactivation

Confirmed	n/a	
<input type="checkbox"/>	<input type="checkbox"/>	Measured viral inactivation is tied to UV-C dose at the substrate surface (not exclusively exposure time)

6. N95 Facepiece and Straps

Results indicate that UV-C can sufficiently decontaminate both sides of N95 facepiece	<input type="checkbox"/> Yes <input style="width: 150px;" type="text" value="State where this information is in the text"/> <input type="checkbox"/> No <input style="width: 150px;" type="text" value="Explain why this information is not reported/not relevant"/>
Authors state position of straps and that straps may require secondary decontamination	<input type="checkbox"/> Yes <input style="width: 150px;" type="text" value="State where this information is in the text"/> <input type="checkbox"/> No <input style="width: 150px;" type="text" value="Explain why this information is not reported/not relevant"/>

*UV-C has been found to be less effective in decontaminating N95 FFR straps [Mills et al., 2018; Heimbuch & Harnish, 2019]. If viral inactivation testing of straps was not performed or found effective, authors should state that secondary decontamination of straps may be required.*

**The Content provided is for INFORMATIONAL PURPOSES ONLY, DOES NOT CONSTITUTE THE PROVIDING OF MEDICAL ADVICE and IS NOT INTENDED TO BE A SUBSTITUTE FOR INDEPENDENT PROFESSIONAL MEDICAL JUDGMENT, ADVICE, DIAGNOSIS, OR TREATMENT.**